Structural Studies of Defects in Two-Dimensional Materials with Atomic Resolution

Qu Chen

Supervised by Professor Jamie H. Warner

Submitted in conformity with the requirements

for the degree of DPhil in Materials Science

Department of Materials

St Peter's College

University of Oxford

September 2017

Declaration

The material contained within this thesis has not previously been submitted for a degree at the University of Oxford or any other university. The research reported within this thesis has been conducted by the author unless indicated otherwise.

Copyright Notice

Abstract

Defective structures in two-dimensional (2D) materials have been proved to have significant influences on the materials' properties. Understanding structural defects in 2D materials at atomic scale is therefore required. With the use of advanced imaging techniques, one of the main approaches applied in this project was aberration-corrected transmission electron microscopy (AC-TEM), the structures are able to be resolved with single-atom sensitivity with the reduction of both spherical aberration and the influence of chromatic aberration. This laid the foundation for the first two experiments, which involve the bond length measurement of each C-C bond within three types of divacancies and Si-C bonds at graphene edges. The former explains the tendency of bond rotations within the divacancies from the perspective of strain inside the defective areas and surrounding lattice; the latter revels the interactions between isolated Si atoms and zigzag/armchair graphene edges.

The use of *in-situ* heating holder in the AC-TEM makes the direct visualization of structures and their dynamics at elevated temperatures possible. The Si-graphene edge interactions, as well as the following two experiments are all designed to study the high-temperature performances for different systems. Gold nanoclusters are introduced to monolayer graphene by thermal evaporation to study the interaction between gold and graphene at elevated temperature. Due to the strong interaction between gold and graphene, gold crystals are able to adapt to planar configurations with two different crystalline forms, and an epitaxial relationship was found for planar gold crystals and graphene. Atomically flat and long line defects and zigzag edges in monolayer molybdenum disulfide (MoS_2) are successfully created by in-situ thermal annealing. The relationship between S vacancy mobility and defect forms are revealed

based on the experiment. High-temperature atomic configurations of line defects and edge terminations are resolved in the first time. Their electronic properties are also explored with the support of density functional theory calculations.

Acknowledgement

First of all, I would like to express my sincere appreciation to my supervisor, Prof. Jamie Warner. It is truly an honour for me to do research in your group. Your guidance and encouragement during the three years have been priceless. The knowledge and skills I have learned from you, especially on electron microscopy, will no doubt benefit me for my research career in the future.

I would also like to thank my collaborators who have greatly supported me on my research. I would like to dedicate my gratitude to Prof. Angus Kirkland for his brilliant comments and suggestions, especially on the crystallography; to Prof. Gun-do Lee at Seoul National University, Prof. Jeffery Grossman and Dr. Huashan Li at Massachusetts Institute of Technology, for their substantial contributions on theoretical calculations which have been crucial for my research; and to Dr. Hidetaka Sawada for providing essential data with his exquisite skills on scanning transmission electron microscopy.

I also want to thank my colleagues, Dr. Alex Robertson, Dr. Kuang He, Dr. Chuncheng Gong, Dr. Christopher Allen, Dr. Ye Fan, Dr. Shanshan Wang, Miss Wenshuo Xu and Dr. Jakyung Lee, for your selfless assistance throughout my PhD project. I would also like to thank all the other colleagues of mine: Miss Yingqiu Zhou, Miss Sha Li, Dr. Zhengyu He, Dr. Youmin Rong, Mr. Xiaochen Wang, Mr. Yuewen Sheng, Mr. Thomas Samuels, Mr. Hefu Huang, Mr. Martin Tweedie, Mr. Si Zhou, Mr. Ren-Jie Chang, Mr. Tongxin Chen. Working and also being friends with you during these years has been such an enjoyable and memorable experience in my life.

A special thank to my family: my father and mother, and my grandparents. My doctorate project would not be accomplished without your support in all aspects. At the very end I would like to express my gratitude to my boyfriend, Mr. Haijie Tan. Your companionship and moral support in every single moment has been truly precious to me.

Publications

This section lists the published works (or currently under review/close to submission) during the course of this doctorate project. Some of the first-authored and all the co-authored work listed below are not within the scope of the discussion in this thesis. A specific publication is labelled where a relevant content is described.

Chapter 4

(1) **Chen, Q.**; Robertson, A. W.; He, K.; Gong, C.; Yoon, E.; Lee, G. D.; Warner, J. H. Atomic Level Distributed Strain within Graphene Divacancies from Bond Rotations. *ACS Nano* **2015**, *9*, 8599–8608.

(2) **Chen, Q.**; Robertson, A. W.; He, K.; Gong, C.; Yoon, E.; Kirkland, A. I.; Lee, G. D.; Warner, J. H. Elongated Silicon–Carbon Bonds at Graphene Edges. *ACS Nano* **2015**, *10*, 142–149.

Chapter 5

(3) **Chen, Q.**; He, K.; Robertson, A. W.; Kirkland, A. I.; Warner, J. H. Atomic Structure and Dynamics of Epitaxial 2D Crystalline Gold on Graphene at Elevated Temperatures. *ACS Nano* **2016**, *10*, 10418–10427.

Chapter 6

(4) **Chen, Q.**; Li, H.; Xu, W.; Wang, S.; Sawada, H.; Allen, C. S.; Kirkland, A. I.; Grossman, J. C.; Warner, J. H. Atomically Flat Zigzag Edges in Monolayer MoS_2 by In-situ Thermal Annealing. *Nano Letters* **2017**, *17*, 5502-5507.

(5) **Chen, Q.**; Li, H.; Zhou, S.; Xu, W.; Sawada, H.; Allen, C. S.; Kirkland, A. I.; Grossman, J. C.; Warner, J. H. Ultralong 1D Atomic Channels for Rapid Vacancy Migration During 2D Void Formation in Monolayer MoS_2. About to submit.

First-Author

(6) **Chen, Q.**; Koh, A. L.; Robertson, A. W.; He, K.; Lee, S.; Yoon, E.; Lee, G. D.; Sinclair, R.; Warner, J. H. Rotating Anisotropic Crystalline Silicon Nanoclusters in Graphene. *ACS Nano* **2015**, *9*, 9497–9506.

Co-Author

(7) Robertson, A. W.; Lee, G. D.; He, K.; Gong, C.; **Chen, Q.**; Yoon, E.; Kirkland, A. I.; Warner, J. H. Atomic Structure of Graphene Subnanometer Pores. ACS Nano **2015**, *9*, 11599–11607.

(8) Tan, H.; Fan, Y.; Zhou, Y.; **Chen, Q.**; Xu, W.; Warner, J. H. Ultrathin 2D Photodetectors Utilizing Chemical Vapor Deposition Grown WS_2 with Graphene Electrodes. *ACS Nano* **2016**, *10*, 7866–7873.

(9) Gong, C.; He, K.; Lee, G. D.; **Chen, Q.**; Robertson, A. W.; Yoon, E.; Hong, S.; Warner, J. H. In Situ Atomic Level Dynamics of Heterogeneous Nucleation and Growth of Graphene from Inorganic Nanoparticle Seeds. *ACS Nano* **2016**, *10*, 9397–9410.

(10) Gong, C.; He, K.; **Chen, Q.**; Robertson, A. W.; Warner, J. H. In Situ High Temperature Atomic Level Studies of Large Closed Grain Boundary Loops in Graphene. *ACS Nano* **2016**, *10*, 9165–9173.

(11) Robertson, A. W.; Lin, Y. C.; Wang, S.; Sawada, H.; Allen, C. S.; **Chen, Q.**; Lee, S.; Lee, G. D.; Lee, J.; Han, S.; et al. Atomic Structure and Spectroscopy of Single Metal (Cr, V) Substitutional Dopants in Monolayer MoS2. ACS Nano **2016**, 10, 10227–10236.

(12) Wang, S.; Sawada, H.; **Chen, Q.**; Han, G. G. D.; Allen, C.; Kirkland, A. I.; Warner, J. H. In Situ Atomic-Scale Studies of the Formation of Epitaxial Pt

Nanocrystals on Monolayer Molybdenum Disulfide. ACS Nano **2017**, *11*, 9057–9067.

(13) Fan, Y.; Robertson, A. W.; Zhou, Y.; **Chen, Q.**; Zhang, X.; Browning, N. D.; Zheng, H.; Rümmeli, M. H.; Warner, J. H. Electrical Breakdown of Suspended Mono- and Few-Layer Tungsten Disulfide via Sulfur Depletion Identified by in Situ Atomic Imaging. *ACS Nano* **2017**, *11*, 9435–9444.

(14) Tan, H.; Xu, W.; Sheng, Y.; Lau, C. S.; Fan, Y.; **Chen, Q.**; Tweedie, M.; Wang, X.; Zhou, Y.; Warner, J. H. Lateral Graphene-Contacted Vertically Stacked WS_2/MoS_2 Hybrid Photodetectors with Large Gain. *Adv. Mater.* **2017**, 1702917.

Table of Contents

Chapter 1

Introduction

1.1 Project Aims

The objective of this doctorate project has been to study the configurations and dynamics of defective structures, including intrinsic point and linear defects, as well as isolated and clustered dopant atoms in monolayer graphene and MoS_2 with single-atom-sensitivity at both ambient and elevated temperatures.

1.2 The Scope of This Thesis

This thesis covers the research carried out over the 3-year course at the Department of Materials and St. Peter's College, University of Oxford. The supportive theoretical calculations have been performed by Professor Gun-Do Lee's group at Seoul National University and Dr. Huashan Li at Massachusetts Institute of Technology. The annular dark-field (ADF) images have been taken by Dr. Hidetaka Sawada at electron Physical Sciences Imaging Centre (ePSIC) at Diamond Light Source.

A literature review mainly focusing on the structural study of 2D materials is present in Chapter 2. It also includes a brief overview of the synthesis methods established for 2D materials and the development of transmission electron microscopy (TEM).

Chapter 3 lists the experimental parameters and procedures that have been applied to this doctorate project, which include synthesis of monolayer graphene and MoS_2 via

chemical vapour deposition (CVD) approach, TEM sample preparation, AC-TEM imaging and data analysis methods.

Imaging of graphene lattice with atomic resolution can be achieved with the use of Oxford-Jeol 2200MCO AC-TEM after both spherical and chromatic aberration are adequately corrected. This makes it feasible to precisely measure the distances between the atoms, which are valuable information for quantitative evaluation of the interactions among the atoms. In Chapter 4, bond length measurement is carried out to investigate two systems: 1) three types of divacancies are studied by exploring the C-C bond length variations within the defects and strain distributions in the surrounding hexagonal lattice, and 2) several silicon-graphene edge interactions are reported with details on Si-C distances along both armchair and zigzag edges.

Except for the study of divacancies described in Chapter 4, all the other experiments have been done with a commercially available heating holder developed by DENS Solutions, which enables the *in-situ* observation of the structures and behaviours of the targets up to 800 °C. The interaction between monolayer graphene and gold nanoclusters introduced by thermal evaporation is described in Chapter 5, where an epitaxial correlation between gold crystalline phases and graphene is discovered. Another 2D material, monolayer MoS_2, is studied in Chapter 6. A simple approach for creating atomically flat and long line defects and zigzag edges in monolayer MoS_2 is realised by *in-situ* heating MoS_2 to 800 °C in vacuum.

Chapter 7 gives a conclusion for the whole thesis as well as an outlook of potential research directions within the field of structural study of defects in 2D materials.

Chapter 2

Literature Review

2.1 Introduction

This Chapter reviews the research field of 2D materials, with particular attention on the structural study of defects in graphene and transition metal dichalcogenides (TMDs) with the use of advanced imaging technologies such as aberration-corrected transmission electron microscopy (AC-TEM) and scanning transmission electron microscopy (STEM). Exploration of the structures *via* theoretical approach is also included, as well as the fabrication methods of layered materials.

2.1.1 An Overview of 2D Materials

The isolation of single-layer graphene in 2004 opened the door for the exploration of 2D materials.[1] 2D materials, as its name, are crystals with a single layer of atoms. So far, more than 600 materials have been theoretically predicted to possess sufficient stability in 2D form, most of which remain to be produced in the real life.[2]

Graphene owns a 2D-honeycomb structure composed of sp^2-coordianted carbon atoms (Figure 2-1(a,b)). The unique and versatile properties of graphene, including high transparency,[3] good thermal conductivity[4,5] and tremendous mechanical strength[6] have drawn enormous attraction from both scientific and industrial fields.[7,8] The electronic properties of graphene is most intriguing. It is a zero band gap semiconductor or namely, semi-metal. This unique band gap guarantees the high electron mobility[9] but it also lays a challenge when using graphene as a semiconductor in electronic devices

such as field effect transistor (FET). Therefore various approaches have been explored to open a band gap in graphene to further deploy the applications of graphene.[10–15] So far, graphene and its derivatives have been widely explored in biological engineering, optical electronics, composite materials and energy storage areas with outstanding progress.[16–18]

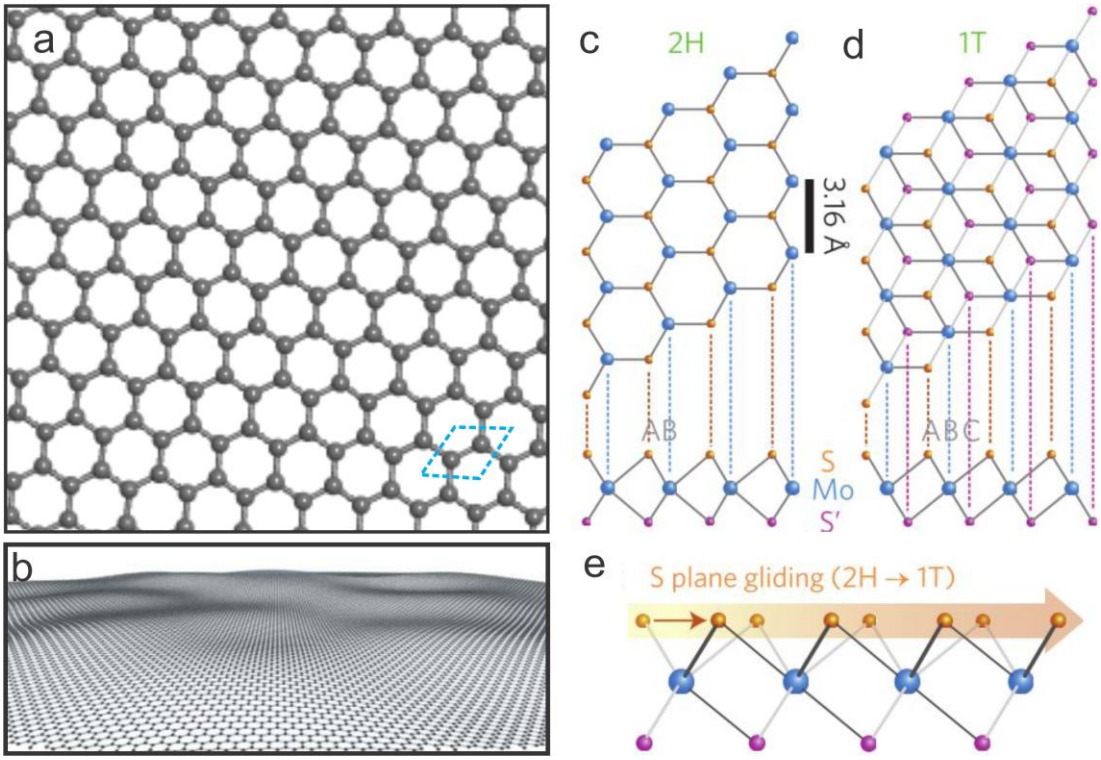

Figure 2-1 Atomic illustrations of 2D materials. (a) Atomic model for monolayer graphene with the unit cell highlighted in blue dashed rhomb. (b) A schematic for corrugated graphene with the roughness imitated to the experimental results. Adapted with permission from ref [22]. © 2007 Nature Publishing Group. (c-e) 2H phase, 1T phase, and 2H to 1T phase transition of MoS_2. Adapted with permission from ref [23]. © 2014 Nature Publishing Group.

Some 2D materials are composed of two elements, such as transition metal dichalcogenides (TMDs) and hexagonal boron-nitride (h-BN). Monolayer TMDs are of the type of MX_2, with M a transition metal atom (Mo, W, Nb, Ta, Sn) and X a chalcogen atom (S, Se and Te).[19] Accurately speaking, this type of 2D materials is of three-atom thick, as the transition metal atoms are sandwiched between two layers of

chalcogen atoms. Two phases have been observed in monolayer TMDs. The more commonly seen one is 2H phase (Figure 2-1(c)), which is semiconducting; the other phase is metallic 1T phase (Figure 2-1(d)). The transition between the two phases is achieved by the glide of one layer of S atoms (Figure 2-1(e)). Monolayer TMDs are semiconductors with direct band gaps between 1-2 eV,[19–21] allowing TMDs to be directly applied in electronics as transistors and in optics as emitters and detectors.[16]

2D materials are able to be synthesized by either top-down or bottom-up strategy, and each category includes various approaches. Top-down fabrication is breaking the van der Waals forces between the layers of a crystal to isolate single or a few layers of the material. This can be achieved by either physical- (Figure 2-2(a,b)) or chemical-based (c) processes. Novoselov and Geim used micromechanical exfoliation to fabricate single-layer graphene for the first time.[1] Since then, other 2D materials including MoS_2,[24] WS_2,[25] and h-BN[24,26] have also been fabricated with the use of scotch tapes. It is a straightforward method which fairly maintains the structure and properties, but the challenge is this method has not been able to scale up for industrial production. Ultrasonic wave has also been applied to induce the exfoliation of van der Waals solids. A suitable solvent and appropriate sonication time are the priorities for a successful exfoliation. So far, tens of solvents have been investigated in order to produce 2D materials with good qualities.[27–32] Although ultrasonic exfoliation is more effective than micromechanical exfoliation, the challenge is to avoid reaggregation and sedimentation of the products. Formation and exfoliation of ionic crystals, for example Li_xMS_2 compound, has been established for fabricating monolayer TMDs with the yield nearly 100%.[33,34] Lithium ions are applied as intercalated layers between the layers of van der Waals crystals, which induce the production of single-layer crystals during agitation.[35] Bottom-up strategies constructs 2D materials from atoms provided

by precursors. In contrast with top-down methods, bottom-up approaches allow 2D crystals grow into larger sizes with designed shapes at a larger scale. Chemical vapour deposition (CVD) has been one of the most commonly used method to grow graphene and other 2D materials. The pioneer of synthesizing thin graphite films by CVD was May, who used Pt as the substrate in 1969.[36] So far, numerous metallic substrates have been explored to grow single-layer graphene including Ni,[37–41] Cu,[42–50] Fe,[51] Co,[52] Ru,[53] Ir,[54] Au[55] and Pd.[56] TMDs and h-BN have also been synthesized and large pieces of continuous film have been able to be achieved by this approach (Figure 2-2(d)).[57–64] 2D materials heterostructures have also been successfully obtained by directly growing a different type of 2D material on the top of the first layer.[65]

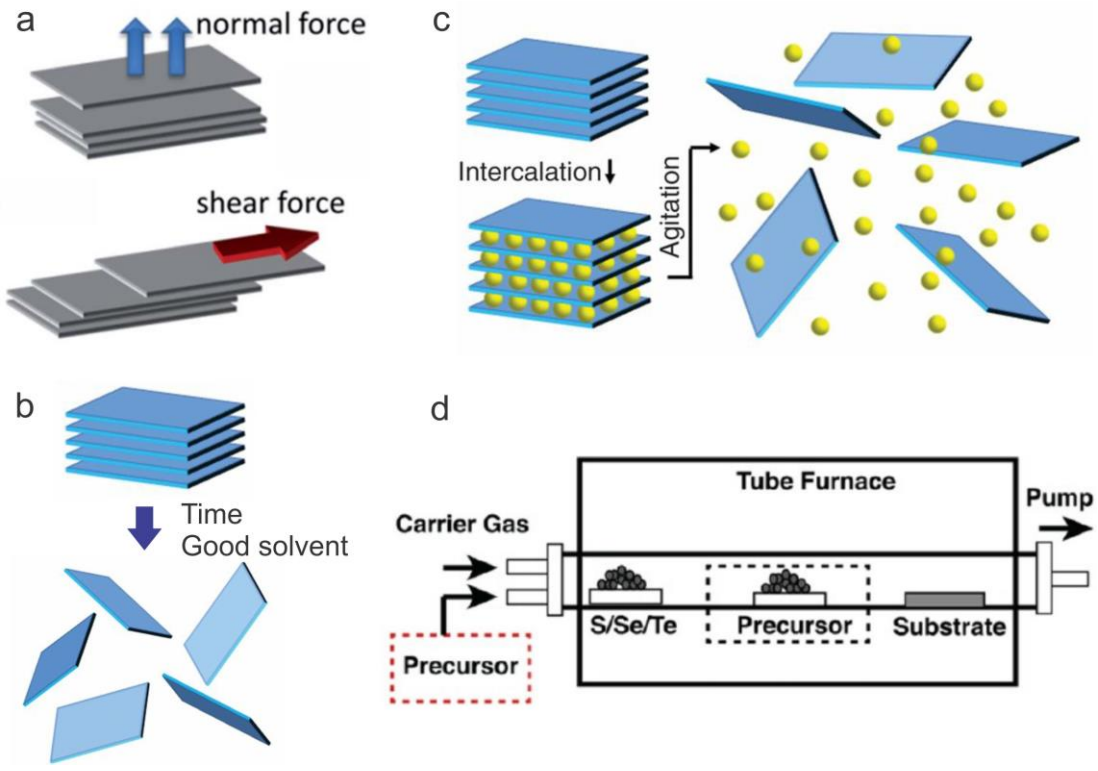

Figure 2-2 Schematic illustrations of top-down (a-c) and bottom-up (d) strategies for the synthesis of 2D materials. (a) Micromechanical exfoliation. Adapted with permission from ref [66]. © 2015 The Royal Society of Chemistry. (b) Ultrasonic exfoliation. Adapted with permission from ref [27]. © 2013 American Association for the Advancement of Science (AAAS). (c) Ion intercalation. Adapted with permission from ref [27]. © 2013 American

Association for the Advancement of Science (AAAS). (d) CVD. Adapted with permission from ref [67]. © 2013 American Chemical Society.

2.1.2 High-Resolution Imaging Technology

2D materials are ideal candidates for defect studies with atomic resolution due to their one to few-atom thicknesses. The most common techniques for structural studies of 2D materials have been scanning tunnelling microscopy (STM),[68–71] TEM[72–81] and STEM.[74,82–87] and this section focuses on the history and principles of the latter two technologies.

TEM has long been considered as a powerful approach for the exploration of lattice deformation in crystals. The very first prototype of electron microscope was proposed by Knoll and Ruska in 1932,[88] which was an extremely crucial step after the wave nature of electrons was experimentally confirmed in 1927.[89,90] The production of commercial TEMs was initiated from 1939 by Siemens and Halske in Germany. Other companies including Hitachi, JEOL and Philips joined the development of the technique after the end of World War II. The resolution of the electron microscope has been the key indicator for the progress of the technology, from around 10 nm in late 1930s, to sub-nanometer in 1960s, and further to 80 pm achieved in the state-of-the-art high-resolution TEM (HRTEM) in recent years.[91] Increasing the accelerating voltage of the electron beam was one important approach for the improvement of the resolution in the early age, but it was then realised that voltage was not everything. The improvement of electron lens technology and the introduction of aberration correction to traditional TEM further boosted the resolving power. Two aberrations have been found to exist in a TEM: spherical (C_S) and chromatic aberration (C_C). Spherical aberration arises when high-angle rays are brought to a premature focus by lens aberrations so that a point object appears as a blurred disk in the image plane.[92] In

1994 Rose proposed a solution for spherical aberration correction for electron microscope, which stunningly enhanced the image resolution.[93] The idea behind the spherical aberration corrected electron microscopes is to introduce a corrector that produces negative spherical aberration, which counteracts the positive aberration of the objective lens to give a total reduced spherical aberration. In practice, taking Oxford's JEOL JEM-2200MCO TEM for example, it is implemented by the addition of two hexapole lenses, with both creating a negative C_S, and the second one reducing the three-fold aberration given rise by the first hexapole. Once C_S is corrected, the issue of C_C needs to be addressed in order to further improve spatial resolution. A monochromator for the electron source is used to decrease the energy dispersion of the electron beam source, further increasing the resolution of a TEM.[94] The energy spread is able to be confined about 0.2 eV for a field emission gun (FEG).

The maturity of the aberration-corrected TEM (AC-TEM) has been provided the opportunity for the observation of 2D materials with sufficient resolution at low accelerating voltage. In 2008, 1Å resolution was achieved by Meyer and his colleagues at the accelerating voltage of 80 kV in an AC-TEM,[73] which has led to further explorations on the structures and real-time dynamics of defects in graphene and other 2D materials with atomic resolution.[91,95]

STEM is a specific type of TEM, which uses focused electron beam raster-scanning over the specimen. This makes STEM suitable for Z-contrast annular dark field (ADF) imaging, a more straightforward approach than TEM to image 2D materials composed of more than one elements, including TMDs and h-BN, as one can directly distinguish the different elements only based on the contrasts. The first STEM was developed by von Ardenne in Berlin in 1938.[96,97] However the development of the technology

creased until 1970s, when Crewe and his colleagues built a field emission electron source for STEM and visualised single heavy atoms on a thin carbon film.[98,99] By the early 1990s, better than 2Å resolution was achieved based on the development of STEM technology, indicating the possibility of direct imaging of atomic structures in some materials systems.[100] The electron probes is able to be focused to sub-angstrom diameter with the combination of an aberration corrector, which boosted the resolution of STEM. In 2000, Dellby and co-workers presented 1.23 Å resolution in high-angle annular dark field (HAADF) images at 100 kV.[101] A more advanced AC-STEM was then developed with 0.5 Å information limit.[102] For the application of STEM on 2D materials atomic structural study, numerous publications can be found in recent years with single-atom sensitivity.[103–105]

2.2 Defects in Graphene

Lattice imperfections are always present in crystalline materials, greatly influencing the electronic, thermal and optical properties. The isolation of graphene initiated a massive body of research on structural defects with the use of modern imaging technologies, and efforts have been made to deliberately introduce such imperfections to manipulate the material's performances.[106] The structural defects in monolayer graphene fall into two main categories: intrinsic and extrinsic, based on whether foreign atoms are involved into the pure carbon system.

2.2.1 Intrinsic defects

Intrinsic defects in graphene include point defects and line defects. Point defects are zero-dimensional, including bond rotations and vacancies, whereas dislocations and grain boundaries are considered as 1D line defects. It has been confirmed that without

the introduction of foreign impurities, the intrinsic defects themselves in graphene are able to tailor the performances of graphene.[107]

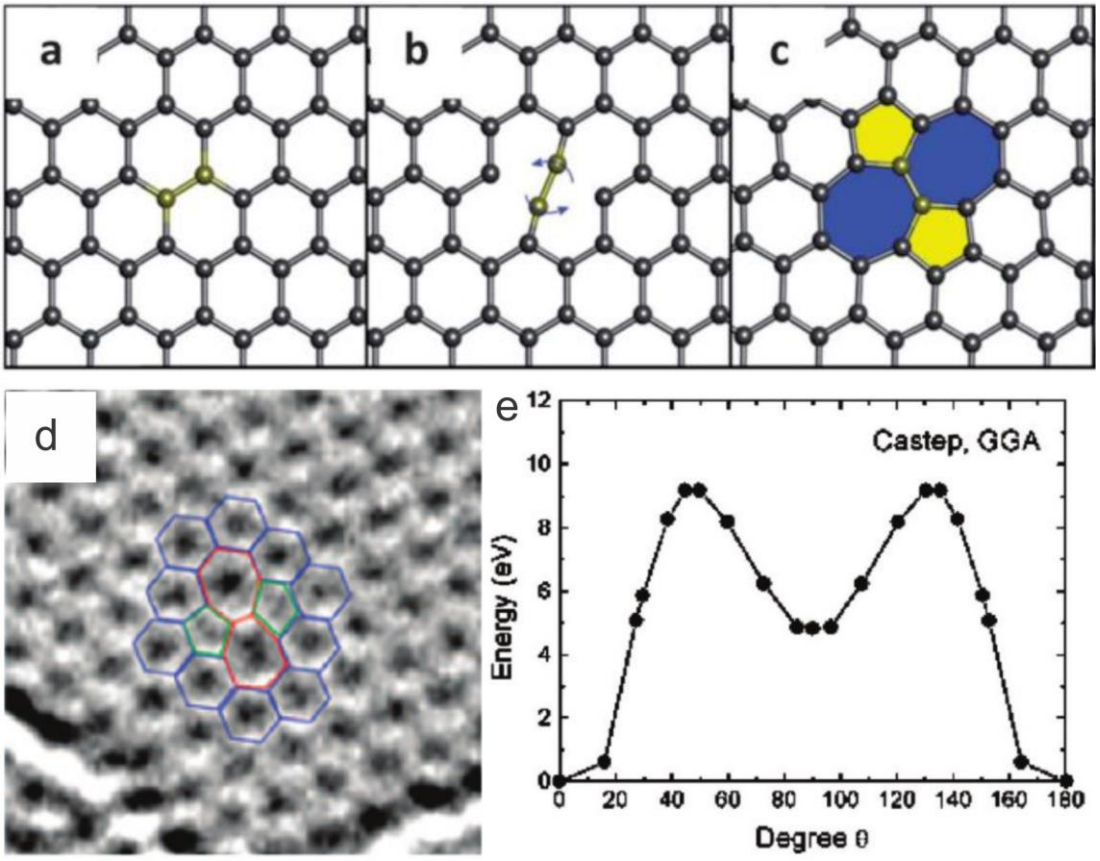

Figure 2-3 (a-c) Schematics of a SW defect formation. Adapted with permission from ref [72], © 2013 The Royal Society of Chemistry. (d) TEM image of a SW defect highlighted in red and green lines. Adapted with permission from ref [73]. © 2008 American Chemical Society. (e) Calculated energy profile for the bond rotation. Adapted with permission from ref [110]. © 2005 American Physical Society.

Without losing or adding atoms, graphene lattice is able to from non-hexagonal rings by in-plane bond rotation. The most basic unit generated by a single rotation is called Stone-Wales (SW) defect, named after Anthony Stone and David Wales who theoretically predicted this type of defect in fullerene.[108] Two pentagonal and two heptagonal rings (55-77) arise after the 90° rotation of a C-C bond, as shown in Figure 2-3(a-d). The SW rotation is calculated to have a formation energy E_f around 5 eV, with the kinetic barrier of the transformation *via* an in-plane bond rotation of 9-10 eV

(Figure 2-3(e)).[109,110] The electron beam impact during imaging in TEM may be responsible for the observation of SW defect. A SW defect not only been observed within pristine graphene lattice, but also within the area where a defect structure has already existed, such as a divacancy (two adjacent C atoms are missing) and multivacancies with three or more C atoms absent.[111,112]

Vacancies in graphene generate when C atom(s) leave their lattice positions completely without recombination. The terminology of the vacancies is based on the number of removed C atoms, from monovacancy (MV), where only a single C atom misses, to tetravacancies, which involve the absence of four adjacent C atoms. Vacancies with even more evaporated atoms are usually sorted into pores rather than vacancies. The complexity of the vacancies is positively correlated with the number of absent atoms, as in some cases the involvement of bond rotations can lead to many derivatives.[112]

MV has been directly observed by TEM and STM in graphene, carbon nanotubes and graphite.[69,73,86,113] A Jahn-Teller distortion has been theoretically predicted and then experimentally observed in a MV, which means that two of the three unsaturated C atoms in a MV tend to move towards each other to form a new bond, resulting in the formation of a closed pentagonal and a nonagonal ring with only one undersaturated carbon atom left (Figure 2-4(a)).[113–119] The reconstructed MV has been predicted to be ~0.2 eV lower than the original monovacancy, with the undersaturated carbon atom undergoing a slight out-of-plane shift of 0.5 Å..[69,115] The calculated formation energy for a MV in graphite is about 7.5 eV, while the energy required for its migration is only 1.5 eV.[115,120] The easy migration of MV provides the opportunity for the formation of other vacancies. DFT (density functional theory) and TBMD (Tight-

binding molecular-dynamics) simulations have derived that the magnetic moment of a monovacancy in graphene is about 1.10 μ_B.[119,121,122]

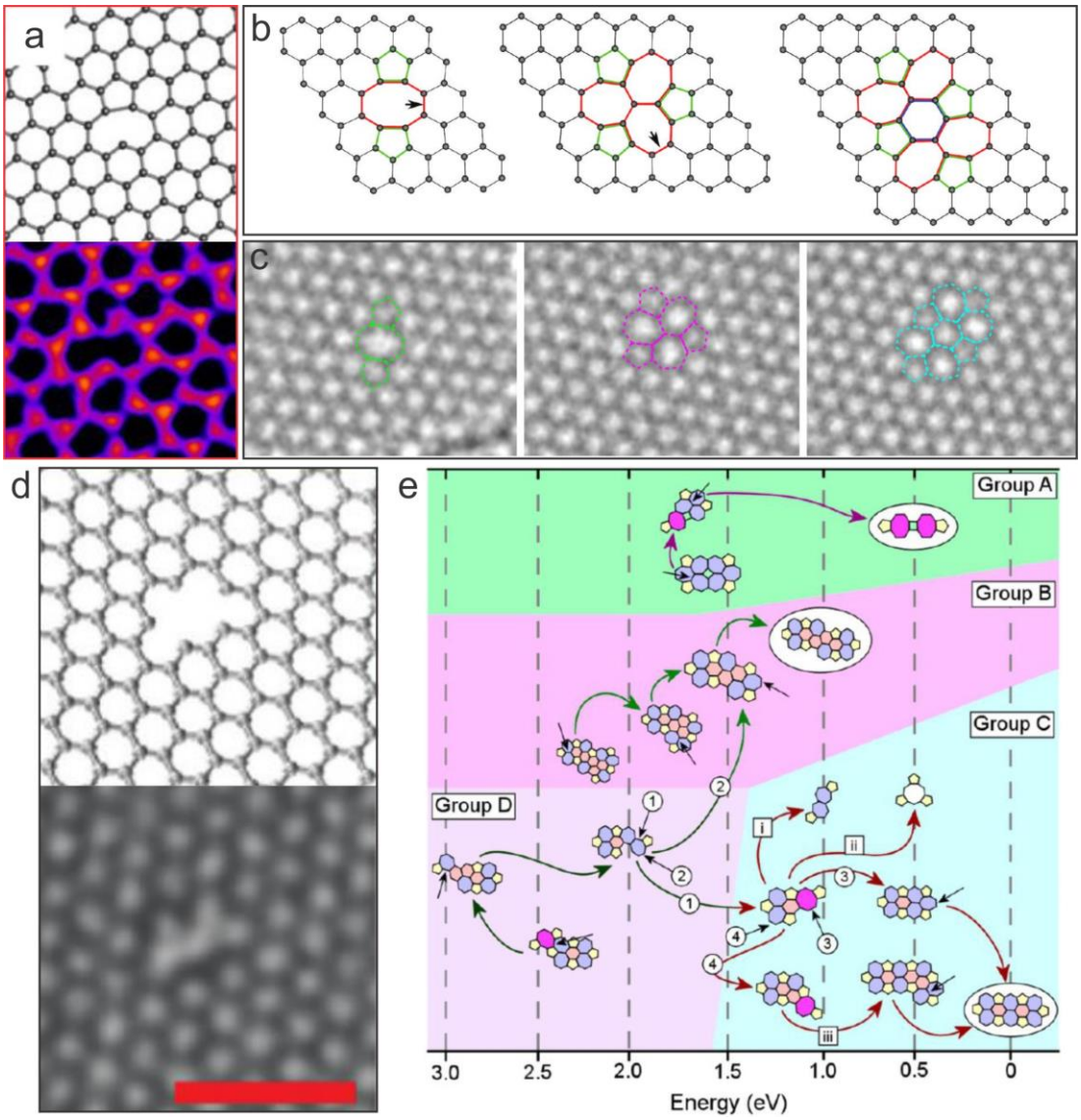

Figure 2-4 Vacancies observed in graphene. (a) Atomic model and AC-TEM image of a MV after the Jahn-Teller reconstruction. Adapted with permission from ref [113]. © 2013 American Chemical Society. (b) Illustrations of the evolution of DVs from 5-8-5 to 555-777 to 5555-6-7777 configuration. Adapted with permission from ref [132]. © 2011 American Chemical Society. (c) TEM images of the three DVs. Adapted with permission from ref [124]. © 2011 American Physical Society. (d) Atomic model and TEM image of a trivacancy. Adapted with permission from ref [133]. © 2009 American Chemistry Society. (e) Pathways for SW rotations in tetravacancies which lead to the most frequently observed configurations (circled). Adapted with permission from ref [112]. © 2014 American Chemistry Society.

Divacancy (DV) is formed by the absence of two adjacent carbon atoms in graphene lattice. An original DV consists of two pentagonal rings and an octagonal ring between them (5-8-5), with all the C atoms saturated.[106,123,124] In addition to the 5-8-5 configuration, two more derivatives of DV with one (555-777) or two times (5555-6-7777) of SW rotations have been observed (Figure 2-4(b,c)).[125–128] Theoretical calculation has indicated 555-777 DV to be 0.93 eV more stable than 5-8-5 DV.[129] Unlike mobile MVs, DVs are far more stubborn with a higher migration barrier of 7 eV.[115]

Investigations have also been made on multivacancies which contains three (Figure 2-4(d)) or more missing C atoms. Vacancies with even number of evaporated C atoms (V_{even}) guarantee the saturation of all C atoms within the defects by slight lattice distortion, whereas at least one dangling bond is present for the case of V_{odd}. Therefore generally speaking, V_{even} defects are more energetically stable than V_{odd}.[130] Wang et al. reported a method for the creation of large vacancies including trivacancies by gold ion/atom bombardment with narrow energy distribution.[131] Roberson et al. thoroughly analysed the structures of 17 types of tetravacancies generated by a focused electron beam for a short period of time in TEM (Figure 2-4(e)).[112] The variety of tetravacancy configurations is contributed by the multiple C–C bonds in a tetravacancy that can undergo SW rotations.

The terminology ‘dislocation’ was firstly proposed by Taylor in 1934 when he tried to explain the plasticity of materials.[134] Two types of dislocations, edge and screw dislocation have been confirmed to present in bulk materials, whereas only the former one appears in graphene due to its 2D nature. Dislocations were firstly observed in TEM by Hirsch in 1956,[135,136] and since then TEM has been widely used for the study

of dislocations. Real-time monitoring of edge dislocations in bulk materials at the atomic scale has never been experimentally achieved due to the thickness of samples. The study of dislocations in graphene, on the contrary, provides an insight of the atomic structures and dynamics of dislocations (Figure 2-5(a-f)). The formation energy of an isolated (1, 0) dislocation core has been predicted to be 6-7 eV,[137,138] therefore they are likely to generate in the graphene lattice under electron beam irradiation. A low accelerating voltage has always been applied to TEM for the observation of dislocation for graphitic materials.[124,139–143] The dislocation in graphene was observed with single-atom sensitivity by Warner in 2012, with the climb and glide motions of a dislocation captured by time sequential TEM frames for the first time.[91]

A grain boundary (GB) forms when two grains with different orientations encounter with each other. Graphene specimens synthesized by CVD have always been polycrystalline with numerous as-grown GB. By selecting the specific diffraction spots for the grains with the use of an objective aperture filter in dark-field imaging mode, grains with different orientations in a polycrystalline graphene were clearly distinguished (Figure 2-5(g)).[87] Detailed atomic structures of GB in graphene have been directly observed by (S)TEM. An alternating pentagon-heptagon chain was imaged between two grains with 27° relative rotation (Figure 2-5(h)).[87] Similar results have also been reported by other researchers.[144–147] Another configuration, 5-8-5 linear GB, was found by Lahiri in CVD grown graphene on Ni (111) (Figure 2-5(i)).[68] A migration mode similar to dislocation has been observed for GBs in graphene, with the involvement of both SW rotation and C dimer evaporation.[144,147,148]

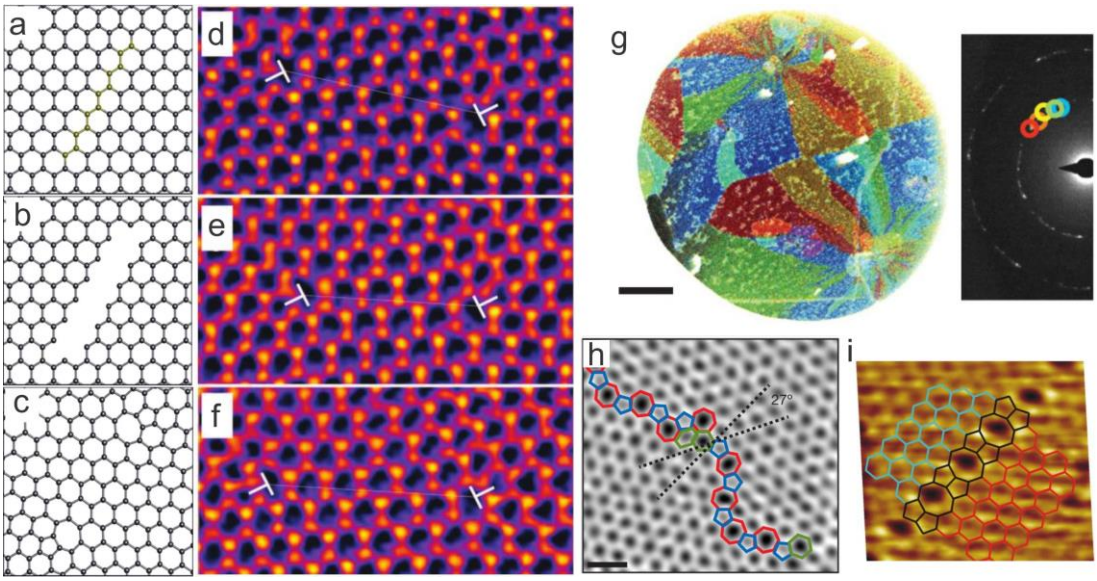

Figure 2-5 Linear defects in graphene. (a-c) Illustrations of the formation process of a dislocation. Adapted with permission from ref [72]. © 2013 The Royal Society of Chemistry. (d-f) AC-TEM frames of climb and glide of a dislocation. Adapted with permission from ref [91]. © 2012 American Association for the Advancement of Science (AAAS). (g) Dark-field TEM image and the diffraction pattern (DP) of polycrystalline graphene. The colours in the image correspond to the circles in DP with the same colour, and (h) STEM image of alternating 5-7 rings along a GB in the same sample. Adapted with permission from ref [87]. © 2011 Nature Publishing Group. (i) STM image of a 5-8-5 GB in graphene. Adapted with permission from ref [68]. © 2010 Nature Publishing Group. Scale bar in (g), 500 nm; (h), 0.5nm.

2.2.2 Extrinsic defects

Introducing foreign dopant atoms to pristine graphene has provided an opportunity to manipulate the key properties, such as carrier density,[149] band structure,[150,151] and magnetism,[152] which have further broadened the practical applications of graphene in nano-electronic applications including semiconductor devices.[153,154] Impurity atoms can be incorporated as either surface adatoms,[155] or as dopants covalently bonded within the graphene lattice. Covalently bonded dopants in graphene have been found to be more robust and explored with a variety of elements, such as N,[156] Si,[157] Fe,[158,159]and Cu.[159] Several forms of impurity dopants have been studied from single atoms to larger 2D membranes containing hundreds of atoms.

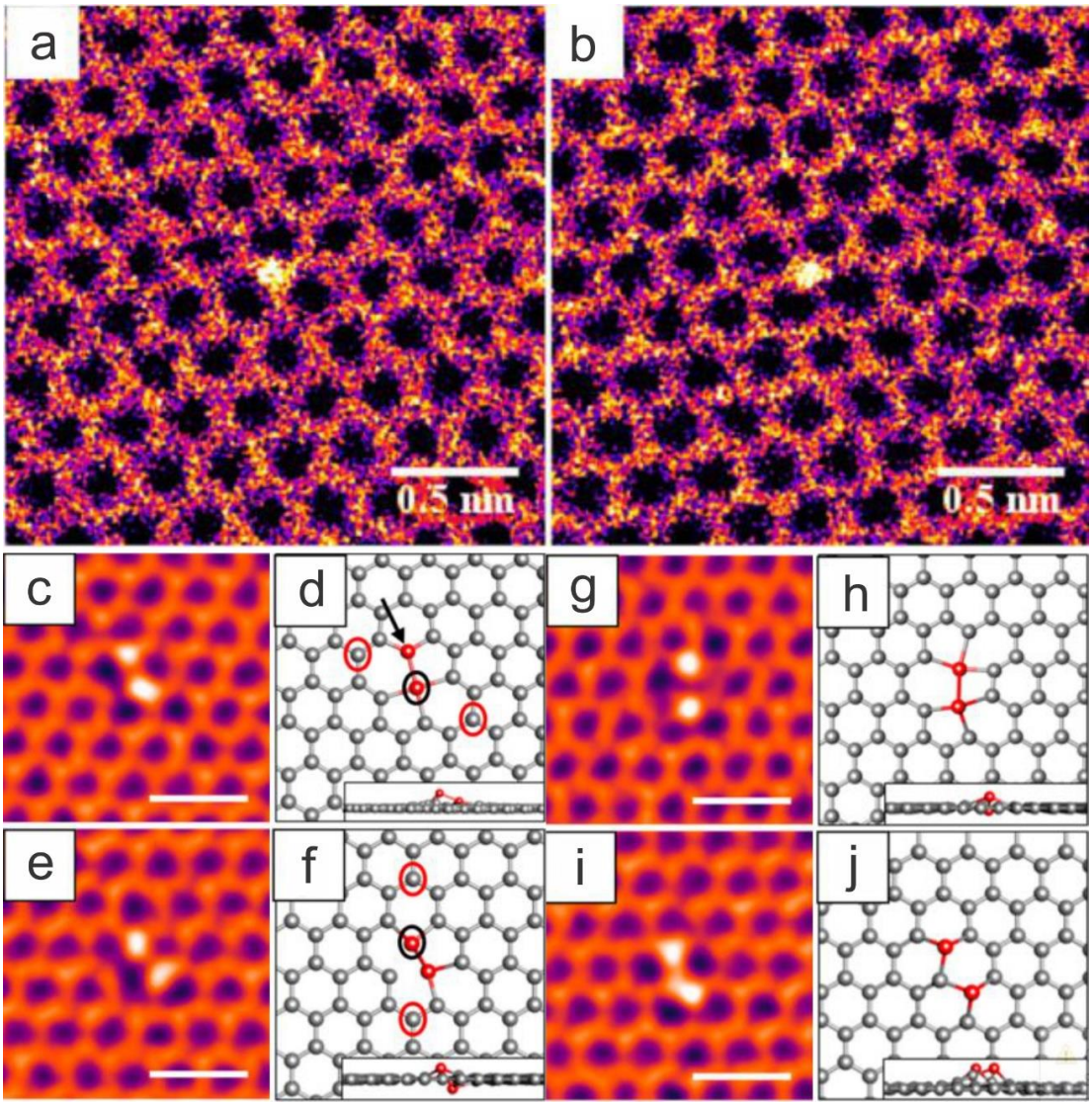

Figure 2-6 False-coloured AC-TEM images of (a) a Fe substitutional defect in a graphene monovacancy and (b) a Fe interstitial defect occupying a divacancy. (a-b) adapted with permission from ref [160]. © 2013 American Chemistry Society. (c-j) Fe dimers in graphene vacancies. (c,d) Smoothed AC-TEM images and atomic model of a pair of Fe atoms in a trivacancy. (e,f) A pair of Fe atoms in an alternative trivacancy. (g,h) A pair of Fe atoms in a quadvacancy and (i,j) a pair of Fe atoms in two adjacent monovacancies. Scale bar in (c,e,g,i), 0.5 nm. (c-j) adapted with permission from ref [162]. © 2014 American Chemistry Society.

Robertson et al. reported the structures and dynamics of single Fe atoms in graphene lattice, where nanoscale control of dopant incorporation was achieved by the use of controlled electron beam irradiation to create the initial vacancy that capture the mobile Fe atoms.[160] Isolated Fe atoms can be trapped in both a MV with three nearest

carbon neighbours (Figure 2-6(a)) and a DV, where four Fe-C bonds are formed (Figure 2-6(b)). 3-fold and 4-fold coordinated Si defects in monolayer graphene have also been observed by Ramasse et al with the combination of STEM and electron energy loss spectroscopy (EELS).[161] Single dopants in graphene can act as traps for additional foreign atoms, leading to dimers formation in graphene. He and his colleagues observed four different stable structures: two variants of a Fe dimer in a graphene trivacancy, a Fe dimer embedded in two adjacent MVs and a Fe dimer trapped by a tetravacancy (Figure 2-6(c-j)).[162] The Fe dimers were found to be mostly magnetic, and offered a way of introducing magnetism into doped graphene. Spin-sensitive DFT calculations indicated that the magnetic moments of the various defect structures vary between 2.00 μ_B to 4.00 μ_B. The observations have opened up exciting possibilities for designing atomic-scale optoelectronic and plasmonic devices by assembling single atoms on monolayer graphene sheets. The capability of various doping chemicals for manipulating band gap of monolayer and bilayer graphene has also been explored theoretically. Denis found that phosphorus doped monolayer graphene has a magnetic moment of 1 μ_B and the band gap was opened to 0.67 eV for 3 at.% of doping.[15] Ti and Au embedded in graphene have been predicted to have the ability to significantly improve the interactions between small gas molecules such as O_2, CO, NO_2 and NH_3, and graphene, indicating potential applications of the doped graphene in gas sensing and spintronics.[163]

In addition to embedding into substitutional sites in graphene, isolated foreign atoms can be adsorbed on graphene surface as well. Plenty of researches have been conducted in this area based on theoretical simulations. The adsorbed sites have been classified as three kinds: top (T), bridge (B), and hollow (H) shown in Figure 2-7(a-c).[164] The preference has been proved to be elemental-dependent, for example, 3d transition

metals have been found to be more stable at hollow sites,[165] while top sites have been predicted to be more favoured by noble metals.[166] Thakur and his colleagues investigated the structures and electronic properties Cr adatoms between an A-B stacked bilayer graphene through theoretical calculations.[167] The top-type doping was proved to be most energetically stable while the hollow-type doped system obtained a half-metallic nature with a 0.28 eV band gap in minority spin channel (Figure 2-7(d-g)).

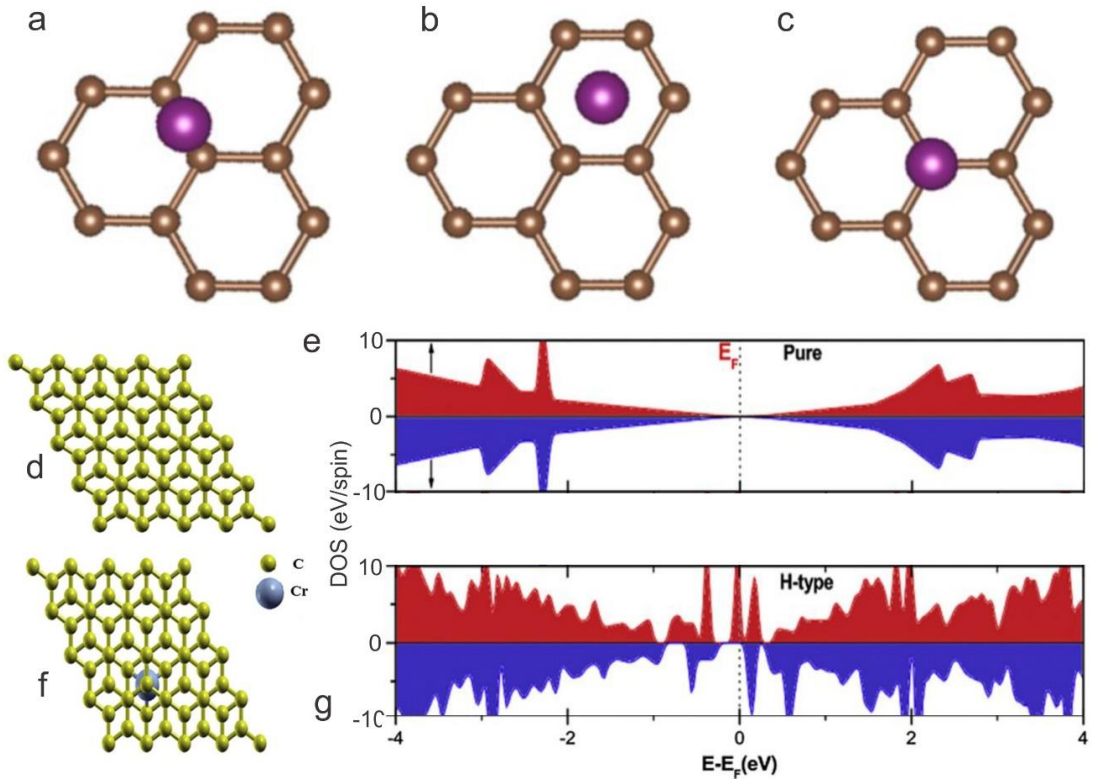

Figure 2-7 Adatoms on graphene. (a-c) Bridge, hollow and top sites for an adatoms. Pink balls are for any foreign atom. Adapted with permission from ref [164]. © 2015 American Chemistry Society. (d-g) Pristine bilayer graphene (d) and corresponding density of state (DOS) around Fermi level, and bilayer graphene with an adatoms at hollow site (f) and its DOS (g). Adapted with permission from ref [167]. © 2015 Elsevier.

Small clusters of impurity atoms in graphene have also been explored. Yang and co-workers have demonstrated that in-situ AC-STEM enabled atomic level monitoring of

critical steps in the process of forming a rotary Si trimer through Si-graphene reactions at a topological defect in a graphene monolayer, as shown in Figure 2-8(a).[157] The experimental observation on the incorporation and relocation of a C dimer, and the dynamic jump of the adsorbed Si atom before being incorporated into the topological defect provided direct evidence on dynamic interactions between dopant atoms and defects in graphene. Lee et al. directly observed three stable configurations with different symmetries for Si_6 clusters trapped in a graphene nanopore, and a conformational structural change between two structures induced by energy transferred from the electron-beam in the electron microscope (Figure 2-8(b,c)).[168] The oscillatory motion of Si atoms between the ground state of the Si_6 cluster and a metastable configuration was directly captured in sequential electron micrographs with atomic resolution. This reveals the possibility of identifying the structure of trapped nanoclusters in graphene pores, as well as the metastable atomic configurations that a particular cluster may assume. Si nanoclusters have also been observed to adapt to an ordered crystalline structure: Si atoms lining up in two rows along zigzag direction in graphene lattice.[169] These anisotropic crystals formed due to the higher stability of the Si-C bond under electron beam irradiation compared to the Si-Si bond. Dynamics of the anisotropic crystalline Si nanoclusters revealed that they can rotate perpendicular to the graphene plane, with oscillations between the two geometric configurations driven by local volume constraints.

Tens to hundreds of Fe atoms suspended within graphene nanopores were observed by Zhao et al using low-voltage AC-TEM (Figure 2-8(d-f)).[170] These 2D Fe nanomembranes were directly imaged with a square lattice with a 2.65 Å lattice constant at room temperature (the most energetically favourable distance is predicted to be 2.35 Å). The potential of perforated graphene as a support for 2D membranes

was shown, indicating the possibility for anticipating new 2D structures from a variety of elements to emerge.

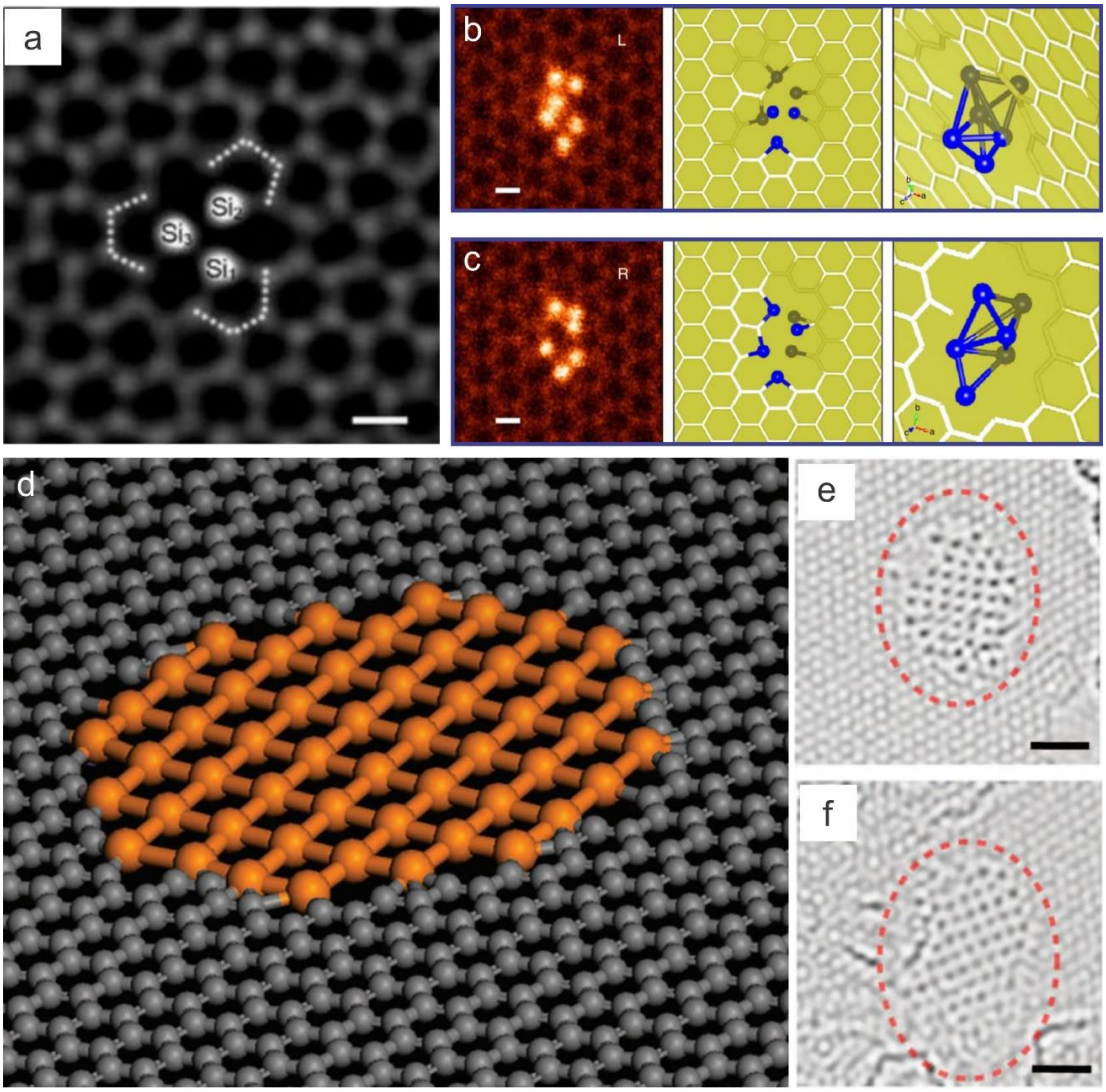

Figure 2-8 Various configurations of the clusters of foreign atoms. (a) STEM-ADT image of a Si trimer in graphene lattice. Adapted with permission from ref [157]. © 2014 Wiley-VCH. (b, c) ADF Z-contrast images of two representative stable Si6 cluster configurations embedded in graphene pore, as well as 3D structures obtained from first-principles calculations. Adapted with permission from ref [168]. © 2013 Nature Publishing Group. Si and C atoms below the graphene plane are shaded. L or R labels are used to highlight when the oscillating Si atom is either at the left or right sites. (d-f) Schematic and TEM images of free-standing Fe membranes within graphene pores. Adapted with permission from ref [170]. © 2014 American Association for the Advancement of Science (AAAS). Scale bar in (a-c), 0.2 nm; in (e,f), 1 nm.

2.3 Defects in TMDs

In the last section, the defects in graphene have been classified based on the existence of foreign atom. While in this section, the defects in TMDs will be sorted by their dimensionalities, from zero-dimensional to two-dimensional. 0D defects include vacancies, substitutional dopants with intrinsic or foreign elements, and adatoms (some examples in Figure 2-9(a)).[171] The agglomeration of vacancies forms vacancy lines, which is one of the linear defects. Other 1D defects include grain boundaries, either between two domains with different orientations or phases or at the interface of lateral heterostructures; as well as edge terminations (Figure 2-9(b,c)).[172,173] Defects with two dimensions include ripples (Figure 2-9(d)),[174] non-Bernal stacking of multilayers, and vertical heterostructures where different types of 2D materials stacking on top of each other (Figure 2-9(e)).[175] Haeckelites is also a special kind of 2D defect in TMDs which is composed of octagonal and tetragonal rings instead of the original hexagons. This defective structure in several TMD systems has been explored theoretically but yet to be created in lab (Figure 2-9(f)).[176] All the defects have been proved to have significant influences on the band structures, magnetic or optical performances, further expanding the applications of TMDs in various fields.

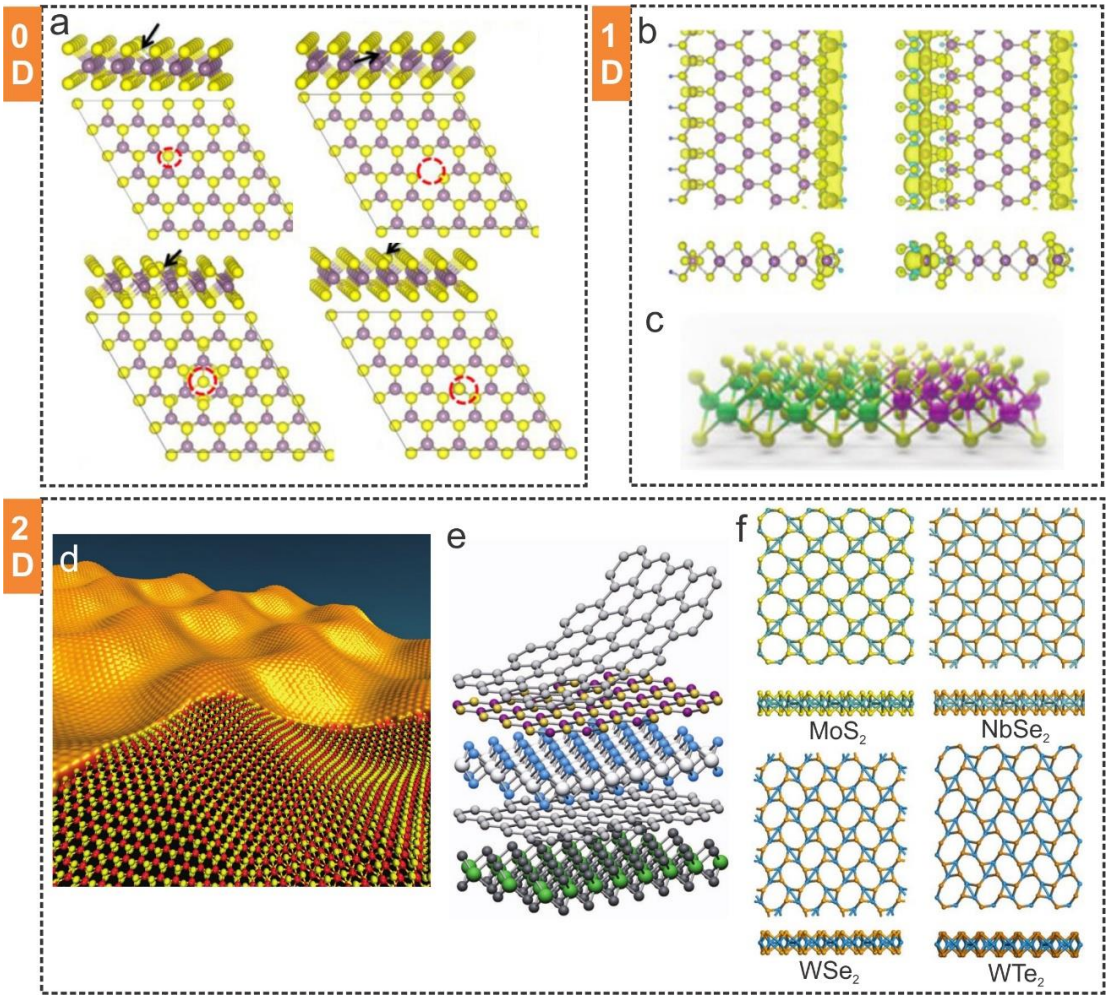

Figure 2-9 An overview of defective structures in TMDs. (a) Models of some typical 0D defects: single and double chalcogen vacancy, a chalcogen atom at the hollow site, and a chalcogen atom substituted metal site. Adapted with permission from ref [171]. © 2014 Institute of Physics. (b) Edge terminations of a TMD nanoribbon and passivation by foreign atoms. Adapted with permission from ref [172]. © 2011 American Chemical Society. (c) Lateral heterojunction of two different TMD monolayers. Adapted with permission from ref [173]. © 2014 Nature Publishing Group. (d) An illustration of ripples in TMDs. Adapted with permission from ref [174]. © 2013 Nature Publishing Group. (e) Vertical heterostructures of TMDs and other 2D materials. Adapted with permission from ref [175]. © 2013 Nature Publishing Group. (f) Models of Haeckelites predicted by theory in four TMDs. Adapted with permission from ref [176]. © 2014 Institute of Physics.

2.3.1 0D defects

The most basic and commonly observed defects in TMDs are vacancies. Taking MoS_2 an example, as S atoms have lower displacement threshold energy than Mo atoms,

which means S atoms require less energy to be removed from their lattice positions. Besides, maximum transferred energy from electron beam irradiation has been proved to be inversely proportional to atomic mass, indicating that Mo atoms are extremely hard to be sputtered out from the lattice.[177] Therefore, when observing MoS_2 with the use of TEM/STEM, monosulphur vacancy (V_S), disulphur vacancy (V_{S2}) have been the two most frequently captured structures, as shown in the upper two frames in Figure 2-10(a,b).[103] Pure Mo vacancies have not been observed as they usually formed complexes with S vacancies. The lower two frames in Figure 2-10(a,b) exhibit two cases, where a Mo vacancy is associated with three V_S (V_{MoS3}) or V_{S2} (V_{MoS6}).

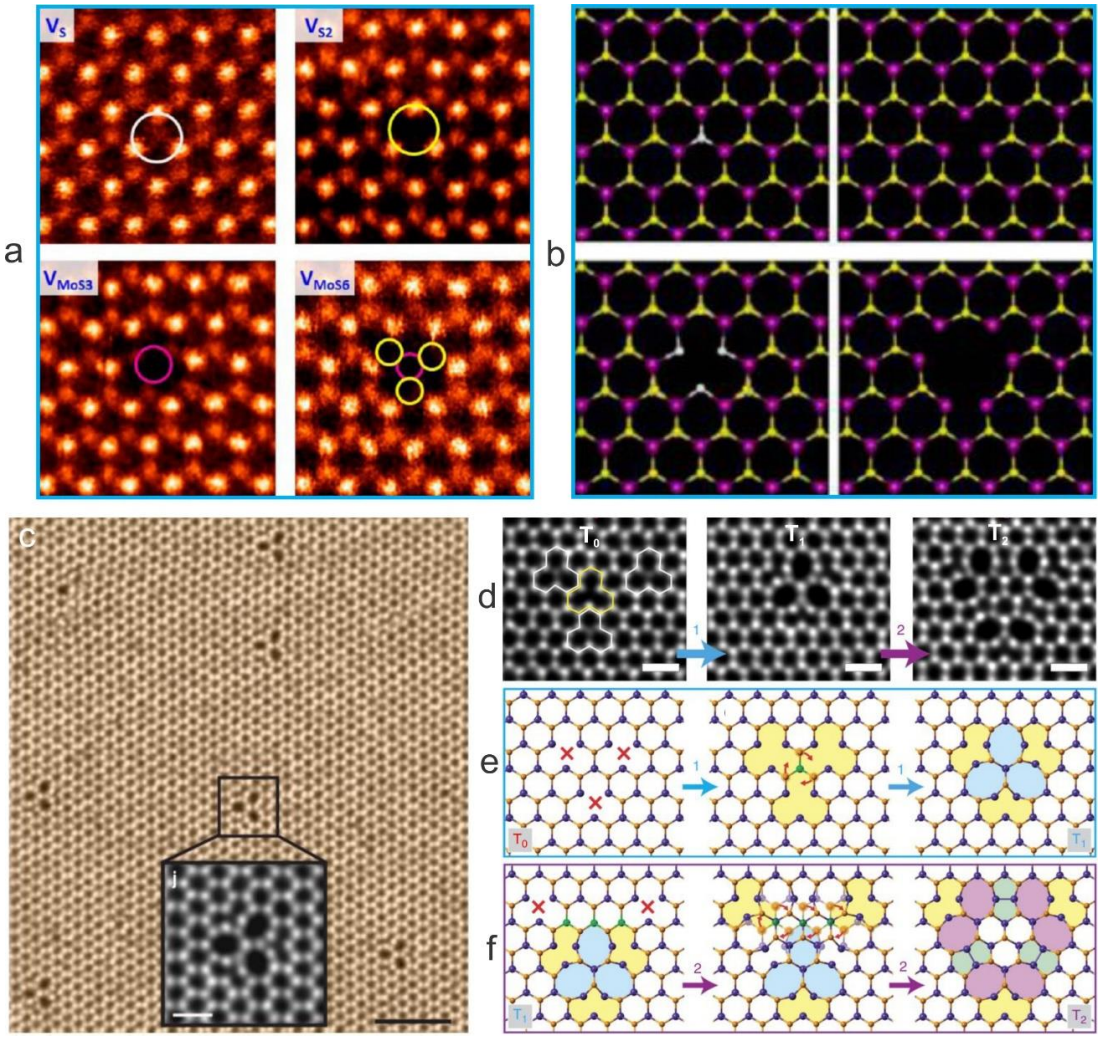

Figure 2-10 Intrinsic point defects in monolayer TMDs. (a) ADF images of four types of point vacancies: V_S (evaporation of one S atom), V_{S2} (evaporation of a S pair) V_{MoS3} (evaporation of

one Mo atom and three adjacent S atoms), V_{MoS6} (evaporation of one Mo atom and three adjacent S pairs). (b) Fully relaxed atomic models for the four structures in (a). (a,b) adapted with permission from ref [103]. © 2013 American Chemical Society. (c) ADF image of monolayer WSe_2 at 500 °C, with several trefoil defects. (d-f) ADF images and atomic models for the formation and evolution of rotational point defect in WSe_2. (c-f) adapted with permission from ref [178]. © 2015 Nature Publishing Group. Scale bar in (c), 2 nm; in (d), 0.5 nm.

Similar to the SW rotation in graphene where a C-C bond rotates 90° in-plane, bond rotations have also been visualised occur in monolayer TMDs. Komsa observed a new type of point defect contributed by bond rotation in monolayer WSe_2 (Figure 2-10(c)) at 500 °C.[178] Metal-chalcogen bonds rotated 60° to achieve the structure after the creation of three V_{S2} vacancies, with the detailed transformation process shown in Figure 2-10(d,e). The final product of this process was a three-fold symmetric trefoil-like defect, which acted as a basic structure for larger defects. Further bond rotations occurred within this type of defect to form larger point defect, as evident from *in-situ* STEM imaging (Figure 2-10(f)), and eventually linear defects consisting of aligned 8–5–5–8 membered rings, similar structure with the 8-5-5-8 type grain boundary observed in graphene.[68]

Vacancies have been proved to act like hosts for dopant atoms, either self-doped or occupied by other atomic species. As TMDs are composed of two elements, the chalcogen sites have been captured to be replaced by transition metal atoms, and *vice versa*, as shown in Figure 2-11(a,b): the first case (Mo_{S2}) is a Mo atom occupying a 2S site, leading to locally unsymmetrical structure, and the second case ($S2_{Mo}$) is two S atoms replacing a Mo atom.[103] The similarity of Mo and W has triggered the formation of solid solution: $Mo_{1-x}W_xS_2$, in single-layer crystals directly by CVD method. By tuning x, the percentage of W within the monolayer alloy, the band gap of the material was tailored from 1.82 eV when x=0.2 to 1.99 when x=1.[181] Similarly, $MoS_{2x}Se_{2(1-x)}$

has also been synthesized with high quality, directly resulting in tunable optical properties.[182]

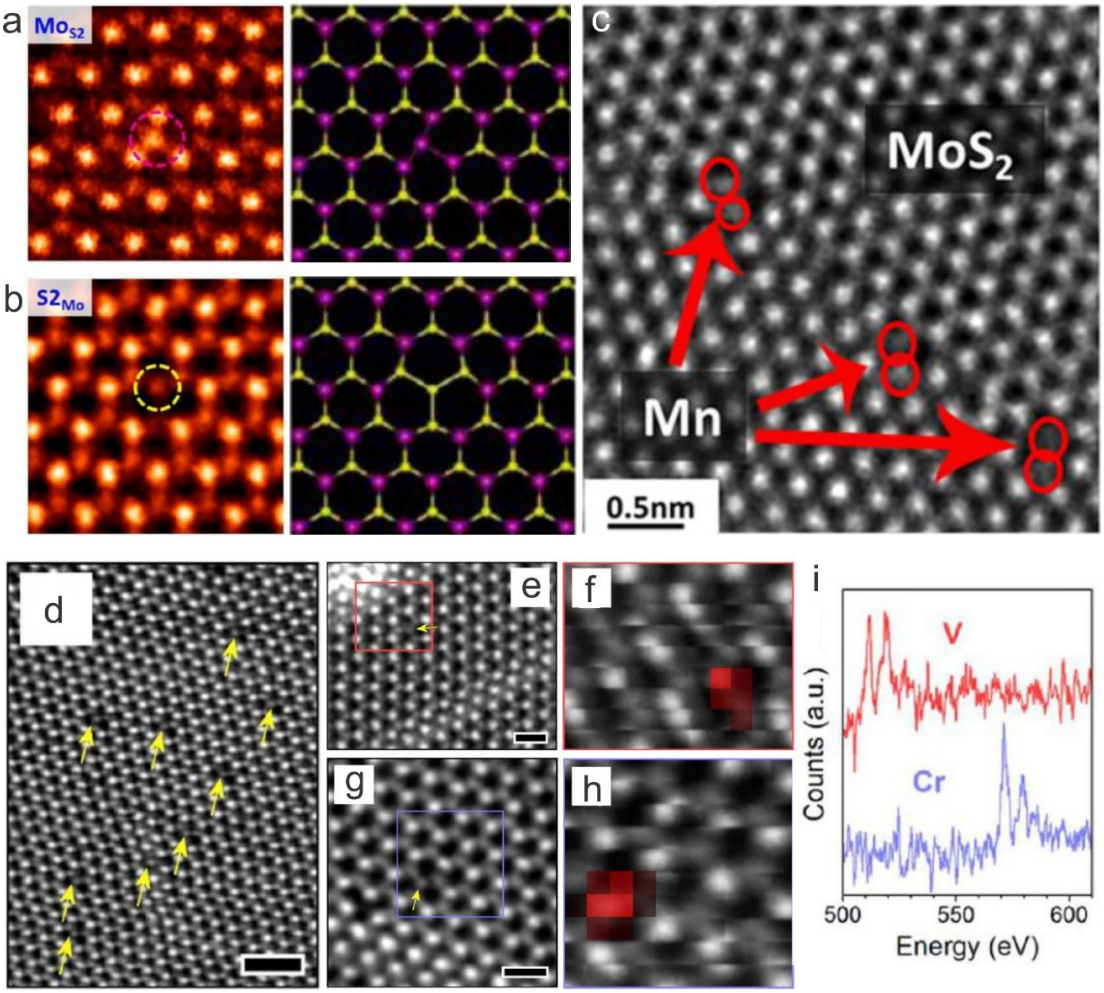

Figure 2-11 Dopant atoms in monolayer TMDs. (a,b) ADF images and corresponding relaxed models of anti-site defects where a Mo atom substituting a 2S column (Mo_{S2}) and two S atoms substituting a Mo site ($S2_{Mo}$). (a,b) adapted with permission from ref [103]. © 2013 American Chemical Society. (c) ADF image of several Mn atoms embedding along a grain boundary of monolayer MoS_2. Adapted with permission from ref [179]. © 2015 American Chemical Society. (d-i) ADF images and simultaneous EELS mappings of Cr and V substitutional dopants. Boxes in (e) and (g) represent the area of EELS mapping. Red: V; blue: Cr. Adapted with permission from ref [180]. © 2016 American Chemical Society. Scale bar in (d), 1 nm; in (e,g), 0.5 nm.

Substitutional elements can also be the ones other than the typical transition metals which are the components of TMDs, and whether they occupy metal sites or chalcogen

sites has been found to depend on their nature, such as electronegativity, ion's size, and valence.[183] Manganese (Mn), for instance, has been intentionally introduced to MoS_2 *via* vapour phase deposition method, which results in the modification of the band structure.[179] Figure 2-11(c) shows several Mn dopant atoms settling at Mo sites along a grain boundary of monolayer MoS_2. Chromium (Cr) and Vanadium (V) have been observed by Robertson and his colleagues in CVD synthesized monolayer MoS_2.[180] They have also been found to act as single atom substitutional dopants at Mo sites, as shown in the ADF image of Figure 2-11(d). These two substitutional dopants can be easily confused with 2S in place of Mo, as they all have similar contrast in ADF frames. Mapping the locations of the substitutional metal atoms by electron energy loss spectroscopy (EELS) have firmly confirmed that the dopants were Cr and V instead of 2S (Figure 2-11 (e-i)). Therefore, in some cases, judging the dopant elements only by the Z-contrast in ADF images may not be conclusive. Platinum (Pt) atoms, however, have been found to favour the S vacancy sites by Li and co-workers.[184] When introducing to MoS_2 lattice, Pt atoms firstly migrated rapidly with a small migration barrier of 0.6-0.82 eV based on DFT calculation and finally settled at V_S or V_{S2}. Other elements, including Nb[185] and Fe,[186] have also been introduced to single to few layer MoS_2 films as substitutional dopants to tailor the optical and electronic properties of the systems.

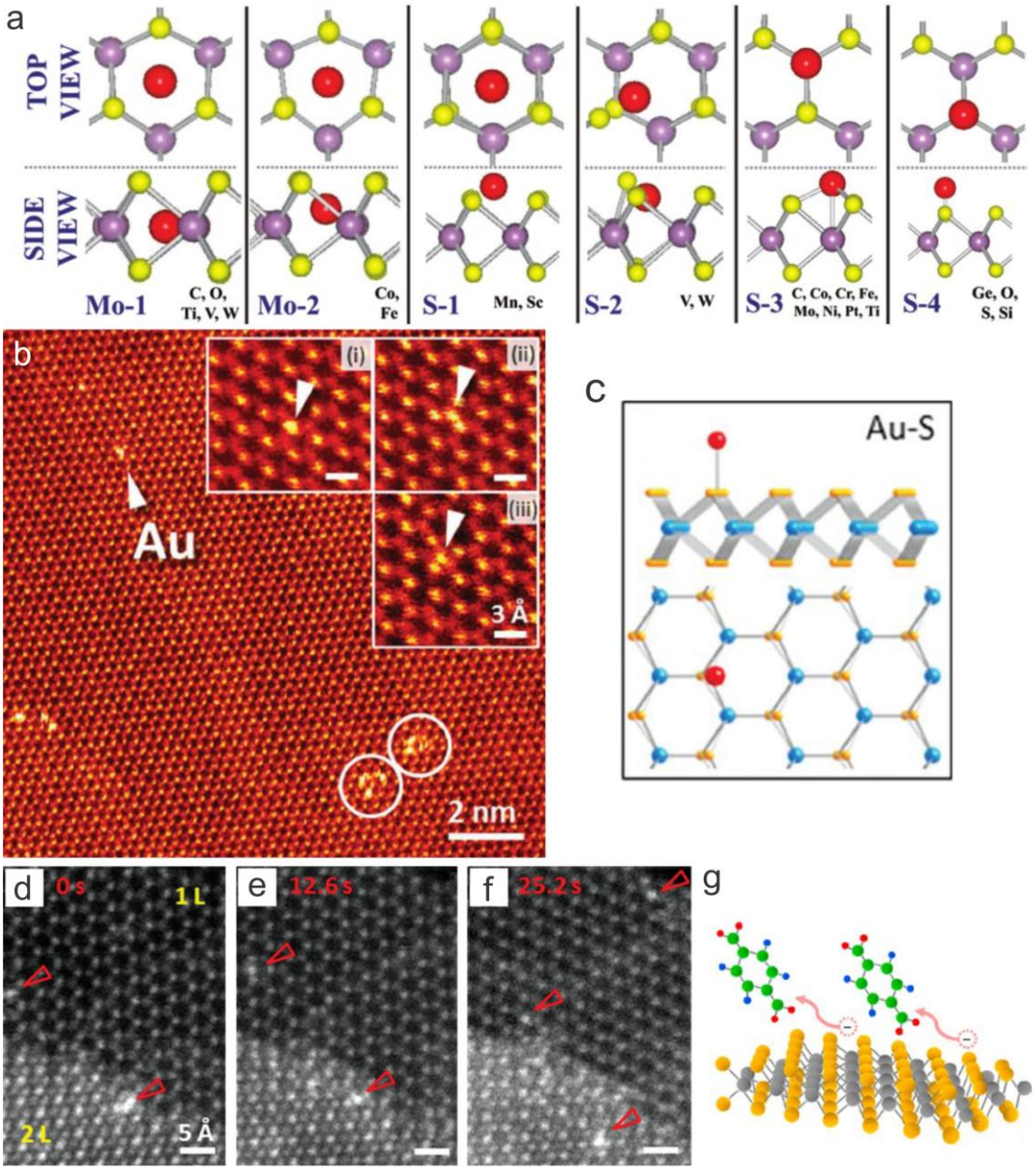

Figure 2-12 Theoretical and experimental results for foreign adatoms in TMDs. (a) Top- and side-view illustration of adsorption structures of 16 types of adatoms in monolayer MoS_2 after relaxation. Red balls are adatoms, and Mo and S are purple and yellow. The elements that applies to the models are listed in each side-view schematic. Mo-n or S-n indicate the initial position of the adatom on the Mo or S plane. Adapted with permission from ref [187]. © 2011 American Chemical Society. (b) ADF image of Au-doped (0.6%) monolayer MoS_2. The insets (i), (ii), and (iii) exhibit Au adatom (indicated by white arrows) located on top of the Mo column, S column, and hollow site, respectively. (c) Top and side view of the model for Au adatom on the top of S atom. (d-f) Dynamics of Au adatoms (pointed by red arrows) on mono- and bilayer areas in 25 s. (b-f) adapted with permission from ref [188]. © 2014 Wiley-VCH.

(g) An illustration of organic molecule doped monolayer TMD. Adapted with permission from ref [189]. © 2013 American Chemical Society.

Foreign atoms can also be adatoms adsorbed on the TMDs' surface rather than substituting onto the lattice. Ataka and Ciraci have conducted a systematic investigation based on theoretical calculation for 16 individual adatoms (C, Co, Cr, Fe, Ge, Mn, Mo, Ni, O, Pt, S, Sc, Si, Ti, V, and W) as adatoms on 2H-MoS_2.[187] Six individual minimum-energy structures of adatom-MoS_2 after relaxation have been found among these elements and the results are listed in Figure 2-12(a). Some atoms, such as C, Co, Fe, O, Ti, V and W, have been predicted to possess two favourable binding sites, while the rest of them only have had one. Decoration of adatoms on MoS_2 surface has been theoretically proved to have crucial influence on the electronic and magnetic properties. Experimental observation of adatoms on single-layer MoS_2 has been achieved by Lin and co-workers, who have found out that for the case of Au dopants, 95% of them were adatoms with high mobility under the electron beam in the dataset of 220 Au atoms captured, with the rest 5% as substitutional dopants.[188] Figure 2-12(b) and its insets display three individual adsorbed sites for Au atoms in their observation: (i) top site of Mo; (ii) top site of S (Figure 2-12(c)); and (iii) Hollow site. The calculated formation energies of these three configurations are very similar, 2.46 eV, 2.33 eV and 2.37 eV respectively, all of which are lower than that of substitutional positions, indicating the favour of adatom sites for Au atoms, consistent with the experimental observations. The mobility of Au atoms under 60 kV electron beam has also been explored, as shown in the consecutive ADF frames in Figure 2-12 (d-f). During 25s, the targeted Au atoms have different positions in each frame in both monolayer and bilayer regions. In broader terms, small organic molecules can also be considered as 0D adsorbates (Figure 2-12 (g)), and doping TMDs with some species

of molecules, both n-type and p-type dopants, has been studied.[189] With the introduction of the molecules the optical and electronic properties of MoS_2 have been proved to be tunable.

2.3.2 1D defects

The most frequently observed linear defects in TMDs have been S vacancy lines (SVLs). Under electron beam irradiation in TEM/STEM, the formation mechanism of the line defect in monolayer TMDs have been believed to be the creation, migration and aggregation of single S vacancies. 2 eV barrier has been predicted for a S vacancy migrating to the adjacent site, which is too high for spontaneous diffusion at ambient temperature.[190] However, under the continuous irradiation of the energetic electrons in TEM, S vacancy migration has been observed in a rather slow speed with a diffusion coefficient of $3.8 \times 10^{-18} cm^2/s$, namely, a S vacancy requires 43 s to make a jump to the adjacent site on average. Therefore they tended to migrate in short distances and formed several line defects simultaneously in a local area, as shown in Figure 2-13(a-d), where several SVLs eventually formed from a number of randomly located S vacancies in the first frame. The simplest SVL is 1SVL, composed of a single line of S vacancy (Figure 2-13(e,f)).[191] The absence of the S vacancy line induces a slight distortion of the surrounded lattice, especially for the positions of S atoms. Out-of-plane distortion has also been predicted by DFT calculation when the structure was relaxed. Broader SVLs with more than one parallel lines of S vacancies have also been observed. As the stoichiometry in the local region of SVLs is different, it induced the alteration of the band structures in the area of SVLs. It has been predicted that the band gap decreases gradually from 1.7 eV in pristine MoS_2 to 0.047 eV in 3SVL, and the 4SVL structure owns metallic properties.[191] As all the SVLs propagate along the three zigzag directions with the intersection angle of 120°, they are highly likely to

encounter with each other at high concentration. Ryu and co-workers have observed the interactions among several SVLs (Figure 2-13(g-o)), with a pore being opened and enlarged at the interacting point.

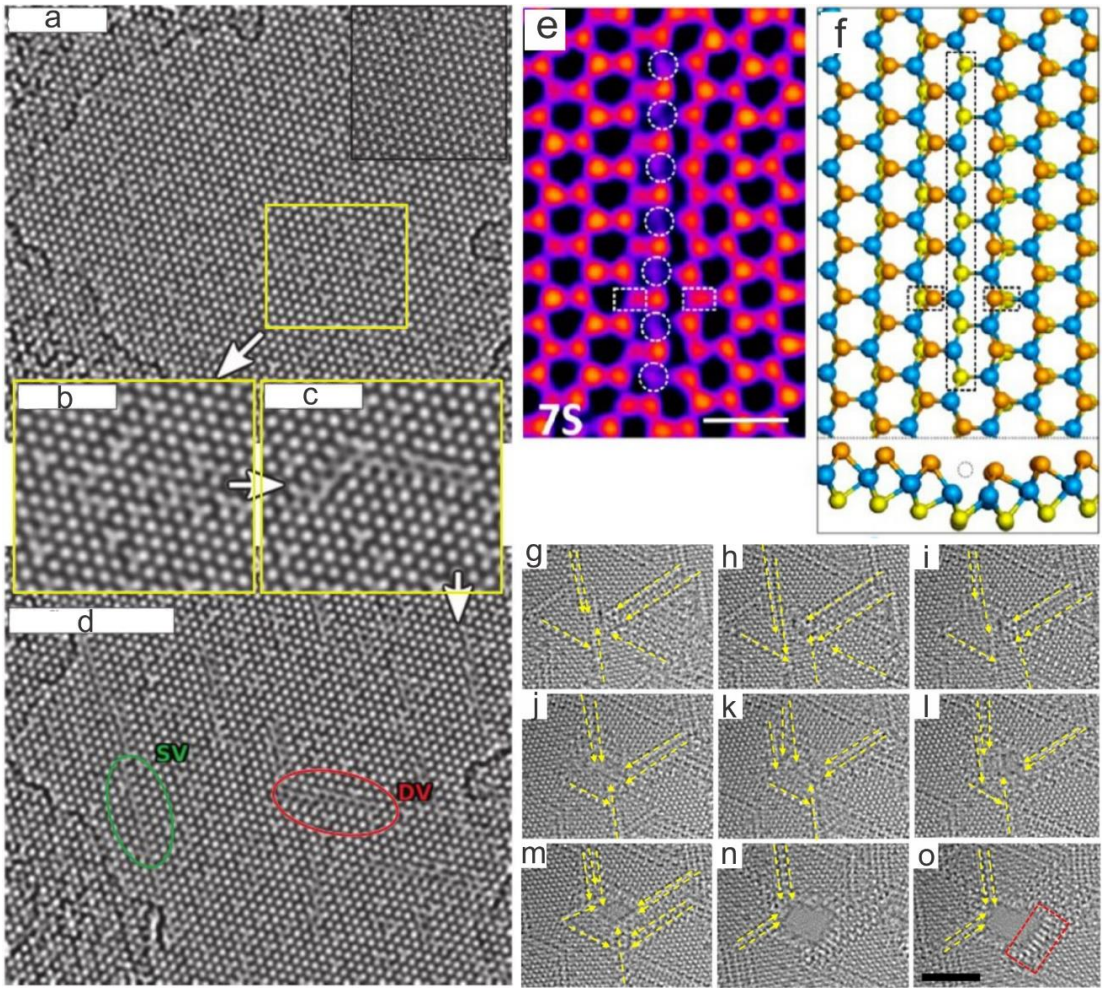

Figure 2-13 Formation mechanism, atomic structure and dynamics of SVLs. (a-d) TEM images showing the creation of SVLs from monovacancies under 80 kV electron beam at (a) initial point, (b) 150 s, (c) 151 s, and (d) 220 s. SV: single Vacancy line (1SVL); DV: double vacancy line (2SVL). (a-d) adapted with permission from ref [190]. © 2013 American Physical Society. (e,f) False-colour ACTEM image and DFT relaxed model of a 1SVL with the length of 7S. Adapted with permission from ref [191]. © 2016 American Chemical Society. (g-o) A series of TEM images showing the dynamics of intersecting SVLs and hole formation. Adapted with permission from ref [192]. © 2016 Institute of Physics. Scale bar in (e), 0.5 nm; in (o), 2 nm.

TMDs synthesized by CVD method are polycrystalline. When two single-crystal domains with different orientations merge during the growth process, grain boundaries (GB) form (Figure 2-14(a,b)). The atomic structures of GB vary with the intersecting angle of the two grains and far more complicated than the case of graphene. Several GB structures, including 4|4 (rhomb-rhomb), 4|6 (rhomb-hexagon), 4|8 (square-octagon), and 6|8 (hexagon-octagon) fold rings have been predicted by first principles theory.[193] The directly observation of GB was firstly achieved by Zhou and his colleagues with the use of high-resolution STEM. A specific example is 60° GB in monolayer MoS_2 (Figure 2-14(c-e)).[103] This type of GB is parallel to the zigzag orientation with a series of point-sharing rhomb rings. The sharing points are at the 2S sites in the pristine MoS_2 lattice. Therefore this GB is denoted as 4|4P structure (P for point sharing). Unlike GBs in graphene where all the carbon atoms maintain sp^2 state, the Mo atoms at 4|4P GB retain 6-fold coordination, whereas the S atoms alter the coordination from 3-fold to 4-fold. It has been predicted that this type of GB could serve as a metallic wire embedded in the semiconducting MoS_2 lattice.[193] GBs are usually not perfect straight lines. Kinks have been observed along this 4|4P GB as octagonal rings, with the illustration shown in Figure 2-14(e). One more 60° GB structure, 4|4E, has also been observed in the same research. The name comes from the edge-sharing structure of the rhomb rings.

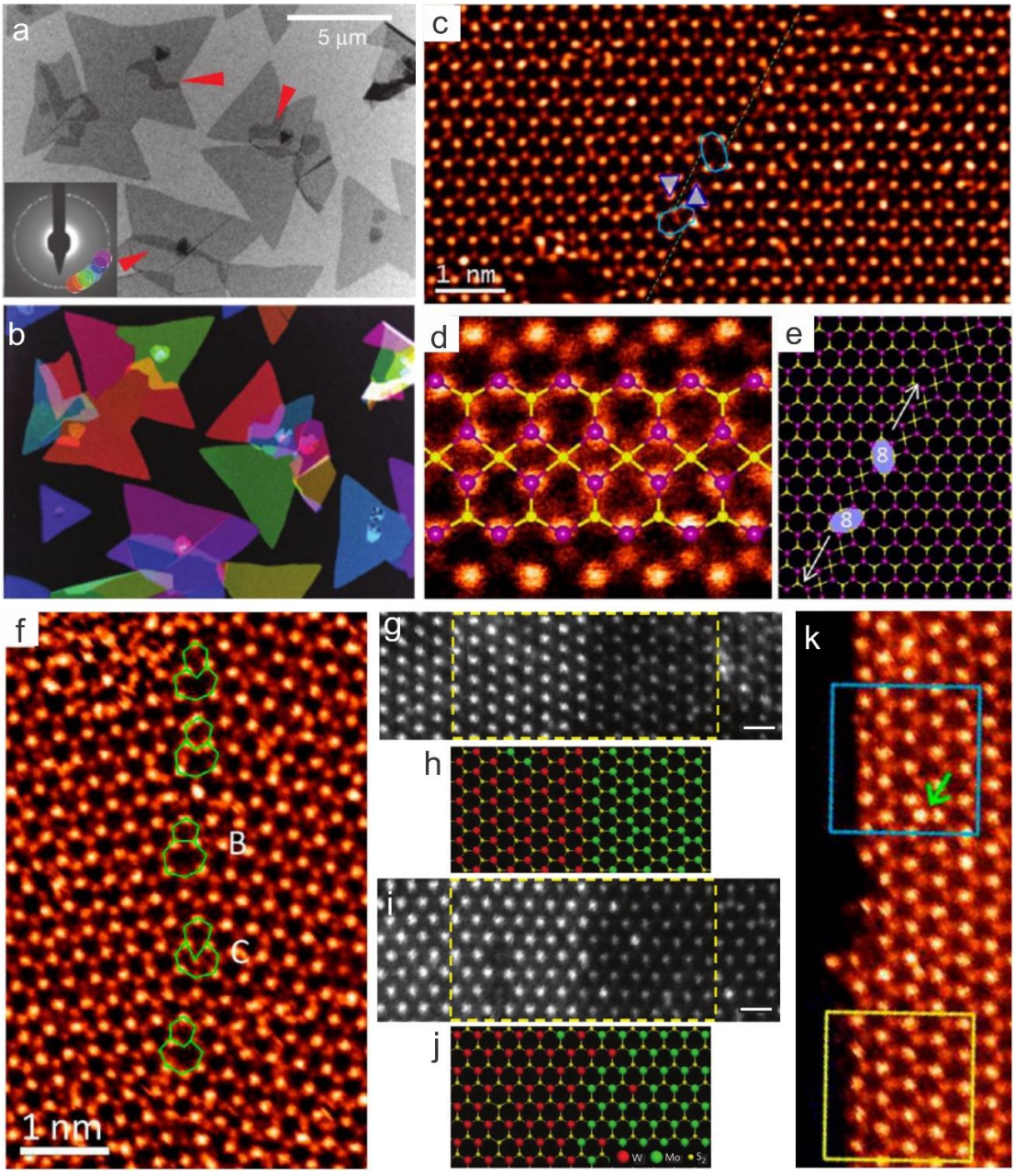

Figure 2-14 Grain boundaries and edge of TMDs. (a) Bright-field image of irregular-shape MoS_2 domains, with the diffraction pattern inset. (b) Coloured dark-field TEM image with the colours correspond to the orientations highlighted in the diffraction pattern with the same colour. (a,b) adapted with permission from ref [85]. © 2013 Nature Publishing Group. (c) ADF image of a 4|4P GB. The dashed line highlights the position of the GB and the two triangles indicate the orientations of the two domains. (d) Zoom-in image of the 4|4P GB with the relaxed atomic model overlaid. (e) Atomic model of the GB shown in (a) with the octagon kinks highlighted. (f) ADF image of an 18.5° GB with a row of dislocation cores highlighted in green lines. (c-f) adapted with permission from ref [103]. © 2013 American Chemical Society. (g-j) ADF images and atomic illustrations of lateral heterojunctions between WS_2 (brighter) and MoS_2 (dimmer) monolayers. (g,h), along zigzag direction; (i,j) along armchair

direction. (g-j) adapted with permission from ref [173]. © 2014 Nature Publishing Group. (k) ADF image of a MoS_2 Mo edge with its original (yellow box) and reconstructed (blue box) configurations. Scale bar in (g,i), 0.5 nm. Adapted with permission from ref [103]. © 2013 American Chemical Society.

In addition to the mirror-symmetric 60° GBs, GBs between two grains with smaller intersection angles have also been studied. One example is shown in Figure 2-14(f), an 18.5° GB which is made of 5|7 and 6|8 pairs. The former can be regarded as the basic dislocation core (B in Figure 2-14(f)) and the latter forms when one or two S atoms adding to the dislocation core (C in Figure 2-14(f)) under S-rich conditions. Similar structures have also been observed in WS_2 with the exploration of the dynamics of the dislocation cores.[194] The interface of lateral heterostructures is another type of GB. WSe_2/MoS_2 lateral heterojunctions have been synthesized with atomically sharp interface.[105] Gong and co-workers also reported a method for directly growth of in-plane MoS_2/WS_2 monolayer by CVD, and the seamless connections along both zigzag and armchair directions have been observed with atomic resolution.[173] For the case of zigzag heterojunction, the interphase was atomically abrupt between WS_2 and MoS_2 lattice within only one atomic row, with the experimental and illustration shown in Figure 2-14(g,h). Occasionally, Mo atoms were founded at the substitutional positions of W atoms in WS_2, and *vice versa*. As for the interface along armchair direction, slight inter-diffusion was found within the width of 1-3 unit cells (Figure 2-14(i,j)). This phenomenon might be due to the lower stability of original armchair edges of TMDs, therefore in TEM/STEM, only zigzag edges have been directly observed (Figure 2-14(k)). The two elemental nature of TMDs determines two distinguish zigzag edge directions: so-called (100) Mo edge and $(\bar{1}00)$ S edge.[195,196] Numerous researches have been done on the prediction of electronic and magnetic

properties of the edges of TMDs.[197–201] The direct observation of both Mo and S edges in monolayer MoS_2 was later achieved with the detailed results shown in Chapter 6.

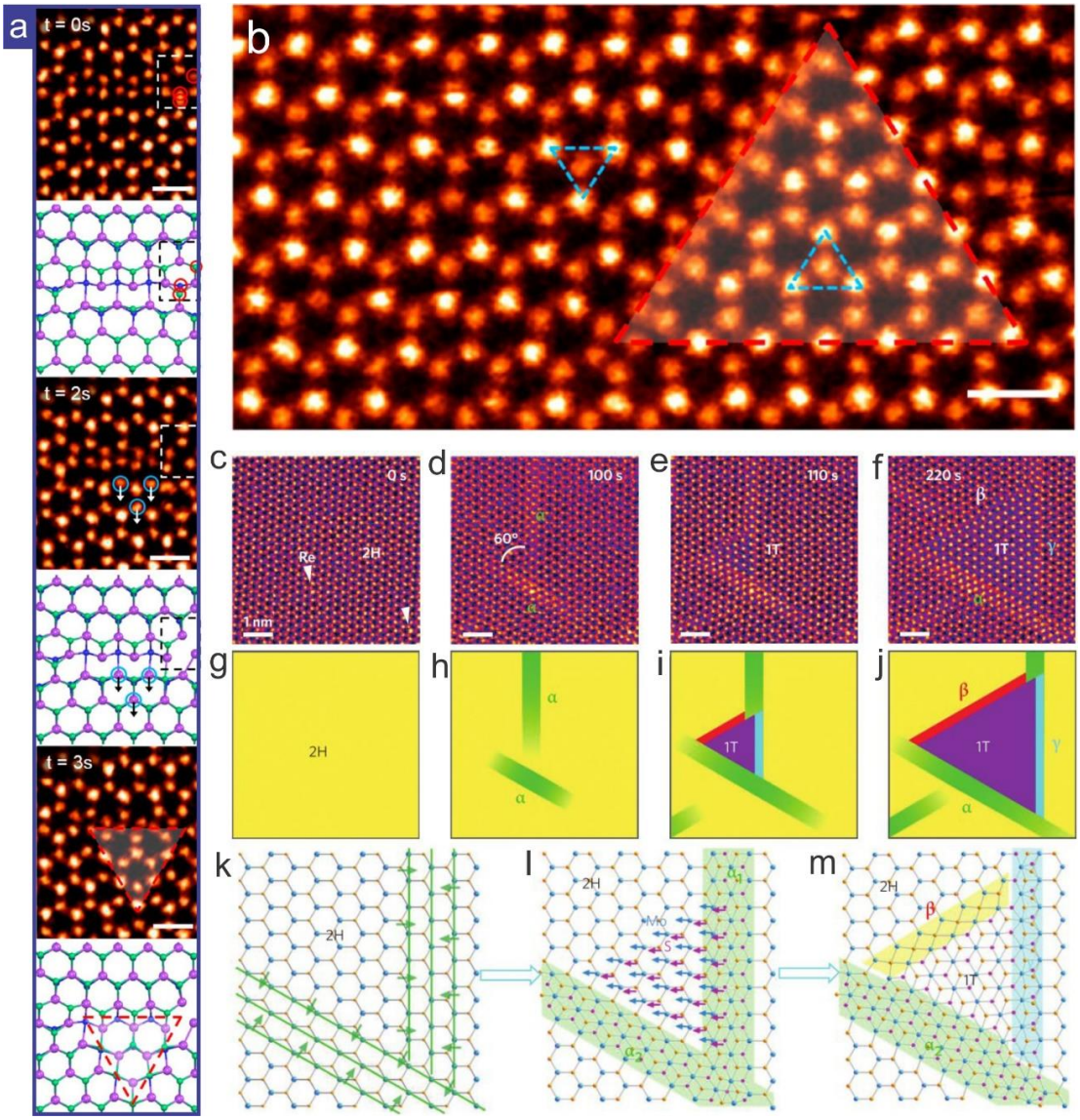

Figure 2-15 Embedding domains within 2H-TMDs. (a,b) Formation of inversion domain in $MoSe_2$. (a) Nucleation of an inversion domain from Se vacancies and gliding of Mo atoms in 3 s. (b) A typical example of an inversion domain within $MoSe_2$ monolayer. (a,b) adapted with permission from ref [104]. © 2015 American Chemical Society. (c-m) Step-by-step movement of the transition from 2H phase to 1T phase in monolayer MoS_2 at 600 °C. (c-f) ADF images showing the process within 220 s. (g-j) Corresponding illustrations with the different structures highlighted in different colours. (k-m) Atomic models demonstrating the atomic movement. (c-m) adapted with permission from ref [23]. © 2014 Nature Publishing Group. Scale bar in (a,b), 0.5 nm.

Two types of triangular domains have been found to be embedded in the monolayer TMDs with 2H phase: inversion domain and 1T phase domain. They are introduced in this section as both of them are intimately connected to linear defects. Lin and his colleagues studied the formation mechanism of an inversion domain in monolayer $MoSe_2$.[104] They found out that annealing $MoSe_2$ monolayer triggered the generation of large-scale inversion domains. An inversion domain is a domain of mirror symmetry with the original lattice, and it is achieved by lattice rotation by 60°. Therefore all the three boundaries should be 60° GBs, although the formation mechanisms are completely different. The formation of an inversion domain has been reported to initiate from the generation of Se vacancies in adjacent positions, which then induces the displacement of Mo atoms. This process has been considered as the nucleation of the inversion domain, as shown in Figure 2-15(a). At this stage, the prototypes of two 4|4P and a 4|4E GBs are revealable. The growth of the inversion domain was further driven by the migration of one of the 4|4P GBs, and the three boundaries were extended equally (Figure 2-15(b)). Similar nucleation and growth mechanism of the inversion domain has also been proposed by Lehtinen.[202]

The mechanism of the 2H to 1T phase transition has been reported by Lin and co-workers with in-situ heating at 600 °C in STEM (Figure 2-15(c-m)).[23] The transition process initialled from the formation of two linear structures (α in Figure 2-15(d,h)) along zigzag directions with intersecting angle of 60°. The two chains consisted of three zigzag chains gradually extended until in contact with each other. At this stage, the atoms at the corner caused by the acute angle were heavily packed, inducing them to glide to the direction where the atoms were less close-packed for stress relaxation (Figure 2-15(l)). The glide of the atoms led to the formation of 1T phase (Figure 2-15(e,i)), which has different contrast at S positions, as well as two new boundaries, β

and γ in Figure 2-15(j). The β phase is similar to the 4|4P structure, one of the 60 GBs. The size of the 1T phase gradually enlarged to 8.5 nm^2 after 220 s continuous scanning of electron beam (Figure 2-15(d)).

2.3.3 2D defects

Similarly to monolayer graphene, suspended TMD monolayers can also be stabilised by the formation of ripples. Quasi-periodical ripples have been observed in MoS_2 surface by atomic force microscope (AFM).[203] The morphologies of the ripples was space-dependent. The heights of the ripples was found from several to tens angstroms, while the wavelength was in the range of hundred nanometers (Figure 2-16(a-d)). Ripples could also be generated by laser-beam scanning over monolayer MoS_2.[204] The generation of the local strain contributed by the ripples has been proved to alter the electronic properties of MoS_2.[203]

In multilayer TMDs, layers are coupled by van der Waals forces, the magnitude of which is sensitive to the spacing between the layers, which have confirmed to be determined by the stacking configuration. Non-Bernal stacking of multilayer TMDs can also be seen as a type of 2D defect in TMDs. Occasionally, it happened in the as-synthesized bilayer MoS_2,[205] but in most cases, the arbitrary stacking angles between TMD layers were the result of manual transfer process (Figure 2-16(e,f)).[206] Moiré pattern appears in the lattice-mismatched regions and the pattern depends on the stacking angle.

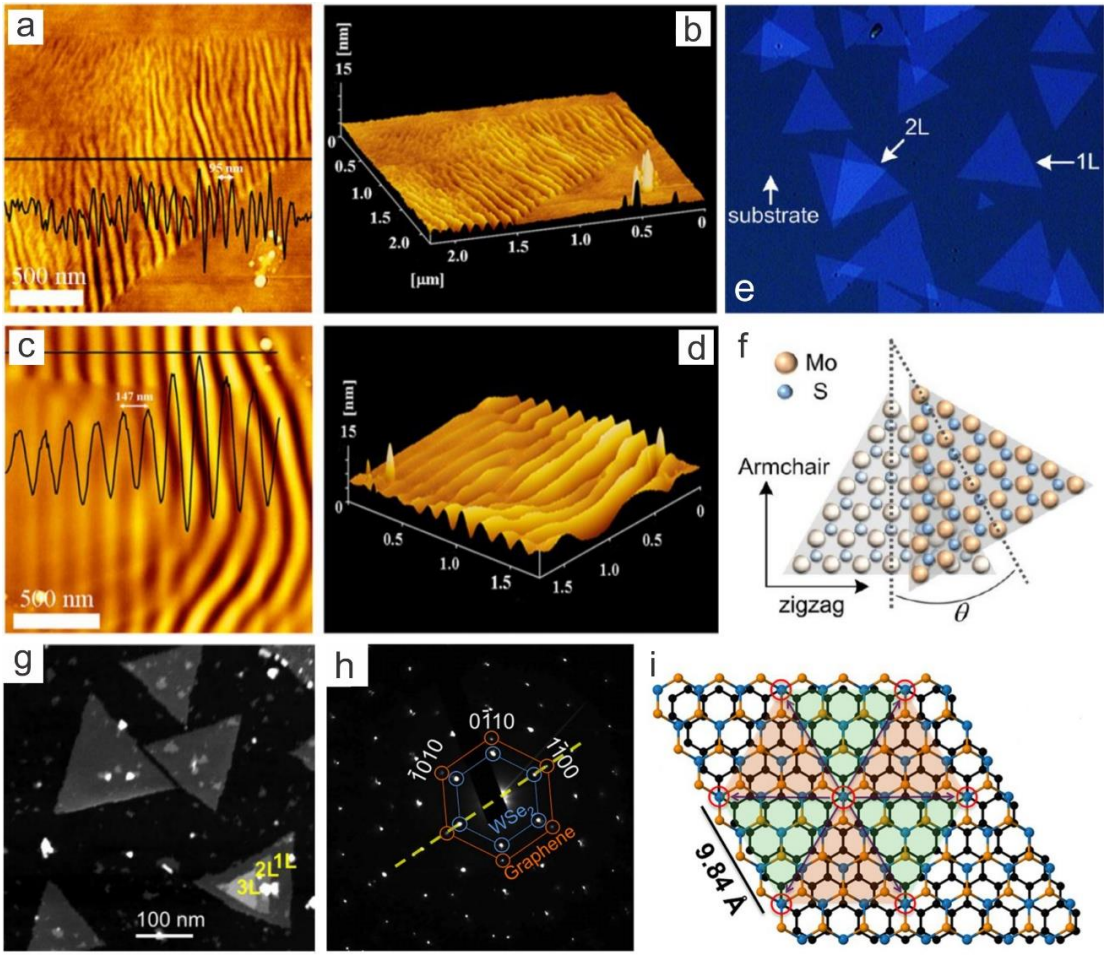

Figure 2-16 Various types of 2D defects in TMDs. (a,c) AFM images and corresponding 3D view (b,d) of MoS_2 ripple structures at two positions. The wavelength of the ripples in (a): 95 nm; in (b): 147 nm. (a-d) adapted with permission from ref [203]. © 2015 Institute of Physics. (e,f) An optical microscopy image and atomic illustration of artificially stacked bilayer MoS_2. Adapted with permission from ref [206]. © 2014 American Chemical Society. (g-i) HAADF image and diffraction pattern of WSe_2/graphene heterostructures, and the atomic model for the vertical-stacking structure showing the lattice mismatch due to the size difference. Adapted with permission from ref [207]. © 2015 American Chemical Society.

Because of the similarity of the lattice structures, different types of 2D materials have been stacked on the top of another to form vertical heterostructures. The interfaces of the lateral heterostructures have been regarded as 1D defects, likewise, the interfaces between the vertical heterostructures can be considered as 2D defects. Azizi and his colleagues directly grew WSe_2 on the top of monolayer graphene and epitaxial relationship between the WSe_2/graphene heterostructures was observed (Figure 2-

16(g,h)).[207] Because of the different lattice size of the two materials, lattice mismatch is inevitable (Figure 2-16(i)). Properties of the heterostructures including electronic, optical and magnetic properties can be tailored by using different stacking layers and different stacking angles, and this research field has attracted many researchers to explore their potential applications.[173–175,208]

2.4 Conclusion

It has been 14 years since the graphene was firstly isolated in lab. A large amount of researches have been done and added building blocks in the field of 2D materials. Top-down and bottom-up fabrication methods have been invented and improved to achieve layered materials with high quality and large scale. New members have been continuously introduced to the 2D materials family and more are expected to be fabricated and investigated in lab, and finally, in industry.

The defective structures of layered materials not only provide a fertile ground for the exploration of fundamental science, but also broaden the potential applications of 2D materials in various fields. This requires a deep and comprehensive understanding of the defects, from their atomic structures to how they affect the physical and chemical properties of the systems. With the development of modern imaging technologies, including AC-TEM and STEM, direct observation of the configurations and dynamics of the defects have been realised. The ultimate goal will be defect engineering in atomic scale, by which specific types of structural defects can be delicately introduced to targeted positions with single-atom-sensitivity. So far, great efforts have been made and promising progress has been achieved in this field, but it is highly likely that we

are still at the very beginning: the rest of the iceberg is still underwater waiting to be explored.

2.5 References

(1) Novoselov, K. S.; Geim, A. K.; Morozov, S. V; Jiang, D.; Zhang, Y.; Dubonos, S. V; Grigorieva, I. V; Firsov, A. A. Electric Field Effect in Atomically Thin Carbon Films. *Science.* **2004**, *306*, 666–669.

(2) Ashton, M.; Paul, J.; Sinnott, S. B.; Hennig, R. G. Topology-Scaling Identification of Layered Solids and Stable Exfoliated 2D Materials. *Phys. Rev. Lett.* **2017**, *118*, 106101.

(3) Nair, R. R.; Blake, P.; Grigorenko, A. N.; Novoselov, K. S.; Booth, T. J.; Stauber, T.; Peres, N. M. R.; Geim, A. K. Fine Structure Constant Defines Visual Transparency of Graphene. *Science.* **2008**, *320*, 1308–1308.

(4) Ghosh, S.; Bao, W.; Nika, D. L.; Subrina, S.; Pokatilov, E. P.; Lau, C. N.; Balandin, A. A. Dimensional Crossover of Thermal Transport in Few-Layer Graphene. *Nat. Mater.* **2010**, *9*, 555–558.

(5) Cai, W.; Moore, A. L.; Zhu, Y.; Li, X.; Chen, S.; Shi, L.; Ruoff, R. S. Thermal Transport in Suspended and Supported Monolayer Graphene Grown by Chemical Vapor Deposition. *Nano Lett.* **2010**, *10*, 1645–1651.

(6) Lee, C.; Wei, X.; Kysar, J. W.; Hone, J. Measurement of the Elastic Properties and Intrinsic Strength of Monolayer Graphene. *Science.* **2008**, *321*, 385–388.

(7) Rasool, H. I.; Ophus, C.; Klug, W. S.; Zettl, A.; Gimzewski, J. K. Measurement of the Intrinsic Strength of Crystalline and Polycrystalline Graphene. *Nat. Commun.* **2013**, *4*, 2811.

(8) Castro Neto, a. H.; Guinea, F.; Peres, N. M. R.; Novoselov, K. S.; Geim, a. K. The Electronic Properties of Graphene. *Rev. Mod. Phys.* **2009**, *81*, 109–162.

(9) Bolotin, K. I.; Sikes, K. J.; Jiang, Z.; Klima, M.; Fudenberg, G.; Hone, J.; Kim, P.; Stormer, H. L. Ultrahigh Electron Mobility in Suspended Graphene. *Solid State Commun.* **2008**, *146*, 351–355.

(10) Castro, E. V.; Novoselov, K. S.; Morozov, S. V.; Peres, N. M. R.; Dos Santos, J. M. B. L.; Nilsson, J.; Guinea, F.; Geim, A. K.; Neto, A. H. C. Biased Bilayer Graphene: Semiconductor with a Gap Tunable by the Electric Field Effect. *Phys. Rev. Lett.* **2007**, *99*, 216802.

(11) Zhang, Y.; Tang, T. T.; Girit, C.; Hao, Z.; Martin, M. C.; Zettl, A.; Crommie, M. F.; Shen, Y. R.; Wang, F. Direct Observation of a Widely Tunable Bandgap in Bilayer Graphene. *Nature* **2009**, *459*, 820–823.

(12) Han, M. Y.; Özyilmaz, B.; Zhang, Y.; Kim, P. Energy Band-Gap Engineering of Graphene Nanoribbons. *Phys. Rev. Lett.* **2007**, *98*, 206805.

(13) Li, X.; Wang, X.; Zhang, L.; Lee, S.; Dai, H. Chemically Derived, Ultrasmooth Graphene Nanoribbon Semiconductors. *Science* **2008**, *319*, 1229–1232.

(14) Agapito, L. A; Kioussis, N.; Widjaja, N.; Zhou, Z. Room-Temperature High On/Off Ratio in Suspended Graphene Nanoribbon Field Effect Transistors. 1–19.

(15) Denis, P. A. Band Gap Opening of Monolayer and Bilayer Graphene Doped with Aluminium, Silicon, Phosphorus, and Sulfur. *Chem. Phys. Lett.* **2010**, *492*, 251–257.

(16) Tan, H.; Fan, Y.; Zhou, Y.; Chen, Q.; Xu, W.; Warner, J. H. Ultrathin 2D Photodetectors Utilizing Chemical Vapor Deposition Grown WS_2 With Graphene Electrodes. *ACS Nano* **2016**, *10*, 7866-7873.

(17) Blake, P.; Brimicombe, P. D.; Nair, R. R.; Booth, T. J.; Jiang, D.; Schedin, F.; Ponomarenko, L. A.; Morozov, S. V; Gleeson, H. F.; Hill, E. W.; *et al.* Graphene-Based Liquid Crystal Device. *Nano Lett.* **2008**, *8*, 1704–1708.

(18) Han, W.; Kawakami, R. K.; Gmitra, M.; Fabian, J. Graphene Spintronics. *Nat Nanotechnol.* **2014**, *9*, 794–807.

(19) Wang, Q. H.; Kalantar-Zadeh, K.; Kis, A.; Coleman, J. N.; Strano, M. S. Electronics and Optoelectronics of Two-Dimensional Transition Metal Dichalcogenides. *Nat. Nanotechnol.* **2012**, *7*, 699–712.

(20) Wilson, J. A.; Yoffe, A. D. The Transition Metal Dichalcogenides Discussion and Interpretation of the Observed Optical, Electrical and Structural Properties. *Adv. Phys.* **1969**, *18*, 193–335.

(21) Radisavljevic, B.; Radenovic, A; Brivio, J.; Giacometti, V.; Kis, A. Single-Layer MoS_2

Transistors. *Nat. Nanotechnol.* **2011**, *6*, 147–150.

(22) Meyer, J. C.; Geim, A. K.; Katsnelson, M. I.; Novoselov, K. S.; Booth, T. J.; Roth, S. The Structure of Suspended Graphene Sheets. *Nature* **2007**, *446*, 60–63.

(23) Lin, Y. C.; Dumcenco, D. O.; Huang, Y. S.; Suenaga, K. Atomic Mechanism of the Semiconducting-to-Metallic Phase Transition in Single-Layered MoS_2. *Nat. Nanotechnol.* **2014**, *9*, 391–396.

(24) Novoselov, K. S.; Jiang, D.; Schedin, F.; Booth, T. J.; Khotkevich, V. V.; Morozov, S. V.; Geim, A. K. Two-Dimensional Atomic Crystals. *Proc. Natl. Acad. Sci.* **2005**, *102*, 10451–10453.

(25) M, T.; Late, D. J. Temperature Dependent Phonon Shifts in Single-Layer WS_2. *ACS Appl. Mater. Interfaces* **2014**, *6*, 1158–1163.

(26) PaciÍ, D.; Meyer, J. C.; Girit, Ç.; Zettl, A. The Two-Dimensional Phase of Boron Nitride: Few-Atomic-Layer Sheets and Suspended Membranes. *Appl. Phys. Lett.* **2008**, *92*, 133107.

(27) Nicolosi, V.; Chhowalla, M.; Kanatzidis, M. G.; Strano, M. S.; Coleman, J. N. Liquid Exfoliation of Layered Materials. *Science.* **2013**, *340*, 1226419.

(28) Coleman, J. N.; Lotya, M.; O'Neill, A.; Bergin, S. D.; King, P. J.; Khan, U.; Young, K.; Gaucher, A.; De, S.; Smith, R. J.; *et al.* Two-Dimensional Nanosheets Produced by Liquid Exfoliation of Layered Materials. *Science.* **2011**, *331*, 568–571.

(29) Smith, R. J.; King, P. J.; Lotya, M.; Wirtz, C.; Khan, U.; De, S.; O'Neill, A.; Duesberg, G. S.; Grunlan, J. C.; Moriarty, G.; *et al.* Large-Scale Exfoliation of Inorganic Layered Compounds in Aqueous Surfactant Solutions. *Adv. Mater.* **2011**, *23*, 3944–3948.

(30) Zhou, K. G.; Mao, N. N.; Wang, H. X.; Peng, Y.; Zhang, H. L. A Mixed-Solvent Strategy for Efficient Exfoliation of Inorganic Graphene Analogues. *Angew. Chemie - Int. Ed.* **2011**, *50*, 10839–10842.

(31) Wang, H.; Yang, X.; Shao, W.; Chen, S.; Xie, J.; Zhang, X.; Wang, J.; Xie, Y. Ultrathin Black Phosphorus Nanosheets for Efficient Singlet Oxygen Generation. *J. Am. Chem. Soc.* **2015**, *137*, 11376–11382.

(32) Kang, J.; Wood, J. D.; Wells, S. A.; Lee, J. H.; Liu, X.; Chen, K. S.; Hersam, M. C. Solvent Exfoliation of Electronic-Grade, Two-Dimensional Black Phosphorus. *ACS*

Nano **2015**, *9*, 3596–3604.

(33) Chhowalla, M.; Shin, H. S.; Eda, G.; Li, L.-J.; Loh, K. P.; Zhang, H. The Chemistry of Two-Dimensional Layered Transition Metal Dichalcogenide Nanosheets. *Nat. Chem.* **2013**, *5*, 263–275.

(34) Jariwala, B.; Voiry, D.; Jindal, A.; Chalke, B. A.; Bapat, R.; Thamizhavel, A.; Chhowalla, M.; Deshmukh, M.; Bhattacharya, A. Synthesis and Characterization of ReS_2 and $ReSe_2$ Layered Chalcogenide Single Crystals. *Chem. Mater.* **2016**, *28*, 3352–3359.

(35) Zeng, Z.; Yin, Z.; Huang, X.; Li, H.; He, Q.; Lu, G.; Boey, F.; Zhang, H. Single-Layer Semiconducting Nanosheets: High-Yield Preparation and Device Fabrication. *Angew. Chemie - Int. Ed.* **2011**, *50*, 11093–11097.

(36) May, J. W. Platinum Surface LEED Rings. *Surf. Sci.* **1969**, *17*, 267–270.

(37) Eizenberg, M.; Blakely, J. M. Carbon Monolayer Phase Condensation on Ni(111). *Surf. Sci.* **1979**, *82*, 228–236.

(38) Arco, L. De; Zhang, Y. Synthesis, Transfer, and Devices of Single-and Few-Layer Graphene by Chemical Vapor Deposition. *Ieee Trans. Nanotechnol.* **2009**, *8*, 135–138.

(39) Wintterlin, J.; Bocquet, M. L. Graphene on Metal Surfaces. *Surf. Sci.* **2009**, *603*, 1841–1852.

(40) Zhang, Y.; Gomez, L.; Ishikawa, F. N.; Madaria, A.; Ryu, K.; Wang, C.; Badmaev, A.; Zhou, C. Comparison of Graphene Growth on Single-Crystalline and Polycrystalline Ni by Chemical Vapor Deposition. *J. Phys. Chem. Lett.* **2010**, *1*, 3101–3107.

(41) Batzill, M. The Surface Science of Graphene: Metal Interfaces, CVD Synthesis, Nanoribbons, Chemical Modifications, and Defects. *Surf. Sci. Rep.* **2012**, *67*, 83–115.

(42) Li, X.; Cai, W.; An, J.; Kim, S.; Nah, J.; Yang, D.; Piner, R.; Velamakanni, A.; Jung, I.; Tutuc, E.; *et al.* Large-Area Synthesis of High-Quality and Uniform Graphene Films on Copper Foils. *Science.* **2009**, *324*, 1312–1314.

(43) Kim, K. S.; Zhao, Y.; Jang, H.; Lee, S. Y.; Kim, J. M.; Kim, K. S.; Ahn, J. H.; Kim, P.; Choi, J. Y.; Hong, B. H. Large-Scale Pattern Growth of Graphene Films for Stretchable Transparent Electrodes. *Nature* **2009**, *457*, 706–710.

(44) Reina, A.; Jia, X.; Ho, J.; Nezich, D.; Son, H.; Bulovic, V.; Dresselhaus, M. S.; Jing, K. Large Area, Few-Layer Graphene Films on Arbitrary Substrates by Chemical Vapor Deposition. *Nano Lett.* **2009**, *9*, 30–35.

(45) Wofford, J. M.; Nie, S.; McCarty, K. F.; Bartelt, N. C.; Dubon, O. D. Graphene Islands on Cu Foils: The Interplay between Shape, Orientation, and Defects. *Nano Lett.* **2010**, *10*, 4890–4896.

(46) Han, G. H.; Güneş, F.; Bae, J. J.; Kim, E. S.; Chae, S. J.; Shin, H. J.; Choi, J. Y.; Pribat, D.; Lee, Y. H. Influence of Copper Morphology in Forming Nucleation Seeds for Graphene Growth. *Nano Lett.* **2011**, *11*, 4144–4148.

(47) Luo, Z.; Lu, Y.; Singer, D. W.; Berck, M. E.; Somers, L. A.; Goldsmith, B. R.; Johnson, A. T. C. Effect of Substrate Roughness and Feedstock Concentration on Growth of Wafer-Scale Graphene at Atmospheric Pressure. *Chem. Mater.* **2011**, *23*, 1441–1447.

(48) Geng, D.; Wu, B.; Guo, Y.; Huang, L.; Xue, Y.; Chen, J.; Yu, G.; Jiang, L.; Hu, W.; Liu, Y. Uniform Hexagonal Graphene Flakes and Films Grown on Liquid Copper Surface. *Proc. Natl. Acad. Sci.* **2012**, *109*, 7992–7996.

(49) Wu, Y. A.; Fan, Y.; Speller, S.; Creeth, G. L.; Sadowski, J. T.; He, K.; Robertson, A. W.; Allen, C. S.; Warner, J. H. Large Single Crystals of Graphene on Melted Copper Using Chemical Vapor Deposition. *ACS Nano* **2012**, *6*, 5010–5017.

(50) Fan, Y.; He, K.; Tan, H.; Speller, S.; Warner, J. H. Crack-Free Growth and Transfer of Continuous Monolayer Graphene Grown on Melted Copper. *Chem. Mater.* **2014**, *26*, 4984–4991.

(51) An, H.; Lee, W. J.; Jung, J. Graphene Synthesis on Fe Foil Using Thermal CVD. *Curr. Appl. Phys.* **2011**, *11*, S81–S85.

(52) Wang, S. M.; Pei, Y. H.; Wang, X.; Wang, H.; Meng, Q. N.; Tian, H. W.; Zheng, X. L.; Zheng, W. T.; Liu, Y. C. Synthesis of Graphene on a Polycrystalline Co Film by Radio-Frequency Plasma-Enhanced Chemical Vapour Deposition. *J. Phys. D. Appl. Phys.* **2010**, *43*, 455402.

(53) Sutter, E.; Albrecht, P.; Sutter, P. Graphene Growth on Polycrystalline Ru Thin Films. *Appl. Phys. Lett.* **2009**, *95*, 133109.

(54) Müller, F.; Grandthyll, S.; Zeitz, C.; Jacobs, K.; Hüfner, S.; Gsell, S.; Schreck, M.

Epitaxial Growth of Graphene on Ir(111) by Liquid Precursor Deposition. *Phys. Rev. B - Condens. Matter Mater. Phys.* **2011**, *84*, 75472.

(55) Oznuluer, T.; Pince, E.; Polat, E. O.; Balci, O.; Salihoglu, O.; Kocabas, C. Synthesis of Graphene on Gold. *Appl. Phys. Lett.* **2011**, *98*, 183101.

(56) Kwon, S. Y.; Ciobanu, C. V.; Petrova, V.; Shenoy, V. B.; Bareño, J.; Gambin, V.; Petrov, I.; Kodambaka, S. Growth of Semiconducting Graphene on Palladium. *Nano Lett.* **2009**, *9*, 3985–3990.

(57) Kim, K. K.; Hsu, A.; Jia, X.; Kim, S. M.; Shi, Y.; Hofmann, M.; Nezich, D.; Rodriguez-Nieva, J. F.; Dresselhaus, M.; Palacios, T.; *et al.* Synthesis of Monolayer Boron Nitride on Cu Foil Using Chemical Vapor Deposition. *Nano Lett.* **2011**, *12*, 161–166.

(58) Ling, X.; Lee, Y.; Lin, Y.; Fang, W.; Yu, L.; Dresselhaus, M. S.; Kong, J. Role of the Seeding Promoter in MoS_2 Growth by Chemical Vapor Deposition. *Nano Lett.* **2014**, *14*, 464–472.

(59) Lee, Y. H.; Zhang, X. Q.; Zhang, W.; Chang, M. T.; Lin, C. T.; Chang, K. D.; Yu, Y. C.; Wang, J. T.; Chang, C. S.; Li, L. J.; *et al.* Synthesis of Large-Area MoS_2 Atomic Layers with Chemical Vapor Deposition. *Adv Mater* **2012**, *24*, 2320–2325.

(60) Nayak, P. K.; Lin, F. C.; Yeh, C. H.; Huang, J.S.; Chiu, P. W. Robust Room Temperature Valley Polarization in Monolayer and Bilayer WS_2. *Nanoscale* **2016**, *8*, 6035–6042.

(61) Shaw, J. C.; Zhou, H.; Chen, Y.; Weiss, N. O.; Liu, Y.; Huang, Y.; Duan, X. Chemical Vapor Deposition Growth of Monolayer $MoSe_2$ Nanosheets. *Nano Res.* **2014**, *7*, 511–517.

(62) Wang, S.; Pacios, M.; Bhaskaran, H.; Warner, J. H. Substrate Control for Large Area Continuous Films of Monolayer MoS_2 by Atmospheric Pressure Chemical Vapor Deposition. *Nanotechnology* **2016**, *27*, 85604.

(63) Sheng, Y.; Tan, H.; Wang, X.; Warner, J. H. Hydrogen Addition for Centimeter-Sized Monolayer Tungsten Disulfide Continuous Films by Ambient Pressure Chemical Vapor Deposition. *Chem. Mater.* **2017**, *29*, 4904–4911.

(64) Rong, Y.; Fan, Y.; Koh, A. L.; Robertson, A. W.; He, K.; Wang, S.; Tan, H.; Sinclair, R.; Warner, J. H. Controlling Sulphur Precursor Addition for Large Single Crystal

Domains of WS_2. *Nanoscale* **2014**, *6*, 12096–12103.

(65) Wang, S.; Wang, X.; Warner, J. H. All Chemical Vapor Deposition Growth of MoS_2 : H-BN Vertical van Der Waals Heterostructures. *ACS Nano* **2015**, *9*, 5246–5254.

(66) Yi, M.; Shen, Z. A Review on Mechanical Exfoliation for the Scalable Production of Graphene. *J. Mater. Chem. A* **2015**, *3*, 11700–11715.

(67) Butler, S. Z.; Hollen, S. M.; Cao, L.; Cui, Y.; Gupta, J. A.; Gutierrez, H. R.; Heinz, T. F.; Hong, S. S.; Huang, J.; Ismach, A. F.; *et al*. Progress, Challenges, and Opportunities in Two-Dimensional Materials beyond Graphene. *ACS Nano* **2013**, *7*, 2898–2926.

(68) Lahiri, J.; Lin, Y.; Bozkurt, P.; Oleynik, I. I.; Batzill, M. An Extended Defect in Graphene as a Metallic Wire. *Nat. Nanotechnol.* **2010**, *5*, 326–329.

(69) Ugeda, M. M.; Brihuega, I.; Guinea, F.; Gómez-Rodríguez, J. M. Missing Atom as a Source of Carbon Magnetism. *Phys. Rev. Lett.* **2010**, *104*, 96804.

(70) Xue, J.; Sanchez-Yamagishi, J.; Bulmash, D.; Jacquod, P.; Deshpande, A.; Watanabe, K.; Taniguchi, T.; Jarillo-Herrero, P.; LeRoy, B. J. Scanning Tunnelling Microscopy and Spectroscopy of Ultra-Flat Graphene on Hexagonal Boron Nitride. *Nat. Mater.* **2011**, *10*, 282–285.

(71) Rohrer, H. Scanning Tunneling Microscopy. *Proc. Natl. Acad. Sci. U. S. A.* **1987**, *84*, 4666.

(72) Robertson, A.; Warner, J. Atomic Resolution Imaging of Graphene by Transmission Electron Microscopy. *Nanoscale* **2013**, *5*, 4079–4093.

(73) Meyer, J. C.; Kisielowski, C.; Erni, R.; Rossell, M. D.; Crommie, M. F.; Zettl, A. Direct Imaging of Lattice Atoms and Topological Defects in Graphene Membranes. *Nano Lett.* **2008**, *8*, 3582–3586.

(74) Robertson, A. W.; Lee, G. D.; He, K.; Yoon, E.; Kirkland, A. I.; Warner, J. H. The Role of the Bridging Atom in Stabilizing Odd Numbered Graphene Vacancies. *Nano Lett.* **2014**, *14*, 3972–3980.

(75) Lehtinen, O.; Kurasch, S.; Krasheninnikov, A. V; Kaiser, U. Atomic Scale Study of the Life Cycle of a Dislocation in Graphene from Birth to Annihilation. *Nat. Commun.* **2013**, *4*, 2098.

(76) Gibb, A. L.; Alem, N.; Chen, J.; Erickson, K. J.; Ciston, J.; Gautam, A.; Linck, M.; Zettl, A. Atomic Resolution Imaging of Grain Boundary Defects in Monolayer Chemical Vapor Deposition-Grown Hexagonal Boron Nitride. *J. Am. Chem. Soc.* **2013**, *135*, 6758–6761.

(77) Komsa, H.P.; Kotakoski, J.; Kurasch, S.; Lehtinen, O.; Kaiser, U.; Krasheninnikov, A. V. Two-Dimensional Transition Metal Dichalcogenides under Electron Irradiation: Defect Production and Doping. *Phys. Rev. Lett.* **2012**, *109*, 35503.

(78) Warner, J. H.; Rümmeli, M. H.; Bachmatiuk, A.; Büchner, B. Atomic Resolution Imaging and Topography of Boron Nitride Sheets Produced by Chemical Exfoliation. *ACS Nano* **2010**, *4*, 1299–1304.

(79) Song, L.; Ci, L.; Lu, H.; Sorokin, P. B.; Jin, C.; Ni, J.; Kvashnin, A. G.; Kvashnin, D. G.; Lou, J.; Yakobson, B. I.; *et al.* Large Scale Growth and Characterization of Atomic Hexagonal Boron Nitride Layers. *Nano Lett.* **2010**, *10*, 3209–3215.

(80) Cretu, O.; Lin, Y.; Suenaga, K. Evidence for Active Atomic Defects in Monolayer Hexagonal Boron Nitride–a New Mechanism of Plasticity in 2D Materials. *Nano Lett.* **2014**, *14*, 1064–1068.

(81) Kotakoski, J.; Jin, C. H.; Lehtinen, O.; Suenaga, K.; Krasheninnikov, a. V. Electron Knock-on Damage in Hexagonal Boron Nitride Monolayers. *Phys. Rev. B - Condens. Matter Mater. Phys.* **2010**, *82*, 113404.

(82) Krivanek, O. L.; Chisholm, M. F.; Nicolosi, V.; Pennycook, T. J.; Corbin, G. J.; Dellby, N.; Murfitt, M. F.; Own, C. S.; Szilagyi, Z. S.; Oxley, M. P.; *et al.* Atom-by-Atom Structural and Chemical Analysis by Annular Dark-Field Electron Microscopy. *Nature* **2010**, *464*, 571–574.

(83) Liu, Z.; Suenaga, K.; Wang, Z.; Shi, Z.; Okunishi, E.; Iijima, S. Identification of Active Atomic Defects in a Monolayered Tungsten Disulphide Nanoribbon. *Nat. Commun.* **2011**, *2*, 213.

(84) Najmaei, S.; Liu, Z.; Zhou, W.; Zou, X.; Shi, G.; Lei, S.; Yakobson, B. I.; Idrobo, J.-C.; Ajayan, P. M.; Lou, J. Vapour Phase Growth and Grain Boundary Structure of Molybdenum Disulphide Atomic Layers. *Nat. Mater.* **2013**, *12*, 754–759.

(85) van der Zande, A. M.; Huang, P. Y.; Chenet, D. A; Berkelbach, T. C.; You, Y.; Lee, G. H.; Heinz, T. F.; Reichman, D. R.; Muller, D. a; Hone, J. C. Grains and Grain

Boundaries in Highly Crystalline Monolayer Molybdenum Disulphide. *Nat. Mater.* **2013**, *12*, 554–561.

(86) Gass, M. H.; Bangert, U.; Bleloch, A. L.; Wang, P.; Nair, R. R.; Geim, A. K. Free-Standing Graphene at Atomic Resolution. *Nat. Nanotechnol.* **2008**, *3*, 676–681.

(87) Huang, P. Y.; Ruiz-Vargas, C. S.; van der Zande, A. M.; Whitney, W. S.; Levendorf, M. P.; Kevek, J. W.; Garg, S.; Alden, J. S.; Hustedt, C. J.; Zhu, Y.; *et al.* Grains and Grain Boundaries in Single-Layer Graphene Atomic Patchwork Quilts. *Nature* **2011**, *469*, 389–392.

(88) Knoll, M.; Ruska, E. Das Elektronenmikroskop (Electron Microscope). *E. Z. Phys.* **1932**, *78*, 318–339.

(89) Davisson, C.; Germer, L. H. Diffraction of Electrons by a Single Crystal of Nickel. *Phys. Rev.* **1927**, *30*, 705–740.

(90) Thomson, G. P.; Reid, A. Diffraction of Cathode Rays by a Thin Film. *Nature*, 1927, *119*, 890.

(91) Warner, J. H.; Margine, E. R.; Mukai, M.; Robertson, A. W.; Giustino, F.; Kirkland, A. I. Dislocation-Driven Deformations in Graphene. *Science.* **2012**, *337*, 209–212.

(92) Williams, D.; Carter, C. *The Transmission Electron Microscope*; Springer: New York, 1996.

(93) Rose, H. Correction of Aberrations, a Promising Means for Improving the Spatial and Energy Resolution of Energy-Filtering Electron Microscopes. *Ultramicroscopy* **1994**, *56*, 11–25.

(94) Wen, J.; Miller, D. J.; Zaluzec, N. J.; Hiller, J. M.; Cook, R. E. Contribution of Cc - Correction to High-Resolution TEM at All Electron Energy Loss Regimes. *Microsc. Microanal.* **2013**, *19*, 594–595.

(95) Gong, C.; He, K.; Lee, G. D.; Chen, Q.; Robertson, A. W.; Yoon, E.; Hong, S.; Warner, J. H. In Situ Atomic Level Dynamics of Heterogeneous Nucleation and Growth of Graphene from Inorganic Nanoparticle Seeds. *ACS Nano* **2016**, *10*, 9397–9410.

(96) von Ardenne, M. Das Elektronen-Rastermikroskop - Theoretische Grundlagen (The Scanning Electron Microscope— Theoretical Foundations). *Z tech Phys* **1938**, *109*, 553–572.

(97) von Ardenne, M. Das Elektronen-Rastermikroskop. Praktische Ausführung (The Scanning Electron Microscope-Practical Construction). *Z tech Phys* **1938**, *19*, 407–416.

(98) Crewe, A. V.; Isaacson, M.; Johnson, D. A Simple Scanning Electron Microscope. *Rev. Sci. Instrum.* **1969**, *40*, 241–246.

(99) Crewe, A. V.; Wall, J.; Langmore, J. Visibility of Single Atoms. *Science.* **1970**, *168*, 1338–1340.

(100) Shin, D. H.; Kirkland, E. J.; Silcox, J. Annular Dark Field Electron Microscope Images with Better than 2 Å Resolution at 100 kV. *Appl. Phys. Lett.* **1989**, *55*, 2456–2458.

(101) Dellby, N.; Krivanek, O. L.; Nellist, P. D.; Batson, P. E.; Lupini, A. R. Progress in Aberration-Corrected Scanning Transmission Electron Microscopy. *J. Electron Microsc. (Tokyo).* **2001**, *50*, 177–185.

(102) Kisielowski, C.; Freitag, B.; Bischoff, M.; van Lin, H.; Lazar, S.; Knippels, G.; Tiemeijer, P.; van der Stam, M.; von Harrach, S.; Stekelenburg, M.; *et al.* Detection of Single Atoms and Buried Defects in Three Dimensions by Aberration-Corrected Electron Microscope with 0.5-Å Information Limit. *Microsc. Microanal.* **2008**, *14*, 469–477.

(103) Zhou, W.; Zou, X.; Najmaei, S.; Liu, Z.; Shi, Y.; Kong, J.; Lou, J.; Ajayan, P. M.; Yakobson, B. I.; Idrobo, J. C. Intrinsic Structural Defects in Monolayer Molybdenum Disulfide. *Nano Lett.* **2013**, *13*, 2615–2622.

(104) Lin, J.; Pantelides, S. T.; Zhou, W. Vacancy-Induced Formation and Growth of Inversion Domains in Transition-Metal Dichalcogenide Monolayer. *ACS Nano* **2015**, *9*, 5189-5197.

(105) Li, M. Y.; Shi, Y.; Cheng, C. C.; Lu, L.S.; Lin, Y.C.; Tang, H. L.; Tsai, M. L.; Chu, C. W.; Wei, K. H.; He, J. H.; *et al.* Epitaxial Growth of a Monolayer WSe_2-MoS_2 Lateral P-N Junction with an Atomically Sharp Interface. *Science.* **2015**, *349*, 524–528.

(106) Robertson, A. W.; Allen, C. S.; Wu, Y. a.; He, K.; Olivier, J.; Neethling, J.; Kirkland, A. I.; Warner, J. H. Spatial Control of Defect Creation in Graphene at the Nanoscale. *Nat. Commun.* **2012**, *3*, 1144.

(107) Carr, L. D.; Lusk, M. T. Defect Engineering: Graphene Gets Designer Defects. *Nat.*

Nanotechnol. **2010**, *5*, 316–317.

(108) Stone, A. J.; Wales, D. J. Theoretical Studies of Icosahedral C60 and Some Related Species. *Chem. Phys. Lett.* **1986**, *128*, 501–503.

(109) Ma, J.; Alfè, D.; Michaelides, A.; Wang, E. Stone-Wales Defects in Graphene and Other Planar sp2-Bonded Materials. *Phys. Rev. B* **2009**, *80*, 33407.

(110) Li, L.; Reich, S.; Robertson, J. Defect Energies of Graphite: Density-Functional Calculations. *Phys. Rev. B* **2005**, *72*, 184109.

(111) Chen, Q.; Robertson, A. W.; He, K.; Gong, C.; Yoon, E.; Lee, G. D.; Warner, J. H. Atomic Level Distributed Strain within Graphene Divacancies from Bond Rotations. *ACS Nano* **2015**, *9*, 8599–8608.

(112) Robertson, A. W.; Lee, G. D.; He, K.; Yoon, E.; Kirkland, A. I.; Warner, J. H. Stability and Dynamics of the Tetravacancy in Graphene. *Nano Lett.* **2014**, *14*, 1634–1642.

(113) Robertson, A. W.; Montanari, B.; He, K.; Allen, C. S.; Wu, Y. A.; Harrison, N. M.; Kirkland, A. I.; Warner, J. H. Structural Reconstruction of the Graphene Monovacancy. *ACS Nano* **2013**, *7*, 4495–4502.

(114) Lu, A. J.; Pan, B. C. Nature of Single Vacancy in Achiral Carbon Nanotubes. *Phys. Rev. Lett.* **2004**, *92*, 105504.

(115) El-Barbary, A. A.; Telling, R. H.; Ewels, C. P.; Heggie, M. I.; Briddon, P. R. Structure and Energetics of the Vacancy in Graphite. *Phys. Rev. B* **2003**, *68*, 144107.

(116) Ewels, C. P.; Telling, R. H.; El-Barbary, A. A.; Heggie, M. I.; Briddon, P. R. Metastable Frenkel Pair Defect in Graphite: Source of Wigner Energy? *Phys. Rev. Lett.* **2003**, *91*, 25505.

(117) Rossato, J.; Baierle, R. J.; Fazzio, A.; Mota, R. Vacancy Formation Process in Carbon Nanotubes: First-Principles Approach. *Nano Lett.* **2005**, *5*, 197–200.

(118) Berber, S.; Oshiyama, A. Reconstruction of Mono-Vacancies in Carbon Nanotubes: Atomic Relaxation vs. Spin Polarization. *Phys. B Condens. Matter* **2006**, *376–377*, 272–275.

(119) Lehtinen, P. O.; Foster, A. S.; Ma, Y.; Krasheninnikov, A. V; Nieminen, R. M. Irradiation-Induced Magnetism in Graphite: A Density Functional Study. *Phys. Rev.*

Lett. **2004**, *93*, 187202.

(120) Krasheninnikov, A. V.; Lehtinen, P. O.; Foster, A. S.; Nieminen, R. M. Bending the Rules: Contrasting Vacancy Energetics and Migration in Graphite and Carbon Nanotubes. *Chem. Phys. Lett.* **2006**, *418*, 132–136.

(121) Yazyev, O. V; Helm, L. Defect-Induced Magnetism in Graphene. *Phys. Rev. B* **2007**, *75*, 125408.

(122) Topsakal, M.; Aktürk, E.; Sevinçli, H.; Ciraci, S. First-Principles Approach to Monitoring the Band Gap and Magnetic State of a Graphene Nanoribbon via Its Vacancies. *Phys. Rev. B* **2008**, *78*, 235435.

(123) Banhart, F.; Kotakoski, J.; Krasheninnikov, A. V. Structural Defects in Graphene. *ACS Nano* **2011**, *5*, 26–41.

(124) Kotakoski, J.; Krasheninnikov, A. V; Kaiser, U.; Meyer, J. C. From Point Defects in Graphene to Two-Dimensional Amorphous Carbon. *Phys. Rev. Lett.* **2011**, *106*, 105505.

(125) Kotakoski, J.; Mangler, C.; Meyer, J. C. Imaging Atomic-Level Random Walk of a Point Defect in Graphene. *Nat. Commun.* **2014**, *5*, 3991.

(126) Kotakoski, J.; Meyer, J. C.; Kurasch, S.; Santos-Cottin, D.; Kaiser, U.; Krasheninnikov, A. V. Stone-Wales-Type Transformations in Carbon Nanostructures Driven by Electron Irradiation. *Phys. Rev. B* **2011**, *83*, 245420.

(127) Leyssale, J. M.; Vignoles, G. L. A Large-Scale Molecular Dynamics Study of the Divacancy Defect in Graphene. *J. Phys. Chem. C* **2014**, *118*, 8200–8216.

(128) Lee, G. D.; Wang, C. Z.; Yoon, E.; Hwang, N. M.; Kim, D. Y.; Ho, K. M. Diffusion, Coalescence, and Reconstruction of Vacancy Defects in Graphene Layers. *Phys. Rev. Lett.* **2005**, *95*, 205501.

(129) Kim, Y.; Ihm, J.; Yoon, E.; Lee, G. D. Dynamics and Stability of Divacancy Defects in Graphene. *Phys. Rev. B - Condens. Matter Mater. Phys.* **2011**, *84*, 75445.

(130) Kotakoski, J.; Krasheninnikov, A. V; Nordlund, K. Energetics, Structure, and Long-Range Interaction of Vacancy-Type Defects in Carbon Nanotubes: Atomistic Simulations. *Phys. Rev. B* **2006**, *74*, 245420.

(131) Wang, H.; Wang, Q.; Cheng, Y.; Li, K.; Yao, Y.; Zhang, Q.; Dong, C.; Wang, P.; Schwingenschlögl, U.; Yang, W.; *et al.* Doping Monolayer Graphene with Single Atom Substitutions. *Nano Lett.* **2012**, *12*, 141–144.

(132) Banhart, F.; Kotakoski, J.; Krasheninnikov, A. V. Structural Defects in Graphene. *ACS Nano* **2011**, *5*, 26–41.

(133) Rodriguez-Manzo, J. A; Banhart, F. Creation of Individual Vacancies in Carbon Nanotubes by Using an Electron Beam of 1 Angstrom Diameter. *Nano Lett.* **2009**, *9*, 2285–2289.

(134) Taylor, G. I. The Mechanism of Plastic Deformation of Crystals. Part I. Theoretical. *Proc. R. Soc. London. Ser. A.* **1934**, *145*, 362–387.

(135) Hirsch, P. B.; Horne, R. W.; Whelan, M. J. Direct Observations of the Arrangement and Motion of Dislocations in Aluminium. *Philos. Mag.* **1956**, *1*, 677–684.

(136) Hirsch, P. B. 50 Years of Transmission Electron Microscopy of Dislocations: Past, Present, and Future. *Her. Russ. Acad. Sci.* **2006**, *76*, 430–436.

(137) Chen, S.; Chrzan, D. C. Continuum Theory of Dislocations and Buckling in Graphene. *Phys. Rev. B* **2011**, *84*, 214103.

(138) Yazyev, O. V; Louie, S. G. Topological Defects in Graphene: Dislocations and Grain Boundaries. *Phys. Rev. B* **2010**, *81*, 195420.

(139) Hashimoto, A.; Suenaga, K.; Gloter, A.; Urita, K.; Iijima, S. Direct Evidence for Atomic Defects in Graphene Layers. *Nature* **2004**, *430*, 870–873.

(140) Liu, Z.; Suenaga, K.; Harris, P. J. F.; Iijima, S. Open and Closed Edges of Graphene Layers. *Phys. Rev. Lett.* **2009**, *102*, 15501.

(141) Warner, J. H.; Young, N. P.; Kirkland, A. I.; Briggs, G. A. D. Resolving Strain in Carbon Nanotubes at the Atomic Level. *Nat. Mater.* **2011**, *10*, 958–962.

(142) Meyer, J. C.; Kurasch, S.; Park, H. J.; Skakalova, V.; Künzel, D.; Gross, A.; Chuvilin, A.; Algara-Siller, G.; Roth, S.; Iwasaki, T.; *et al.* Experimental Analysis of Charge Redistribution due to Chemical Bonding by High-Resolution Transmission Electron Microscopy. *Nat. Mater.* **2011**, *10*, 209–215.

(143) Suenaga, K.; Koshino, M. Atom-by-Atom Spectroscopy at Graphene Edge. *Nature*

2010, *468*, 1088–1090.

(144) Kurasch, S.; Kotakoski, J.; Lehtinen, O.; Skakalova, V.; Smet, J.; Krill, C. E.; Krasheninnikov, A. V.; Kaiser, U. Atom-by-Atom Observation of Grain Boundary Migration in Graphene. *Nano Lett.* **2012**, *12*, 3168–3173.

(145) An, J.; Voelkl, E.; Suk, J.; Li, X.; Magnuson, C. W.; Fu, L.; Tiemeijer, P.; Bischoff, M.; Freitag, B.; Popova, E.; *et al.* Domain (Grain) Boundaries and Evidence of " Twin-Like " Structures in CVD Grown Graphene. *ACS Nano* **2011**, *5*, 2433–2439.

(146) Yang, B.; Xu, H.; Lu, J.; Loh, K. P. Periodic Grain Boundaries Formed by Thermal Reconstruction of Polycrystalline Graphene Film. *J. Am. Chem. Soc.* **2014**, *136*, 12041–12046.

(147) Gong, C.; He, K.; Chen, Q.; Robertson, A. W.; Warner, J. H. In Situ High Temperature Atomic Level Studies of Large Closed Grain Boundary Loops in Graphene. *ACS Nano* **2016**, *10*, 9165–9173.

(148) Kim, D.; Kim, Y.; Ihm, J.; Yoon, E.; Lee, G. D. Atomic-Scale Mechanism of Grain Boundary Motion in Graphene. *Carbon N. Y.* **2015**, *84*, 146–150.

(149) Bae, S.; Kim, H.; Lee, Y.; Xu, X.; Park, J. S.; Zheng, Y.; Balakrishnan, J.; Lei, T.; Kim, H. R.; Song, Y. I; *et al.* Roll-to-Roll Production of 30-Inch Graphene Films for Transparent Electrodes. *Nat Nano* **2010**, *5*, 574–578.

(150) Zhou, S. Y.; Siegel, D. A.; Fedorov, A. V; Lanzara, A. Metal to Insulator Transition in Epitaxial Graphene Induced by Molecular Doping. *Phys. Rev. Lett.* **2008**, *101*, 86402.

(151) Elias, D. C.; Nair, R. R.; Mohiuddin, T. M. G.; Morozov, S. V; Blake, P.; Halsall, M. P.; Ferrari, A. C.; Boukhvalov, D. W.; Katsnelson, M. I.; Geim, A. K.; *et al.* Control of Graphene's Properties by Reversible Hydrogenation: Evidence for Graphene. *Sci.* **2009**, *323*, 610–613.

(152) Wang, Y.; Huang, Y.; Song, Y.; Zhang, X.; Ma, Y.; Liang, J.; Chen, Y. Room-Temperature Ferromagnetism of Graphene. *Nano Lett.* **2008**, *9*, 220–224.

(153) Novoselov, K. S.; Fal'ko, V. I.; Colombo, L.; Gellert, P. R.; Schwab, M. G.; Kim, K. A Roadmap for Graphene. *Nature* **2012**, *490*, 192–200.

(154) Arsat, R.; Breedon, M.; Shafiei, M.; Spizziri, P. G.; Gilje, S.; Kaner, R. B.; Kalantar-zadeh, K.; Wlodarski, W. Graphene-like Nano-Sheets for Surface Acoustic Wave Gas

Sensor Applications. *Chem. Phys. Lett.* **2009**, *467*, 344–347.

(155) Warner, J. H.; Rümmeli, M. H.; Bachmatiuk, A.; Wilson, M.; Büchner, B. Examining Co-Based Nanocrystals on Graphene Using Low-Voltage Aberration-Corrected Transmission Electron Microscopy. *ACS Nano* **2010**, *4*, 470–476.

(156) Warner, J.; Lin, Y.; He, K.; Koshino, M.; Suenaga, K. Stability and Spectroscopy of Single Nitrogen Dopants in Graphene at Elevated Temperatures. *ACS Nano* **2014**, 11806–11815.

(157) Yang, Z.; Yin, L.; Lee, J.; Ren, W.; Cheng, H. M.; Ye, H.; Pantelides, S. T.; Pennycook, S. J.; Chisholm, M. F. Direct Observation of Atomic Dynamics and Silicon Doping at a Topological Defect in Graphene. *Angew. Chemie - Int. Ed.* **2014**, *53*, 8908–8912.

(158) Sevinçli, H.; Topsakal, M.; Durgun, E.; Ciraci, S. Electronic and Magnetic Properties of $3d$ Transition-Metal Atom Adsorbed Graphene and Graphene Nanoribbons. *Phys. Rev. B* **2008**, *77*, 195434.

(159) Krasheninnikov, A. V.; Lehtinen, P. O.; Foster, A. S.; Pyykkö, P.; Nieminen, R. M. Embedding Transition-Metal Atoms in Graphene: Structure, Bonding, and Magnetism. *Phys. Rev. Lett.* **2009**, *102*, 126807.

(160) Robertson, A. W.; Montanari, B.; He, K.; Kim, J.; Allen, C. S.; Wu, Y. A.; Olivier, J.; Neethling, J.; Harrison, N.; Kirkland, A. I.; *et al.* Dynamics of Single Fe Atoms in Graphene Vacancies. *Nano Lett.* **2013**, *13*, 1468–1475.

(161) Ramasse, Q. M.; Seabourne, C. R.; Kepaptsoglou, D.-M.; Zan, R.; Bangert, U.; Scott, A. J. Probing the Bonding and Electronic Structure of Single Atom Dopants in Graphene with Electron Energy Loss Spectroscopy. *Nano Lett.* **2013**, *13*, 4989–4995.

(162) He, Z.; He, K.; Robertson, A. W.; Kirkland, A. I.; Kim, D.; Ihm, J.; Yoon, E.; Lee, G. D.; Warner, J. H. Atomic Structure and Dynamics of Metal Dopant Pairs in Graphene. *Nano Lett.* **2014**, *14*, 3766–3772.

(163) Zhou, M.; Lu, Y. H.; Cai, Y. Q.; Zhang, C.; Feng, Y.-P. Adsorption of Gas Molecules on Transition Metal Embedded Graphene: A Search for High-Performance Graphene-Based Catalysts and Gas Sensors. *Nanotechnology* **2011**, *22*, 385502.

(164) Tristant, D.; Puech, P.; Gerber, I. C. Theoretical Study of Graphene Doping Mechanism by Iodine Molecules. *J. Phys. Chem. C* **2015**, *119*, 12071–12078.

(165) Cao, C.; Wu, M.; Jiang, J.; Cheng, H. P. Transition Metal Adatom and Dimer Adsorbed on Graphene: Induced Magnetization and Electronic Structures. *Phys. Rev. B - Condens. Matter Mater. Phys.* **2010**, *81*, 205424.

(166) Liu, X.; Wang, C. Z.; Hupalo, M.; Lu, W. C.; Tringides, M. C.; Yao, Y. X.; Ho, K. M. Metals on Graphene: Correlation between Adatom Adsorption Behavior and Growth Morphology. *Phys. Chem. Chem. Phys.* **2012**, *14*, 9157–9166.

(167) Thakur, J.; Kashyap, M. K.; Saini, H. S.; Reshak, A. H. Enhanced Magnetic Response and Metallicity in AB Stacked Bilayer Graphene via Cr-Doping. *J. Alloys Compd.* **2015**, *649*, 1300–1305.

(168) Lee, J.; Zhou, W.; Pennycook, S. J.; Idrobo, J.-C.; Pantelides, S. T. Direct Visualization of Reversible Dynamics in a Si6 Cluster Embedded in a Graphene Pore. *Nat. Commun.* **2013**, *4*, 1650.

(169) Chen, Q.; Koh, A. L.; Robertson, A. W.; He, K.; Lee, S.; Yoon, E.; Lee, G. D.; Sinclair, R.; Warner, J. H. Rotating Anisotropic Crystalline Silicon Nanoclusters in Graphene. *ACS Nano* **2015**, *9*, 9497–9506.

(170) Zhao, J.; Deng, Q.; Bachmatiuk, A.; Sandeep, G.; Popov, A.; Eckert, J.; Rümmeli, M. H. Free-Standing Single-Atom-Thick Iron Membranes Suspended in Graphene Pores. *Sci.* **2014**, *343*, 1228–1232.

(171) KC, S.; Longo, R. C.; Addou, R.; Wallace, R. M.; Cho, K. Impact of Intrinsic Atomic Defects on the Electronic Structure of MoS_2 Monolayers. *Nanotechnology* **2014**, *25*, 375703.

(172) Ataca, C.; Şahin, H.; Aktürk, E.; Ciraci, S. Mechanical and Electronic Properties of MoS2 Nanoribbons and Their Defects. *J. Phys. Chem. C* **2011**, *115*, 3934–3941.

(173) Gong, Y.; Lin, J.; Wang, X.; Shi, G.; Lei, S.; Lin, Z.; Zou, X.; Ye, G.; Vajtai, R.; Yakobson, B. I.; *et al.* Vertical and in-Plane Heterostructures from WS_2/MoS_2 Monolayers. *Nat. Mater.* **2014**, *13*, 1135–1142.

(174) Terrones, H.; López-Urías, F.; Terrones, M. Novel Hetero-Layered Materials with Tunable Direct Band Gaps by Sandwiching Different Metal Disulfides and Diselenides. *Sci. Rep.* **2013**, *3*, 1549.

(175) Geim, A. K.; Grigorieva, I. V. Van Der Waals Heterostructures. *Nature* **2013**, *499*, 419–

425.

(176) Terrones, H.; Terrones, M. Electronic and Vibrational Properties of Defective Transition Metal Dichalcogenide Haeckelites: New 2D Semi-Metallic Systems. *2D Mater.* **2014**, *1*, 11003.

(177) Garcia, A.; Raya, A. M.; Mariscal, M. M.; Esparza, R.; Herrera, M.; Molina, S. I.; Scavello, G.; Galindo, P. L.; Jose-Yacaman, M.; Ponce, A. Analysis of Electron Beam Damage of Exfoliated MoS_2 Sheets and Quantitative HAADF-STEM Imaging. *Ultramicroscopy* **2014**, *146*, 33–38.

(178) Komsa, H.; Teng, P.; Yeh, C.; Huang, F.; Lin, Y.; Suenaga, K. Three-Fold Rotational Defects in Two-Dimensional Transition Metal Dichalcogenides. *Nat. Commun.* **2015**, *6*, 6736.

(179) Zhang, K.; Feng, S.; Wang, J.; Azcatl, A.; Lu, N.; Addou, R.; Wang, N.; Zhou, C.; Lerach, J.; Bojan, V.; *et al.* Manganese Doping of Monolayer MoS_2: The Substrate Is Critical. *Nano Lett.* **2015**, *15*, 6586–6591.

(180) Robertson, A. W.; Lin, Y. C.; Wang, S.; Sawada, H.; Allen, C. S.; Chen, Q.; Lee, S.; Lee, G. D.; Lee, J.; Han, S.; *et al.* Atomic Structure and Spectroscopy of Single Metal (Cr, V) Substitutional Dopants in Monolayer MoS_2. *ACS Nano* **2016**, *10*, 10227–10236.

(181) Chen, Y.; Xi, J.; Dumcenco, D. O.; Liu, Z.; Suenaga, K.; Wang, D.; Shuai, Z.; Huang, Y. S.; Xie, L. Tunable Band Gap Photoluminescence from Atomically Thin Transition-Metal Dichalcogenide Alloys. *ACS Nano* **2013**, *7*, 4610–4616.

(182) Li, H.; Duan, X.; Wu, X.; Zhuang, X.; Zhou, H.; Zhang, Q.; Zhu, X.; Pan, A.; Duan, X. Growth of alloy$MoS_2xSe_{2(1-x)}$ Nanosheets with Fully Tunable Chemical Compositions and Optical Properties. **2014**, *2*, 8–11.

(183) Lin, Z.; Carvalho, B. R.; Kahn, E.; Lv, R.; Rao, R.; Terrones, H.; Pimenta, M. A.; Terrones, M. Defect Engineering of Two-Dimensional Transition Metal Dichalcogenides. *2D Mater.* **2016**, *3*, 22002.

(184) Li, H.; Wang, S.; Sawada, H.; Han, G. G. D.; Samuels, T.; Allen, C. S.; Kirkland, A. I.; Grossman, J. C.; Warner, J. H. Atomic Structure and Dynamics of Single Platinum Atom Interactions with Monolayer MoS_2. *ACS Nano* **2017**, *11*, 3392–3403.

(185) Laskar, M. R.; Nath, D. N.; Ma, L.; Lee, E. W.; Lee, C. H.; Kent, T.; Yang, Z.; Mishra, R.; Roldan, M. A.; Idrobo, J. C.; *et al.* P-Type Doping of MoS_2 Thin Films Using Nb. *Appl. Phys. Lett.* **2014**, *104*, 92104.

(186) Wang, S. Y.; Ko, T. S.; Huang, C. C.; Lin, D. Y.; Huang, Y. S. Optical and Electrical Properties of MoS_2 and Fe-Doped MoS_2. *Jpn. J. Appl. Phys.* **2014**, *53*, 04EH07.

(187) Ataca, C.; Ciraci, S. Functionalization of Single-Layer MoS_2 Honeycomb Structures. *J. Phys. Chem. C* **2011**, *115*, 13303–13311.

(188) Lin, Y. C.; Dumcenco, D. O.; Komsa, H. P.; Niimi, Y.; Krasheninnikov, A. V.; Huang, Y. S.; Suenaga, K. Properties of Individual Dopant Atoms in Single-Layer MoS_2: Atomic Structure, Migration, and Enhanced Reactivity. *Adv. Mater.* **2014**, *26*, 2857–2861.

(189) Mouri, S.; Miyauchi, Y.; Matsuda, K. Tunable Photoluminescence of Monolayer MoS_2 via Chemical Doping. *Nano Lett.* **2013**, *13*, 5944–5948.

(190) Komsa, H. P.; Kurasch, S.; Lehtinen, O.; Kaiser, U.; Krasheninnikov, A. V. From Point to Extended Defects in Two-Dimensional MoS_2: Evolution of Atomic Structure under Electron Irradiation. *Phys. Rev. B - Condens. Matter Mater. Phys.* **2013**, *88*, 35301.

(191) Wang, S.; Lee, G. D.; Lee, S.; Yoon, E.; Warner, J. H. Detailed Atomic Reconstruction of Extended Line Defects in Monolayer MoS_2. *ACS Nano* **2016**, *10*, 5419–5430.

(192) Ryu, G. H.; Lee, J.; Kim, N. Y.; Lee, Y.; Kim, Y.; Kim, M. J.; Lee, C.; Lee, Z. Line-Defect Mediated Formation of Hole and Mo Clusters in Monolayer Molybdenum Disulfide. *2D Mater.* **2016**, *3*, 14002.

(193) Zou, X.; Liu, Y.; Yakobson, B. I. Predicting Dislocations and Grain Boundaries in Two-Dimensional Metal-Disulfides from the First Principles. *Nano Lett.* **2013**, *13*, 253–258.

(194) Azizi, A.; Zou, X.; Ercius, P.; Zhang, Z.; Elías, A. L.; Perea-López, N.; Stone, G.; Terrones, M.; Yakobson, B. I.; Alem, N. Dislocation Motion and Grain Boundary Migration in Two-Dimensional Tungsten Disulphide. *Nat. Commun.* **2014**, *5*, 4876.

(195) Hansen, L. P.; Ramasse, Q. M.; Kisielowski, C.; Brorson, M.; Johnson, E.; Topsøe, H.; Helveg, S. Atomic-Scale Edge Structures on Industrial-Style MoS_2 Nanocatalysts. *Angew. Chemie - Int. Ed.* **2011**, *50*, 10153–10156.

(196) Kisielowski, C.; Ramasse, Q. M.; Hansen, L. P.; Brorson, M.; Carlsson, A.;

Molenbroek, A. M.; Topsøe, H.; Helveg, S. Imaging MoS_2 Nanocatalysts with Single-Atom Sensitivity. *Angew. Chemie - Int. Ed.* **2010**, *49*, 2708–2710.

(197) Bollinger, M.; Jacobsen, K.; Nørskov, J. Atomic and Electronic Structure of MoS_2 Nanoparticles. *Phys. Rev. B* **2003**, *67*, 85410.

(198) Gibertini, M.; Marzari, N. Emergence of One-Dimensional Wires of Free Carriers in Transition-Metal-Dichalcogenide Nanostructures. *Nano Lett.* **2015**, *15*, 6229–6238.

(199) Li, Y.; Zhou, Z.; Zhang, S.; Chen, Z. MoS_2 Nanoribbons: High Stability and Unusual Electronic and Magnetic Properties. *J. Am. Chem. Soc.* **2008**, *130*, 16739–16744.

(200) Bollinger, M. V.; Lauritsen, J. V.; Jacobsen, K. W.; Nørskov, J. K.; Helveg, S.; Besenbacher, F. One-Dimensional Metallic Edge States in MoS_2. *Phys. Rev. Lett.* **2001**, *87*, 196803.

(201) Xiao, S. L.; Yu, W. Z.; Gao, S. P. Edge Preference and Band Gap Characters of MoS_2 and WS_2 Nanoribbons. *Surf. Sci.* **2016**, *653*, 107–112.

(202) Lehtinen, O.; Komsa, H.; Pulkin, A.; Whitwick, M. B.; Chen, M.; Lehnert, T.; Mohn, M. J.; Yazyev, O. V; Kis, A.; Kaiser, U.; *et al.* Atomic Scale Microstructure and Properties of Se-Deficient Two-Deiensional $MoSe_2$. *ACS Nano* **2015**, *9*, 3274–3283.

(203) Luo, S.; Hao, G.; Fan, Y.; Kou, L.; He, C.; Qi, X.; Tang, C.; Li, J.; Huang, K.; Zhong, J. Formation of Ripples in Atomically Thin MoS_2 and Local Strain Engineering of Electrostatic Properties. *Nanotechnology* **2015**, *26*, 105705.

(204) Liu, H.; Chi, D. Dispersive Growth and Laser-Induced Rippling of Large-Area Singlelayer MoS_2 Nanosheets by CVD on C-Plane Sapphire Substrate. *Sci. Rep.* **2015**, *5*, 11756.

(205) Hussain, S.; Singh, J.; Vikraman, D.; Singh, A. K.; Iqbal, M. Z.; Khan, M. F.; Kumar, P.; Choi, D.C.; Song, W.; An, K.-S.; *et al.* Large-Area, Continuous and High Electrical Performances of Bilayer to Few Layers MoS_2 Fabricated by RF Sputtering via Post-Deposition Annealing Method. *Sci. Rep.* **2016**, *6*, 30791.

(206) Hsu, W. T.; Zhao, Z. A.; Li, L. J.; Chen, C. H.; Chiu, M. H.; Chang, P. S.; Chou, Y. C.; Chang, W. H. Second Harmonic Generation from Artificially Stacked Transition Metal Dichalcogenide Twisted Bilayers. *ACS Nano* **2014**, *8*, 2951–2958.

(207) Azizi, A.; Eichfeld, S.; Geschwind, G.; Zhang, K.; Jiang, B.; Mukherjee, D.; Hossain,

L.; Piasecki, A. F.; Kabius, B.; Robinson, J. A.; *et al.* Freestanding van Der Waals Heterostructures of Graphene and Transition Metal Dichalcogenides. *ACS Nano* **2015**, *9*, 4882–4890.

(208) Georgiou, T.; Jalil, R.; Belle, B. D.; Britnell, L.; Gorbachev, R. V; Morozov, S. V; Kim, Y.J.; Gholinia, A.; Haigh, S. J.; Makarovsky, O.; *et al.* Vertical Field-Effect Transistor Based on Graphene-WS_2 Heterostructures for Flexible and Transparent Electronics. *Nat. Nanotechnol.* **2013**, *8*, 100–103.

Chapter 3

Methodology

3.1 Introduction

This chapter covers the experimental and analytical techniques which have been employed in this project. This includes chemical vapour deposition (CVD) synthesis of graphene and monolayer MoS_2, TEM samples preparation and imaging, as well as data analysis methods. The focus of this chapter is to introduce the techniques that have been applied to this project, rather than to dig into the fundamental principles. For instance, the section on transmission electron microscopy will describe the details related to the specific microscope model, such as TEM operation procedures and acceptable aberration parameters, etc. All the experiments and analysis conducted in this project are expected to be replicable with the provided details in this chapter.

3.2 CVD Synthesis

3.2.1 Monolayer Graphene

Graphene was synthesized by atmospheric pressure CVD using the equipment set-up demonstrated in Figure 3-1. This method was firstly developed by Dr. Y. Wu[1] and then modified by Dr. Y. Fan.[2] Tungsten (Alfa Aesar, 99.95% purity, 0.05 mm thickness) and high purity copper foils (Alfa Aesar, Puratonic 99.999% pure, 0.1 mm thickness) were cut into 1×1 cm^2 pieces. The copper pieces were then ultra-sonicated in hydrochloric acid solution (Alfa Aesar, 37% HCl:H_2O = 1:3) for 2-3 min to remove

the oxidised layer, and both tungsten and copper pieces were cleaned by sonication in acetone and 2-propanol (IPA) for about 15 min before being loaded into ceramic boat(s) with Cu on top as catalysts and W at the bottom as substrates. With all the metal substrates and catalysts being placed into the 1-inch quartz tube in the furnace, 80 s.c.c.m. of H_2/Ar (25%/75%) and 200 s.c.c.m. of pure Ar was applied to flush the system until it stabilised at 1090 °C for 30 min. 10 s.c.c.m. CH_4/Ar (1%/99%) was then added to the gas flow to start the growth of graphene for 90 min, followed by a secondary growth at 1060 °C for 30 min. The methane was immediately stopped once the secondary growth of graphene was done. The samples were subsequently removed from the heating zone of the tube and cooled in air to room temperature. At most 10 pieces of graphene samples could be produced in one batch with the use of two ceramic boats. More than this would lead to incomplete melting of Cu foils and undesirable sample qualities. After taken out from the furnace, the graphene sides of the samples were immediately coated with a poly-methyl-methacrylate (PMMA) (8% wt in anisole, 495A molecular weight) supportive scaffold by spin coater at 4700 rpm for 60 s, followed by baking at 180 °C for 90 s in air for PMMA solidification. The final products are shown in Figure 3-1(b).

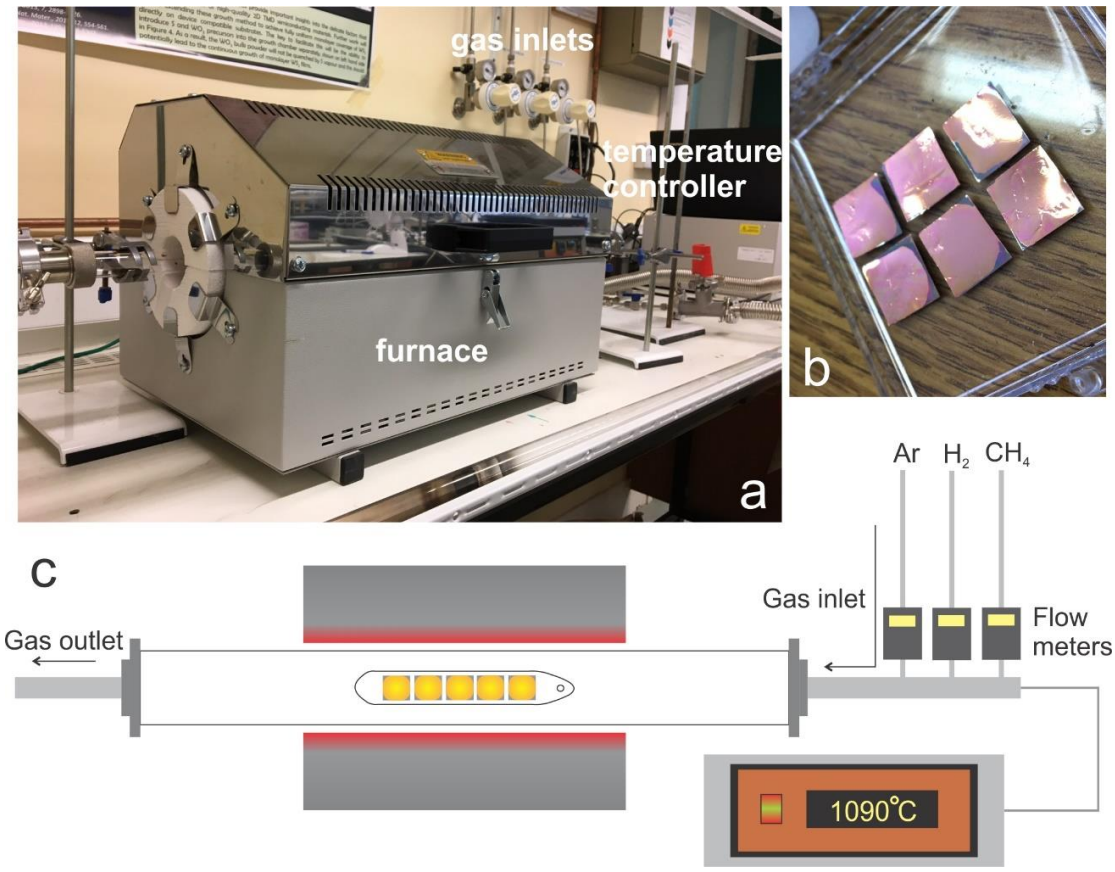

Figure 3-1 A photograph (a) and schematic illustration (c) of the CVD setup for graphene synthesis in this project. (b) A photograph of six pieces of graphene samples with PMMA coating.

3.2.2 Monolayer MoS_2

Monolayer MoS_2 was produced by atmospheric pressure CVD using the equipment set-up demonstrated in Figure 3-2. This method was originally developed by Dr S. Wang and her colleagues.[3] In this project, MoS_2 synthesis was carried out by Miss W. Xu. The MoS_2 domains were grown on a SiO_2 (300 nm)/Si substrate (University Wafer), which was sonicated in acetone and IPA for 15 min sequentially, followed by an oxygen plasma treatment. The growth was carried out in a double-furnace CVD system using 20 mg of MoO_3 powder (Sigma-Aldrich, 99.5% purity) and 500 mg of S (Sigma-Aldrich, 99.5% purity) as the precursor with Ar as carrier gas under atmospheric pressure. The S powder was placed at the central area of the first furnace

in the outer 1 inch quartz tube, while the MoO_3 was loaded separately upstream in the second furnace in an inner quartz tube having a smaller diameter of 1 cm. The Si substrate was placed horizontally at the centre of the second furnace. The growth system was first flushed with 500 s.c.c.m. of Ar gas for 30 min, followed by a pre-introduction of S vapour by heating the S powder to ~180 °C for 10 min under an Ar flow rate of 150 s.c.c.m. The second furnace was maintained at 200 °C at the same time to avoid any deposition of solid S on the substrate surface. This ensured the reaction occurring under a S atmosphere effectively controlling the initial MoS_2 nucleation density. The second furnace was heated at a rate of 40 °C min^{-1} to 800°C, while the MoO_3 powder reached an approximate maximum temperature of 300 °C. The reaction was conducted at 800 °C for 20 min with 10 sccm Ar. After completion of the reaction a fast cooling process was applied to quickly stop the growth. Figure 3-2(b) shows an optical image of the as synthesized MoS_2 domains. A thin film of PMMA was then spin-coated on the MoS_2 surface after growth, using the same chemicals and parameters for graphene samples described in section 3.2.1.

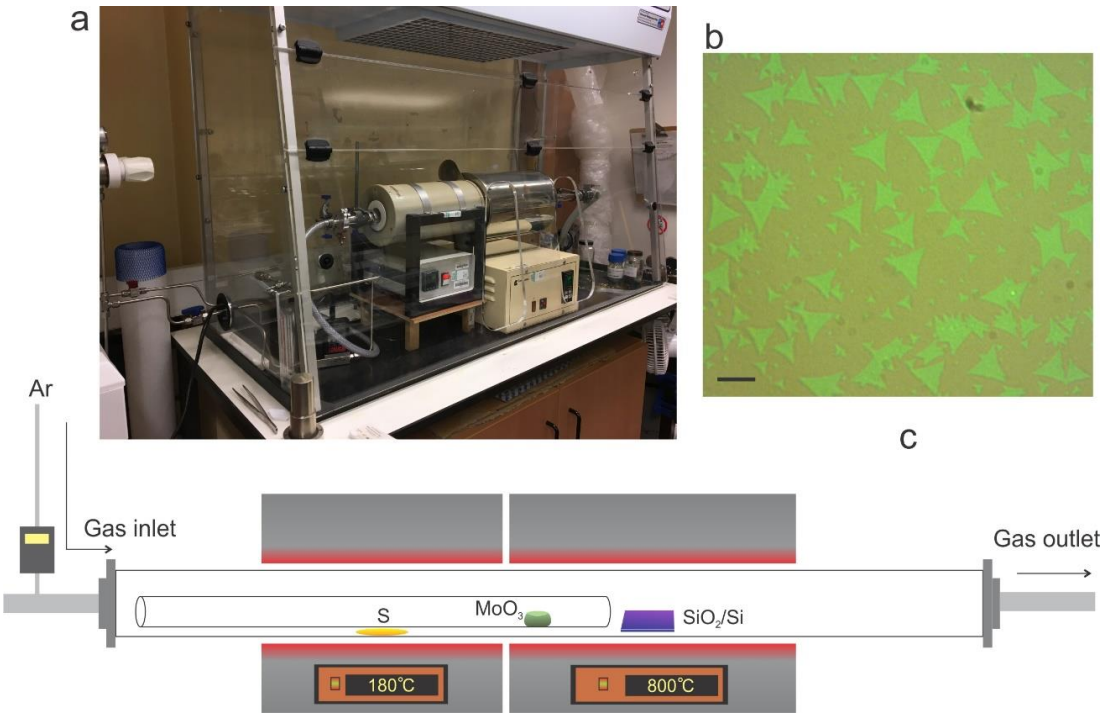

Figure 3-2 A photograph (a) and schematic illustration (c) of the CVD setup for MoS_2 synthesis. (b) An optical image for MoS_2 domains. Scale bar in (b), 100 µm.

3.3 TEM sample preparation

3.3.1 Graphene TEM Sample

Electrochemical etching in sodium hydroxide solution (2M) was applied to remove tungsten substrate, with a copper foil serving as anode.[2] The copper was then etched away by floating the samples on ammonium persulfate solution (0.1M). The transparent graphene samples with PMMA scaffold were then transferred onto the top of deionised water for 1 hour. This process was repeated three times to fully remove any ionic residue on the graphene surface, followed by transferring them onto Si_3N_4 grids (Agar Scientific Y5385) or prefabricated in-situ heating chips and drying in air for 3 hours. 30 minutes of bake at 180 °C was applied to the sample to reinforce the

adhesion between graphene and the wafer. PMMA scaffold was removed by submerging the TEM grids in acetone for 12 hours.

3.3.2 MoS_2 TEM Sample

Etching of SiO_2 is accomplished by floatation (PMMA side up) on 1M KOH. After the completely remove of SiO_2, the Si chip would detached from the PMMA/MoS_2 film. The following rinsing and transfer steps are identical to the ones for graphene TEM samples. Only in-situ heating samples were made for MoS_2.

3.3.3 Thermal Deposition of Gold Nanoparticles

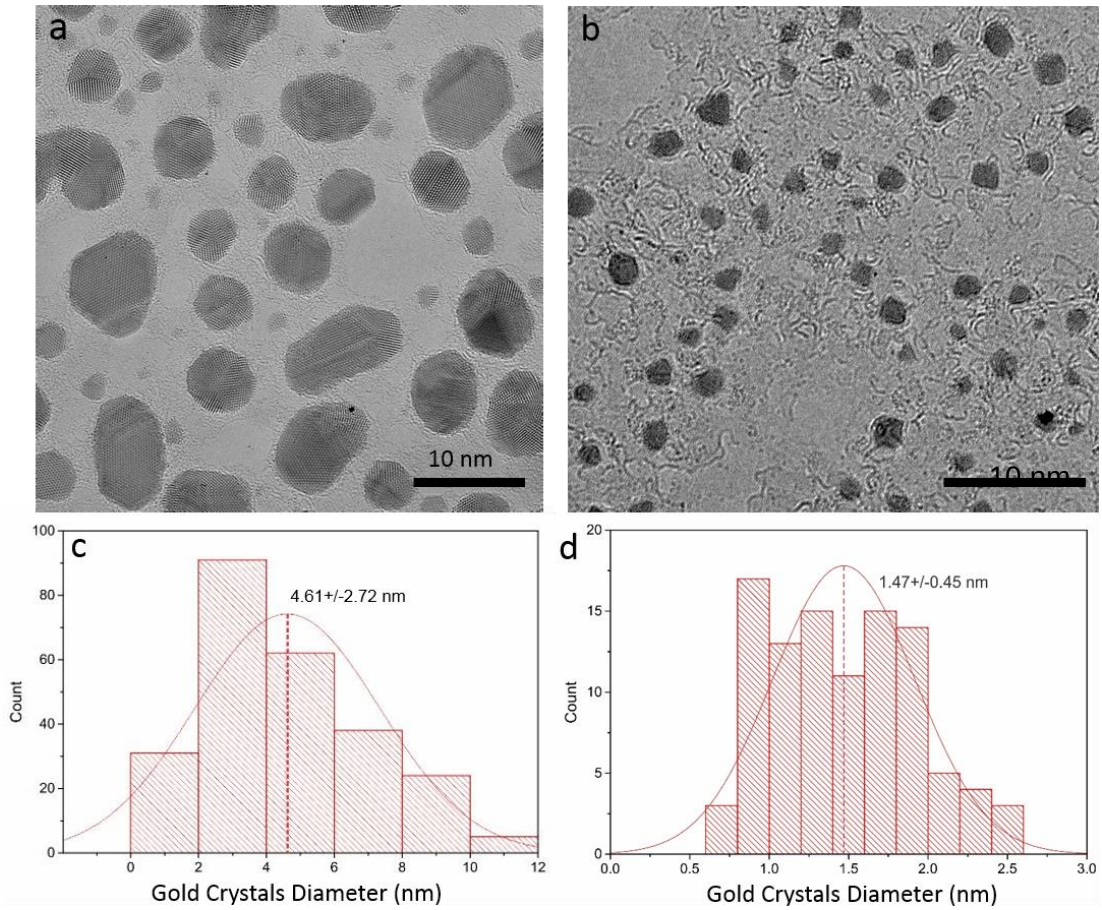

Figure 3-3 Gold nanoparticle size distribution versus evaporation time. (a) Low magnification AC-TEM image with gold nanoparticles on graphene with 4 min deposition time. (b) Low magnification AC-TEM image with gold nanoparticles on graphene with 1 min deposition time. (c,d) Corresponding histograms for gold particle size distribution in (a) and (b).

The graphene/gold nanoparticles sample mentioned in Chapter 5 was produced by depositing gold nanoparticles on the graphene in-situ heating sample by a commercial thermal evaporator. The current was precisely controlled to provide an extremely slow deposition rate (0.1 nm/min). Instead of producing a continuous thin film of gold, isolated gold particles were achieved by this method, and the particle size could be tailored by varying the applied deposition time. Figure 3-3 shows two TEM images of graphene/gold nanoparticles hybrids with deposition durations of 1 min and 4 min respectively. 1 min deposition sample was used for the experiment in Chapter 5.

3.4 Atomic Resolution Imaging Techniques

3.4.1 Aberration-Corrected Transmission Electron Microscopy

The high resolution TEM images analysed in Chapter 4-6 were captured using Oxford's JEOL JEM-2200MCO TEM operated at 80 kV accelerating voltage with a CEOS imaging aberration corrector. The targeted values for different aberrations modes are listed in Table 3-1, which are all essential to achieve sufficient spatial resolution for graphene and MoS_2 samples. In practice it was done by initially, finding a thin amorphous area on the sample (Si_3N_4 grid) or directly using the thin Si_3N_4 membrane on the in-situ heating chip. The amorphous area on the samples were usually hydrocarbon adsorbates or PMMA residues. Secondly, the sample was brought towards focus (slightly below the focus) for the manual correction of A1, the two-fold astigmatism at 500,000X magnification. Defocus was then introduced by adjusting the height of the sample, until there were about 2-3 rings within the view. At this stage, a Zemlin tableau was acquired automatically by the software with predefined tilt angles. After each run, a phase plate was shown and the values for aberrations were listed,

which was the guidance for the corrections that should further be made. The correction completed when all the values were within the range of the targeted values. One example is shown in Figure 3-4.

Table 3-1 Aberration modes and corresponding targeted values

Aberration Mode	Notation	Targeted Value
Two-fold astigmatism	A1	< 1nm
Axial coma	B2	<20 nm
Three-fold astigmatism	A2	<50 nm
Spherical aberration	C3	-5 µm – 2 µm
Four-fold astigmatism	A3	<1 µm
Star aberration	S3	<1 µm

TEM images shown in Chapter 4 were taken with a double Wein filter monochromator[4] with a 5 µm slit to reduce the energy spread of the electron beam to 217 meV. The addition of monochromator significantly boosted the resolution of the image, but the drawback is that it requires fine manual adjustment of aberration, which prolongs the time for imaging. Therefore there is a trade-off between practical operation and image quality. Monochromator was only applied when highest resolution was needed, for example, the study of bond length variations of C-C and Si-C bonds described in Chapter 4.

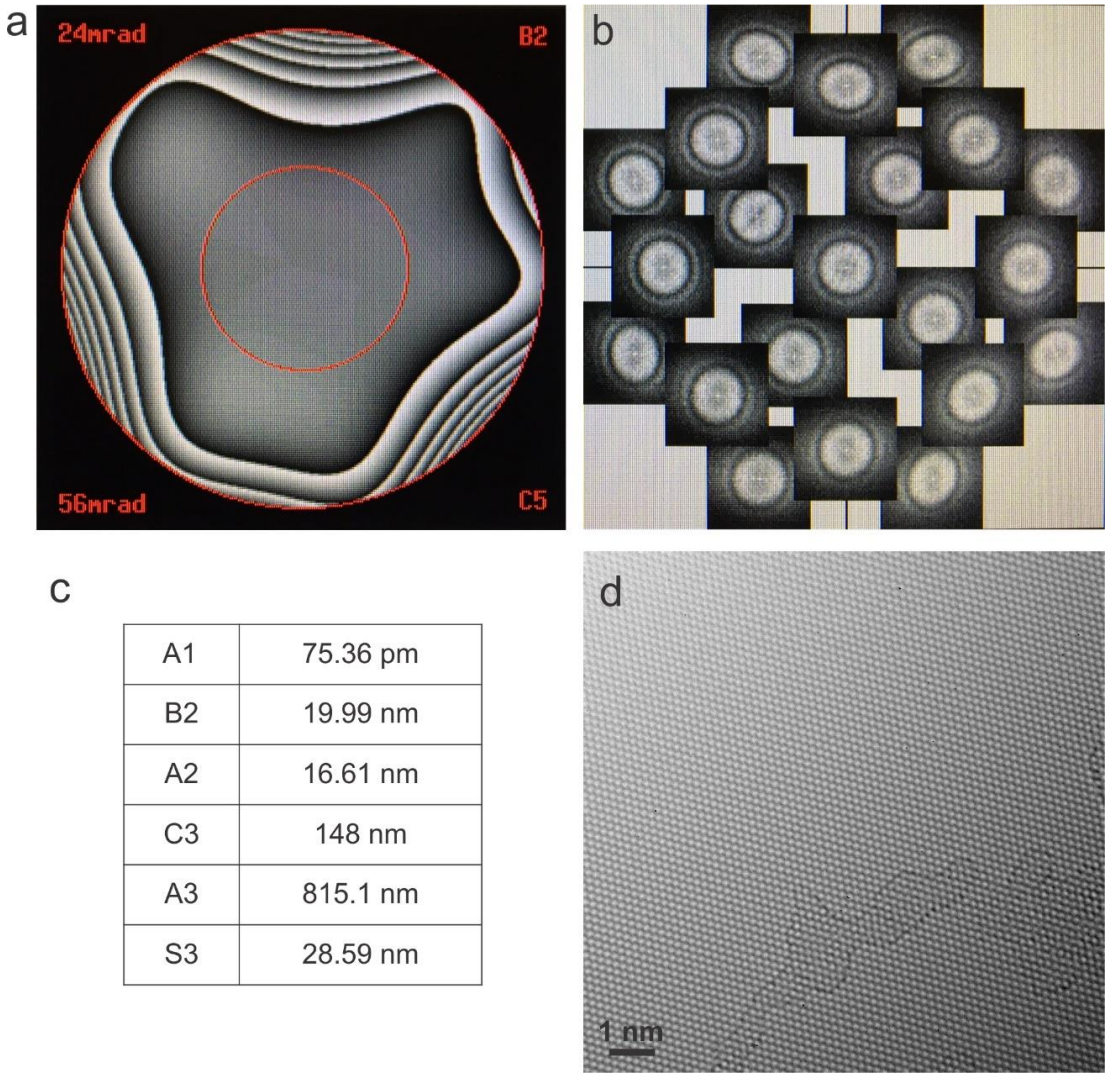

A1	75.36 pm
B2	19.99 nm
A2	16.61 nm
C3	148 nm
A3	815.1 nm
S3	28.59 nm

Figure 3-4 A Zemlin tableau taken with an outer tilt angle of 25 mrad. (a) Phase plate and (b) diffractograms. (c) The corresponding values of aberrations. (d) An image of monolayer graphene lattice captured after this correction with 2M magnification.

3.4.2 Annular Dark Field-Scanning Transmission Electron Microscopy

ADF-STEM imaging was carried out by Dr. H. Sawada in the electron Physical Sciences Imaging Centre (ePSIC) at Diamond Light Source. JEOL ARM300CF STEM equipped with a JEOL ETA corrector[5] was operated at an accelerating voltage of 60 kV for the ADF images shown in Chapter 6. The camera length was 16 cm with a convergence semi-angle was 31.5 mrad, ensuring the annular detector to capture sufficient diffracted electron beams from the sample in an angular range of 49.5–198

mrad. The spherical aberration (Cs) and chromatic aberration (Cc) were 0.4 µm and 0.89 mm respectively.

3.5 In-situ Heating Holder

In-situ heating experiments up to 800 °C were carried out by the using of a commercially available heating holder (DENS Solutions SH30-4M-FS) and heating chip (DENS Solutions DENS-C-30). The central area of the chip, as shown in Figure 3-5(a,b), is composed of platinum resistive coil and thin Si_3N_4 membranes (c). This was the place where graphene or MoS_2 was attached to for in-situ heating experiments. Although the Si_3N_4 membrane was ideal for running the aberration corrector in our microscope, it was too thick for the imaging of 2D materials. Therefore focused ion beam (FIB) was used to open three 0.2×3 µm windows (Figure 3-5(c)) on each Si_3N_4 membrane for observation. During in-situ heating process, the temperature of the sample could be controlled and monitored precisely by the control system.

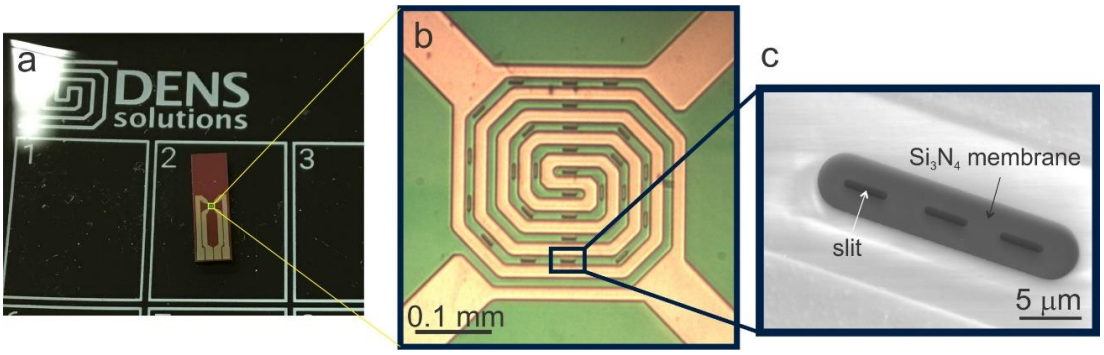

Figure 3-5 A photograph (a), optical image (b) and SEM image (c) for the overall and detailed structures of the in-situ heating chip.

3.6 Image Processing

Image processing was necessary for enhancing the signal-to-noise ratio of raw data, both TEM and ADF-STEM. Figure 3-6 shows the treatment for AC-TEM images step-by-step by using ImageJ. Firstly, a bandpass filter was applied to the raw image (Figure 3-6(a)). The filter (Figure3-6(b)) was set to filter large structures down to 100 pixels and small structures up to 1 pixel, and the structures within the 1 to 100 pixel range passed based on a Gaussian distribution. The filtered image shown in Figure 3-6(c), and it is obvious that the shading effect caused by uneven illustration when the image was captured is significantly reduced. A Gaussian filter was then applied to the image with the radius selected according to the specific noise level and the resolution, usually within the range of 1 to 5 pixels. The example shown in Figure 3-6(d) was treated with a Gaussian filter with 5 pixels. Contrast inverse, false colour (fire) and brightness/contrast adjustment were applied to the image sequentially to improve visual contrast (Figure 3-6(e)). There is a trade-off between the signal-to noise level and information when a filter is applied to an image, therefore the parameters for the filters were selected with great care to avoid severe loss of useful information or introduction of artefacts to the image.

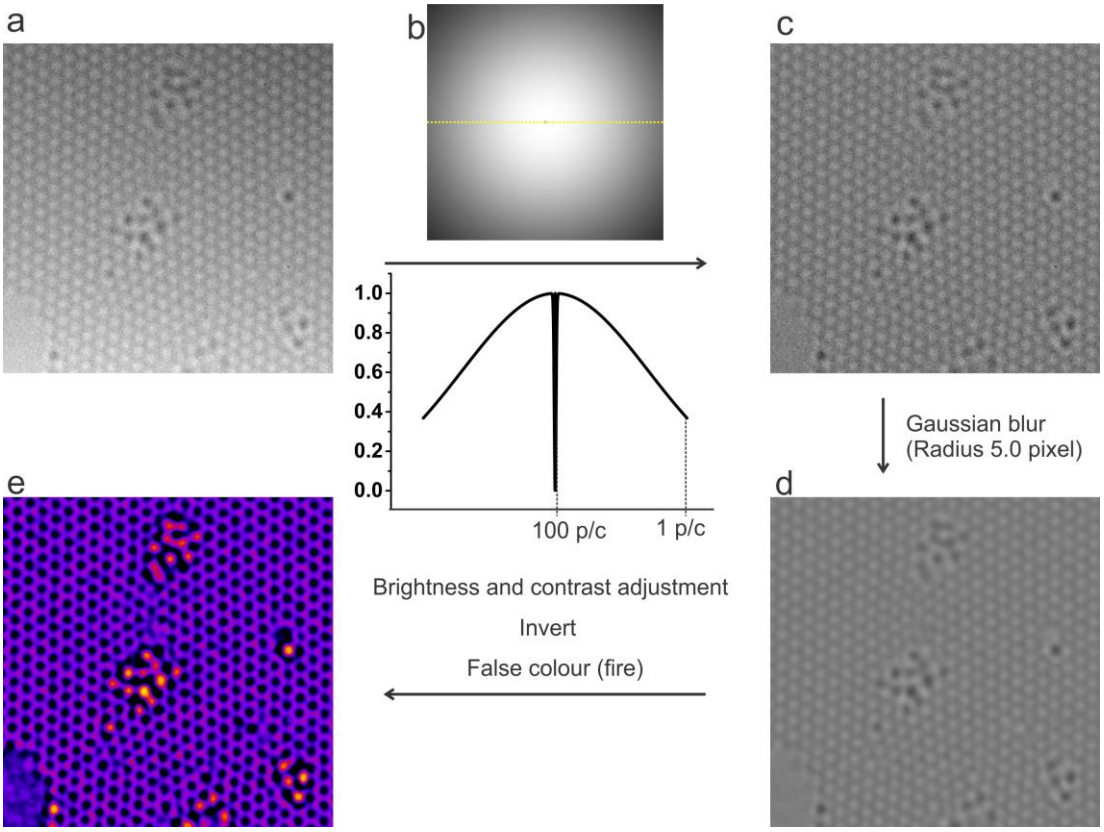

Figure 3-6 Image processing steps for AC-TEM image. (a) Unprocessed image. (b) The band pass filter that applied to (a), with its line profile (yellow line) below the arrow. p/c = pixel/cycle. (c) After band pass filter. (d) After Gaussian blur with 5 radius filter. (e) Final image after all the treatment.

Another technique to improve the signal-to-noise ratio is averaging several consecutive frames where the same feature was captured. It is only suitable for the target that possessed sufficient stability during image acquisition, as shown in Figure 3-7(a-c), a defect structure within monolayer graphene lattice which did not move or change. TEM frames must be carefully aligned to compensate any tiny drift during the imaging, otherwise the result image would be of even lower quality. Any change of defocus among the images is undesirable as well. The averaging of the frames was done by ImageJ with a function called ‘image calculator’ in ‘average’ mode. It can be seen that after averaging the three frames the signal is enhanced and the noise is reduced significantly (Figure 3-7(d)). The contrast before (Figure 3-7(e)) and after

(Figure 3-7(f)) the process is more apparent in the image with false colour. Most of the high-resolution AC-TEM images shown in Chapter 4 were achieved by this method.

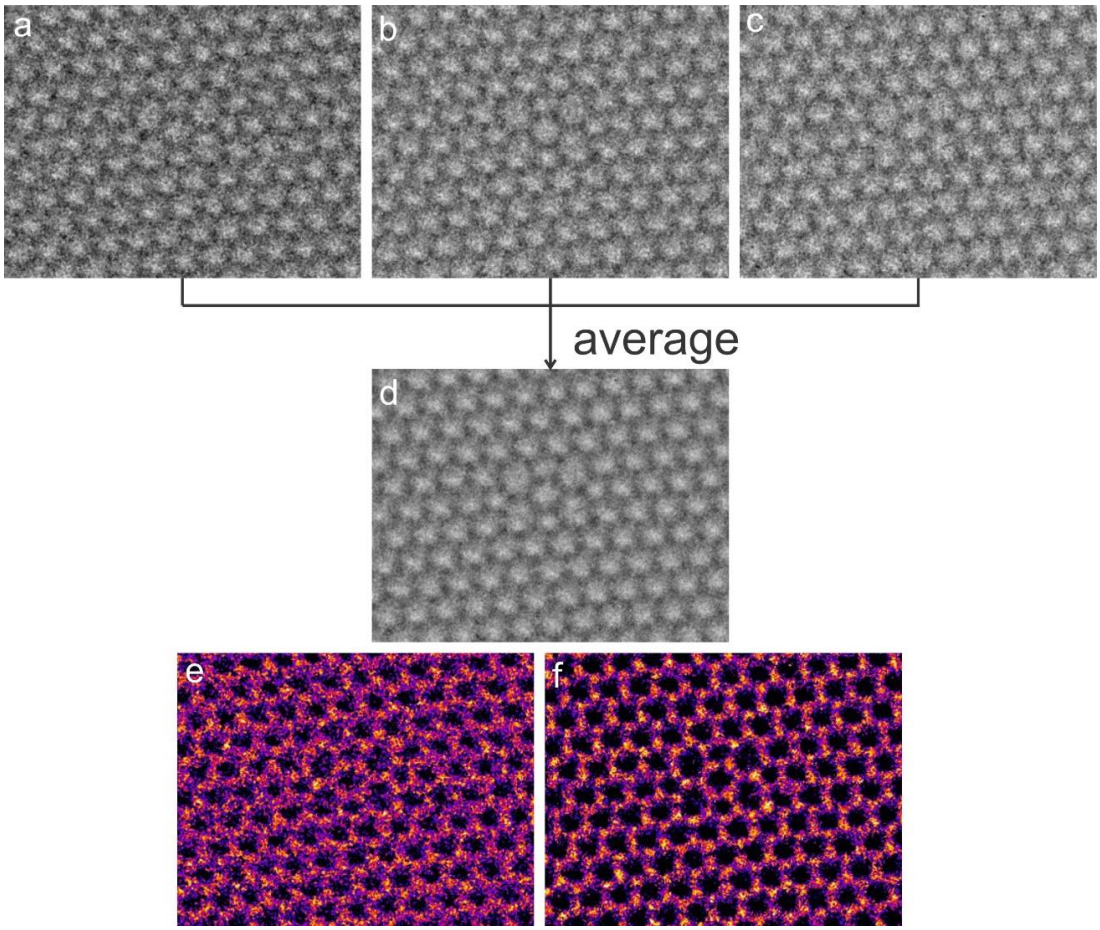

Figure 3-7 Improving signal-to-noise ratio of TEM frames by averaging several frames. (a-c) Unprocessed frames (d) The average image for (a) to (c). (e-f) TEM images with false colour before (e) and after (f) averaging.

For ADF-STEM images shown in Chapter 6, the image processing procedures are similar to that for AC-TEM images shown in Figure 3-6. The only different part is that no bandpass filter was applied to ADF images and a different false colour 'red hot' was used.

3.7 Image analysis and simulation

Creation of atomic models was extensively carried out whenever the atomic structures of the materials were explored. Atomic models were generated in Accelrys Discovery Studio 4.0 Client based on the observation in AC-TEM or ADF-STEM images. In almost all cases, the atomic model generated in this software served as an initial value for density functional theory (DFT) calculations, which will generate the fully relaxed structures. The only exception is the atomic model shown in Figure 5-7 in Chapter 5, where the atomic model were manually made without relaxation by any theoretical calculation.

3.7.1 DFT and TBMD Calculations

The DFT and TBMD (Tight-binding molecular-dynamics) calculations for graphene and graphene/Si dopants system (Chapter 4) were carried out by Prof. Gun-Do Lee at Seoul National University. DFT calculations were performed within the generalized gradient approximation of Perdew-Burke-Ernzerhof (PBE) functional using Vienna *ab initio* simulation package (VASP) code.[6,7] The basis set contains plane waves up to an energy cut-off of 400 eV. The structures were fully relaxed until the force on each atom is smaller than 0.02 eV/Å. In the TBMD simulation, the modified environment-dependent tight binding carbon potential was used to studying carbon sp^2 bond networks.[8]

The DFT calculations for MoS_2 (Chapter 6) were performed by Dr. H. Li at MIT using the VASP (v5.4) package.[7] Plane-wave and projector-augmented-wave (PAW) type pseudopotentials[9] were implemented with the GGA-PBE exchange-correlation functional.[6] The kinetic-energy cut-off was set to 400 eV during geometric optimization, which was increased to 600 eV to ensure the convergence of electronic

structures. The van der Waals interaction was accounted for by the DFT-D2 method of Grimme,[10] with a 50 Å cut-off radius for pair interactions. Dipole correction was applied to correct the leading errors introduced by the large dipole moment in finite periodic simulation box in the direction across the nanoribbon. The structures were relaxed until all forces were smaller than 0.01 eV/ Å. The Brillouin zone was sampled by a dense Monkhorst-Pack[11] k-point grid of 1×1×41. A large spacing of 15 Å was constructed to avoid fake interactions in non-periodic directions.

3.7.2 Image simulation

By comparing the image simulation of an atomic model and corresponding experimental result, one can know whether it is the correct model for the observation. All simulations shown in Chapter 4-6 were performed in the JEMS software developed by Dr P. A. Stadelmann. By inputting the parameters for the microscope, either OJ2200 or JEOL ARM300CF including accelerating voltage, energy spread, astigmatisms, and defocus, the software can provide a simulated image for the loaded atomic model based on these settings.

3.7.3 Geometric Phase Analysis

Geometric phase analysis (GPA) was carried out using Koch's FRWR tools plugin in Digital Micrograph, based on the methods reported by Hÿtch et al.[12] It is an efficient method for measuring and mapping displacement and strain fields within periodic lattices by comparing the targeted area with the reference, which was selected manually and usually a pristine area remote from the target area. In Chapter 4 and 6, this method was used to determine the strain fields of surrounded graphene hexagonal lattice of graphene divacancy defects and MoS_2 line defects.

3.8 References

(1) Wu, Y. A.; Fan, Y.; Speller, S.; Creeth, G. L.; Sadowski, J. T.; He, K.; Robertson, A. W.; Allen, C. S.; Warner, J. H. Large Single Crystals of Graphene on Melted Copper Using Chemical Vapor Deposition. *ACS Nano* **2012**, *6*, 5010–5017.

(2) Fan, Y.; He, K.; Tan, H.; Speller, S.; Warner, J. H. Crack-Free Growth and Transfer of Continuous Monolayer Graphene Grown on Melted Copper. *Chem. Mater.* **2014**, *26*, 4984–4991.

(3) Wang, S.; Pacios, M.; Bhaskaran, H.; Warner, J. H. Substrate Control for Large Area Continuous Films of Monolayer MoS_2 by Atmospheric Pressure Chemical Vapor Deposition. *Nanotechnology* **2016**, *27*, 85604.

(4) Mukai, M.; Kim, J. S.; Omoto, K.; Sawada, H.; Kimura, A.; Ikeda, A.; Zhou, J.; Kaneyama, T.; Young, N. P.; Warner, J. H.; *et al.* The Development of a 200kV Monochromated Field Emission Electron Source. *Ultramicroscopy* **2014**, *140*, 37–43.

(5) Hosokawa, F.; Sawada, H.; Kondo, Y.; Takayanagi, K.; Suenaga, K. Development of Cs and Cc Correctors for Transmission Electron Microscopy. *J. Electron Microsc. (Tokyo).* **2013**, *62*, 23–41.

(6) Perdew, J. P.; Burke, K.; Ernzerhof, M. Generalized Gradient Approximation Made Simple. *Phys. Rev. Lett.* **1996**, *77*, 3865–3868.

(7) Kresse, G.; Furthmüller, J. Efficient Iterative Schemes for Ab Initio Total-Energy Calculations Using a Plane-Wave Basis Set. *Phys. Rev. B* **1996**, *54*, 11169–11186.

(8) Lee, G. D.; Wang, C. Z.; Yoon, E.; Hwang, N.-M.; Ho, K. M. Vacancy Defects and the Formation of Local Haeckelite Structures in Graphene from Tight-Binding Molecular Dynamics. *Phys. Rev. B* **2006**, *74*, 245411.

(9) Blöchl, P. E. Projector Augmented-Wave Method. *Phys. Rev. B* **1994**, *50*, 17953–17979.

(10) Grimme, S. Semiempirical GGA-Type Density Functional Constructedwith a Long-Range Dispersion Correction. *J. Comput. Chem.* **2006**, *27*, 1787–1799.

(11) Pack, J. D.; Monkhorst, H. J. Special Points for Brillouin-Zone Integrations-a Reply. *Phys. Rev. B* **1977**, *16*, 1748–1749.

(12) Hÿtch, M. J.; Snoeck, E.; Kilaas, R. Quantitative Measurement of Displacement and Strain Fields from HREM Micrographs. *Ultramicroscopy* **1998**, *74*, 131–146.

Chapter 4

Bond Length Studies of Graphene Divacancies and Silicon Decorated Graphene Edge

This chapter focuses on understanding defective structures in graphene by measuring the distances between the atoms within the defects. AC-TEM with C_S corrector and monochromator effectively reduces spherical and chromatic aberration effects and increases spatial resolution in order to resolve the position of individual atoms, which is necessary for measuring bond lengths. Two defective systems are included here, divacancies in monolayer graphene and Si decorated graphene edge. Elevated temperature was applied to the latter in order to reduce the chemical etching process. The bond length information directly indicates the strain distribution within the defects and the interactions between doped atoms and graphene.

4.1 Introduction

4.1.1 Divacancies

Removing carbon atoms from the bulk graphene lattice produces vacancies, such as monovacancies (MVs), divacancies (DVs), and multi-vacancies, which can migrate and agglomerate together to form more complex defect structures.[1] The DV consisting of a pentagon-octagon-pentagon (5-8-5) structure forms easily from a monovacancy by removing one of the three under-saturated carbon atoms. Reconstruction is achieved

by bonding of all three nearest carbon neighbours, i.e., to maintain a sp^2 hybridization state.[2–4] This process is depicted in Figure 4-1(a-d). The reconstruction process and loss of carbon atoms is likely to lead to changes in the electronic charge density within certain bonds in the DV and this will influence the bond lengths within and around the defect. The 5-8-5 DV can transform into the triple pentagon-triple heptagon (555-777) DV by an in-plane 90° rotation of one of the two shared bonds between the pentagons and octagon, as shown in Figure 4-1(e-h). Similarly, 555-777 DV can further evolve into the quadruple pentagon-hexagon-quadruple heptagon (5555-6-7777) DV by one more Stone-Wales (SW) bond rotation (Figure 4-1 (i-l)).[5–8]

Previous work has explored the formation and dynamics of divacancies in graphene.[5,9,10] Theoretical calculations indicate that bond rotations lead to lower energy divacancy defects.[9] Herein I have focused on the study AC-TEM images of the three types of divacancies with sufficient spatial resolution to resolve individual C-C bond lengths. Multi-frame averaging is used to substantially increase the signal to noise ratio and this enables more accurate measurements of atomic positions. By combining the experimental AC-TEM images with multislice image simulations based on DFT calculations the effect of bond rotations on the local strain in the divacancy structures can be understood. The local defect area should ideally be planar, as the out-of-plane ripples of graphene give deviations in apparent bond length measurements for the two-dimensional projections of the three-dimensional object.[11–13] The flatness of each divacancy region is evaluated with the help of the DFT calculated models, where each atom has a specific position in three-dimensional space. To further explore the influence of a divacancy defect on its surrounding hexagonal neighbours, geometric phase analysis is used to map the strain field around the three types of the divacancy defects.

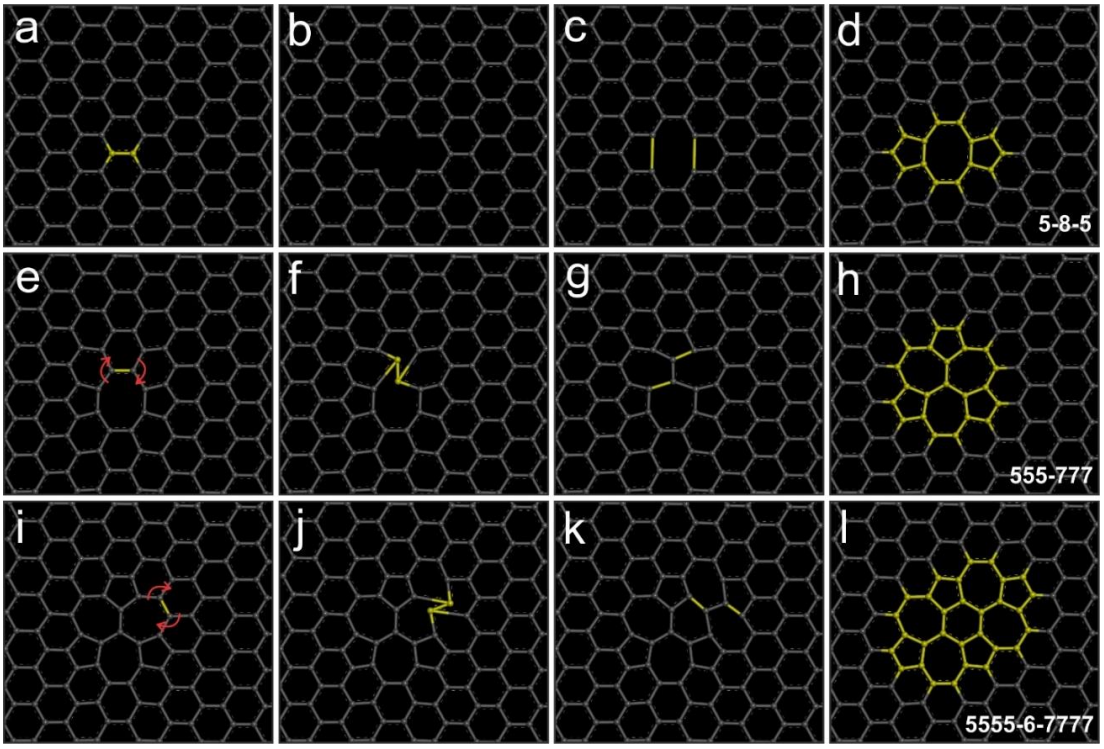

Figure 4-1 (a-l) Schematic atomic models showing the 5-8-5 divacancy defect and its relation to the 555-777 and 5555-6-7777 divacancy defects by bond rotation.

4.1.2 Silicon Decorated Graphene Edge

The high edge/bulk ratio of graphene edge has great influence on the nanoconstraint structures, for example, nanoribbons, nanojunctions and quantum dots.[14–17] Four periodic graphene edge structures have been observed: armchair, zigzag, reconstructed zigzag, and extended Klein (EK) edges, by STM, micro-Raman spectroscopy, and AC-TEM.[18–21] With the different edge structures there will be a range of dopants bonding sites and the interactions between the dopant atoms and graphene is diverse. Under the electron beam at room temperature, graphene edges are rapidly degraded by chemical etching, which causes impurity atoms to exhibit irregular diffusion along the edge as well as assist in the sputtering of carbon atoms from the edge.[22] The etching processes of several types of single dopants at graphene edges have also been explored by STEM and electron energy loss spectroscopy (EELS).[23] The interaction between single gold atoms and the graphene edge has also been studied by AC-TEM, which involves

reduplicative trapping and detrapping processes under electron-beam irradiation, indicating the possibility for manipulating the dopant-graphene edge structures.[24] However, due to the unstable nature of graphene edges and the high mobility of edge dopant atoms during room temperature TEM imaging, it has been challenging to accurately measure bond lengths that define the dopant-edge interactions with sufficient resolution. Chemical etching of graphene edges under the electron beam has been shown to be rapidly reduced at elevated temperatures, as the absorbates are evaporated from the graphene surface.[25] Therefore, in order to observe the detailed atomic structure of Si dopants at the graphene edge, high-temperature *in-situ* AC-TEM is performed.

A hole in graphene with suitable size was opened by a focused electron beam,[26] and Si atoms that are decorated across the graphene surface will eventually migrate and attach to the newly created edges of the hole, as shown in Figure 4-2. The brighter atoms are assigned to Si atoms based on the weight percentage and relative contrast values in TEM images. According to the EDX spectrum (Figure A1), Si, Au, Pt and Fe are all present within the graphene sample with various weight percentage. However, with the consideration of their relative content and the atomic masses, the possibility for observing a Si atom is far higher than an Au or Pt atom (the weight percentage of Fe is lower than 0.1% thus can be neglected). The contrast information also help to rule out the possibility of heavy atoms like Au and Pt. In Figure A2, the intensities of a Si atom is compared with Au atoms based on both TEM and simulated images. Although it is not straightforward Z-contrast, there is still a profound difference between the contrasts of Si and the heavy atoms like Au. More than 500 AC-TEM images have been recorded for several different holes with multiple Si dopants attached to the edge.

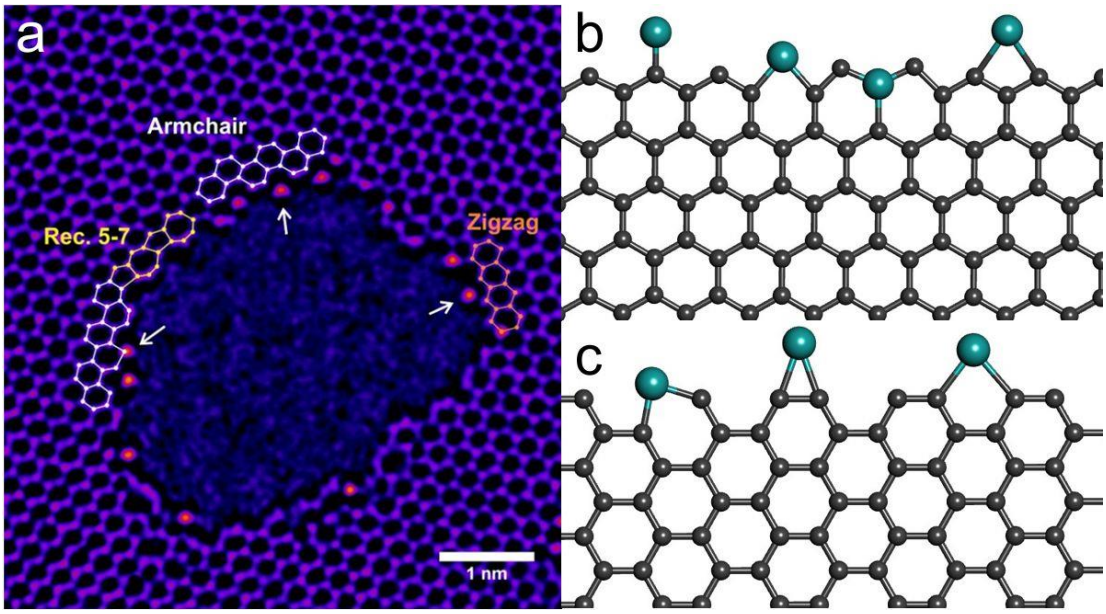

Figure 4-2 (a) AC-TEM image of a hole in graphene with single Si atoms attached to the edge (white arrows). Si atoms are at either the armchair or zigzag edge with both substitutional and attached configurations. T = 800 ℃. (b) Schematic atomic model showing Si atoms at various sites on a zigzag edge. (c) Schematic atomic model showing Si atoms at various sites on an armchair edge.

4.2 Atomic Level Distributed Strain within Graphene Divacancies from Bond Rotations

4.2.1 Bond Length Variations within Divacancies

Figure 4-3(a-c) show an AC-TEM image, bond length measurement and plot of bond strain for an isolated 5-8-5 divacancy defect with the bond length values marked in picometers. Figures 4-3(d-f) show the multislice image simulation, with corresponding bond lengths and bond strains. The reference C-C bond length shown in the lower right of Figure 4-3(a) is the average bond length of pristine graphene measured far from the defect structure, averaged over many bond measurements. To maximise the accuracy of the C-C distance values, the scale is calibrated individually for all six directions according to the $\{10\bar{1}0\}$ or $\{11\bar{2}0\}$ d-spacings in FFT. The maximum difference of

the scale is measured to be 4%, which is mainly due to the astigmatism when forming the image (Figure A3). An error value lower than 2% is achieved after the elimination of the slight distortion in the image. For the C-C bond lengths within the defect, the scale is set to be either the same with the nearest crystal plane of pristine graphene, or the average of the two nearest planes if the bond orientation is in the middle region. The bond lengths in the AC-TEM image are measured by box-average intensity profiles and subsequently fitted to double Gaussian curves, similar to previous reports.[27,28] The bond length values displayed in Figure 4-3(e) are measured using double Gaussian fitting from the image simulation. The coloured bonds shown in the atomic models (Figure 4-3(c,f)) visually illustrate the bond length variations (BLVs) within the defect area, with the values calculated by dividing every measured or calculated bond length (B_m, or B_c) in the defect by the reference bond distance (B_r), i.e. BLV = B_m/B_r. The warm colours (orange-red) indicate bond elongation (BLV> 1) while the cold colours represent contraction of a bond (BLV<1). When the measured bond length is longer than 147 pm or shorter than 139 pm, the bond length variation is beyond two standard deviations and has statistical significance. Correspondingly, the deformation ratio must be higher than 1.03 or lower than 0.97. The most significant elongation occurs at the interface between the octagon and pentagons, which are 17.5% and 15.4% elongated respectively from the experimental result. The asymmetry between the two bonds, probably caused by the slightly non-equivalent surrounding environment, does not change the conclusive elongation of the bonds. The theoretical calculated result agrees well with the TEM result, but with a slightly higher elongation value of 19.7%. These regions of bond elongation are indicated with small white dashed ellipses in Figures 4-3(c,f). The four bonds at the two ends of the octagons are also slightly elongated with an average 7%. Compression is detected at the end of the

two pentagons, indicated with the larger white dashed ellipses. However the contraction is not as certain as the elongation measurements due to it being comparable with the noise level.

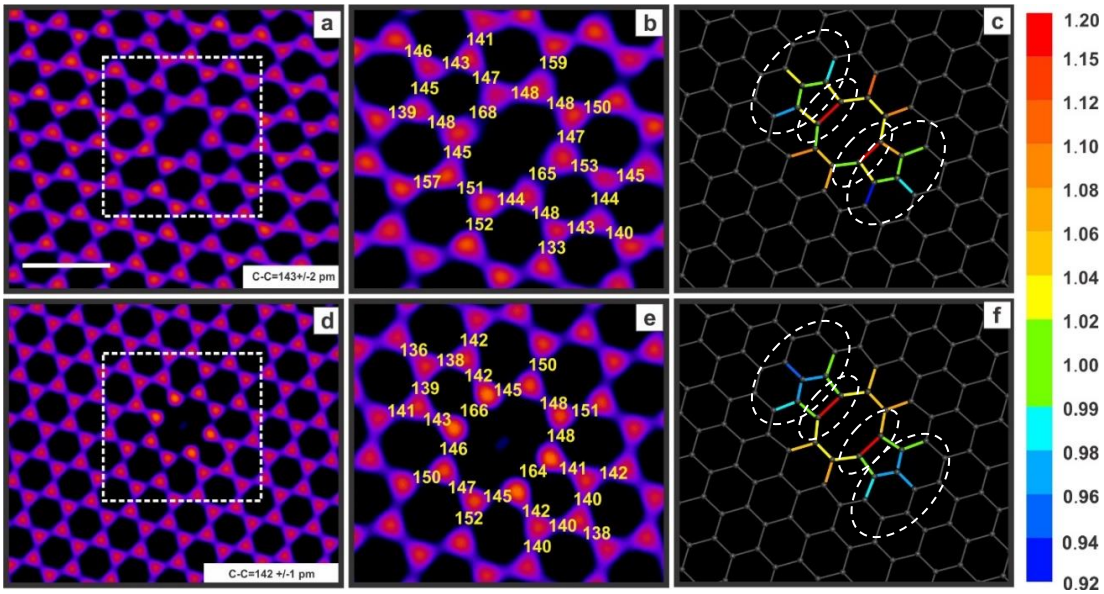

Figure 4-3 Bond length variations in 5-8-5 defect. **(**a) TEM image of an isolated 5-8-5 divacancy with a 'fire' colour LUT for display. (b) TEM image showing the region in the white dashed box of (a) at the defect with bond length values in picometers. (c) Atomic model showing the ratio of local bond length to the average bond length of pristine graphene based on TEM. (d) Multislice image simulation based on the DFT calculation of a 5-8-5 defect. (e) Simulation image showing the region in the white dashed box of (d) at the defect with bond length values directly determined from the image simulation. (f) Atomic model showing the ratio of local bond length to the average bond length of pristine graphene based on DFT. Small white dashed ellipses indicate regions of bond elongation, whilst larger white dashed ellipses indicate regions of bond contraction. Scale bar in (a), 500 pm.

After bond rotation of the 5-8-5 DV to the 555-777 DV, the bond lengths within the defect area also vary significantly (Figure 4-4). Overall, the range of the bond lengths in the 555-777 DV is narrower than the original 5-8-5 DV defect. The most elongated bonds are the six bonds shared by the three heptagons and the three pentagons, with average elongation ratio of 1.10 and 1.07 for TEM and DFT result respectively. This fits in well with the report by Rasool *et al*, who explored pentagon-heptagon structures

along graphene grain boundary and found most of the shared bonds between pentagon and heptagon have been elongated to some extent.[28] The surrounding bonds around the 555-777 defect shows regular change: the bonds at the ends of the 7-membered rings are elongated while the bonds at the ends of the 5-membered rings are contracted, indicated with white dashed ellipses.

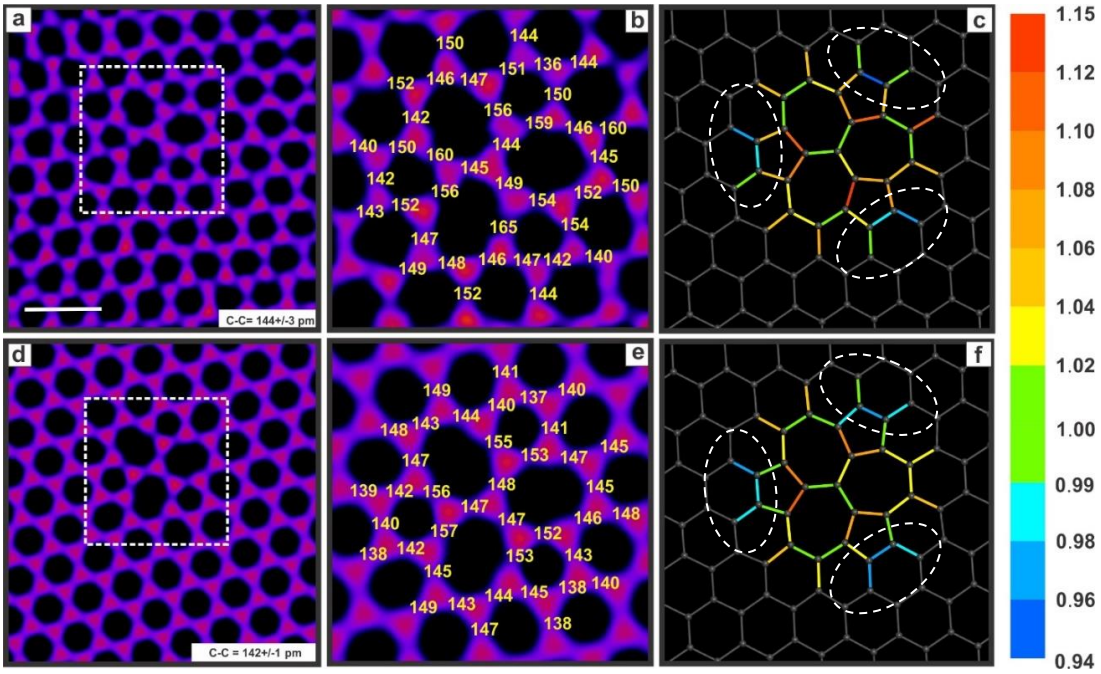

Figure 4-4 Bond length variations in 555-777 defect. (a) TEM image of an isolated 555-777 divacancy with a 'fire' colour LUT for display. (b) TEM image showing the region in the white dashed box of (a) at the defect with bond length values in picometers. (c) Atomic model showing the ratio of local bond length to the average bond length of pristine graphene based on TEM. (d) Multislice image simulation based on the DFT calculation of a 555-777 defect. (e) Simulation image showing the region in the white dashed box of (d) at the defect with bond length values directly determined from the image simulation. (f) Atomic model showing the ratio of local bond length to the average bond length of pristine graphene based on DFT. Scale bar in (a), 500 pm.

A second bond rotation converts the 555-777 DV into the larger 5555-6-7777 DV, shown in Figure 4-5. Unlike the former two DV defects examined in Figures 4-3 and 4-4, where elongated bonds were observed, the bond length variation within the 5555-6-7777 DV defect structure is reduced. However, the spatial trend of the elongation

and contraction for 5-8-5 and 555-777 structures is still apparent in the 5555-6-7777 defect. The joint bonds between pentagons and heptagons are all elongated, although the deformation ratio decreases to 1.03-1.05. Shortened bonds are observed at the ends of the pentagons (the left and right ends), just like the situation of the former two DV structures.

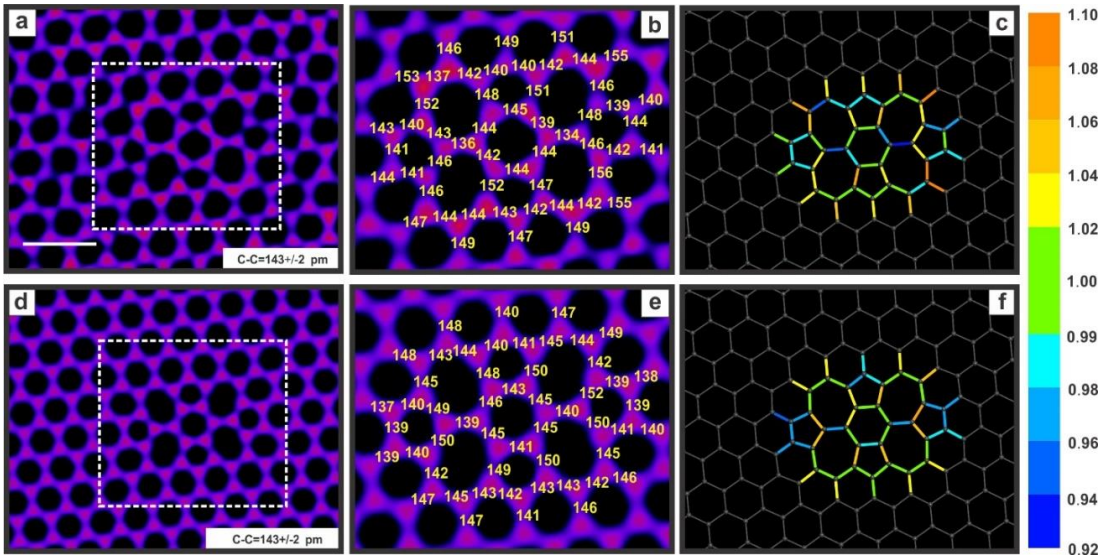

Figure 4-5 Bond length variations in 5555-6-7777 defect. (a) TEM image of an isolated 5555-6-7777 divacancy with a 'fire' colour LUT for display. (b) TEM image showing the region in the white dashed box of (a) at the defect with bond length values in picometer. (c) Atomic model showing the ratio of local bond length to the average bond length of pristine graphene based on TEM. (d) Multislice image simulation based on the DFT calculation of a 5555-6-7777 defect. (e) Simulation image showing the region in the white dashed box of (d) at the defect with bond length directly determined from the image simulation. (f) Atomic model showing the ratio of local bond length to the average bond length of pristine graphene based on DFT. Scale bar in (a), 500 pm.

To further explore the distribution of the bond lengths within the three types of divacancy defects, histograms (Figure 4-6) with Gaussian fits are plotted for both TEM and DFT results from Figure 4-3 to Figure 4-5. It can be seen that experimental and theoretical results share the same trend. With the addition of bond rotations, both distribution width and average bond length are reduced, indicating that the bond

rotation decreases the peak value for elongated and compressed bonds. The larger local defect area also contributes to the reduced average bond length as more bonds are involved in to share the variation caused by the two missing carbon atoms. Therefore, 555-777 and 5555-6-7777 are more stable than the original DV defect (5-8-5), which is also confirmed by the energy state of the three defects: the formation energy of 5-8-5 is 0.53 eV higher than 555-777, which is the lowest energetic structure among the three divacancies, while the difference in the formation energy between the 5555-6-7777 and the 555-777 is small (~0.1eV) according to the DFT calculation. Similar results of the relative formation energies of the three DVs have also been reported by Leyssale and Vignoles.[7]

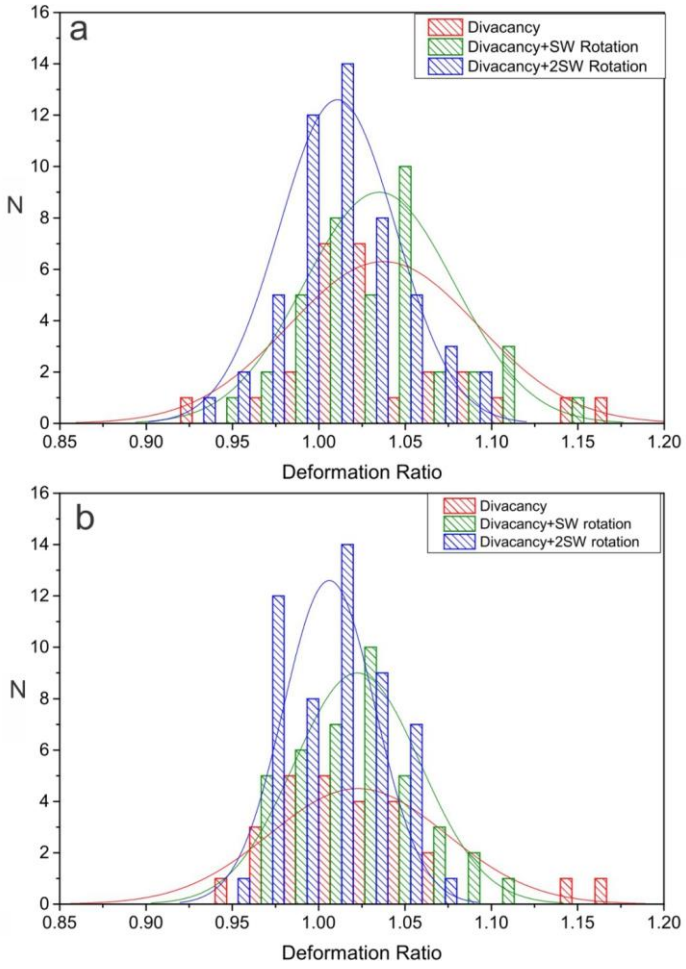

Figure 4-6 Histograms of the bond length ratios of the three divacancies measured from both TEM (a) and DFT (b) results, with Gaussian distribution fitting.

4.2.2 Flatness of Defective and Surrounding Areas

Defective graphene does not have perfect flat (2D) structure due to out-out-plane distortions that help stabilize the strain in the bonds. Atomic models calculated by DFT show the height variations within a graphene sheet and can be used to determine the effect of out-of-plane distortions on the apparent bond length contraction in the 2D projection of a TEM image. Figure 4-7(a-c) shows the z-plot (out-of-plane distance) of graphene with divacancies at the central area. The colour map shows directly the height change, with red regions referring to the peaks while blue regions indicating the valleys. The colour scale bar is in Angstroms. The defect is in the pale blue and green area, with much less distortion than the edge area, where dark blue and red are dominating. The tilt angle θ along x or y direction is defined as the height variation within a single pixel (pixel $= 0.1 \times 0.1$ Å^2).

$$\frac{|Z_1 - Z_2|}{0.1} = \tan\theta$$

Where z is the height in Å, 0.1 Å is the pixel width. The tilt-angle maps for the three DVs along the x and y directions are shown in Figure 4-7(d-i). The biggest tangent value within the maps for the 5-8-5 DV is around 0.11, indicated by the white arrow in Figure 4-7(d), thus theta is 6.3°. This value is compatible with the experimental findings by Meyer et al (±5°),[29] while smaller than the results presented by Bangert et al, which is 12° with ripple height of approximately 5 Å.[30] This is possibly due to the size of the unit cell for the DFT calculation artificially suppresses the calculated height variation. The height changes more gradually around the defect area (the centre of the defect is marked by the white cross, and the dashed circle highlights the fourth nearest hexagons around the defect), with θ smaller than 4°. Figure 4-7(j-o) demonstrate the

deviation of projected distance from true distance caused by the tilting angle in x and y directions. The deviation is determined by

$$1 - \cos\theta = 1 - \cos(\tan^{-1}\frac{Z_1 - Z_2}{0.1})$$

Among the six maps, the largest deviation value is 6.0×10^{-3} (0.6%), pointed out by the white arrow in Figure 4-7(j), which is significantly smaller than the observational error during the bond length measurement. The deviation is even smaller within the defect regions, from 0 to 0.24%. Therefore, it can be concluded from these maps that the graphene lattice possesses sufficient flatness around the DV defect regions and out-of-plane distortions are negligible for impacting bond length measurements.

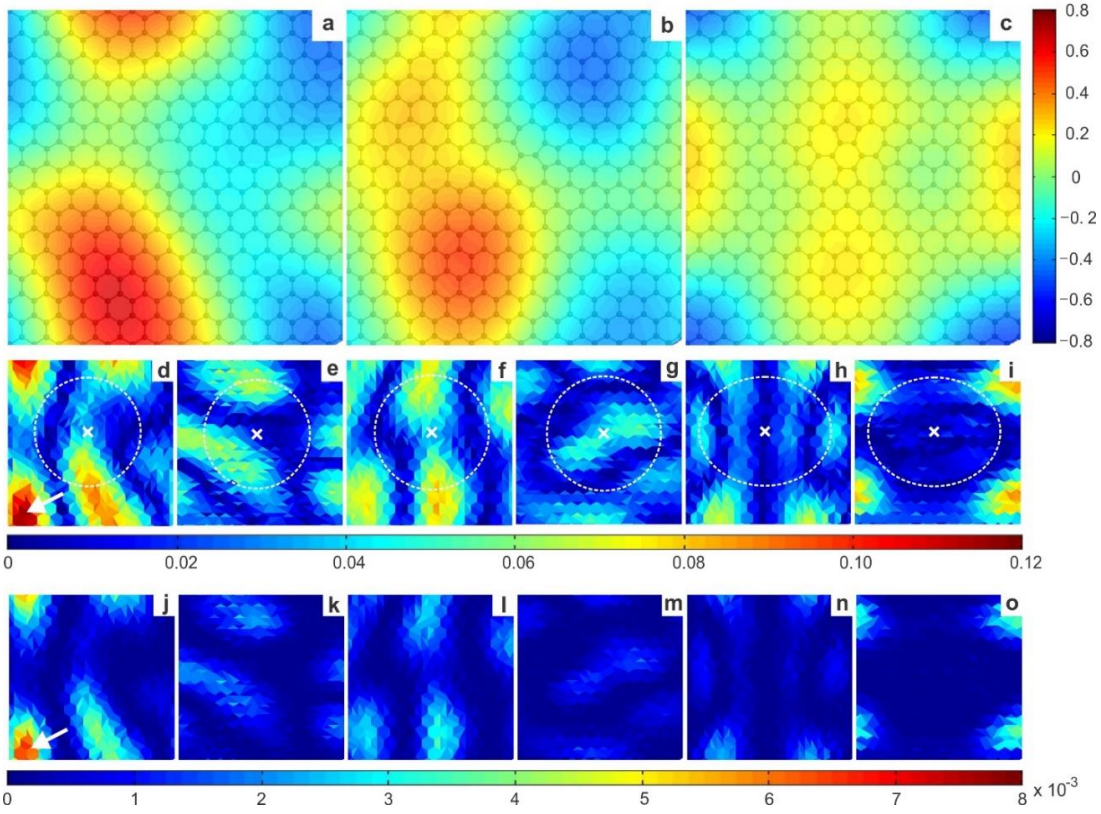

Figure 4-7 (a-c) Z height mappings for 5-8-5 (a), 555-777 (b) and 5555-6-7777 (c) based on the DFT calculation. Unit of colour scale: Å. (d-i) Tilt angle maps for 5-8-5 (d,e), 555-777 (f,g), and 5555-6-7777 (h,i). d, f, h) Along x direction: $\partial z/\partial x$. (e,g,i)Along y direction: $\partial z/\partial y$. (j-o) Deviation of projected distance from the true value by height fluctuation for 5-8-

5 (j,k), 555-777 (l,m), and 5555-6-7777 (n,o). (j,l,n) Along x direction. (k,m,o) along y direction. The white dashed ellipses in (d-i) correspond to the fourth nearest hexagons to the defects, with white crosses at the defect centres.

4.2.3 Strain Distributions of Hexagonal Neighbours of Divacancies

Introduction of a DV defect disrupts the periodic structure of the graphene lattice and is likely to give rise to a certain strain fields that could extend out to the surrounding hexagonal lattice. Geometric phase analysis (GPA) is a useful tool to show the four types of strain (normal strain ε_{xx} and ε_{yy}, shear strain ε_{xy}, and rotation) by plotting strain in colour scale.[31] As GPA investigates the periodicity deviation in 2D projection, it cannot distinguish the strain caused by bond elongation (contraction) or out-of-plane distortion. However, it has already confirmed that the largest tilting angle among the three defects and their surrounding graphene lattice (from the defect edge to the fourth nearest hexagon) is 6.3°, beyond the sensitivity of GPA. Previous work showed that the 'apparent' strain measured as a d-spacing lattice change (not real strain), caused by out-of-plane distortions, give apparent bond shorting when imaged by AC-TEM requires the tilting angle to reach at least 15°.[11] It means that in this case, the strain values can be regarded as pure in-plane distortions generated from altered bond lengths and orientation.

The four strain modes are all measured for the three divacancies, both on AC-TEM images and simulated image based on DFT models (Figure A4 and A5). $\{10\bar{1}0\}$ spots in FFT were selected with the aperture size of 0.5 nm. The absolute values of stains might be suppressed due to the resulting spatial averaging of the strain measurements (over a 5 Å region), but should not significantly influence the conclusion from the results. Due to the symmetrical structures of the divacancies, the strains can be seen as the fluctuation around 0 with various amplitudes, with larger amplitudes representing

higher strain values. Therefore, oval profiles are plotted to evaluate the strain distributions at different distances away from the defects, and standard deviations are calculated to represent the magnitude of the strain. The oval profiles along the nearest hexagonal neighbours for the three divacancies with four strain modes are exhibits in Figure A6 and A7 in Appendix A. The background noise at pristine area has predicted to be from -0.02 to 0.02 for all strain types, with standard deviation of 0.01. Therefore, the strains of neighbours of divacancies can be regarded as 'above the noise' when their standard deviations are higher than 0.02, twice of the standard deviation of noise.

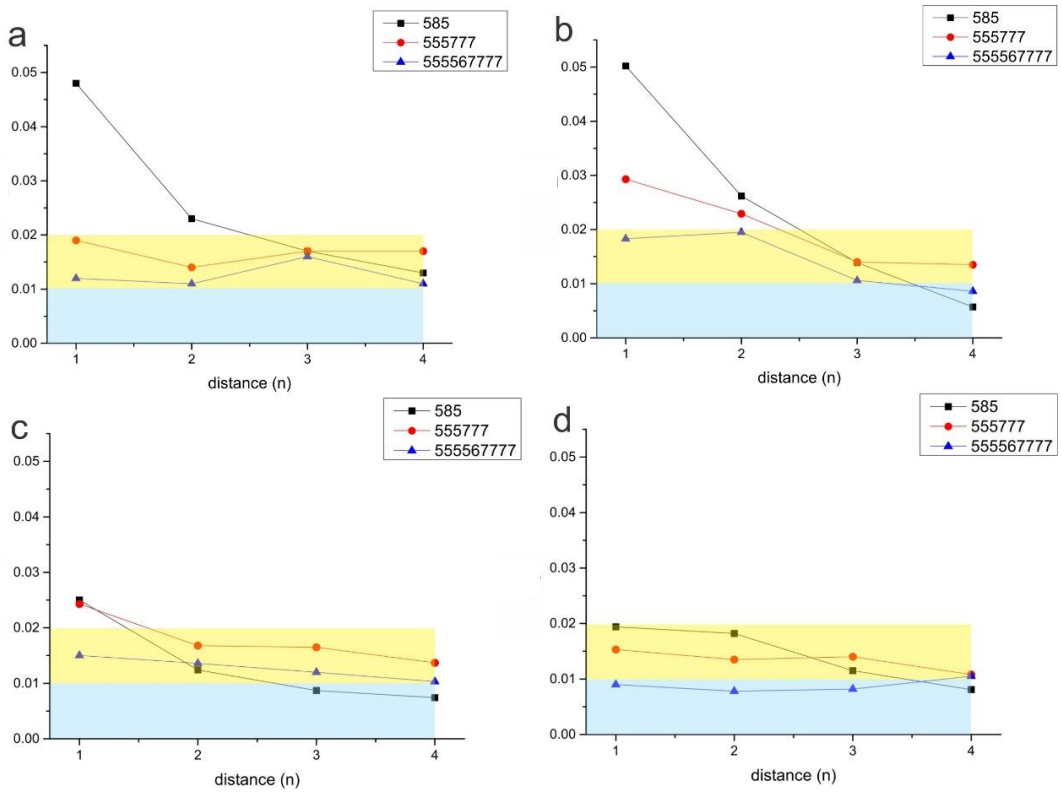

Figure 4-8 Standard deviations of strains from the first to fourth nearest neighbours measured on TEM images represented for (a) ε_{xx}, (b) rotation, (c) ε_{yy} and (d) ε_{xy}. The pale blue regions (0-0.01) represent for the standard deviation of the background and the pale yellow boxes reach the value of double standard deviations (0.02).

According to the results, ε_{xx} and rotation are more obvious than the other two stain modes. Figure 4-8 concludes the standard deviations of the strains from the first to

fourth nearest neighbours (the ellipses are shown in Figure A4) measured on TEM images. For both ε_{xx} (Figure 4-8(a)) and rotation (Figure 4-8(b)), it is obvious that strain decays with the increase of the distance to the defect, and the strain along the third nearest hexagon is submerged into the background noise level (double standard deviations). 5-8-5 defect can expand its strain to the second nearest hexagons. After one SW rotation, the strain field narrows down to the nearest neighbours. However, when one more SW rotation occurs, the strain is further compensated by the defect itself, as almost all standard deviation of the 5555-6-7777 defect is at the same level as the background. For ε_{yy} and ε_{xy}, the strains are confined within the defective area, as none of the standard deviation value is significantly above the noise. The profiles measured on simulated images based on DFT models are included in Figure A8.

4.3 Elongated Silicon-Carbon Bonds at Graphene Edges

4.3.1 Si-Graphene Armchair Edge Configurations

The armchair edge dominates for holes in graphene at 800 ºC.[25] The most common observed Si-edge interaction is the formation of pentagons, as shown in Figure 4-9(a), with the inset detailing the bond distances around the dopant. The bond length measurement is accomplished using a previously reported method based on intensity line profiles along a bond and fitting to double Gaussian curves to determine the position of each atom.[27] The Si-C bond lengths measured from the TEM images (194 ± 10 pm) match well with that from a DFT calculated model (193 pm) and also measured from an image simulation (186 pm), Figure 4-9(b,c), due to the planer nature of the dopant-edge interaction. The angle between the two Si-C bonds is $93 \pm 4°$ measured from TEM images, corresponding to 92° in the simulation image.

The binding energy of this pentagon structure is calculated to be 5.08 eV by DFT, indicating a reasonable stability of the configuration. This stableness is also confirmed by experimental results, where a pentagonal configuration appearing in six continuous frames (about 1 min) without migration (Figure A9). Si atoms are also observed to occupy three neighbour pentagonal sites to form an extended pentagonal configuration, as in Figure 4-9(e,f), which was stable for about 30 s under electron beam irradiation. Figure 4-9(d) shows the other Si-edge configuration along armchair edge, where the Si atom sits at the substitutional position by replacing one of the two carbon atoms of the armrest to form a hexagonal ring. This structure, however, is far rarer and less stable compared to the pentagon configuration. The frequencies of the two types of Si-C bonding at the armchair edge is shown in Figure 4-9(g). Within the examination of 100 TEM frames, the pentagonal structure of Si-C bonding at the armchair edge is by far the most dominant. All Si-C bonds showed significant elongation compared to C-C bonds.

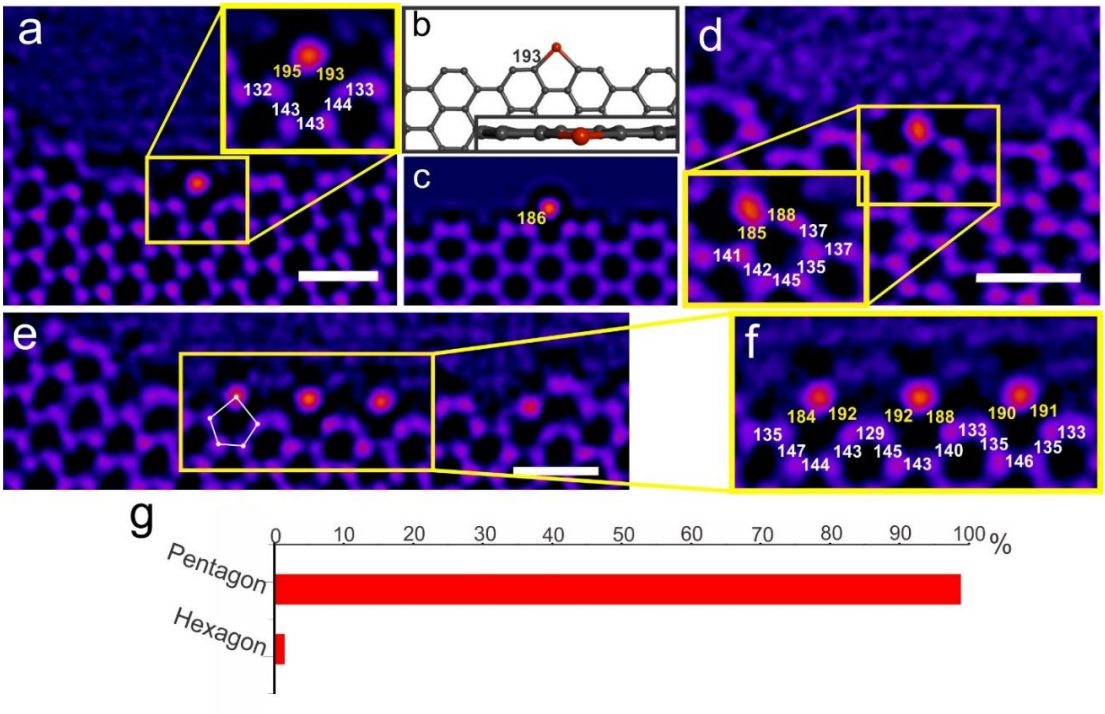

Figure 4-9 The two observed Si dopant configurations for the armchair edge. (a) AC-TEM image of a pentagonal configuration. (b,c) DFT calculated atomic model and multislice simulation of the pentagonal structure. (d) AC-TEM image of a substitutional hexagonal configuration. (e,f) AC-TEM image of an extended pentagonal structure. (g) Percentage of the occurrence of the two configurations (in 100 frames). Bond length values are in picometers. Scale bars in (a,d,e), 500 pm.

4.3.2 Si-Graphene Zigzag Edge Configurations

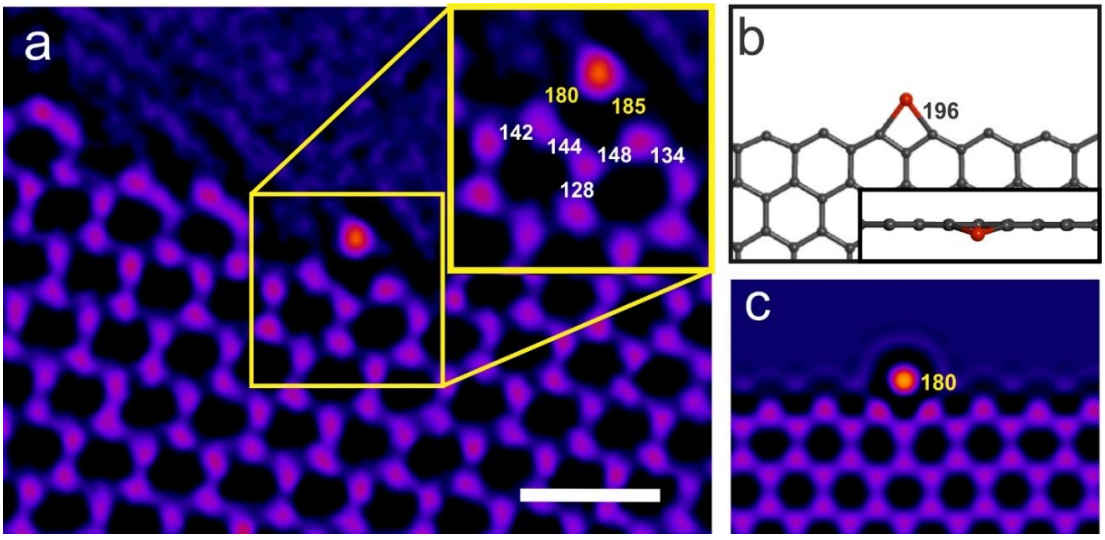

Figure 4-10 (a) AC-TEM image of a tetragonal configuration along the zigzag edge. (b) DFT calculated model of (a). (c) Multislice simulation of (b). Bond length values are in picometers. Scale bar in (a), 500 pm.

More variation in the Si-C bonding configurations were found for Si atoms at the zigzag edge compared to the armchair edge. Figure 4-10 shows a tetragon structure at the zigzag edge formed by two Si-C bonds. DFT results further confirm the stability of the structure, the binding energy of which is 7.55 eV, which is higher than the pentagonal structure of the armchair edge. Figure A10 shows a tetragonal structure lasting in 11 frames (about 2 min). The average Si-C bond length in this case is 183 $\pm$ 10 pm based on 10 TEM frames with the tetragonal configuration. The larger Si-C bond distance in the DFT model (Figure 4-10(b)) is due to the slightly out-of-plane structure of the tetragonal configuration, as shown in the inset of Figure 4-10(b). The

included angle of the two Si-C bond is 80 ± 3° based on the TEM images, and similar value shown in the image simulation of DFT model, which is 77°.

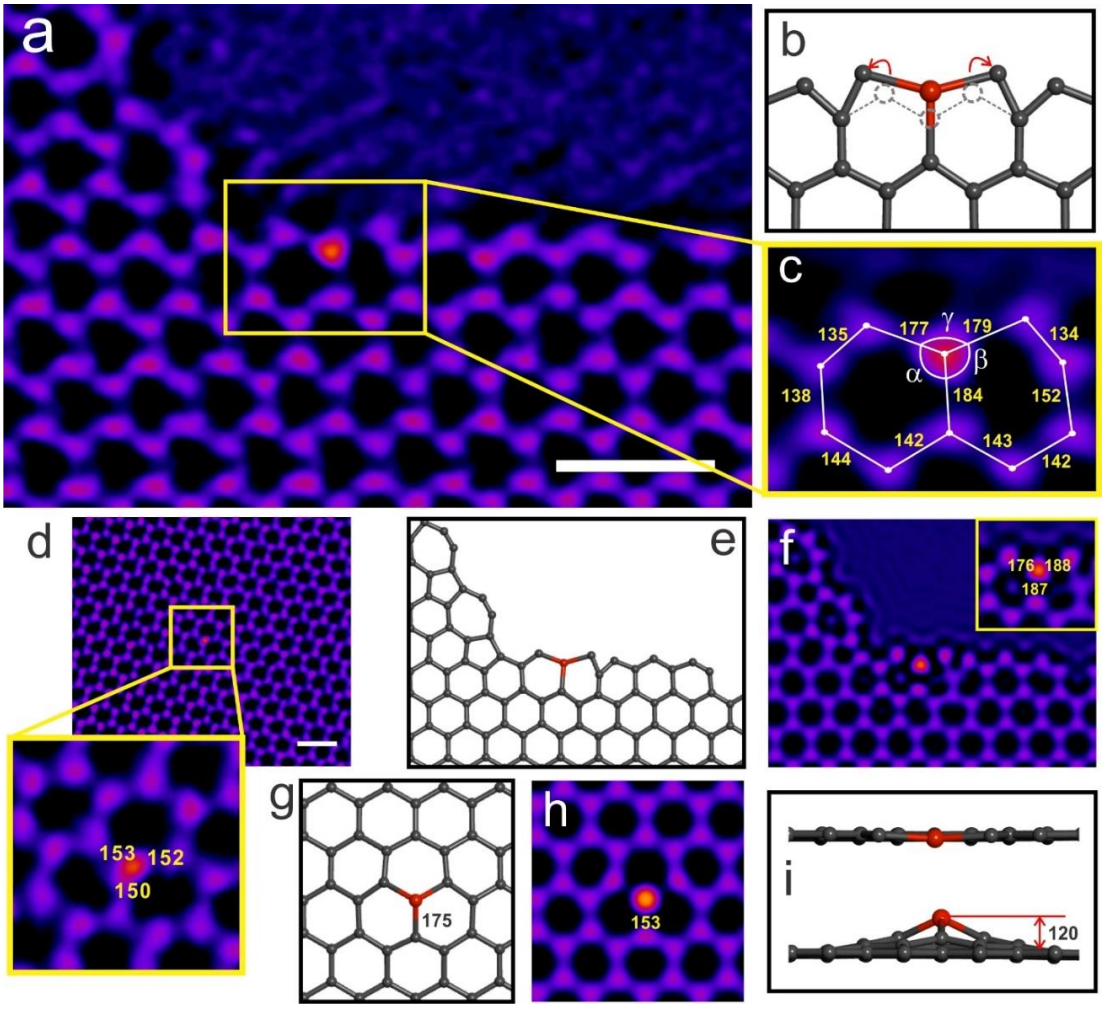

Figure 4-11 (a) AC-TEM image of a Si atom at a substitutional position (three-fold coordinated) at the zigzag edge. (b) Atomic model showing bond distortion around the Si dopant, with the original zigzag edge highlighted by the grey dashed circle. (c) TEM image of the region in the yellow box in a), with measured bond lengths in picometers. (d) AC-TEM image of a three-fold-coordinated Si dopant in bulk graphene with bond lengths values. (e) DFT calculated model of (a). (f) Multislice simulation image of (e) with Si-C bond distance values. (g) DFT model of (d). (h) Multislice simulation image of (g). (i) Lateral view of the DFT models of (e) (upper) and (g) (lower). Bond length values are in picometers. Scale bars in (a,d), 500 pm.

Two substitutional positions are available along zigzag edge: Si atoms at both the three-fold and two-fold coordinated positions were observed. Figure 4-11(a) shows a

Si dopant bonded with three nearest carbon neighbours. Measurements of the bond length reveals that the Si atom pushes the three nearest carbon neighbours away, inducing distortion within the local area, as shown in Figure 4-11(b), where grey dashed lines and circles indicate the original position of carbon atoms at the zigzag edge. The angles between each two Si-C bonds, labelled as α, β and γ in Figure 4-11(c), are 114°, 110° and 136°, matching perfectly with the corresponding angles in image simulation for the DFT calculated model (Figure 4-11(e,f)), where $\alpha = \beta = 112°, \text{and } \gamma = 136°$. To further understand the three-fold coordinated Si dopant, I compare it with its counterpart within bulk graphene lattice, as shown in Figure 4-11(d), where the Si dopant resides within a monovacancy position. This can be regarded as equivalent position with the Si dopant in Figure 4-11(a) due to the same coordination number. Figures 4-11(g) shows the DFT calculated models for the structure with their corresponding multislice simulation image in Figure 4-11(h). The Si-C bond distances for the Si edge dopant are about 180 ± 10 pm, while for the Si atom at monovacancy, the corresponding bond distances is shorter. The difference between the value from the DFT model (175 pm) and its image simulation (153 pm) is due to the 2D projection of the 3D structure and the resulting shortening of the bond length in projection. Figure 4-11(i) provides the lateral views of both of the three-fold coordinated structures. It can be seen that the Si atom is within the graphene plane when the Si atom is at graphene edge, while for the Si atom in bulk graphene, it is 120 pm out of the graphene plane, which means that although they are both three-fold coordinated, the hybridization is slightly different due to the bond angle. A Si dopant in graphene adopts sp^3 hybridization, which is also confirmed by Zhou et al,[32] whereas the Si atom at graphene edge prefers sp^2 hybridization, as the three Si-C bonds are in the same plane.

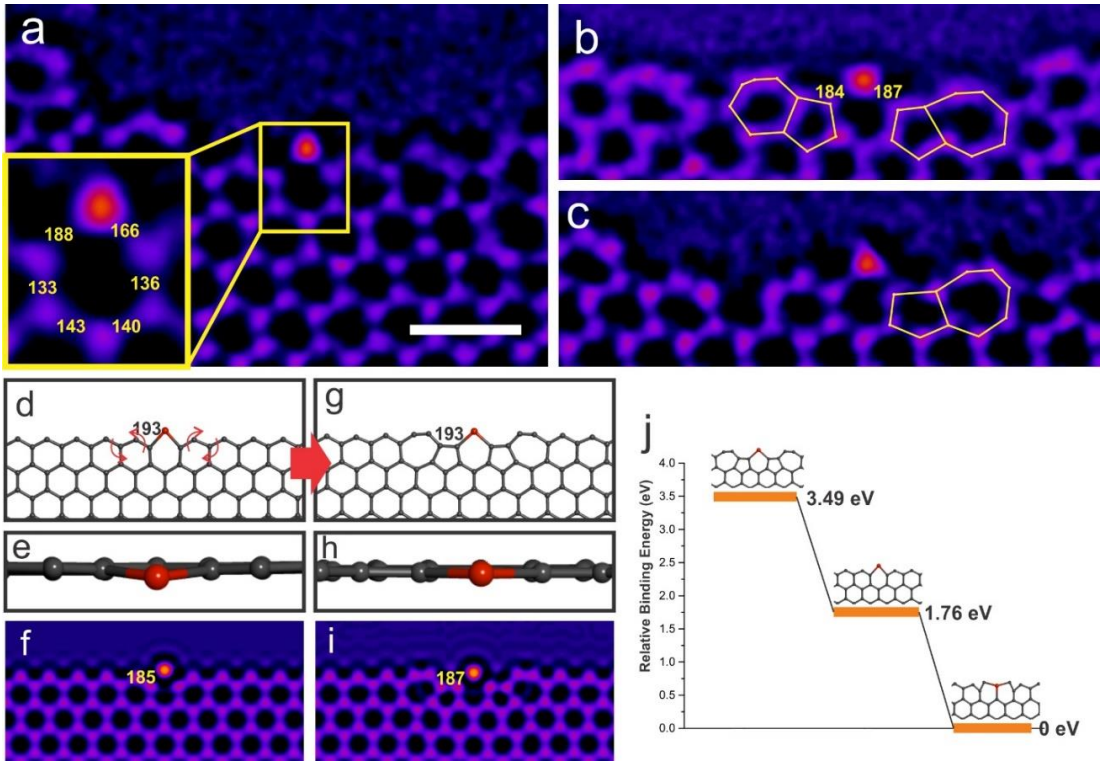

Figure 4-12 (a) AC-TEM image of a Si atom at a substitutional position (two-fold coordinated) at the zigzag edge. (b,c) AC-TEM images of two-fold coordinated Si atom at a reconstructed zigzag edge. d) DFT calculated atomic model of (a), with the side view in (e). (f) Multislice simulation image of (d). (g) DFT calculated atomic model of (b), with the side view in (h). (i) Multislice simulation image of (g). (j) Relative binding energies calculated by DFT of the Si atoms at substitutional positions. Scale bar in (a), 500 pm.

The two-fold coordinated substitutional position is at the crest of the zigzag edge, as shown in Figure 4-12(a), and the Si-C bond lengths show asymmetry. Interestingly, this Si-pristine zigzag edge configuration is rather rare, where in most cases the reconstructed 5-7 edge is involved, as shown in Figure 4-12(b,c). The pentagon-heptagon structure is found to be symmetrical, where pentagons prefer to be next to the Si atom, followed by the heptagons. This edge reconstruction is accomplished by Stone-Wales (SW) bond rotation, as demonstrated in Figure 4-12(d). It has been reported that the zigzag edge in graphene nanoribbon is changed to the reconstructed 5-7 edge by SW bond rotation.[33] The DFT calculated models show the two carbon bonds rotated 90^{o} by the direction indicated by the red arrows. The final structure is

shown in Figure 4-12(g). The bond transformation not only alters the periodic structure along zigzag edge, but also provides more space for the Si atom to sit in the graphene plane. Figure 4-12(e,h) show the lateral views of the models in Figure 4-12(d,g), and the Si atom shifts from a slightly out-of-plane position to completely in-plane when undergoing the SW rotation. The bond distances, however, are not really affected by the reconstruction, remaining approximately 190 pm. The intersection angle between the two Si-C bonds measured from the TEM images indicates a 10° dilation after the bond rotation, from 89° to 99°. The same phenomenon happens in the two simulation images (from 85° to 98°), due to the transformation of the configuration from 3D to 2D. The reconstructed edge also releases energy for the structure, resulting in a more stable configuration. Figure 4-12(j) compares the binding energy for the three substitutional Si-edge configurations, where higher binding energy indicates a more stable structure. The binding energies are relative values where the smallest energy (most unstable structure) is set to be 0 eV. It can be seen that the two-fold coordinated Si atoms are more stable than the three-fold coordinated counterpart, and the binding energy with the reconstructed zigzag edge is 1.73 eV higher than the one before reconstruction.

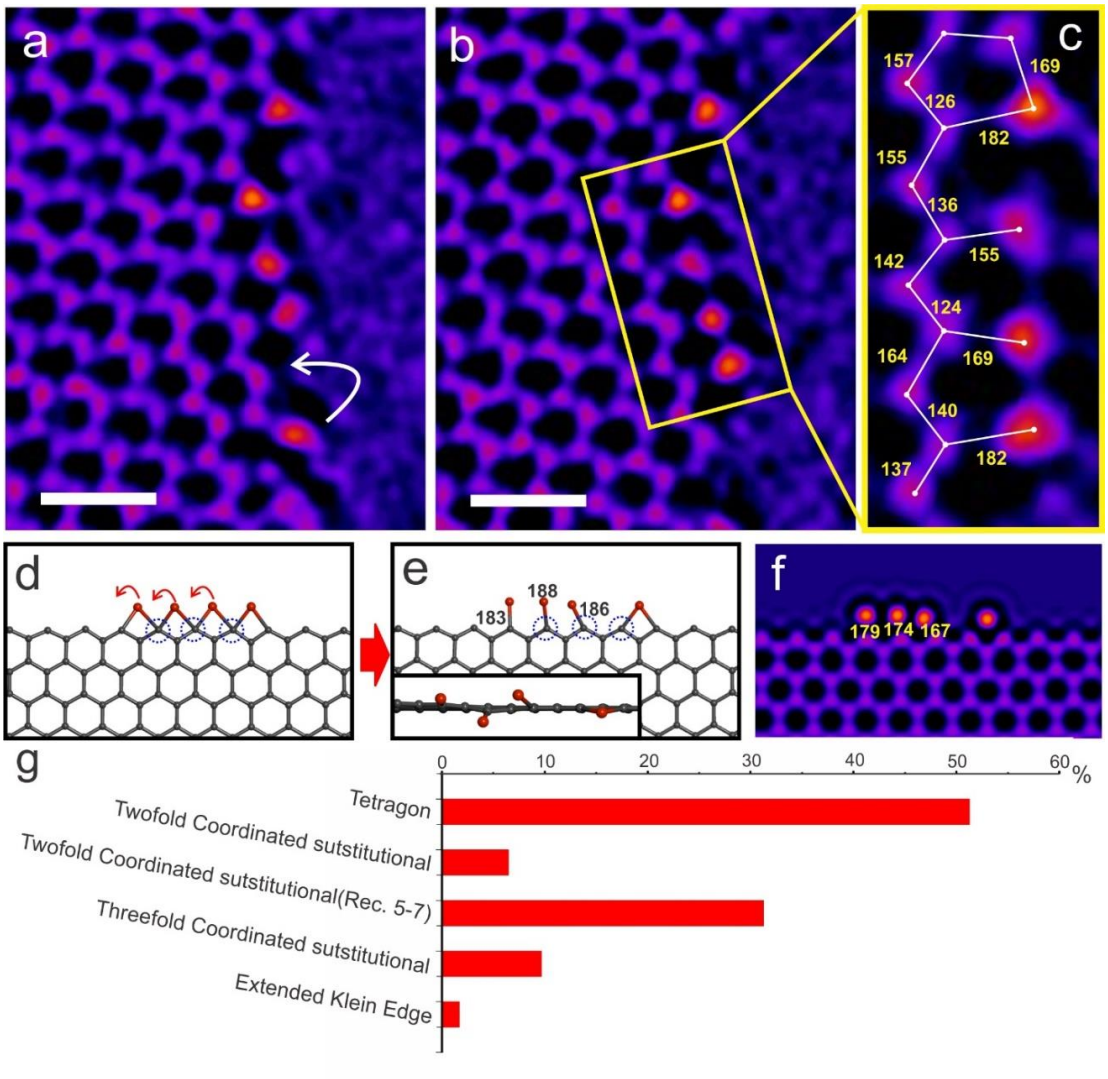

Figure 4-13 Structure and dynamics of an Extended Si Klein edge. (a) AC-TEM image of a Si EK edge with two Si atoms. (b) AC-TEM image after 10 s with one more nearby Si atom joining. (c) AC-TEM image from the yellow-box region in b). (d,e) DFT calculated models showing a possible route for the generation of a prolonged Si Klein edge, with the inset of (e) showing the lateral view. (f) Multislice image simulation of (e). (g) Percentage of the occurrence of all the Si-edge configurations along the zigzag edge (in 100 frames). Scale bars in (a,b), 500 pm.

The Extended Klein (EK) edge is the fourth periodic edge of graphene, which was recently confirmed by experimental results.[19] An EK edge is generated by a group of isolated carbon atoms protruding from the zigzag edge.[21,34,35] Si atoms can form a similar configuration by bonding to the zigzag edge. Bonding between Si atoms along the zigzag edge helps immobilize them to increase the length of the Si Klein edge,

shown in Figure 4-13(a,b). The bond length values displayed in Figure 4-13(c) show some fluctuations, from 155 to 182 pm, which can be explained by the DFT calculations. Figure 4-13(d,e) provide a plausible route for the generation of a Si EK edge. Unlike the situation along armchair edges, where Si atoms adopt a series of continuous valley positions, if Si atoms sit in the concave sections along zigzag edge, the binding energy of the configuration is so small and it will evolve into the Si EK edge structure with higher stability, shown in Figure 4-13(e). The left three Si atoms shift to left by approximately 123 pm, the lattice spacing of the $\{11\bar{2}0\}$ planes.[36] In the DFT structural relaxation, the three highlighted four-fold coordinated carbon atoms are released to form three-fold coordination without any energy barriers, which is much more energetically favoured in the two-dimensional structure of graphene. The left three Si atoms can be regarded as a small section of a Si EK edge, corresponding to the AC-TEM image. The side view of the Si EK edge (inset in Figure 4-13(e)) indicates its three-dimensional nature, where Si atoms alternate above or beneath the graphene plane. The variability in the degree of out of plane distortion of the Si atoms will cause differences in the 2D projection observed during the AC-TEM imaging. Figure 4-13(g) lists the frequency of observation for all the Si-edge configurations along the zigzag edge. More than half of the Si-edge interactions have tetragonal structure, which is the most stable, followed by the two-fold coordinated substitutional position with reconstructed edge, while the other three structures are not frequently observed.

4.4 Conclusion

In both of the divacancies and Si doped graphene edge studies, bond length measurement are used to evaluate the strain fields and the interactions between the

foreign dopants and carbon atoms. For divacancies, the significant bond length changes caused by the removal of two carbon atoms from a small local region are reduced by the involvement of bond rotations, which have been confirmed by the DFT calculated results. The local areas of the divacancy defects possess reasonable flatness, where the out-of-plane distortion caused by the rippling nature of graphene can be neglected in measured bond lengths. The strain distributions within the hexagonal neighbours around the three divacancies are studied, and the original divacancy (5-8-5) has the largest influence to the surrounding 6-numbered rings. The strain is released by SW rotation and for 5555-6-7777 defect, the strain is limited to the defect, with no obvious strain beyond the defect boundary. These experimental and theoretical results are the visualized evidence for the fact that 555-777 and 5555-6-7777 divacancy structures are more energetic favourable than the original 5-8-5 divacancy due to more evenly distributed bond lengths and released strain field. The large bond strain found in interface between pentagon and octagon rings is likely an explanation for why these are less frequent in larger defect clusters, which are primarily made up of pentagons and heptagons, or 558-558 alternating sequences.

Si dopants can interact with graphene edges by several bonding structures along both armchair and zigzag edges. Pentagonal structures at the armchair edge are most commonly observed and this is confirmed by both the experimental and theoretical results. Both substitutional and edge bonded Si atoms were found along the zigzag edge with reasonable stability, where edge reconstruction may also be involved to release energy. A group of Si atoms along zigzag edge can form an extended Si Klein edge, and this structure is supported by DFT calculation results. The detailed information provided here on the various Si-C bond lengths and structures may be

important for future applications that involve the decoration of graphene edges with Si or other elements.

4.5 References

(1) Robertson, A.; Warner, J. Atomic Resolution Imaging of Graphene by Transmission Electron Microscopy. *Nanoscale* **2013**, *5*, 4079–4093.

(2) Robertson, A. W.; Allen, C. S.; Wu, Y.; He, K.; Olivier, J.; Neethling, J.; Kirkland, A. I.; Warner, J. H. Spatial Control of Defect Creation in Graphene at the Nanoscale. *Nat. Commun.* **2012**, *3*, 1144.

(3) Banhart, F.; Kotakoski, J.; Krasheninnikov, A. V. Structural Defects in Graphene. *ACS Nano* **2011**, *5*, 26–41.

(4) Kotakoski, J.; Krasheninnikov, A. V; Kaiser, U.; Meyer, J. C. From Point Defects in Graphene to Two-Dimensional Amorphous Carbon. *Phys. Rev. Lett.* **2011**, *106*, 105505.

(5) Kotakoski, J.; Mangler, C.; Meyer, J. C. Imaging Atomic-Level Random Walk of a Point Defect in Graphene. *Nat. Commun.* **2014**, *5*, 3991.

(6) Kotakoski, J.; Meyer, J. C.; Kurasch, S.; Santos-Cottin, D.; Kaiser, U.; Krasheninnikov, A. V. Stone-Wales-Type Transformations in Carbon Nanostructures Driven by Electron Irradiation. *Phys. Rev. B* **2011**, *83*, 245420.

(7) Leyssale, J. M.; Vignoles, G. L. A Large-Scale Molecular Dynamics Study of the Divacancy Defect in Graphene. *J. Phys. Chem. C* **2014**, *118*, 8200–8216.

(8) Lee, G. D.; Wang, C. Z.; Yoon, E.; Hwang, N. M.; Kim, D. Y.; Ho, K. M. Diffusion, Coalescence, and Reconstruction of Vacancy Defects in Graphene Layers. *Phys. Rev. Lett.* **2005**, *95*, 205501.

(9) Kim, Y.; Ihm, J.; Yoon, E.; Lee, G. D. Dynamics and Stability of Divacancy Defects in Graphene. *Phys. Rev. B - Condens. Matter Mater. Phys.* **2011**, *84*, 75445.

(10) Botello-Mendez, A. R.; Declerck, X.; Terrones, M.; Terrones, H.; Charlier, J.-C. One-Dimensional Extended Lines of Divacancy Defects in Graphene. *Nanoscale* **2011**, *3*,

2868–2872.

(11) Warner, J. H.; Fan, Y.; Robertson, A. W.; He, K.; Yoon, E.; Lee, G. D. Rippling Graphene at the Nanoscale through Dislocation Addition. *Nano Lett.* **2013**, *13*, 4937–4944.

(12) Fasolino, A.; Los, J. H.; Katsnelson, M. I. Intrinsic Ripples in Graphene. *Nat Mater* **2007**, *6*, 858–861.

(13) Meyer, J. C.; Geim, A. K.; Katsnelson, M. I.; Novoselov, K. S.; Booth, T. J.; Roth, S. The Structure of Suspended Graphene Sheets. *Nature* **2007**, *446*, 60–63.

(14) Han, M. Y.; Özyilmaz, B.; Zhang, Y.; Kim, P. Energy Band-Gap Engineering of Graphene Nanoribbons. *Phys. Rev. Lett.* **2007**, *98*, 206805.

(15) Akola, J.; Heiskanen, H. P.; Manninen, M. Edge-Dependent Selection Rules in Magic Triangular Graphene Flakes. *Phys. Rev. B* **2008**, *77*, 193410.

(16) Cocchi, C.; Ruini, A.; Prezzi, D.; Caldas, M. J.; Molinari, E. Designing All-Graphene Nanojunctions by Covalent Functionalization. *J. Phys. Chem. C* **2011**, *115*, 2969–2973.

(17) Cocchi, C.; Prezzi, D.; Ruini, A.; Caldas, M. J.; Molinari, E. Optical Properties and Charge-Transfer Excitations in Edge-Functionalized All-Graphene Nanojunctions. *J. Phys. Chem. Lett.* **2011**, *2*, 1315–1319.

(18) Hämäläinen, S. K.; Sun, Z.; Boneschanscher, M. P.; Uppstu, A.; Ijäs, M.; Harju, A.; Vanmaekelbergh, D.; Liljeroth, P. Quantum-Confined Electronic States in Atomically Well-Defined Graphene Nanostructures. *Phys. Rev. Lett.* **2011**, *107*, 236803.

(19) Tao, C.; Jiao, L.; Yazyev, O. V.; Chen, Y. C.; Feng, J.; Zhang, X.; Capaz, R. B.; Tour, J. M.; Zettl, A.; Louie, S. G.; *et al.* Spatially Resolving Spin-Split Edge States of Chiral Graphene Nanoribbons. *Nat. Phys.* **2011**, *7*, 616–620.

(20) Cai, J.; Ruffieux, P.; Jaafar, R.; Bieri, M.; Braun, T.; Blankenburg, S.; Muoth, M.; Seitsonen, A. P.; Saleh, M.; Feng, X.; *et al.* Atomically Precise Bottom-up Fabrication of Graphene Nanoribbons. *Nature* **2010**, *466*, 470–473.

(21) He, K.; Lee, S.; Yoon, E.; Lee, G. D.; Warner, J. H.; Robertson, A. W. Extended Klein Edges in Graphene. *ACS Nano* **2014**, *8*, 12272–12279.

(22) Zhao, J.; Deng, Q.; Avdoshenko, S. M.; Fu, L.; Eckert, J.; Rummeli, M. H. Direct in

Situ Observations of Single Fe Atom Catalytic Processes and Anomalous Diffusion at Graphene Edges. *Proc. Natl. Acad. Sci.* **2014**, *111*, 15641–15646.

(23) Ramasse, Q. M.; Zan, R.; Bangert, U.; Boukhvalov, D. W.; Son, Y.; Novoselov, K. S. Direct Experimental Evidence of Metal-Mediated Etching of Suspended Graphene. *ACS Nano* **2012**, *6*, 4063–4071.

(24) Wang, H.; Li, K.; Cheng, Y.; Wang, Q.; Yao, Y.; Schwingenschlögl, U.; Zhang, X.; Yang, W. Interaction between Single Gold Atom and the Graphene Edge: A Study via Aberration-Corrected Transmission Electron Microscopy. *Nanoscale* **2012**, *4*, 2920–2925.

(25) He, K.; Robertson, A. W.; Fan, Y.; Allen, C. S.; Lin, Y.; Suenaga, K.; Kirkland, A. I.; Warner, J. H. Temperature Dependence of the Reconstruction of Zigzag Edges in Graphene. *ACS Nano* **2015**, *9*, 4786–4795.

(26) He, K.; Robertson, A. W.; Gong, C.; Allen, C. S.; Xu, Q.; Zandbergen, H.; Grossman, J. C.; Kirkland, A. I.; Warner, J. H. Controlled Formation of Closed-Edge Nanopores in Graphene. *Nanoscale* **2015**, 11602–11610.

(27) Warner, J. H.; Lee, G. D.; He, K.; Robertson, A. W.; Yoon, E.; Kirkland, A. I. Bond Length and Charge Density Variations within Extended Arm Chair Defects in Graphene. *ACS Nano* **2013**, *7*, 9860–9866.

(28) Rasool, H. I.; Ophus, C.; Klug, W. S.; Zettl, A.; Gimzewski, J. K. Measurement of the Intrinsic Strength of Crystalline and Polycrystalline Graphene. *Nat. Commun.* **2013**, *4*, 2811.

(29) Meyer, J. C.; Geim, A. K.; Katsnelson, M. I.; Novoselov, K. S.; Booth, T. J.; Roth, S. The Structure of Suspended Graphene Sheets. *Nature* **2007**, *446*, 60–63.

(30) Bangert, U.; Gass, M. H.; Bleloch, A. L.; Nair, R. R.; Geim, A. K. Manifestation of Ripples in Free-Standing Graphene in Lattice Images Obtained in an Aberration-Corrected Scanning Transmission Electron Microscope. *Phys. Status Solidi* **2009**, *206*, 1117–1122.

(31) Hytch, M. J.; Putaux, J. L.; Penisson, J. M. Measurement of the Displacement Field of Dislocations to 0.03A by Electron Microscopy. *Nature* **2003**, *423*, 270–273.

(32) Zhou, W.; Kapetanakis, M. D.; Prange, M. P.; Pantelides, S. T.; Pennycook, S. J.; Idrobo, J. C. Direct Determination of the Chemical Bonding of Individual Impurities

in Graphene. *Phys. Rev. Lett.* **2012**, *109*, 206803.

(33) Lee, G. D.; Wang, C. Z.; Yoon, E.; Hwang, N. M.; Ho, K. M. Reconstruction and Evaporation at Graphene Nanoribbon Edges. *Phys. Rev. B* **2010**, *81*, 195419.

(34) Klein, D. J. Graphitic Polymer Strips with Edge States. *Chem. Phys. Lett.* **1994**, *217*, 261–265.

(35) Klein, D. J.; Bytautas, L. Graphitic Edges and Unpaired π-Electron Spins. *J. Phys. Chem. A* **1999**, *103*, 5196–5210.

(36) Jamie H. Warner, Franziska Schäffel, Alicja Bachamatiuk, M. H. R. *Graphene Fundamentals and Emergnt Allication*; First edit.; Elsevier Inc.: Waltham, 2013.

Chapter 5

Atomic Structure and Dynamics of Epitaxial 2D Crystalline Gold on Graphene at Elevated Temperatures

This chapter concentrates on understanding the interaction between gold nanoparticles and monolayer graphene at 800 °C. At this high temperature, individual gold atoms and nanoclusters are mobile across the surface of graphene and attach to defect sites and migrate along the edges of holes in graphene. Gold nanoclusters on clean graphene show crystallinity at temperatures above their predicted melting point for equivalent sized clusters due to strong epitaxial interactions with the underlying graphene lattice. Gold nanoclusters anchored to defect sites in graphene exhibit discrete rotations between fixed orientations while maintaining epitaxial correlations to the graphene. It has been found that gold nanoclusters can be 2D with monolayer thickness and switch their crystal structure between two different phases.

5.1 Introduction

Graphene is a promising candidate for heterogeneous catalyst support under harsh conditions, such as acid and alkaline environments, and elevated temperatures due to its large surface area, excellent mechanical properties, large conductivity, chemical inertness and thermal stability.[1–4] Various types of graphene supported catalytic metal/alloy/oxide have been explored in recent years, such as Pd,[5] Pt,[6] Au,[1,3,4,7] TiO_2,[8] MnO_2,[9] and RuCu,[10] providing versatile applications such as fuel cells and water

treatment. Gold particles have high catalytic performance in certain areas, including automobile exhaust clean-up and biomedical applications.[11,12]

The morphology of gold nanoparticles strongly affects its catalytic behaviour. The structural form of gold nanoparticles can vary under different conditions, from face centred cubic (FCC) to multiply twinned decahedral or icosahedral.[13,14] A quantitative phase map of gold nanoparticles based on first principles calculations has been established by Barnard *et al*, with the consideration of temperature and the nanoparticle diameter.[15] For a supported catalytic system, the morphology of the nanoparticles is also determined by the interaction between the particle and the substrate, in addition to the balance between the surface energy and internal strain,[16] leading to gold crystals with unique morphologies. Gold with a 2D planar structure has been formed on the surface of graphene by Sasaki *et al*.[17] Both theoretical and experimental studies have been conducted to investigate the bonding between metals and graphene sheets.[18–21] Metal nanoparticles including gold are more likely to attach to the defective areas within graphene such as vacancies, dopants, and also the surface hydrocarbon contaminants, rather than have direct contact with the pristine graphene lattice regions.[1,22–25] The non-hexagonal rings and amorphous carbon have higher chemical reactivity and offer anchor sites to stabilize the metal particles, preventing them from migrating around on the surface. The anchor effect is especially essential to catalysts made from noble metals, enabling smaller particles to be better dispersed and remain stable during catalytic reactions. The aggregation of metal catalyst nanoparticles into larger clusters is one of the main aspects behind loss of catalytic efficiency during cycled catalytic testing. Understanding the catalyst-substrate interactions at high temperatures is essential for knowing the mechanisms of

agglomeration and can help develop new ways to sustain isolated nanoparticle catalysts.

Here, the study of structure and dynamics of epitaxial two-dimensional gold nanocrystals on graphene at elevated temperatures is carried out by using an *in-situ* heating holder within an AC-TEM. The gold nanoparticles show crystalline phases at elevated temperatures to 800 °C, which is above its melting point according to the depression of the melting points of nanoparticles in comparison with the bulk crystal (more details in Appendix B).[26] Stability of the gold nanocrystals on the surface of graphene is due to attachment to gold dopants already located within the graphene lattice. Melting and recrystallization processes have been captured with atomic resolution, which provides the opportunity for an analysis for the relationship between orientations of graphene and gold nanocrystals. This knowledge is essential for understanding how gold nanocrystals interact with monolayer graphene, as well as offers important data for targeted and efficient design of metal/graphene catalytic systems.

5.2 Gold Nanoparticles on Monolayer Graphene

Figure 5-1(a,c) show an AC-TEM image of the distribution of gold nanoparticles on monolayer graphene, as well as the corresponding selected electron diffraction pattern (SAED), with both graphene and gold lattice observed in the SAED. Gold nanoparticles with average diameter of 1.5 nm on graphene (Figure 5-1(b)) were produced by thermal evaporation with deposition rate carefully controlled at 0.1 nm/min. Energy Dispersive X-ray spectroscopy (EDX) shows significant peaks for gold, and a strong peak for silicon that comes from the silicon nitride support

membrane within the heating chip used for the *in-situ* temperature experiments. The gold particles are located only on the amorphous hydrocarbon surface contaminates and not on the pristine area of graphene, which agrees with the previous results.[23]

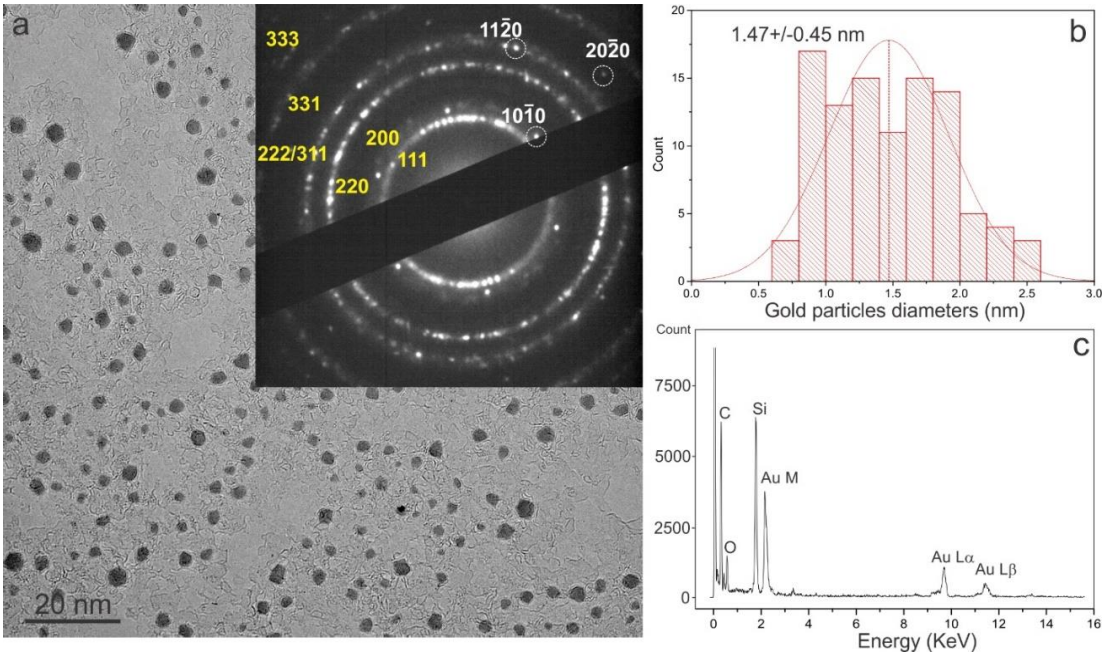

Figure 5-1 Distribution of gold particles deposited on graphene. (a) Low magnification AC-TEM image, with the inset of its diffraction pattern (indices of crystal planes for graphene and gold are in white and yellow respectively). (b) Histogram for the diameters of 100 gold particles. (c) Corresponding EDX spectrum from 0 to 16 keV. All images are taken at room temperature.

During the *in-situ* heating process, amorphous hydrocarbons crystallize under electron beam irradiation, forming a polycrystalline film on the top of the monolayer graphene, as shown in the multilayer area in Figure 5-2(a). This phenomenon has also been reported in details elsewhere.[27] The growth of multilayer graphene occurs in regions that have not been exposed to electron beam irradiation and indicates it is an intrinsic phenomenon and not driven by the electron beam. The newly grown graphene are robust at high temperature and under the electron beam, with the gold nanoparticles encapsulated showing no signs of melting and no migration across the surface. Some gold clusters are found on defective graphene region (Figure 5-2(b,c)). These gold

atoms may have escaped from the larger gold clusters before the multilayer graphene fully encapsulate them. It is also possible for the gold atoms to be embedded into graphene as substitutional dopants (Figure 5-2(d)). The large contrast from the single heavy atoms in graphene are significantly larger than the contrast seen for Si or Fe dopants, which can be found in graphene samples.[28–30] The large contrast is not seen in samples that have not had gold deposited onto them and provides strong support that these are single gold atoms. Similar strong contrast atoms are found at the edge of graphene holes and the contrast matches those that are bonded in the lattice. The small gold clusters bonded in the lattice of graphene are potential anchor sites for pinning gold nanocrystals that are freely migrating across the graphene surface. Figure 5-2(e) shows a gold array (highlighted in yellow box) with lattice contrast visible attaching to a graphene edge. Such a small gold cluster are expected to be molten at 800 °C due to the melting-point depression, described the decrease of the melting point with reducing in size for free standing nanoparticles.[26] As labelled in the inset, the direction of one orientation of the gold atoms array (orange arrow) is parallel to one of the armchair direction of the surrounding graphene lattice, referring to a specific interaction between the graphene and gold crystalline phase.

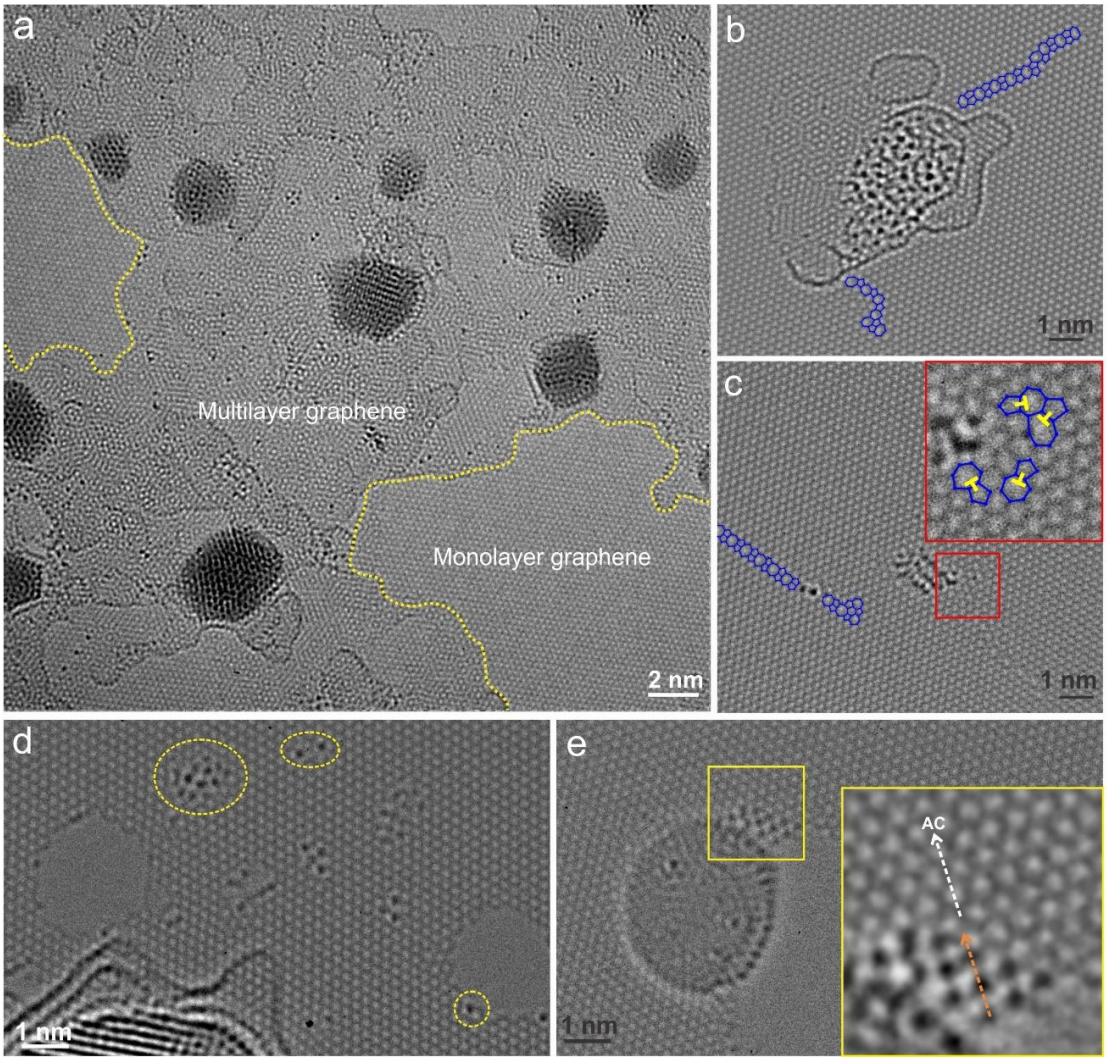

Figure 5-2 AC-TEM image of gold particles at 800 °C. (a) Gold nanocrystals at polycrystalline graphene and amorphous regions, with the boundaries of monolayer/multilayer graphene highlighted by yellow dashed curves. (b,c) A disordered gold crystal and a small gold cluster at defective region of monolayer graphene. (d) Gold atoms and small clusters embedded into monolayer a graphene region and edge sites. (e) A small gold cluster with ordered phase attaching to a graphene edge.

5.3 Dynamics of Gold Nanoclusters

Figure 5-3 shows a partially crystalline gold nanoparticle at the edge of a graphene hole. The size of the graphene hole is stable during the imaging period, and it can be observed that half of the gold particle is on the surface of the graphene region, and the

other half is free-standing, with no support substrate underneath. The graphene-supported region of the gold particle is crystalline, with the contrast spots arranging in order, while the free-standing part shows blurring, indicating molten state. During the migration, some gold atoms break away from the gold cluster, forming ordered ultra-small clusters with two periodic type, one is square (Figure 5-3(c,d,h)), the other one is triangular (Figure 5-3(e,f,g)), which has the same periodic structure with the gold cluster but with different orientations (highlighted in yellow dots and lines in Figure 5-3(f)). The distance between each two adjacent gold atoms is around 0.28 nm for both cases, corresponding to the distance between atoms in monolayer {100} and {111} planes of gold crystal. The partially crystalline gold cluster was finally broke apart by the electron beam, leaving ordered ultra-small clusters with the two types of ordered phases along the graphene shown in Figure 5-4. The partially crystalline gold nanoparticles attached to the edge of graphene further suggest that bonding interactions between the two materials helps to increase the crystallinity at these high temperatures.

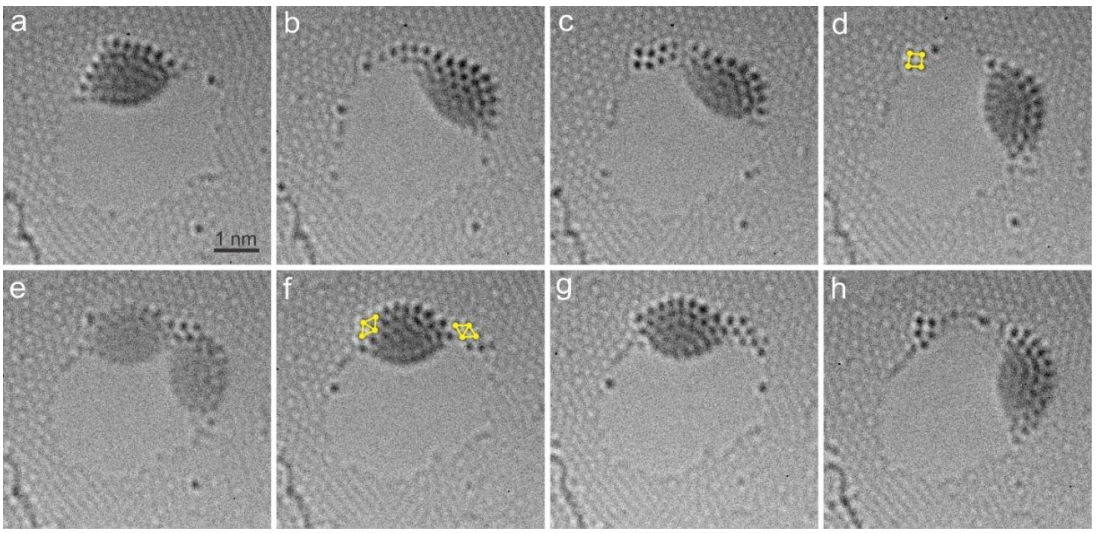

Figure 5-3 (a-h) AC-TEM images showing the dynamics of a gold nanoparticles moving around the edge of a hole in graphene. Time between each frame: ~10 s.

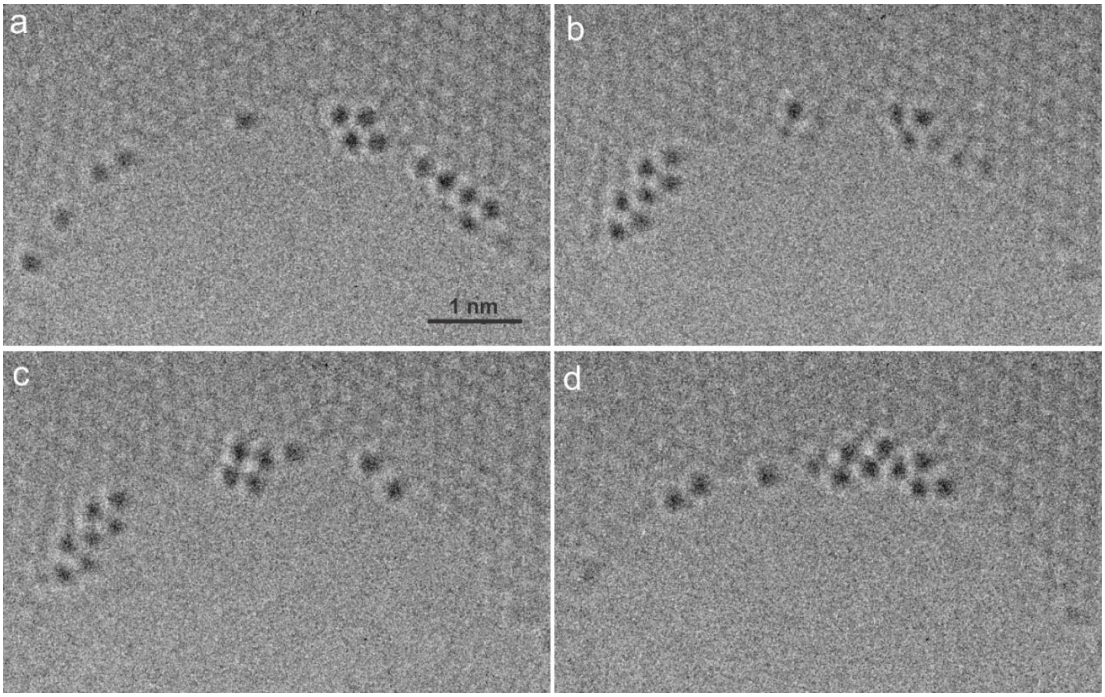

Figure 5-4 (a-d) Ordered ultra-small gold nanoclusters at graphene edge after the disintegration of the partially crystalline gold particle showing in Figure 5-3. Time between each frame: ~10 s.

Non-encapsulated gold clusters were found to be mobile across the surface of graphene, only sticking to edges of holes or defect clusters. These sites provide anchoring points that temporarily slow down the gold cluster movement. In Figure 5-5 two different examples are examined where gold clusters move around the edge of a hole and then jump across to a defect site in the graphene lattice. In both cases, the gold cluster adheres to the graphene edge (Figure 5-5(a,d)), and then hops onto the defective area (highlighted by red circles) nearby, fixing itself onto the position. The image sequence shows that there is a pinning effect with the small defect site acting as anchoring point.

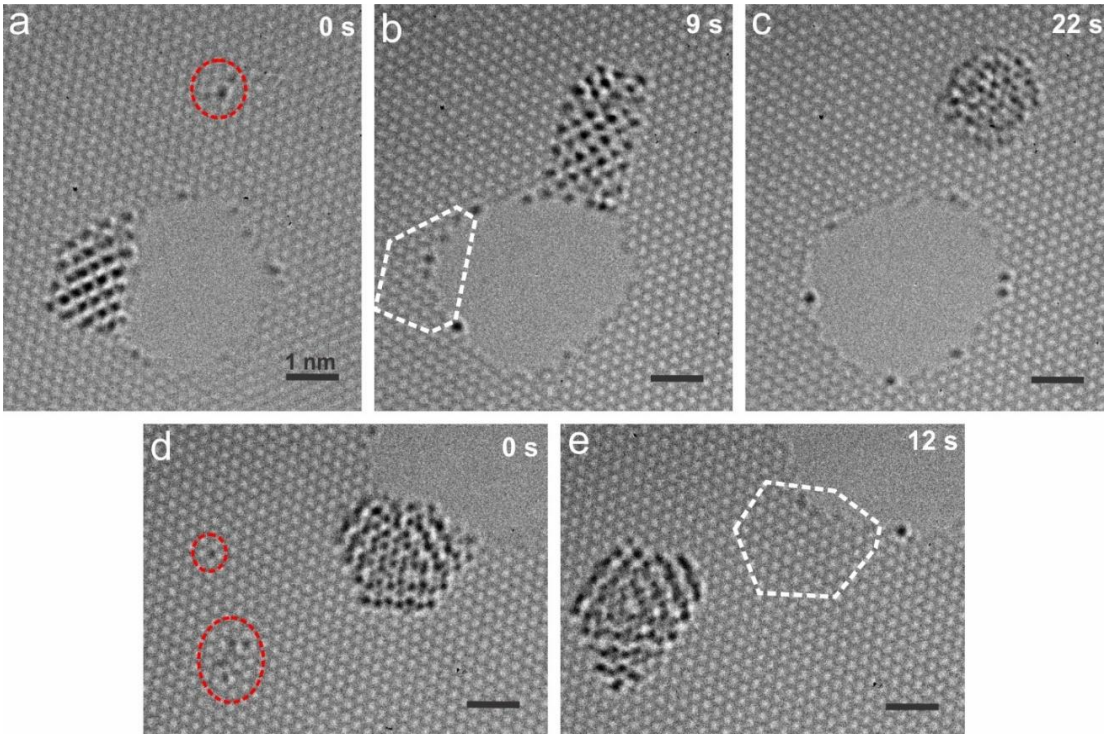

Figure 5-5 AC-TEM images showing gold clusters moving from the edge of a graphene hole to a defective site (highlighted by red dash circles).(a-c) Example 1, (d-e) Example 2. White dash boxes in (b) and (e) indicates the position of the gold crystal in the previous frame.

Gold clusters anchored to graphene exhibited several structural rearrangements, as shown in Figure 5-6. During the reconstruction process, the gold clusters can form unambiguous structures, with each contrast spot being isolated, as in Figure 5-6(b,e,h), while the rest of the frames between them possess vague configurations. The former structures indicate highly ordered crystalline phases, whereas the latter ones represent amorphous and molten states during transitions between the stable crystalline phases. A detailed phase transition of a gold crystal from square to hexagonal form is presented in Figure 5-6(i). This observation shows that a strong interactions presents between the highly crystalline graphene and the gold particles which helps the crystallization of these small gold nanoparticles above their expected melting point.

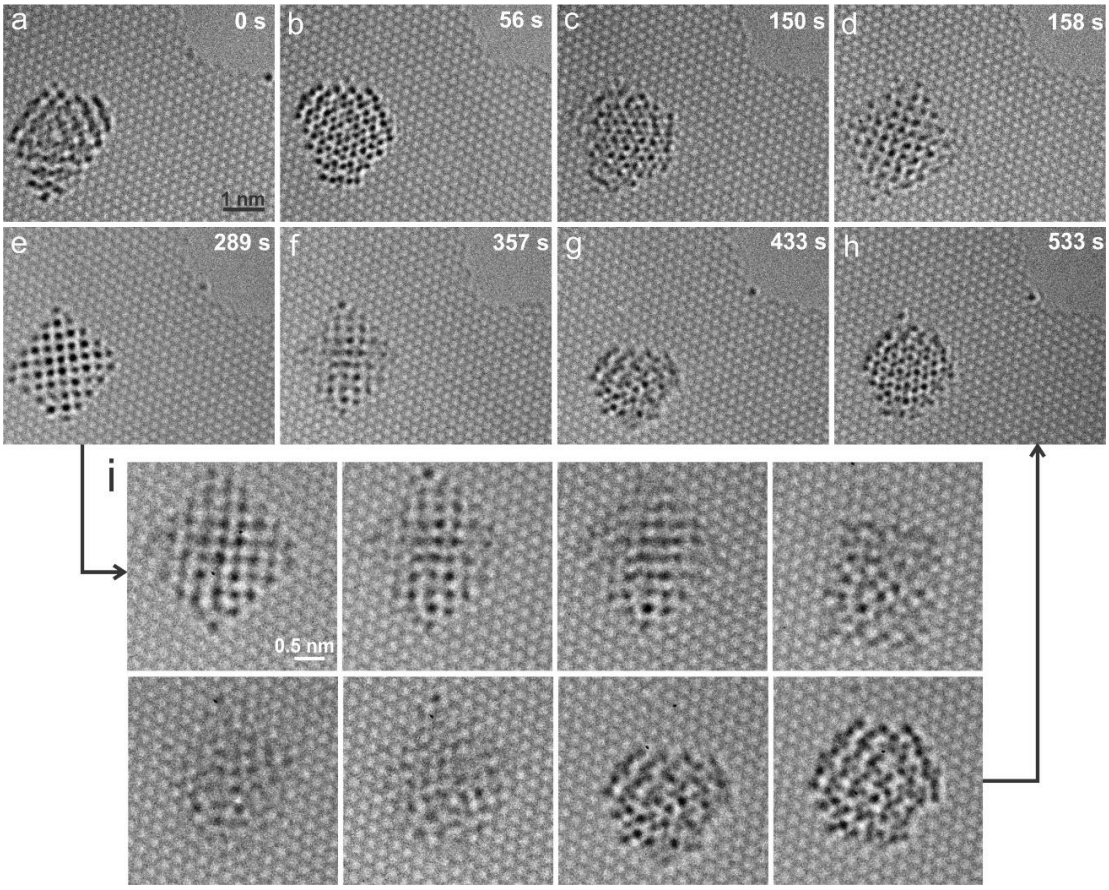

Figure 5-6 (a-h) Time series of AC-TEM images showing the dynamics of a gold cluster anchored to a defect site in graphene over a 9 minute period. a) The same gold cluster as the one shown in Figure 5-5(e). (b-h) Structural reconstructions of the gold cluster between the two crystalline phases: square and hexagonal. (i) Detailed phase transitions from the square crystalline phase to the hexagonal phase between (e) and (h).

5.4 Crystallographic Structures of the Planar Gold Nanocrystals

The number of contrast spots in Figure 5-6(b,e,h) may provide an insight into the loss or gain of gold atoms during the transformation process. Due to the slightly blurred areas at the edge of the crystal, only estimation of the number of atoms can be obtained. The hexagonal crystal in Figure 5-6(b) consists of about 87 contrast spots, while in (e) only 50 spots are observed. When the crystal restructures to the hexagonal phase (Figure 5-6(h)), the number of contrast spots goes back to around 80. It is unlikely that

more than 30 gold atoms are lost during the first phase transition, and then a similar number of atoms came back within the second transition. Furthermore, the nearby graphene hole remains relatively free from gold atoms during the whole period and if gold atoms were being released from the cluster one would expect a significant number to attach to this edge. Therefore, a plausible explanation is that no significant atom loss occurred during the process, but rather at some positions within the square crystal, one atomic column corresponds to more than one gold atom in the projected direction of viewing in AC-TEM. This structure does not obey the stacking rule for the second layer of atoms for a traditional FCC crystal, however when a material is ultrathin down to several atomic layers, the structure of it may significantly deviate from its bulk.

The partial-double-layer feature of the square shaped gold crystal is further confirmed by the examination of the relative contrast for each lattice site in the TEM image. The contrast intensity for a single atomic column within a gold crystal lattice image is determined by firstly, the number of the atoms along the projected direction, as well as the stability during the 2 s acquisition time. Due to the heavy nature of gold atoms and reasonable stability of the gold crystal, the number of gold atoms in z direction dominates the intensity value of a contrast spot. Figure 5-7(e) shows two distinct Gaussian distributions for the values of contrast associated with a single atomic column within the square crystal. The peak positions of the fitted Gaussian curves for the left side are ~125, and the right side ~175. The two Gaussian distributions are attributed to atomic columns having either one or two gold atoms within the square gold cluster. The contrast values of atomic columns for the hexagonal crystalline phase are shown in Figure 5-7(f), and show only one Gaussian curve is needed to fit the distribution. The peak value of the Gaussian curve is ~122, similar to that for the single atomic column value of the square gold cluster in Figure 5-7(e), indicating this is only

one atom thick. To further confirm the single and double atom stacking features of the two gold crystals, 20 isolated gold atoms along graphene edges are carefully selected with sufficient stability (3 examples shown in Figure 5-7(d)) during the 2 s exposure time to obtain a typical contrast value for single gold atoms, as shown in Figure 5-7(g). The selection criteria is shown in Figure B1. The peak position of the fitted Gaussian curve in Figure 5-7(g) gives a contrast value of the single gold atoms as ~132. All three images in Figure 5-7(a,b,d) have been adjusted so that the contrast value of the carbon lattice is near identical, meaning the analysis of the gold atom contrast values are consistent across all images. These results confirm the monolayer feature of the hexagonal crystal, the contrast spots with smaller intensity values are due to a certain amount of instability within the exposure time. For the case of the square gold crystal, both single- and double-layer areas exist, as suggested by the atomic model in Figure 5-7(i), vertically stacking of two gold atoms occurred at 24 sites, leaving the rest of the 26 sites as monolayer gold atoms. To further investigate the validity of the atomic model, I compare the experimental TEM image of the square gold cluster with a multislice image simulation (Figure 5-7(j)) based on the relative atomic model, where the defocus is set to match the TEM imaging conditions. The brightness and contrast of the simulated image has been adjusted to make the relative contrast of carbon atoms in the graphene lattice matched to the carbon atoms in the TEM image and therefore act as the reference value for the gold atom intensity. Figure 5-7(k) shows the intensity profiles for the contrast spots within the blue box in (h) and (j), and the experimental and theoretical results agree well. With this atomic model, the total gold atoms within the square crystal is 74, in error within +/- 5 atoms due to the influence of the noise level. Losing around 10 gold atoms during the first reconstruction is far more

reasonable than 35, and it also matches the number of atoms after the second reconstruction, which is counted as 80 atoms.

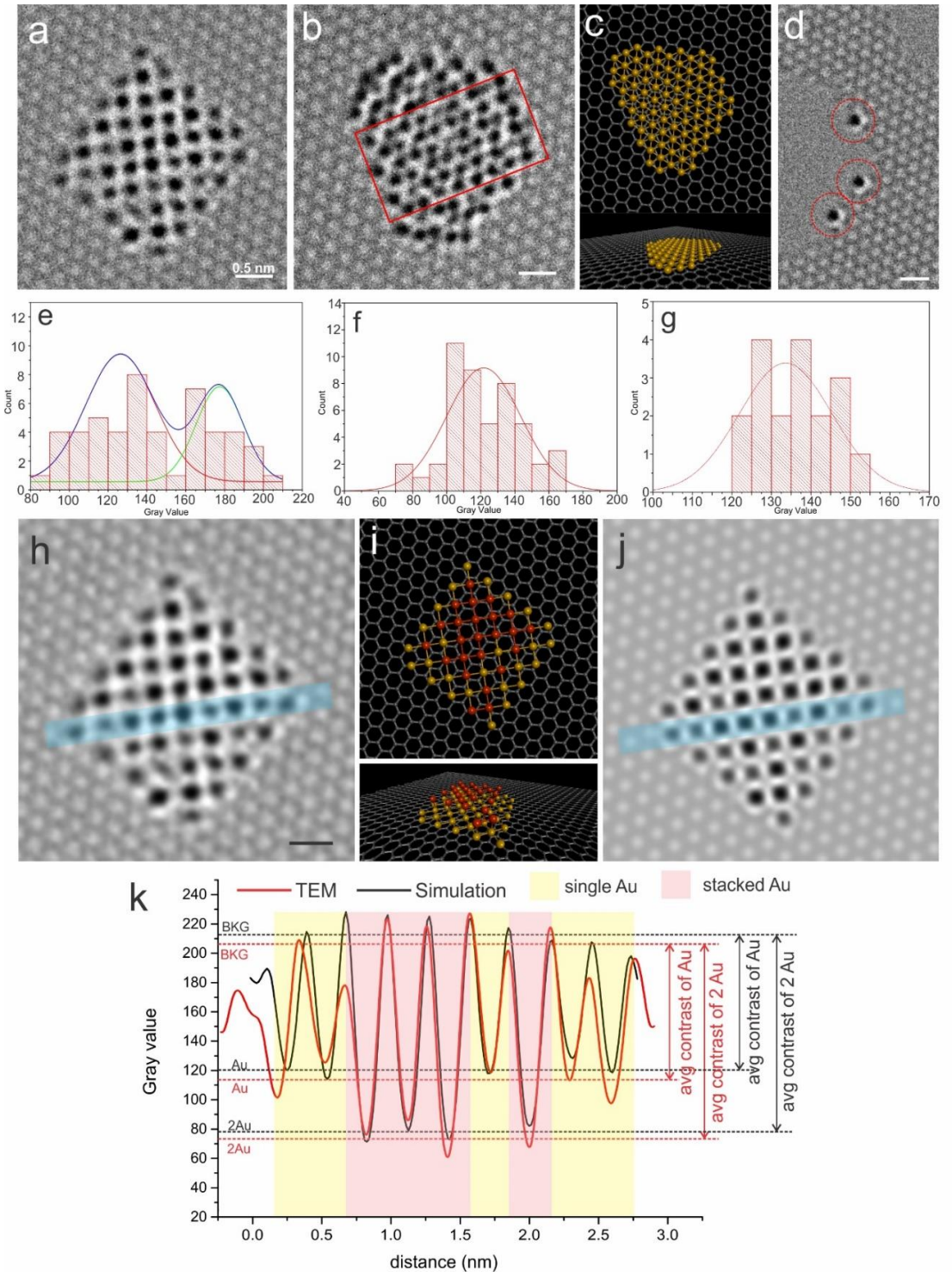

Figure 5-7 Analysis of gold cluster thickness. (a) AC-TEM image of the square gold crystalline phase (same with Figure 5-6(e)). (b) AC-TEM image of the hexagonal gold crystalline phase (same with Figure 5-6(b)). (c) Top and perspective views of the atomic model

of (b). (d) Isolated gold atoms adhering to the graphene edge. (e) Histogram of intensity values measured from the 50 contrast spots within the gold crystal shown in a). (f) Histogram of intensity values of the 50 gold atoms contained in the red box shown in (b). (g) Histogram of intensity values of 20 isolated gold atoms at graphene edges. (h) Smoothed AC-TEM image of the squared gold crystal. (i) Top and perspective view of the atomic model of the squared crystal, with golden balls representing the first-layer gold atoms, and red balls representing the second layer. (j) Multislice image simulation based on the model in (i). (k) Box-average intensity profiles of gold contrast spots for the blue areas in (h,j). Scale bars in (b,d,h), 0.5 nm.

When comparing the Fast Fourier Transform (FFT) patterns of the area with the two gold crystalline phases (Figure 5-8(c,i)) to the pristine graphene lattice (Figure 5-8(b,h)), the spots for gold and graphene can be easily separated. The corresponding d-spacing for each FFT spot of the gold crystals are obtained, based on the reference of the graphene lattice (Figure B2). With the consideration of the FCC structure of gold crystal, the incident beam direction (observation direction) for the case of the hexagonal crystalline phase has to be from one of the <111> crystal directions (taking $[\bar{1}11]$ in Figure 5-8(d) for an example), because of the regular triangular shape formed by every three adjacent contrast spots in the TEM image, as well as the regular hexagonal FFT pattern of the gold particle. The magnified image in Figure 5-8(d) shows the Miller Indices for all the FFT patterns of both the gold crystal (yellow) and graphene (white) with the incident beam direction of $[\bar{1}11]$ based on the ratios and included angles measured from the FFT pattern. Spots associated with the fractional lattice planes: 1/3{202}, 1/3{422} and 2/3{202}, occur in addition to the expected {202} reflections. These forbidden reflections generate from the incompleteness of the FCC crystal, as the hexagonal crystalline phase consists of only one layer of {111} plane, and at least three layers are needed to form a complete unit cell of FCC.[31]

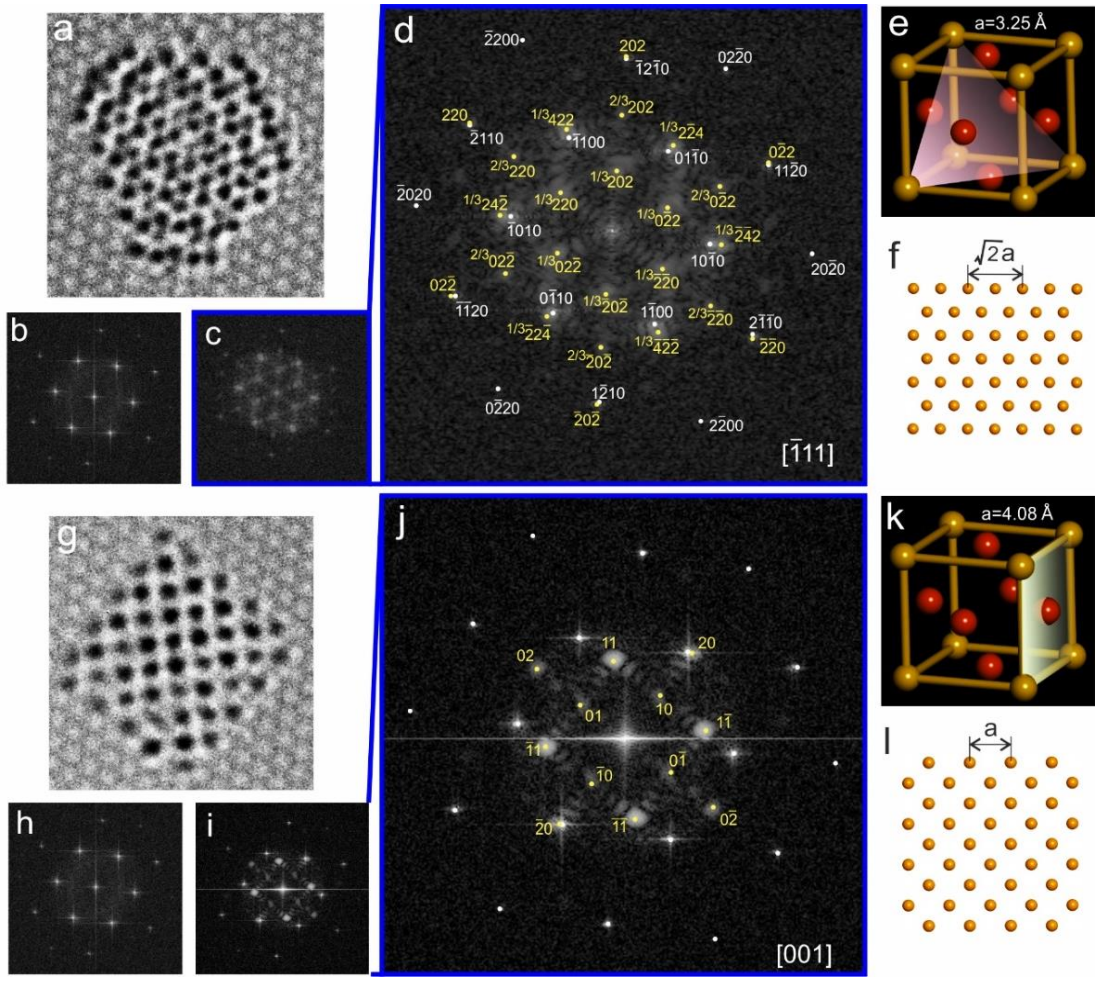

Figure 5-8 Crystallography of the two crystalline phases. (a) The hexagonal gold crystal. (b,c) Fast Fourier Transform (FFT) pattern of pristine graphene and graphene and gold crystal shown in a). (d) FFT pattern in (c) with Miller Indices of each crystal planes. (e) 3D atomic model for a face-centred cubic (FCC) unit cell for gold crystal, with a {111} plane highlighted by pink colour. (f) Atomic model of {111} plane sliced from the FCC crystal. g) The square gold crystal. (h,i) Fast Fourier Transform (FFT) pattern of pristine graphene and graphene and gold crystal shown in (e). (j) FFT pattern in (i) with Miller Indices of each crystal planes. (k) 3D atomic model for an FCC unit cell for gold crystal, with a {001} plane highlighted by green colour. (l) Atomic model of {001} plane sliced from the FCC crystal.

Thermal expansion of gold crystals should be taken into consideration when discussing the lattice constant at elevated temperature. A 0.9% of expansion of gold lattice has been observed in prior work at 785°C,[32] and therefore the lattice constant for a bulk gold crystal at 800°C should be about 4.11 Å. In the case of the hexagonal crystalline phase, the lattice constant calculated from the Miller Indices is about 3.25 Å (Figure

5-8(e,f)), corresponding to a 20% contraction in comparison to the bulk gold crystal. This shrinkage is significantly larger than previous reports, where only 2% reduction of the lattice constant was observed within the 2 nm gold crystals.[33] The larger contraction may be caused by the single-atom-thickness of the crystal with smaller coordination number of 6 (for a FCC crystal, the coordination number of each atom is 12 in bulk crystal), and the interaction between the particle and graphene substrate. However, one cannot exclude the possibility that the hexagonal crystal is composed of two layers of atoms with A-B stacking. In this case, there is still only one atom in each column but with different height, resulting in a more reasonable contraction smaller than 20%. For the case of the square crystalline phase (Figure 5-8(g-l)), the observation direction is <001> (taking [001] for example), and a forbidden reflection {10} emerges also because of the ultrathin structure, as shown in Figure 5-8(j). The lattice constant in this case is 4.08 Å, which is significantly larger than the hexagonal crystal and only slightly smaller than the expected bulk value at this temperature. It is worthwhile to mention that as the second layer of gold atoms sit directly on the top of the first layer, one can regard the structure as simple cubic (SC), rather than FCC shown in Figure 5-8(k). This unique stacking sequence deviated from its bulk structure may due to the ultrathin nature of the gold crystal, as well as the strong interaction between gold and graphene.

5.5 Epitaxial Orientations of 2D Crystalline Gold on Graphene

When examining the relative orientations between the gold cluster and graphene based on their FFT patterns, a parallel relationship is found between the planes of the gold crystal and graphene. For the case of the hexagonal gold crystal, the first epitaxial

situation is that the directions of the six spots representing for the d-spacing of $\frac{1}{3}\{422\}$ planes for gold coincide with the six spots for graphene $\{10\bar{1}0\}$ plane in reciprocal space, which means, in the real space, the {202} crystal plane of gold is parallel to the armchair direction of graphene, and {422} crystal plane is parallel to the zigzag direction, as shown in the arrows in Figure 5-9(a). The d-spacing of $\frac{1}{3}\{422\}$ plane of gold and $\{10\bar{1}0\}$ plane of graphene show an approximately 6% mismatch, as shown in the inset of Figure 5-9(c), where the centre of graphene and gold spots are not concentric. This orientation lasts 60 s, indicating some degree of stability. Figure 5-9(b) reveals the orientation of the same gold crystal after 60 s. The TEM image and the corresponding FFT pattern (Figure 5-9(d)) show that the gold crystal rotates 30° clockwise, which is the other epitaxial orientation, with the {422} crystal plane of gold parallel to the armchair direction of graphene, and {202} crystal plane parallel to the zigzag direction. This orientation also lasts nearly 60 s. The shape of the hexagonal gold crystal does not change much during the rotation. During the lifetime of this gold crystal, every time the highly crystalline phase with hexagonal structure appears, it shows either of the two epitaxial orientations. This indicates strong interaction between the gold crystal and graphene lattice, even though there may be some bonding between the anchoring defect and the 2D gold crystal to initially anchor it to the local region. Similar alignment between the gold and graphene lattice also occurs for the square gold crystalline phase, which is surprising given that cubic crystal structure does not have many epitaxial correlated atomic sites with the hexagonal crystal phase of graphene. The square crystalline phase oscillates between two preferred orientations, just like the case of the hexagonal crystalline phase. Figure 5-9(e) shows the first epitaxial orientation, with {20} (or {10}) crystal plane parallel to one of armchair directions and the zigzag direction that is vertical to the armchair direction, due to the

orthogonality of each plane in {20} group. After 36 s, the second epitaxial orientation appears, with the {11} crystal plane parallel to one armchair and one zigzag direction (Figure 5-9(f,i)). In this case, the square gold crystal rotates 15° clock wise. The gold crystal then rotates 15° anti-clockwise to the original epitaxial orientation in 12 s (Figure 5-9(g,j)).

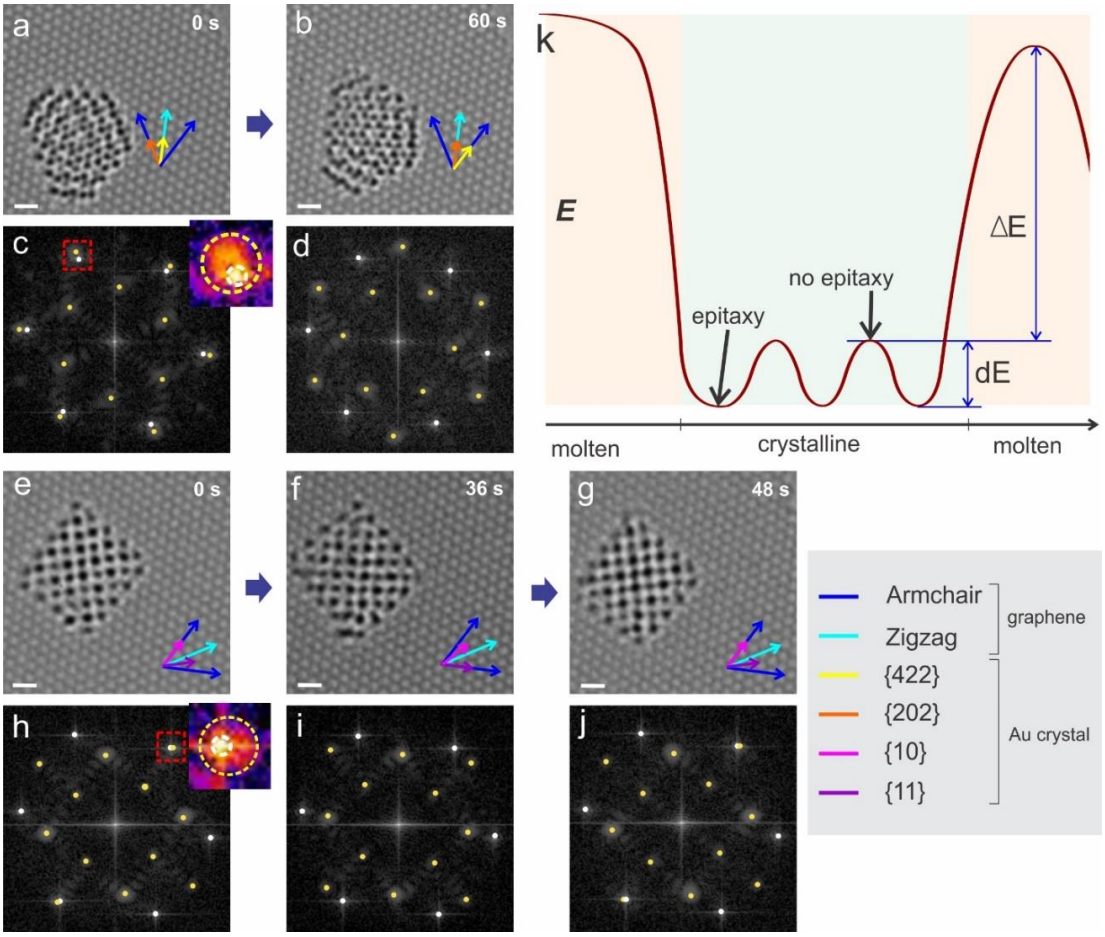

Figure 5-9 Epitaxial orientations of the gold crystalline phases on graphene. (a,d) Two favoured orientations for the hexagonal crystalline phase and corresponding FFT patterns, with the inset showing the detailed relationship between the 1/3{422} of gold crystal and $\{10\bar{1}0\}$ of graphene. (e-j) Transition between two epitaxial orientations of the squared gold crystal and corresponding FFT patterns, with the inset showing the detailed relationship between the {20} of gold crystal and $\{10\bar{1}0\}$ of graphene. (k) A schematic diagram illustrating possible energy barriers between each stable orientation. Scale bars in (a,b,e-g), 0.5 nm.

The observations of rotation indicates that the crystalline phases are more energetically favourable than the molten states when on clean graphene surface, and energy is required for the transitions between the two crystalline phases (square and hexagonal). When the gold is in its crystalline phases, matching graphene lattice directions are always found and indicate these are the low energy states. Energy is required to rotate between different graphene lattice directions of fixed stability. A schematic illustration in Figure 5-9(k) shows the possible energy variations between each crystallographic state. It is the interactions between the graphene and gold lattice that prevent the gold cluster from being in a molten state and instead adopting a high degree of crystalline order. This behaviour is not seen for gold clusters sitting on the amorphous carbon or on highly defective regions of monolayer carbon that have lost the periodic hexagonal lattice structure, further supporting the notion that epitaxial interactions drive the crystallization of gold.

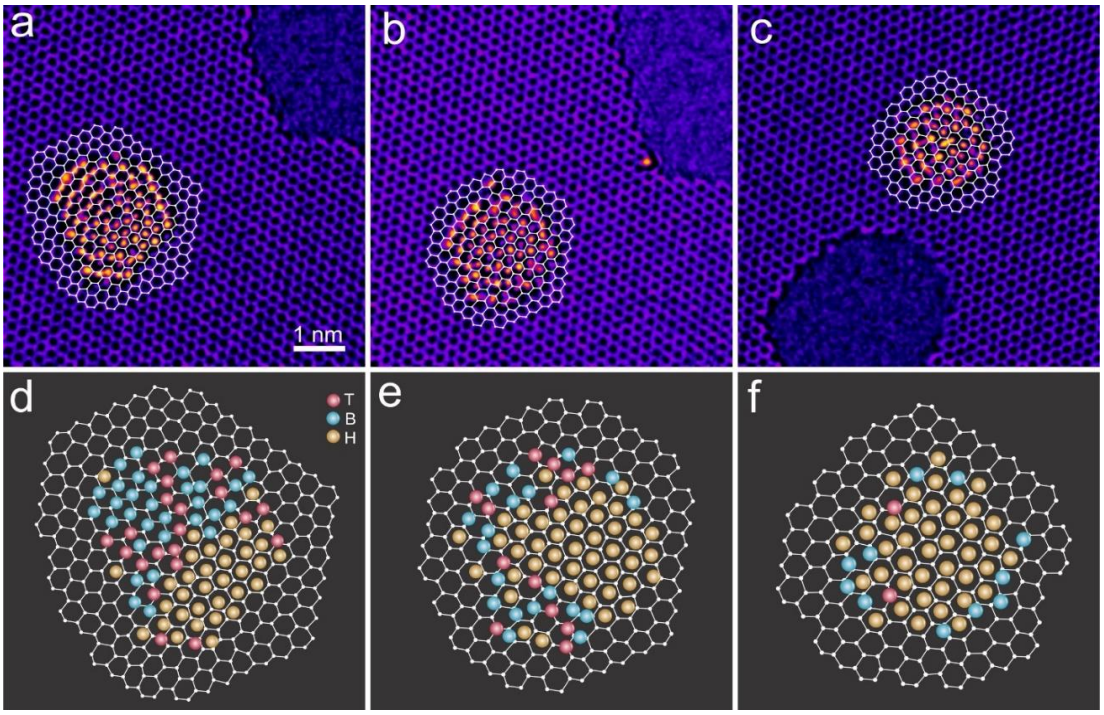

Figure 5-10 The relative positions gold atoms within the crystalline phases with respect to the graphene lattice structure. (a-c) AC-TEM images with false colour showing the hexagonal

crystalline phase of gold clusters, with underneath graphene lattice generated using a continuation of the surrounding area. (d-f) Atomic models indicating the three types of positions gold atoms can adopt with respect to the graphene lattice, where red spheres correspond to atop sites, blue spheres correspond to bridge sites, and golden spheres corresponding to hollow sites.

The graphene lattice underneath the gold crystal contributes little contrast to the image in this region. However, by reconstructing of the image by selecting the FFT pattern for graphene only, one can see the difference between the vacuum area and the region underneath the crystal (Figure B3). Although there must be a small defective site somewhere in the covered graphene area, it is quite small and therefore an extension of the surrounding area can be created into the region below the gold cluster by continuation of the hexagonal ring pattern, as shown in Figure 5-10(a-c), where the graphene lattice structures have been highlighted by white lines. It provides detailed information about how individual gold atoms within a crystal locate with respect to the carbon atoms in graphene. According to previous research, single gold adatoms can sit in three sites on the surface of graphene: top, bridge and hollow sites, and the former two sites are more energetically favourable than the hollow site based on the DFT calculations.[34] For isolated gold adatoms on a graphene surface, the binding energy for the three sites are 0.79 eV for top, 0.74 eV for bridge, and 0.52 eV for hollow.[34] At high temperature (i.e., 800 ^{o}C) the thermal energy is sufficient to overcome the energy barrier between these three configurations and therefore individual gold atoms are mobile across the graphene surface and do not bind to any particular site in pristine areas for an appreciable amount of time to image by TEM. The behaviour of the gold atoms within a 2D crystal differs from isolated ones due to the bonding with other gold atoms in the cluster, stabilizing the cluster. Figure 5-10(d-f) records the position of each gold atom based on their corresponding TEM images,

with the graphene lattice projected into the gold cluster region to examine the possible correlations between the gold atom site and carbon atom sites. Hollow sites are found to be favoured by these gold atoms (represented by the golden balls) across the three images in Figure 5-10. This conclusion is valid for both hypotheses, either the gold crystal is planar monolayer or zigzag A-B stacking structure. Gold atoms in the top and bridge sites mostly occur at the edge areas of the crystalline phase, along with severe distortions. The coordination number of the gold atoms at the central area is 6, while for the edge atoms it is 3 to 5. Fewer bonding to nearest neighbours induces variations of the distances between them and the edge atoms were loosely bonded and easily escaped from a crystal.[35]

5.6 Conclusion

The observations of crystalline phase transitions and local rotations between the epitaxial orientations, indicates that the crystalline phases are more energetically favourable than the molten states when on clean graphene surfaces. When the gold is in its crystalline phases, epitaxial orientations matching graphene lattice directions are always found and indicate these are the low energy states. Energy is required to rotate between different graphene lattice directions of fixed stability. This indicates that it is the interactions between the graphene and gold lattice that is preventing the gold cluster from being in a molten state and instead adopting a high degree of crystalline order. This behaviour is not seen for gold clusters on the amorphous carbon contamination or highly defective regions of monolayer carbon, further supporting the notion that epitaxial interactions drive the crystallization of gold.

Observing the epitaxial interactions between larger gold clusters deposited onto graphene was hindered by the formation of a multilayer graphene encapsulation around the preformed gold nanoparticles that sealed them up and prevented further transformations. However, there were sufficient free gold atoms and small gold clusters that were able to migrate across the surfaces and form crystalline phases that depended on the nature of the carbon structure below. These results indicate that the amorphous carbon contamination on the surface of graphene is the major inhibiting factor for the formation of large scale 2D gold on graphene. One possible way that this could be overcome in future work is to heat graphene to high temperatures first to clean its surface and then deposit gold at elevated temperature on the clean surface. These results shed important light into the gold-carbon interactions that are important for a variety of catalyst reactions, where small gold clusters are attached to carbon supports of various kinds ranging from graphene to carbon black.

5.7 References

(1) Julkapli, N. M.; Bagheri, S. Graphene Supported Heterogeneous Catalysts: An Overview. *Int. J. Hydrogen Energy* **2015**, *40*, 948–979.

(2) Deng, D.; Novoselov, K. S.; Fu, Q.; Zheng, N.; Tian, Z.; Bao, X. Catalysis with Two-Dimensional Materials and Their Heterostructures. *Nat. Nanotechnol.* **2016**, *11*, 218–230.

(3) Yu, X.; Huo, Y.; Yang, J.; Chang, S.; Ma, Y.; Huang, W. Reduced Graphene Oxide Supported Au Nanoparticles as an Efficient Catalyst for Aerobic Oxidation of Benzyl Alcohol. *Appl. Surf. Sci.* **2013**, *280*, 450–455.

(4) Choi, Y.; Gu, M.; Park, J.; Song, H. K.; Kim, B. S. Graphene Multilayer Supported Gold Nanoparticles for Efficient Electrocatalysts toward Methanol Oxidation. *Adv. Energy Mater.* **2012**, *2*, 1510–1518.

(5) Scheuermann, G. M.; Rumi, L.; Steurer, P.; Bannwarth, W.; Mülhaupt, R. Palladium Nanoparticles on Graphite Oxide and Its Functionalized Graphene Derivatives as Highly Active Catalysts for the Suzuki-Miyaura Coupling Reaction. *J. Am. Chem. Soc.* **2009**, *131*, 8262–8270.

(6) Layek, R. K.; Samanta, S.; Nandi, A. K. The Physical Properties of Sulfonated Graphene/poly(vinyl Alcohol) Composites. *Carbon* **2012**, *50*, 815–827.

(7) Kumar, S.; Selvaraj, C.; Munichandraiah, N.; Scanlon, L. G. Gold Nanoparticles Anchored Reduced Graphene Oxide as Catalyst for Oxygen Electrode of Rechargeable Li–O_2 Cells. *RSC Adv.* **2013**, *3*, 21706-21714.

(8) Liang, Y.; Wang, H.; Casalongue, H. S.; Chen, Z.; Dai, H. TiO2 Nanocrystals Grown on Graphene as Advanced Photocatalytic Hybrid Materials. *Nano Res.* **2010**, *3*, 701–705.

(9) Chen, S.; Zhu, J.; Wu, X.; Han, Q.; Wang, X. Graphene Oxide−MnO_2 Nanocomposites for Supercapacitors. *ACS Nano* **2010**, *4*, 2822–2830.

(10) Cao, N.; Hu, K.; Luo, W.; Cheng, G. RuCu Nanoparticles Supported on Graphene: A Highly Efficient Catalyst for Hydrolysis of Ammonia Borane. *J. Alloys Compd.* **2014**, *590*, 241–246.

(11) Campbell, C. T. The Active Site in Nanoparticle Gold Catalysis. *Science* **2004**, *306*, 234–235.

(12) Sperling, R. A.; Gil, P. R.; Zhang, F.; Zanella M.; Parak, W. J. Biological Applications of Gold Nanoparticles. *Chem. Soc. Rev.* **2008**, *37*, 1896-1908.

(13) Young, N. P.; van Huis, M. A.; Zandbergen, H. W.; Xu, H.; Kirkland, A. I. Transformations of Gold Nanoparticles Investigated Using Variable Temperature High-Resolution Transmission Electron Microscopy. *Ultramicroscopy* **2010**, *110*, 506–516.

(14) Marks, L. D. Experimental Studies of Small Particle Structures. *Rep. Prog. Phys.* **1994**, *57*, 603–649.

(15) Barnard, A. S.; Young, N. P.; Kirkland, A. I.; Van Huis, M. A.; Xu, H. Nanogold: A Quantitative Phase Map. *ACS Nano* **2009**, *3*, 1431–1436.

(16) Yacamán, M. J.; Ascencio, J. a.; Liu, H. B.; Gardea-Torresdey, J. Structure Shape and

Stability of Nanometric Sized Particles. *J. Vac. Sci. Technol. B Microelectron. Nanom. Struct.* **2001**, *19*, 1091-1103.

(17) Sasaki, Y.; Kitaura, R.; Yamamoto, Y.; Arai, S.; Suzuki, S.; Miyata, Y.; Shinohara, H. Preparation and Observation of an Atomic Layer of Gold Formed on the Surface of Graphene. *Appl. Phys. Express* **2012**, *5*, 065103.

(18) Amft, M.; Sanyal, B.; Eriksson, O.; Skorodumova, N. V. Small Gold Clusters on Graphene, Their Mobility and Clustering: A DFT Study. *J. Phys. Condens. Matter* **2011**, *23*, 205301.

(19) Brito, W. H.; Miwa, R. H. Adsorption and Diffusion of Gold Adatoms on Graphene Nanoribbons: An Ab Initio Study. *Phys. Rev. B: Condens. Matter Mater. Phys.* **2010**, *82*, 045417.

(20) Grantier, J.; Lazar, P.; Prucek, R.; Šafářová, K.; Zbořil, R. Interaction of Graphene with Noble Metals. *J. Phys. Chem. C* **2012**, *116*, 14151−14162.

(21) Pulido, A.; Boronat, M.; Corma, A. Theoretical Investigation of Gold Clusters Supported on Graphene Sheets. *New J. Chem.* **2011**, *35*, 2153–2161.

(22) Zan, R.; Bangert, U.; Ramasse, Q.; Novoselov, K. S. Interaction of Metals with Suspended Graphene Observed by Transmission Electron Microscopy. *J. Phys. Chem. Lett.* **2012**, *3*, 953–958.

(23) Zan, R.; Bangert, U.; Ramasse, Q.; Novoselov, K. S. Metal - Graphene Interaction Studied via Atomic Resolution Scanning. **2011**, *11*, 1087–1092.

(24) Li, S.; Guo, S.; Yang, H.; Gou, G.; Ren, R.; Li, J.; Dong, Z.; Jin, J.; Ma, J. Enhancing Catalytic Performance of Au Catalysts by Noncovalent Functionalized Graphene Using Functional Ionic Liquids. *J. Hazard. Mater.* **2014**, *270*, 11–17.

(25) Liu, W.; Sun, D.; Fu, J.; Yuan, R.; Li, Z. Assembly of Evenly Distributed Au Nanoparticles on Thiolated Reduced Graphene Oxide as an Active and Robust Catalyst for Hydrogenation of 4-Nitroarenes. *RSC Adv.* **2014**, *4*, 11003–11011.

(26) Buffat, P.; Borel, J. P. Size Effect on the Melting Temperature of Gold Particles. *Phys. Rev. A* **1976**, *13*, 2287–2298.

(27) Gong, C.; He, K.; Lee, G. D; Chen, Q.; Robertson, A. W.; Yoon, E.; Hong, S.; Warner, J. H. In Situ Atomic Level Dynamics of Heterogeneous Nucleation and Growth of

Graphene from Inorganic Nanoparticle Seeds. *ACS Nano* **2016**, *10*, 9397–9410.

(28) Chen, Q.; Koh, A. L.; Robertson, A. W.; He, K.; Lee, S.; Yoon, E.; Lee, G. D.; Sinclair, R.; Warner, J. H. Rotating Anisotropic Crystalline Silicon Nanoclusters in Graphene. *ACS Nano* **2015**, *9*, 9497–9506.

(29) He, Z.; He, K.; Robertson, A. W.; Kirkland, A. I.; Kim, D.; Ihm, J.; Yoon, E.; Lee, G. D.; Warner, J. H. Atomic Structure and Dynamics of Metal Dopant Pairs in Graphene. *Nano Lett.* **2014**, *14*, 3766–3772.

(30) Robertson, A. W.; Montanari, B.; He, K.; Kim, J.; Allen, C. S.; Wu, Y. A.; Olivier, J.; Neethling, J.; Harrison, N.; Kirkland, A. I.; *et al.* Dynamics of Single Fe Atoms in Graphene Vacancies. *Nano Lett.* **2013**, *13*, 1468–1475.

(31) Kirkland, A. I.; D. A. Jefferson, D. G. Duff, P. P. Edwards, I. Gameson, B. F. G. Johnson, D. J. S. Structural Studies of Trigonal Lamellar Particles of Gold and Silver. *R. Soc.* **1993**, *440*, 589–609.

(32) Nix, F. C.; MacNair, D. The Thermal Expansion of Pure Metals: Copper, Gold, Aluminum, Nickel, and Iron. *Phys. Rev.* **1941**, *60*, 597–605.

(33) Boswell, F. W. C. Precise Determination of Lattice Constants by Electron Diffraction and Variations in the Lattice Constants of Very Small Crystallites. *Proc. Phys. Soc. Sect. A* **1951**, *64*, 465–476.

(34) Varns, R.; Strange, P. Stability of Gold Atoms and Dimers Adsorbed on Graphene. *J. Phys. Condens. Matter* **2008**, *20*, 225005.

(35) Wang, H.; Feng, Q.; Cheng, Y.; Yao, Y.; Wang, Q.; Li, K.; Schwingenschlögl, U.; Zhang, X. X.; Yang, W. Atomic Bonding between Metal and Graphene. *J. Phys. Chem. C* **2013**, *117*, 4632–4638.

Chapter 6

Atomically Flat Line Defects and Zigzag Edges in Monolayer MoS_2 by In-situ Thermal Annealing

This chapter introduces an approach for the formation of atomically flat line defects and zigzag edges by in-situ heating in TEM, as well as understanding their growing mechanisms. Heating in vacuum is able to evaporate almost all surface hydrocarbon contaminations, which dramatically reduces the hindrance for S vacancy migration, further resulting in the formation of ultra-long line defects. Pores are formed where the vacancy migration is limited, and smooth zigzag edges can be created during hole propagation into pristine area. New atomic structures of line defects and edges are also observed in this experiment, all of which are successfully predicted by DFT calculations.

6.1 Introduction

By the introduction of structural imperfections, two-dimensional materials are endowed with brand new and versatile properties including electronic, optical and chemical aspects.[1–3] Explorations have been made from 0D point defects[4,5] to 1D defects such as dislocations,[6] grain boundaries[7,8] and edges[9] in graphene[10,11] and other 2D materials.[12–14] MoS_2, a quasi-2D material with a direct band gap, has shown the potential in making electronic and optoelectronic devices.[15–17] One of the commonly observed linear defects in monolayer MoS_2 is extended line defect, which is composed of one or several lines of sulfur (S) vacancies.[18] This group of defects has been proved

to significantly alter the band structures by introducing new states within the original bad gap, leading to a local semiconducting-to-metallic transition with the width of the line defect increased.[19]

Edge termination in TMDs is another 1D defects which has also attracted interests of researchers due to the predicted metallic states that cross the bulk energy gap along MoS_2 or WS_2 zigzag edges.[20–24] These edge states can be magnetic,[22] induce 1D plasmonic excitations,[25] exhibit high catalytic activity,[26–29] and show increased photoluminescence emission and non-linear optical responses.[30,31] The influence of the MoS_2 edge structure is key to realizing the idealized properties of MoS_2 nanoribbons.[1,22,24,32]

One thing worthwhile mentioning is that these unique properties introduced by the line defects and edge terminations are all predicted in the circumstance where all of the defective structures are infinity in length and with perfect atomic flatness. In the environment of TEM, the formation mechanism of the line defect in monolayer MoS_2 is believed to be the creation, migration and aggregation of single S vacancies.[33] There is an energy barrier of about 2 eV for a S vacancy migrating to the adjacent site, and under the continuous irradiation of the energetic electrons in TEM, S vacancy migration is able to happen but in a rather slow speed.[33] Therefore they tend to migrate in short distances and form several line defects simultaneously in a local area. The growth ceases when a line defect bumps into the middle part of another adjacent line defect, and due to the locally high density of line defects with all three zigzag orientations, it has been observed that the length of the line defects usually no more than 3-4 nm.[18,19] Similar case also happens in edge formation, although theoretical studies for MoS_2 indicate an energetic preference for zigzag terminations, in real

situation the edges are always lack of atomic smoothness.[20,34–37] Therefore, approaches which can create long and atomically smooth line defects and edges are required to be invented.

Here an approach for fabricating line defects and edges with perfect atomic smoothness and length of several tens nanometers is introduced by in-situ heating in TEM. With the evaporation of hydrocarbon residues on the MoS_2 surface, the mobility of S vacancies is dramatically enhanced. Line defect and edge propagations at 800 °C have been tracked and the high-temperature structure of the defects has been studied with single-atom sensitivity.

6.2 Surface Condition, S Vacancy Mobility, and Line Defect Length

CVD grown MoS_2 has to undergo a polymer-based wet-transfer process during the preparation of a TEM sample which will leave a certain amount of hydrocarbon residue on the sample surface. These hydrocarbons are amorphous and are difficult to observe directly using AC-TEM. The unavoidable amorphous hydrocarbon thin films correspond to the uniform halo shown in the power spectrum (inset in Figure 6-1(a)). After Fourier filtering to mask the reflections due to MoS_2 the amorphous carbons on the surface can be directly observed (Figure 6-1(e)). Increasing the temperature under electron beam radiation (Figure 6-1(i)) induces crystallisation of the amorphous carbons, as shown in the FFT patterns in Figure 6-1(b,c), where the uniform halo of carbon becomes a sharp ring with a diameter of 0.21/nm, corresponding to the $\{10\bar{1}0\}$ crystal plane of graphene. The presence of the ring in the FFT patterns indicates a polycrystalline structure within the carbon film and with increasing temperature the ordered structures expand, as shown in the magnified images in Figure 6-1(j-m). In

order to eliminate the interference of the carbon film the electron beam was blanked until the temperature was stable at 800 °C, as in the temperature profile shown in Figure 6-2(a) . Under this condition the surface of MoS_2 did not show any form of carbon contamination, therefore when the FFT pattern of MoS_2 is manually removed, only vacuum background remains in the inverse FFT image shown in Figure 6-1(h).

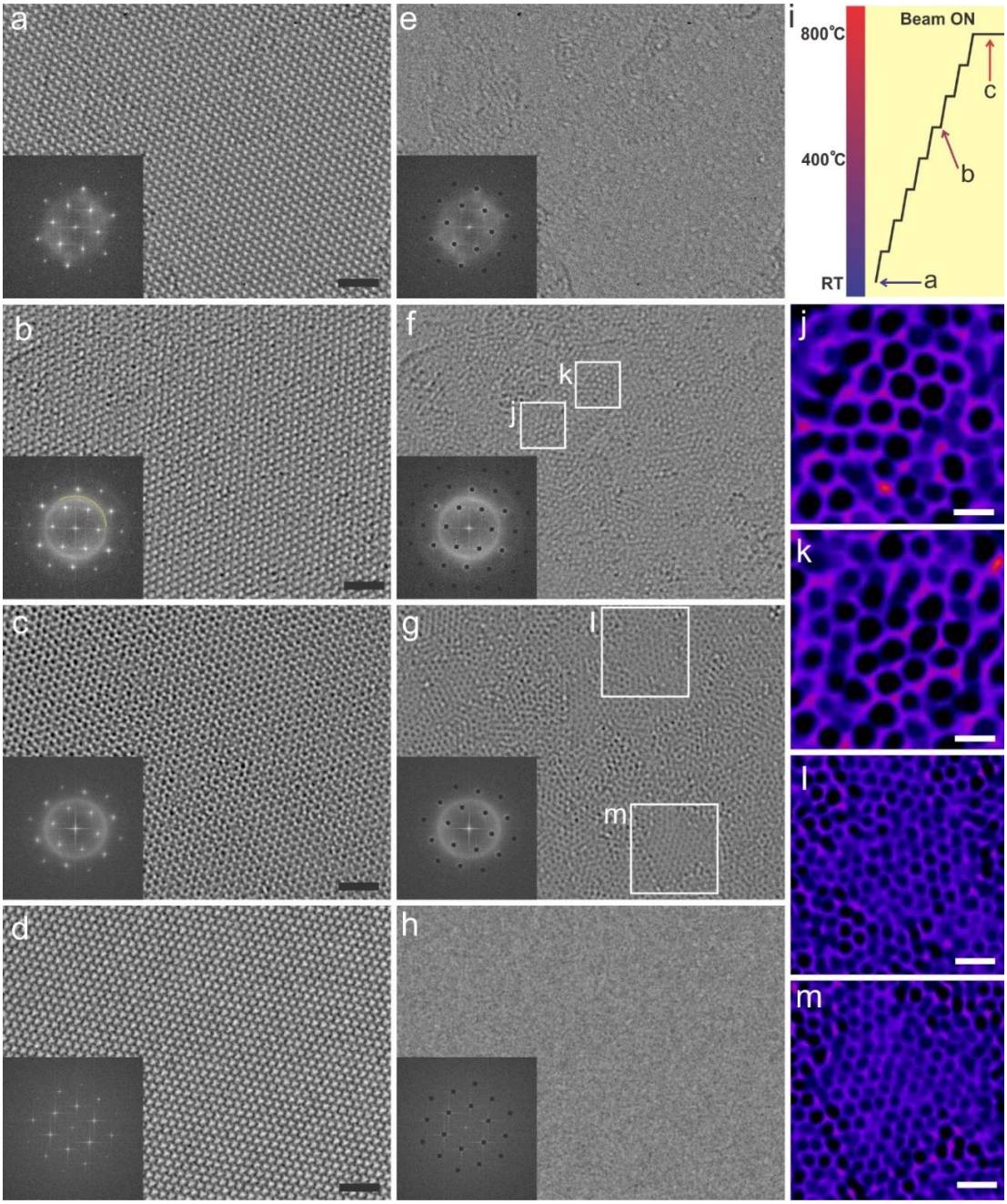

Figure 6-1 Estimation of the states of hydrocarbon contaminates at different conditions. AC-TEM images taking at (a) room temperature, (b) 500 °C, with electron beam irradiation

(electron dose ~ $10^5 e/nm^2/s$) during the increase of the temperature. (c) 800 °C, with electron beam irradiation during the increase of the temperature. (d) 800 °C, with the electron beam blocked until the temperature reached 800 °C. Insets in a-d show the power spectrum from the FFT. (e-h) Images corresponding to (a-d), but using a mask of the FFT power spectrum to remove the contributions from the MoS_2. Masks are shown in the insets in (e-h). (i) Temperature profile and imaging points for a-c). (j,k) Magnified images after smoothing and applying a false colour for the two boxes highlighted in (f) showing the local crystalline graphene-like areas. (l,m) Magnified images after smoothing and applying a false colour for the two boxes highlighted in (g) showing the larger local crystalline graphene-like areas. Scale bars in (a-d), 1 nm; (j-k), 0.2 nm; (l-m), 0.4 nm.

The cleanness of the MoS_2 surface strongly influences the morphology of line defects based on the observations. Figure 6-2 compares the line defects generated in two different surface conditions at the same temperature. Figure 6-2(b) shows the line defects created in the super-clean MoS_2 lattice after the opening the electron beam at 800 °C. HAADF images are very sensitive to the surface contaminates thus it can be easily seen that all the line defects shown in Figure 6-2(b) are in clean lattice area. Line defects only orient along zigzag directions, and three zigzag directions are present in monolayer MoS_2 (Figure 6-2(c)). Strong contrast is shown in Figure 6-2(d), where the line defects are formed with the presence of surface carbon film, same condition described in Figure 6-1(c). With the interference of carbon film on the top of MoS_2 surface, the line defects in this case are much shorter and higher density, similar with the counterparts created at room temperature.[19] By comparing the line defects morphology at same temperature but with different surface conditions, it can be concluded that the latter has greater impact on the migration of S vacancies. Line defects are the energetically favourable configuration for S vacancies agglomeration, and with high surface cleanness the S vacancies are able to migrate to a longer distance in a short period of time, therefore only a few of long line defects are created in this circumstance (Figure 6-2(e-g)). However, the measurement of the speed of the

migration is challenged due to the limited time resolution of the TEM. This phenomenon is similar to the grain finning mechanism in metallurgy, where high degree of super-cooling is used to obtain abundantly fine crystals while higher temperature is applied when large and few grains is the targeted morphology.

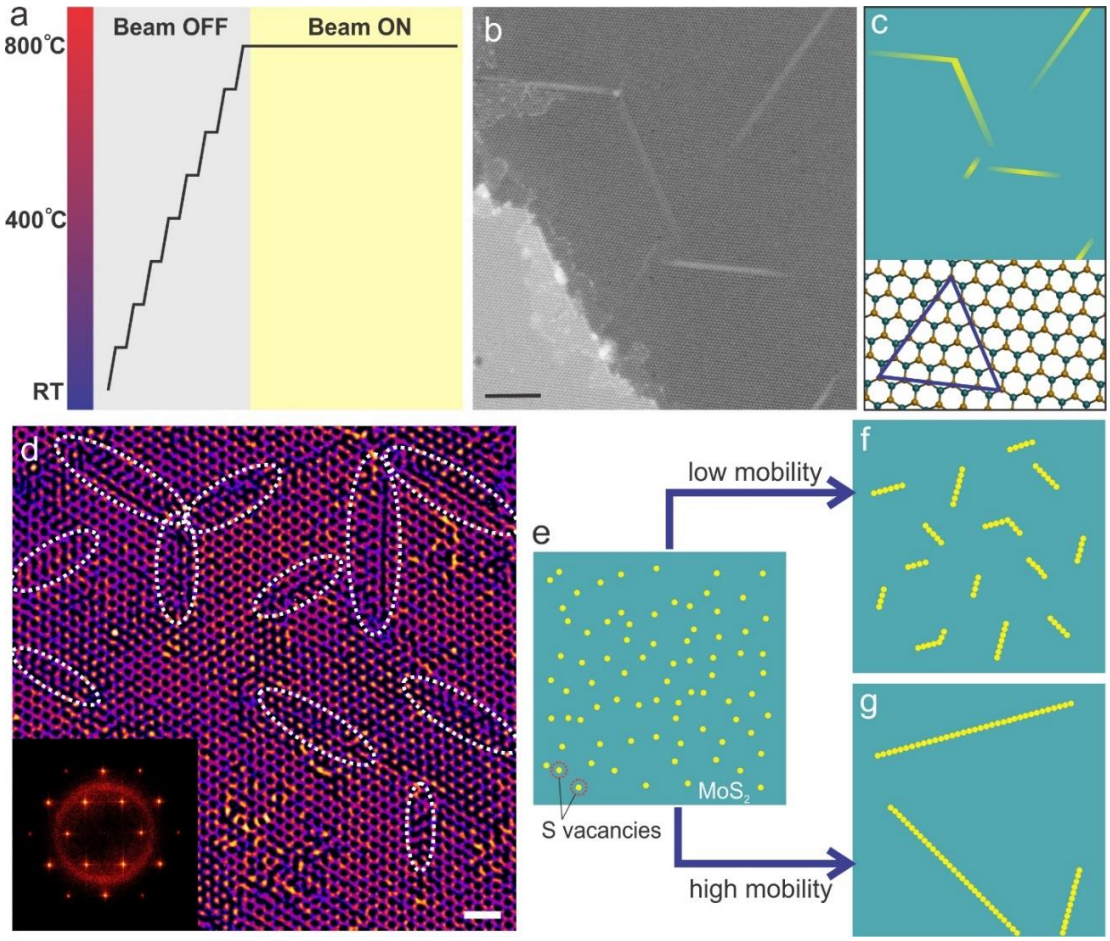

Figure 6-2 Line defects at different surface conditions. (a) Temperature profile and electron beam conditions for the production of long line defects. (b) A HAADF image of a few line defects created in the clean area after the treatment shown in (a). (c) Schematic illustration of (b) and atomic model of MoS_2 lattice showing the orientation of the crystal. Zigzag edges are highlighted by the blue triangle. (d) ACTEM image of the short line defects created at 800 °C but with crystalline carbon film on the surface indicated by the inset power spectrum. (e-g) Schematics of the formation of line defects with low and high S vacancy mobility. Scale bars in (b), 5 nm; (d), 1 nm.

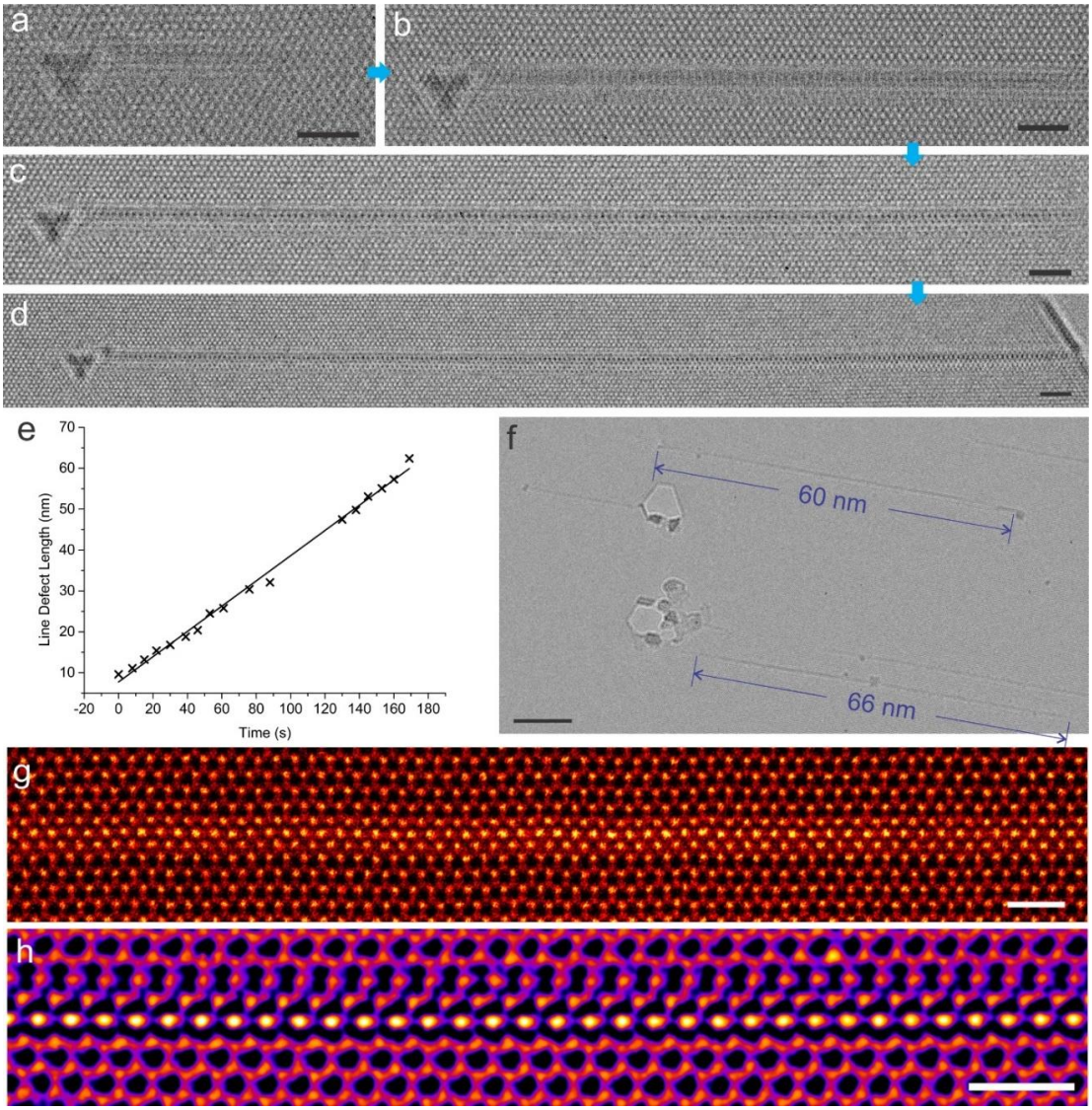

Figure 6-3 Propagation of line defects at elevated temperature and atomic flatness. (a-d) Four snapshots during the continuous growth of a line defect. (e) The line defect length vs. time under electron dose about $10^5 e/nm^2/s$ at 800 °C. (f) A low magnification TEM image of several long line defects. (g,h) High magnification HAADF and ACTEM images of a segment of line defects showing the atomic smoothness. Scale bars in (a-d), 2 nm; (f), 10 nm; (g,h), 1 nm.

At the accelerating voltage at 80 kV (electron dose about $10^5 e/nm^2/s$),[38] the propagation of a line defect from beginning to end is able to be tracked (Figure 6-3(a-d)), although isolated S vacancies are barely observed as it shuffles around during 1-2 seconds acquisition time. At the end the line defect bumps into an edge without which the line defect would grow further. The propagation speed of the line defect is rather

constant, 0.31 nm/s, referring to one lattice per second (Figure 6-3(e)). Statistically, about 35% line defects are capable to grow longer than 50 nm, two more examples are shown in Figure 6-3(f). The atomic smoothness of the line defects are detected at higher magnifications. Figure 6-3(g,h) exhibit the segments of two types of long line defects observed in STEM and TEM with perfect atomic flatness, without any kinks or other defects in the local area.

6.3 Atomic structures and Strain Field of Line defects

Two types of typical line defects (Figure 6-4(a,b)) have been observed, both of which are composed of two adjacent S vacancy lines in staggered configuration, which has been confirmed to be the most energetically stable structure.[33] The two structures are quite similar, with slightly different degree of out-of-plane distortion. The extra bright atom column in Figure 6-4(b) is the superposition of one Mo and S atom in projection, given that the HAADF image is Z-contrast. Figure 6-3(h) is the AC-TEM image for the second type of line defect, and the ultra-bright line is also obvious. Both of the structures are successfully predicted by the DFT calculations with different unit cell, corresponding to the unit cells highlighted in Figure C2(a, b). The former unit cell is sufficient to enable curvature along the perpendicular direction to the line defect length (Figure 6-4(c,e)), while the latter possesses a terrace-like configuration due to the rigidity of the MoS_2 lattice with relatively small size (Figure 6-4(d,f)). The experimental observations and simulated images of the theoretical models are well matched (Figure C1). The more severe out-of-plane distortion of the second model directly leads to the overlapping of Mo and S atoms (red box in Figure 6-4(f)). The two structures share similar degree of contraction in the projection, approximately 20% along the width of the line defect measured in the HAADF image. A simplified process

for the formation of the line defects are shown in Figure 6-4(g-j), with removed S atoms as well as atoms reallocations highlighted. The real case is far more complicated than this process, as the S vacancy lines are formed by the aggregation of S vacancies instead of direct elimination of S atoms arrays.

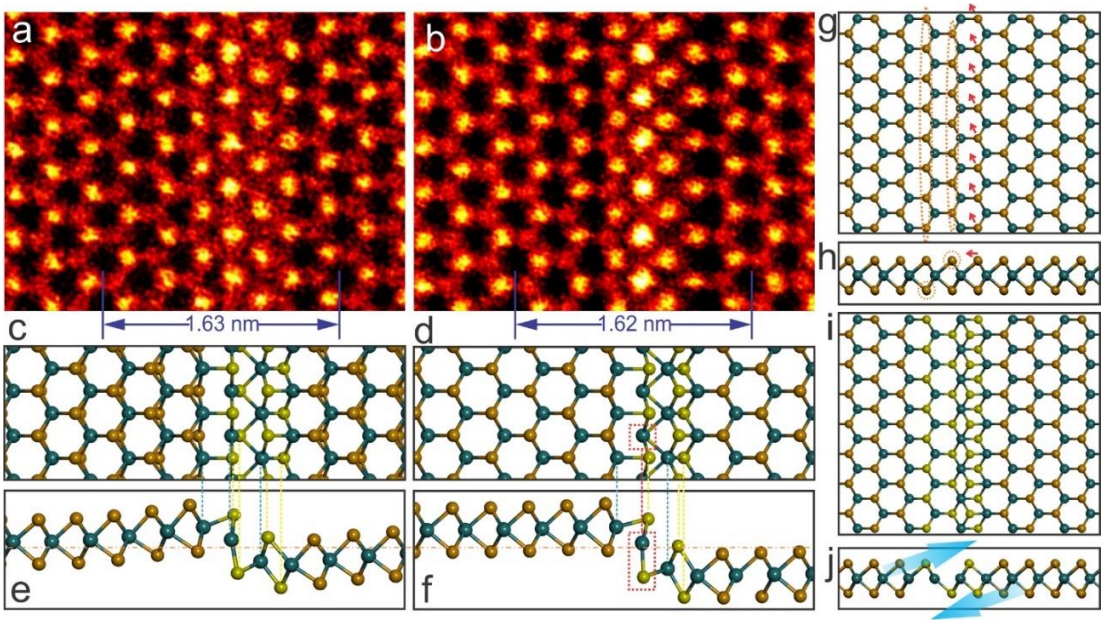

Figure 6-4 Atomic structures of two types of line defects at elevated temperature. (a,b) HAADF images of two types of line defects observed. (c,d) DFT calculated atomic models for the two line defects, with their side views in (e,f). The red box highlighted the atom column where the Mo atoms and S atom are superposition along projection. The orange dash line at the middle of (e,f) indicates the original Mo atoms plane. (g-j) A simplified procedure on the formation of the line defects. The orange ellipses: removed S atoms; red arrows: the migration direction of the S atoms; blue arrows: out-of-plane distortion.

When several line defects are presented in a large pristine MoS_2 area, in most cases they are all parallel to each other (examples are given in Figure C2(c-e)). In suspended pristine MoS_2 lattice, there always be intrinsic ripples due to the thinness of the material as reported previously.[39,40] It has been observed that the ripples in monolayer MoS_2 exhibit a quasi-periodical structure with all ripples being almost parallel, and the height varies from several angstroms to tens nanometers.[39] Compressional strain has been reported to significantly lower the activation energy for the diffusion of

monovacancies in graphene,[41] and also apply to bulk materials like metals.[42] Therefore it is plausible to hypothesize that the compressional strain field induced by the ripples is able to attract S vacancies to agglomerate into line defects along the perpendicular direction of the ripple wavelength, as indicated in the arrows in Figure C2(f), and the height of the ripples determines the type of line defect, i.e., mild ripples result in the first type of line defect while the second type is formed at bigger ripples with more out-of-plane distortion. However, the rippling nature of MoS_2 is hard to be confirmed in TEM images as the amplitude of the ripples is not big enough to induce detectable compressional strain that can be measured in GPA.

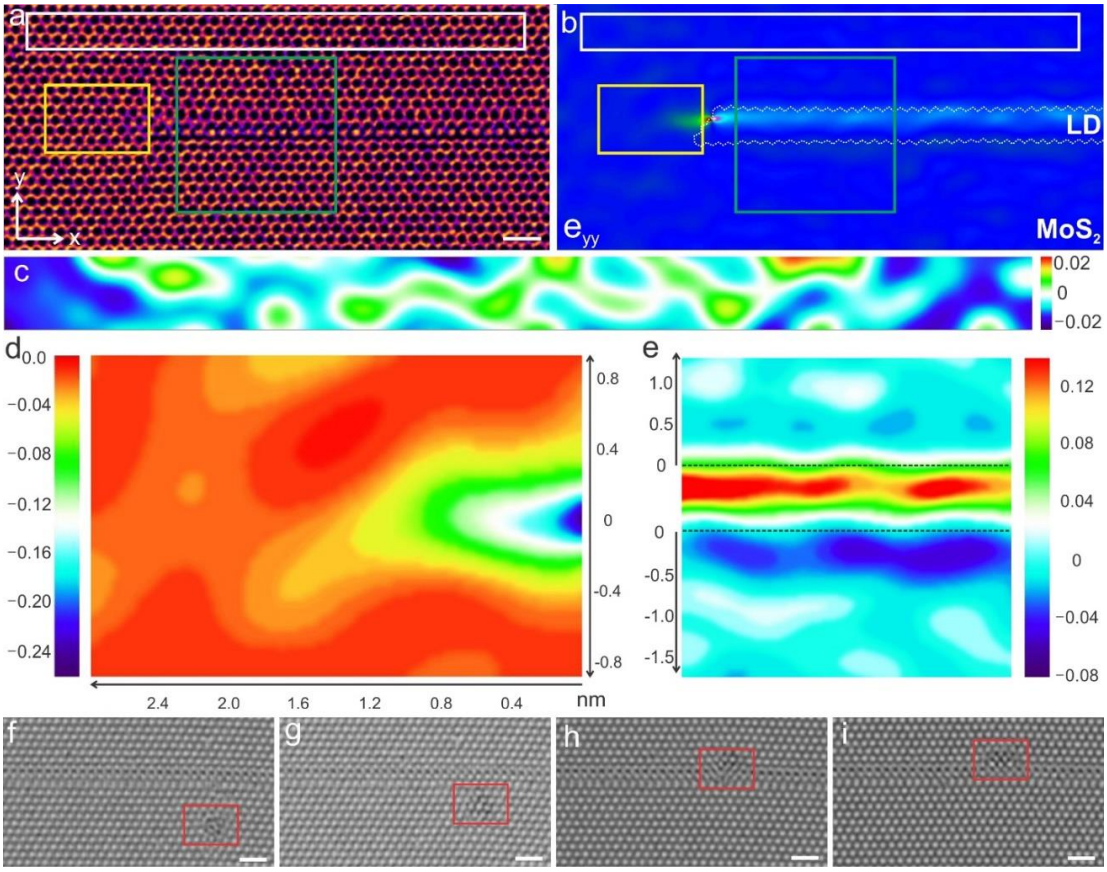

Figure 6-5 Surrounded strain field of type 2 line defect. (a) AC-TEM image of a line defect (type 2). (b) Corresponding normal strain field along y direction, with the contour of the line defect indicated by the while zigzag lines. (c) Background strain field detected in the white box in (a, b) showing the background noise level within ±2%. (d) Strain field from the tip of the line defect (yellow box in (a,b)) with better contrast. (e) Strain field at within the green box

in (a,b) indicating the asymmetrical strain field along the two sides. (f-i) Consecutive TEM images of the migration of a Mo cluster which finally trapped by the compressional side of the line defect. Scale bars in (a, f-i), 1 nm.

Unlike the broad line defects with more than three S vacancy lines created at room temperature, the line defects created at elevated temperature are always slim, composed of two S vacancy lines, indicating that the S vacancies prefer to contribute to the line defect tip rather than side. This behaviour may be explained by the strain distributions. Figure 6-5(a) shows a line defect (type 2) with its normal strain field in y direction (width direction) demonstrated in Figure 6-5(b) (ε_{yy}). $\{10\bar{1}0\}$ spots in FFT were selected with the aperture size of 0.7 nm. The strain inside the line defect has been discussed elsewhere so will not be included here.[19] A compressional strain field is detected beyond the tip of the line defect (Figure 6-5(d)), with the affected area of about 3×4 hexagonal lattice. Within this area, the compressional strain decays from 25% to 4% (background fluctuation is about $\pm 2\%$, as shown in Figure 6-5(c), which is most likely induced by the out-of-plane distortion because of the terrace structure. The obvious compressional strain field at the line defect tip can act as a sink for S vacancies.[41] Although direct observation is absent due to the fast migration of S vacancies in comparison to the imaging acquisition time, one can easily imagine that a S vacancy created far away from the line defect tip will firstly walk randomly until it is biased by the compressional strain field and finally contribute to the line defect growth. The strain field at the side area is asymmetrical with one side nearly no strain and the other side a compressional strain field ending at the second row of the hexagonal rings from the line defect boundary (Figure 6-5(e)). The compressional strain field is in the range of 4-6%, most likely to be in-plane bond length variation, much lower than the tip site, which explains the strong tendency for S vacancies to migrate to the defect tip when it is highly mobile. However, this mild compressional

strain at the side of the line defect can serve as a trap for freely migrated Mo clusters, as shown in Figure 6-5(f-i). The small Mo cluster with a few Mo atoms eventually settles at the compressional side of the line defect. To confirm this observation is not accidental, one more example is shown in Figure C3.

6.4 Line defect as Mo Cluster Transport Channel

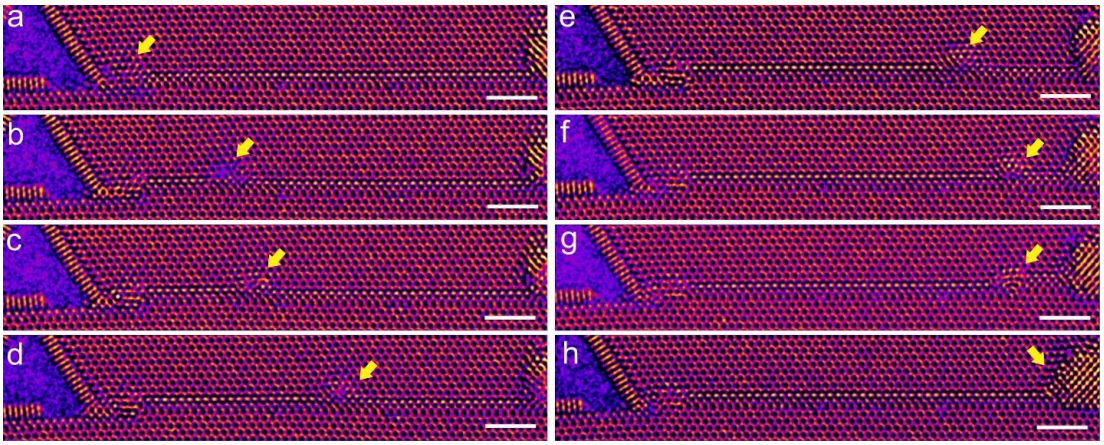

Figure 6-6 (a-h) Consecutive TEM images showing the migration of a Mo cluster (indicated by blue arrows) from a hole to the other end of the line defect. Scale bars in (a-h), 2 nm.

One interesting behaviour of the line defect is that it is able to serve as a transport channel for Mo atoms. When a line defect is connected to a hole in MoS_2 lattice, the redundant Mo atoms generated from the hole formation uses the line defect as a 'motorway' to transport itself to the other end of the line defect, where gradually a Mo cluster is accumulated on the MoS_2 surface. This process is clearly shown in the consecutive images of Figure 6-6. As expected, the Mo cluster is always at the side of the line defect with compressional strain. The cluster eventually joins the bulk Mo crystal with cubic lattice structure at the other end. Similar phenomenon also shows in Figure 6-3(f), where small clusters are observed at the end of the line defects. This phenomenon explains that in some cases, freely migrating Mo clusters on the MoS_2

surface are found, which probably results from the detachment of the Mo cluster at the line defect ends.

6.5 Formation of Holes and Edge Terminations

Within the clean area the accumulation form of S vacancies are always line defects. Occasionally, there is some areas where the carbon contaminations are not completely removed, as shown in Figure 6-7(a-c) where the contaminated areas are highlighted in yellow contour. If S vacancies are generated in these areas or trapped at the boundaries of the carbon film, no line defect is able to be created. Instead, S vacancies agglomerate into pores in these area as the S vacancy migration is extremely limited. All the pores are observed in the contaminated area without exception. This means pores formation are favoured when the mobility of S vacancies is lowered by any factor such as low temperature, surface contaminations, or encapsulation. This explains the fact that when graphene was used to encapsulate MoS_2 for radiation protection, the radiation damage after a longer period of time exposure becomes pores instead of line defects observed within free-standing MoS_2.[43] Therefore it can be concluded that the S vacancy agglomeration form is dominated by the S vacancy mobility. With the increase of the mobility of S vacancies, the agglomeration form transfers from pores to short line defects, eventually to long line defects. Therefore it is essential to ensure the high surface cleanness for the formation of long line defects. The pores generated in the contaminated areas, however, provide the opportunity to create edges in MoS_2. As shown in Figure 6-7(d-f), when a pore propagates into a pristine area under the continuous electron beam irradiation, preferred orientations of the edge terminations start to show, associated with the hexagonal symmetry of monolayer MoS_2; $(10\bar{1}0)$

Mo and ($\bar{1}$010) S, as indicated with blue and yellow lines in Figure 6-7(d-g). Figure C4 shows the propagation of a hole within the carbon film covered area, where the edge contours are irregular, with no atomically smooth edges. Mo atoms tend to agglomerate into several small clusters attached to edge sites.

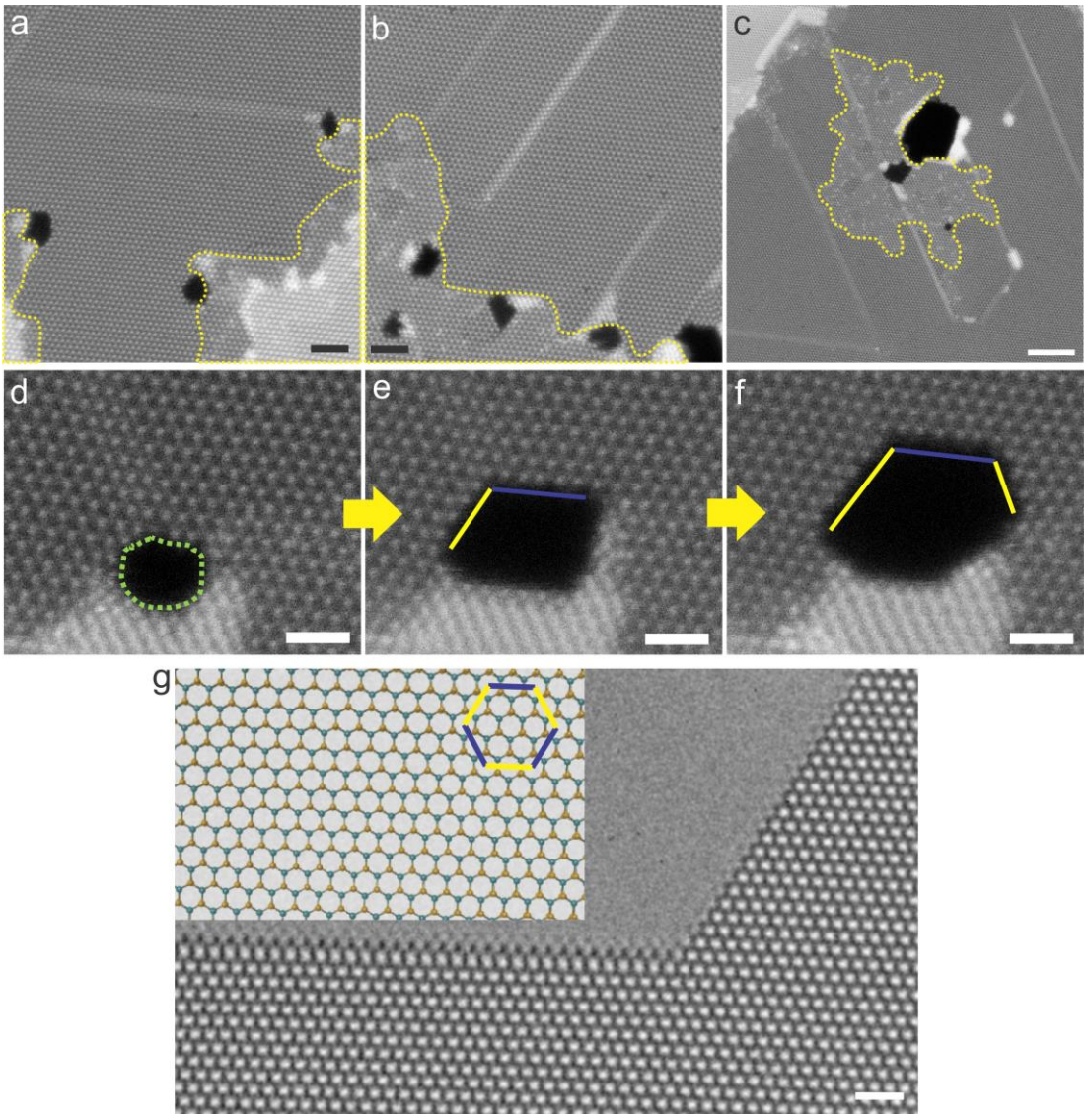

Figure 6-7 Formation of pores and edge terminations. (a-c) HAADF images of MoS_2 areas with carbon contaminations. Line defects are all in clean areas while pores are all created in the contaminated areas. (d-f) Three consecutive images of the propagation of a pore from contaminated area to clean area. Yellow and dark blue lines are indicative of S and Mo edge orientations. (g) AC-TEM image of a joint of two types of zigzag edges, with inset an atomic model showing the lattice orientation and the zigzag directions. Scale bars in (a,b), 2 nm; (c), 5 nm; (d-g), 1 nm.

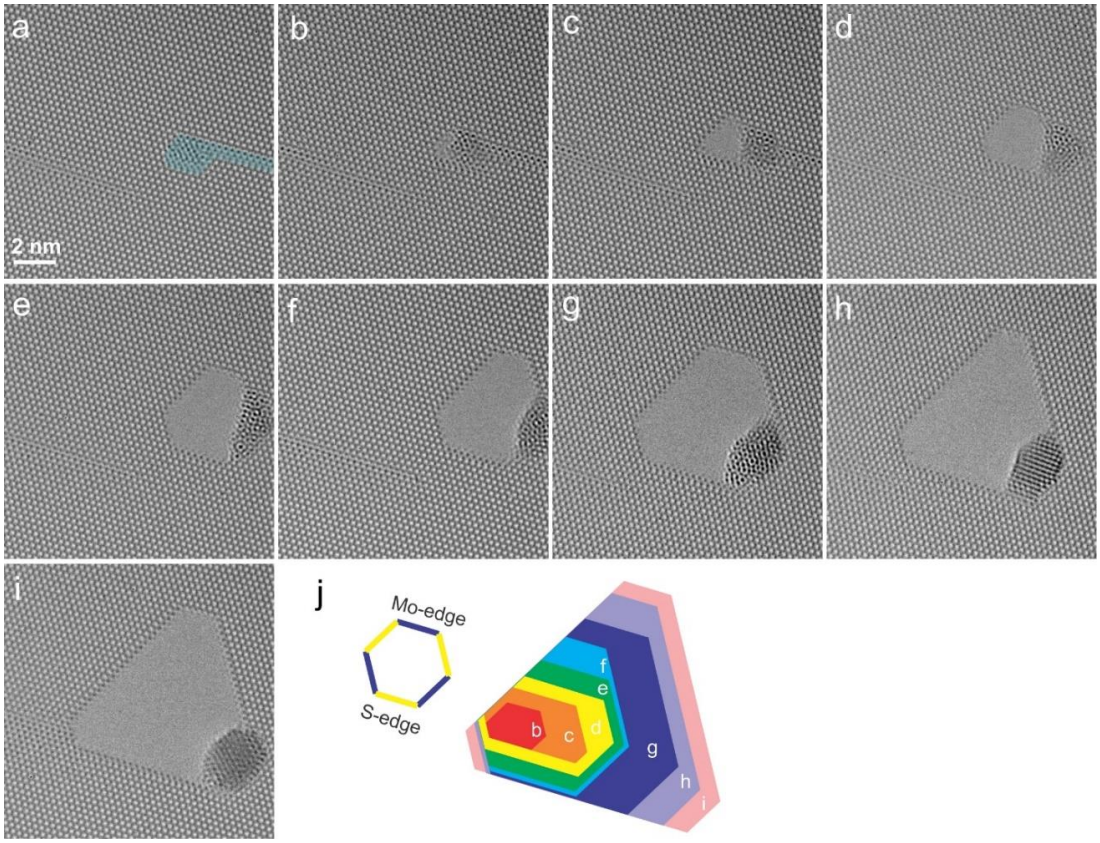

Figure 6-8 A series of TEM images showing the creation (a) and propagation of a MoS_2 hole (b-i). (j) Schematic of the overlapping contours of the pores depicting the evolution of the pore.

The formation and propagation of a hole in MoS_2 with a clean surface is radically different, as shown in Figure 6-8. A small pore is first opened at the tip of a line defect highlighted in pale blue in Figure 6-8(a). All edges generated during the hole propagation lie along zigzag directions and are atomically flat. It is observed that the shapes of the pore during growth are either hexagons or truncated triangles with longer S-edges and shorter Mo-edges with the included angle between two adjacent edges always 120°, i.e., two Mo edges (S edges) do not connect directly. By overlapping frames from the image series the propagation rate along each edge is shown vividly (Figure 6-8(j)). Without the hindrance factor caused by surface carbon film, redundant Mo atoms generated from the hole propagation aggregate into a single Mo cluster at

one corner of the hole with a certain degree of crystallinity, which is induced by reducing the total surface energy of system.

With the continuous propagation of the holes under bean irradiation, the edges of holes are able to be extended into long and atomically smooth edges. Atomically flat edges along both zigzag directions (Figure 6-9(a-d)) have average and maximum lengths of ~12 nm and 25 nm respectively (Figure 6-9(e)) and different atomic terminations. At elevated temperature (800 °C) S vacancies possess high mobility during imaging, but can still be occasionally detected (Figure 6-9(a)).

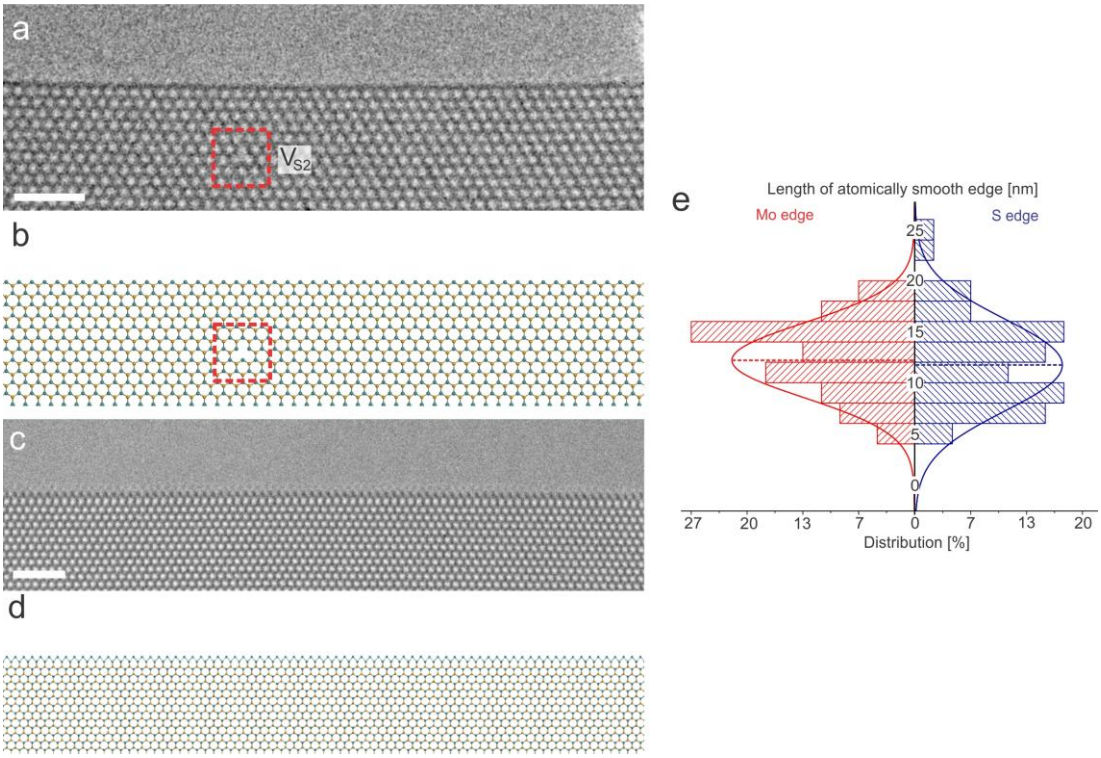

Figure 6-9 AC-TEM images recorded at 800ºC showing atomically flat edges in monolayer MoS_2. (a) AC-TEM image of a Mo edge, with the presence of a disulphur vacancy (V_{S2}) highlighted by a red dashed box. (b) Corresponding atomic model for the Mo edge in a), cyan balls represent Mo and gold balls 2S. (c) AC-TEM image of a S-edge. (d) Atomic model corresponding to (c). (e) Length distributions of atomically flat Mo- and S-edges. Scale bars in (b,d), 2 nm.

6.6 Atomic Structures and Etching Dynamics of Zigzag Terminations

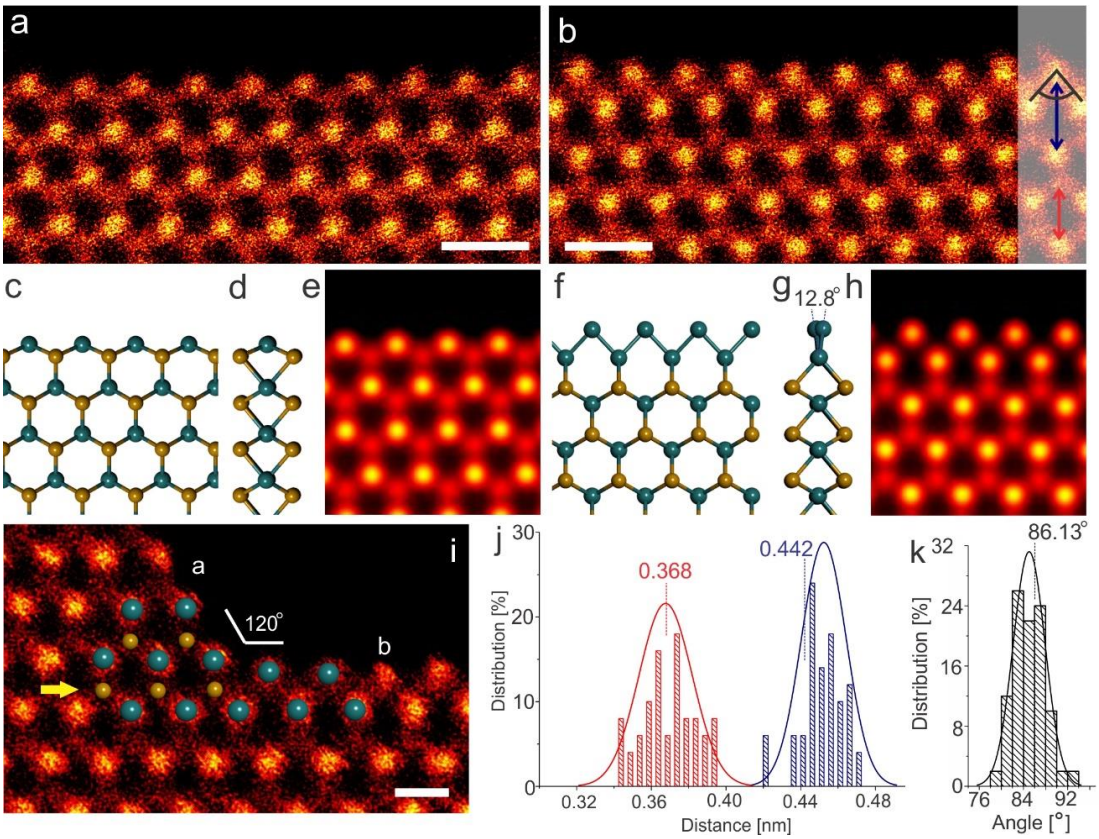

Figure 6-10 (a,b) ADF images of a Mo edge and Mo-replaced S edge. (c, d) Top and side view of the atomic model of a Mo edge calculated using DFT. (e) Image simulation of the model in (c). (f,g) Top and side view of the DFT model of a Mo-replaced S edge, with the black box showing the out-of-plane distortion of the outmost Mo atoms (Red dashed line corresponds to the centre of the MoS_2 lattice plane). (h) Image simulation of the model in (f). (i) False coloured ADF image of a joint between a Mo-edge and S-edge; letters a and b correspond to the same edge structures shown in (a) and (b). Cyan and gold balls represent Mo and 2S sites respectively. The yellow arrow indicates a line of 2S atoms which are absent at the beginning of the Mo-replaced S edge. (j) Diameter distributions based on experimental data of the 6-atom ring in projection at the Mo-replaced S edge compared to the normal 6-atom ring in MoS_2 lattice, which are 0.452±0.012 nm and 0.368±0.014 nm respectively. DFT calculated values are 0.442 nm, 0.368 nm respectively. (k) Distribution of Mo-Mo-Mo angles based on experimental data: 85±3° (86.1° theoretically). Scale bars in (a-b), 0.5 nm; (i), 0.3 nm.

ADF-STEM was used to determine the position of Mo and S atoms in reconstructed edges (Figure 6-10). The structure of the Mo edge ($(10\bar{1}0)$ Mo) shown in Figure 6-10(a) was predicted by density functional theory (DFT) and previously observed by

STM and HAADF-STEM.[12,20,34,36,44] The edges along the $(\bar{1}010)$ S direction (Figure 6-10(b)) have Mo atoms substituting at 2S positions, leading to Mo termination for all edges in the sample. The intersection of both zigzag edge directions highlights the different Mo terminations (Figure 6-10(i)). The edge reconstruction induces a 22% elongation (20% theoretically) in comparison to the bulk (Figure 6-10(j,k)). DFT calculations indicate that the outermost Mo atoms have an energetically favourable (0.056eV) out-of-plane distortion of 12.8° (Figure 6-10(g)). The Mo-replaced S edge has an intermediate state before this Mo terminated reconstruction occurs, and details are explained in Figure C5 and related content.

The atomically flat edges are formed by a layer-by-layer etching process (Figure 6-11) starting from a single point, followed by gradually atom-by-atom removal towards both directions until the entire atomic row is removed before repeating this process (Figure 6-11(g)) in similar fashion edge growth in graphene.[45] Some transient contrast arising from Mo migration along the edge during image acquisition is also observed, highlighted in the yellow boxes in Figure 6-11(d,e). Similar layer-by-layer process is also observed along Mo-replaced S edge (Figure C6). The atomically flat zigzag edges are maintained after cooling back to room temperature (Figure C7) and can only be disrupted by extensive electron beam irradiation. However, carbon contaminants rapidly absorb back onto the MoS_2 surface during cooling and hence efforts were taken to minimise exposure to electron beam during cooling. No obvious deterioration are found in the profile of the edges on cooling, demonstrating the stability of the smooth edges at low temperatures.

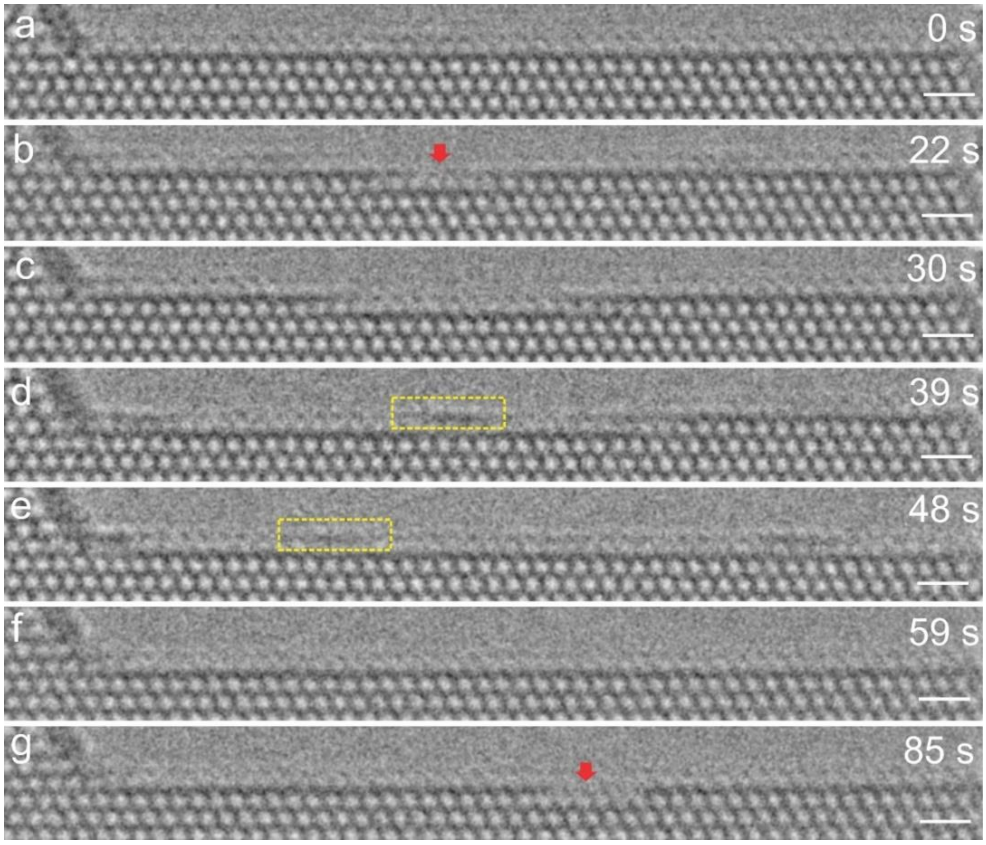

Figure 6-11 AC-TEM image sequence showing the etching of the outermost layer of a Mo edge. Red arrows indicate the position of the opened breach, and the yellow dashed boxes highlight atoms migrating along the edge. Scale bars in (a-g), 1 nm.

This atom-by-atom etching from the edge enables fabrication of nanoribbons in MoS_2 with atomically flat edges with different structures on opposite sides (Figure 6-12(a)). Etching and atomic migration at the edge of the ribbon occur simultaneously, causing broadening (Figure 6-12(a-c)) and narrowing (Figure 6-12(d-f)) processes in different local regions. DFT calculations suggest novel electronic and magnetic properties for the MoS_2 nanoribbons, and the model used to conduct the calculation is shown in Figure 6-12(g). MoS_2 nanoribbon shows a metallic nature rather than semiconductor, as the densities of state for both spin-up and spin-down mode are not zero, which mainly contributed by Mo atoms (blue lines in Figure 6-12(h)).

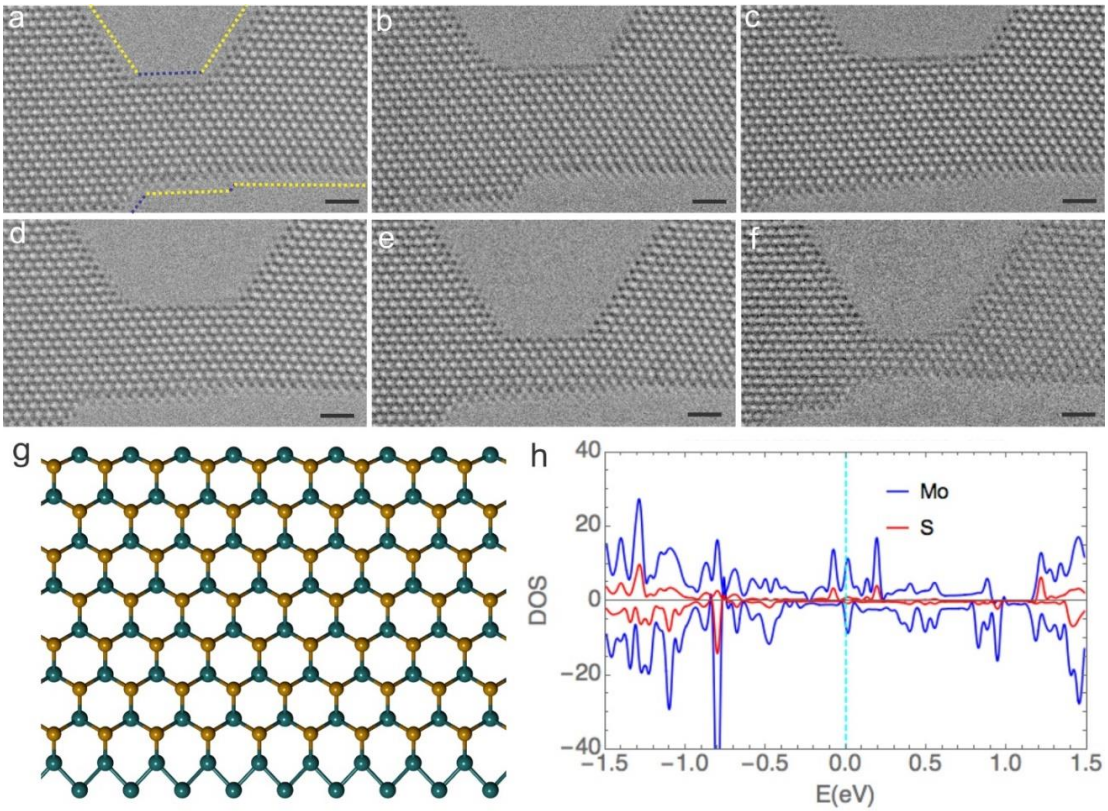

Figure 6-12 Atomic structure of a MoS_2 nanoribbon and DFT calculated properties. (a-f) AC-TEM image sequence of a MoS_2 nanoribbon showing initial widening followed by narrowing. Time duration, 15 s. (h) DOS of the MoS_2 nanoribbon (g) with the upper region (positive y axis) showing spin-up and the lower region (negative y axis) showing spin-down. Scale bars in (a-f), 1nm.

6.7 Conclusion

This work has focused on the creation of atomically smooth line defects and edges in monolayer MoS_2 as well as their growth mechanisms. By in-situ heating to 800 °C, line defects with perfect atomic flatness are able to be created with the maximum length of nearly 70 nm. This is attributed to the high S vacancy mobility on the clean MoS_2 surface and elevated temperature. Two types of typical line defect structures have been observed, both with two absent S lines but slightly different out-of-plane distortion. The compressional strain fields at the tip and side of line defects are able to

trap S vacancies and mobile Mo cluster on the surface. Line defects have also been observed to act as a transport channel for Mo atoms on the surface. Pores are opened at the contaminated areas with carbon film encapsulation, and gradually propagate into pristine MoS_2 area with atomically flat zigzag edges. Two distinct atomic configurations have been observed for both Mo edge and S edge, both are terminated by Mo atoms. The layer-by-layer etching process of both types of edges have also been explored. Unique electronic properties emerges in MoS_2 nanoribbon with the edge structures. These results may provide guidance for the defect engineering in MoS_2 and other members in TMDs.

6.8 References

(1) Han, Y.; Zhou, J.; Dong, J. Electronic and Magnetic Properties of MoS_2 Nanoribbons with Sulfur Line Vacancy Defects. *Appl. Surf. Sci.* **2015**, *346*, 470–476.

(2) Faccio, R.; Mombrú, A. W. Magnetism in Multivacancy Graphene Systems. *J. Phys. Condens. Matter* **2012**, *24*, 375304.

(3) Topsakal, M.; Aktürk, E.; Sevinçli, H.; Ciraci, S. First-Principles Approach to Monitoring the Band Gap and Magnetic State of a Graphene Nanoribbon via Its Vacancies. *Phys. Rev. B* **2008**, *78*, 235435.

(4) Komsa, H.-P.; Kotakoski, J.; Kurasch, S.; Lehtinen, O.; Kaiser, U.; Krasheninnikov, A. V. Two-Dimensional Transition Metal Dichalcogenides under Electron Irradiation: Defect Production and Doping. *Phys. Rev. Lett.* **2012**, *109*, 35503.

(5) Komsa, H.; Teng, P.; Yeh, C.; Huang, F.; Lin, Y.; Suenaga, K. Three-Fold Rotational Defects in Two-Dimensional Transition Metal Dichalcogenides. *Nat. Commun.* **2015**, *6*, 6736.

(6) Azizi, A.; Zou, X.; Ercius, P.; Zhang, Z.; Elías, A. L.; Perea-López, N.; Stone, G.; Terrones, M.; Yakobson, B. I.; Alem, N. Dislocation Motion and Grain Boundary Migration in Two-Dimensional Tungsten Disulphide. *Nat. Commun.* **2014**, *5*, 4876.

(7) Barja, S.; Wickenburg, S.; Liu, Z.; Zhang, Y.; Ryu, H.; Ugeda, M. M.; Hussain, Z.; Shen, Z.-X.; Mo, S.; Wong, E.; *et al.* Charge Density Wave Order in 1D Mirror Twin Boundaries of Single-Layer $MoSe_2$. *Nat. Phys.* **2016**, *12*, 751–756.

(8) van der Zande, A. M.; Huang, P. Y.; Chenet, D. A; Berkelbach, T. C.; You, Y.; Lee, G. H.; Heinz, T. F.; Reichman, D. R.; Muller, D. A; Hone, J. C. Grains and Grain Boundaries in Highly Crystalline Monolayer Molybdenum Disulphide. *Nat. Mater.* **2013**, *12*, 554–561.

(9) Liu, Z.; Suenaga, K.; Wang, Z.; Shi, Z.; Okunishi, E.; Iijima, S. Identification of Active Atomic Defects in a Monolayered Tungsten Disulphide Nanoribbon. *Nat. Commun.* **2011**, *2*, 213.

(10) Lahiri, J.; Lin, Y.; Bozkurt, P.; Oleynik, I. I.; Batzill, M. An Extended Defect in Graphene as a Metallic Wire. *Nat. Nanotechnol.* **2010**, *5*, 326–329.

(11) Botello-Mendez, A. R.; Declerck, X.; Terrones, M.; Terrones, H.; Charlier, J.-C. One-Dimensional Extended Lines of Divacancy Defects in Graphene. *Nanoscale* **2011**, *3*, 2868–2872.

(12) Zhou, W.; Zou, X.; Najmaei, S.; Liu, Z.; Shi, Y.; Kong, J.; Lou, J.; Ajayan, P. M.; Yakobson, B. I.; Idrobo, J. C. Intrinsic Structural Defects in Monolayer Molybdenum Disulfide. *Nano Lett.* **2013**, *13*, 2615–2622.

(13) Liu, Y.; Zou, X.; Yakobson, B. I. Dislocations and Grain Boundaries in Two-Dimensional Boron Nitride. *ACS Nano* **2012**, *6*, 7053–7058.

(14) Enyashin, A. N.; Bar-Sadan, M.; Houben, L.; Seifert, G. Line Defects in Molybdenum Disulfide Layers. *Phys. Chem. C.* **2013**, *117*, 10842–10848.

(15) Radisavljevic, B.; Radenovic, A; Brivio, J.; Giacometti, V.; Kis, A. Single-Layer MoS_2 Transistors. *Nat. Nanotechnol.* **2011**, *6*, 147–150.

(16) Nourbakhsh, A.; Zubair, A.; Sajjad, R. N.; Tavakkoli K. G., A.; Chen, W.; Fang, S.; Ling, X.; Kong, J.; Dresselhaus, M. S.; Kaxiras, E.; *et al.* MoS_2 Field-Effect Transistor with Sub-10-Nm Channel Length. *Nano Lett.* **2016**, *16*, 7798–7806.

(17) Liu, Y.; Guo, J.; Wu, Y. C.; Zhu, E.; Weiss, N. O.; He, Q.; Wu, H.; Cheng, H.-C.; Xu, Y.; Shakir, I.; *et al.* Pushing the Performance Limit of Sub-100 Nm Molybdenum Disulfide Transistors. *Nano Lett.* **2016**, *16*, 6337–6432.

(18) Ryu, G. H.; Lee, J.; Kim, N. Y.; Lee, Y.; Kim, Y.; Kim, M. J.; Lee, C.; Lee, Z. Line-Defect Mediated Formation of Hole and Mo Clusters in Monolayer Molybdenum Disulfide. *2D Mater.* **2016**, *3*, 14002.

(19) Wang, S.; Lee, G. D.; Lee, S.; Yoon, E.; Warner, J. H. Detailed Atomic Reconstruction of Extended Line Defects in Monolayer MoS_2. *ACS Nano* **2016**, *10*, 5419–5430.

(20) Bollinger, M.; Jacobsen, K.; Nørskov, J. Atomic and Electronic Structure of MoS_2 Nanoparticles. *Phys. Rev. B* **2003**, *67*, 85410.

(21) Gibertini, M.; Marzari, N. Emergence of One-Dimensional Wires of Free Carriers in Transition-Metal-Dichalcogenide Nanostructures. *Nano Lett.* **2015**, *15*, 6229–6238.

(22) Li, Y.; Zhou, Z.; Zhang, S.; Chen, Z. MoS_2 Nanoribbons: High Stability and Unusual Electronic and Magnetic Properties. *J. Am. Chem. Soc.* **2008**, *130*, 16739–16744.

(23) Bollinger, M. V.; Lauritsen, J. V.; Jacobsen, K. W.; Nørskov, J. K.; Helveg, S.; Besenbacher, F. One-Dimensional Metallic Edge States in MoS_2. *Phys. Rev. Lett.* **2001**, *87*, 196803.

(24) Xiao, S. L.; Yu, W. Z.; Gao, S. P. Edge Preference and Band Gap Characters of MoS_2 and WS_2 Nanoribbons. *Surf. Sci.* **2016**, *653*, 107–112.

(25) Andersen, K.; Jacobsen, K. W.; Thygesen, K. S. Plasmons on the Edge of MoS_2 Nanostructures. *Phys. Rev. B - Condens. Matter Mater. Phys.* **2014**, *90*, 161410.

(26) Chianelli, R. R.; Siadati, M. H.; De la Rosa, M. P.; Berhault, G.; Wilcoxon, J. P.; Bearden, R.; Abrams, B. L. Catalytic Properties of Single Layers of Transition Metal Sulfide Catalytic Materials. *Catal. Rev. Eng.* **2006**, *48*, 1–41.

(27) Search, H.; Journals, C.; Contact, A.; Iopscience, M.; Address, I. P. Chemistry of One-Dimensional Metallic Edge States in MoS_2 Nanoclusters. *Nanotechnology* **2003**, *14*, 385–389.

(28) Jaramillo, T. F.; Jorgensen, K. P.; Bonde, J.; Nielsen, J. H.; Horch, S.; Chorkendorff, I. Identification of Active Edge Sites for Electrochemical H_2 Evolution from MoS_2 Nanocatalysts. *Science.* **2007**, *317*, 100–102.

(29) Lauritsen, J. V.; Bollinger, M. V.; Lægsgaard, E.; Jacobsen, K. W.; Nørskov, J. K.; Clausen, B. S.; Topsøe, H.; Besenbacher, F. Atomic-Scale Insight into Structure and Morphology Changes of MoS_2 Nanoclusters in Hydrotreating Catalysts. *J. Catal.* **2004**,

221, 510–522.

(30) Gutiérrez, H. R.; Perea-López, N.; Elías, A. L.; Berkdemir, A.; Wang, B.; Lv, R.; López-Urías, F.; Crespi, V. H.; Terrones, H.; Terrones, M. Extraordinary Room-Temperature Photoluminescence in Triangular WS_2 Monolayers. *Nano Lett.* **2013**, *13*, 3447–3454.

(31) Yin, X.; Ye, Z.; Chenet, D. a; Ye, Y.; O'Brien, K.; Hone, J. C.; Zhang, X. Edge Nonlinear Optics on a MoS_2 Atomic Monolayer. *Science* **2014**, *344*, 488–490.

(32) Fan, D. D.; Liu, H. J.; Cheng, L.; Jiang, P. H.; Shi, J.; Tang, X. F. MoS_2 Nanoribbons as Promising Thermoelectric Materials. *Appl. Phys. Lett.* **2014**, *105*, 133113.

(33) Komsa, H. P.; Kurasch, S.; Lehtinen, O.; Kaiser, U.; Krasheninnikov, A. V. From Point to Extended Defects in Two-Dimensional MoS_2: Evolution of Atomic Structure under Electron Irradiation. *Phys. Rev. B - Condens. Matter Mater. Phys.* **2013**, *88*, 35301.

(34) Helveg, S.; Lauritsen, J.; Laegsgaard, E.; Stensgaard, I.; Norskov, J.; Clausen, B.; Topsoe, H.; Besenbacher, F. Atomic-Scale Structure of Single-Layer MoS_2 Nanoclusters. *Phys. Rev. Lett.* **2000**, *84*, 951–954.

(35) Hansen, L. P.; Ramasse, Q. M.; Kisielowski, C.; Brorson, M.; Johnson, E.; Topsøe, H.; Helveg, S. Atomic-Scale Edge Structures on Industrial-Style MoS_2 Nanocatalysts. *Angew. Chemie - Int. Ed.* **2011**, *50*, 10153–10156.

(36) Lauritsen, J. V.; Kibsgaard, J.; Topsøe, H.; Helveg, S.; Clausen, B. S.; Laegsgaard, E.; Besenbacher, F. Size-Dependent Structure of MoS_2 Nanocrystals. *Nat. Nanotechnol.* **2007**, *2*, 53–58.

(37) Schweiger, H.; Raybaud, P.; Kresse, G.; Toulhoat, H. E. Shape and Edge Sites Modifications of MoS_2 Catalytic Nanoparticles Induced by Working Conditions: A Theoretical Study. *J. Catal.* **2002**, *207*, 76–87.

(38) Robertson, A. W.; Allen, C. S.; Wu, Y. a.; He, K.; Olivier, J.; Neethling, J.; Kirkland, A. I.; Warner, J. H. Spatial Control of Defect Creation in Graphene at the Nanoscale. *Nat. Commun.* **2012**, *3*, 1144.

(39) Luo, S.; Hao, G.; Fan, Y.; Kou, L.; He, C.; Qi, X.; Tang, C.; Li, J.; Huang, K.; Zhong, J. Formation of Ripples in Atomically Thin MoS_2 and Local Strain Engineering of Electrostatic Properties. *Nanotechnology* **2015**, *26*, 105705.

(40) Miro, P.; Ghorbani-Asl, M.; Heine, T. Spontaneous Ripple Formation in MoS_2

Monolayers: Electronic Structure and Transport Effects. *Adv. Mater.* **2013**, *25*, 5473–5475.

(41) Trevethan, T.; Latham, C. D.; Heggie, M. I.; Briddon, P. R.; Rayson, M. J. Vacancy Diffusion and Coalescence in Graphene Directed by Defect Strain Fields. *Nanoscale* **2014**, *6*, 2978–2986.

(42) Kuhlmann-Wilsdorf, D. Theory of the Interaction of Vacancies with Stress Fields in Metals. II. The Interaction between Vacancies and Dislocations. *J. Appl. Phys.* **1965**, *36*, 637–646.

(43) Algara-Siller, G.; Kurasch, S.; Sedighi, M.; Lehtinen, O.; Kaiser, U. The Pristine Atomic Structure of MoS_2 Monolayer Protected from Electron Radiation Damage by Graphene. *Appl. Phys. Lett.* **2013**, *103*, 203107.

(44) Yu, S.; Zheng, W. Fundamental Insights into the Electronic Structure of Zigzag MoS_2 Nanoribbons. *Phys. Chem. Chem. Phys.* **2016**, *18*, 4675–4683.

(45) Warner, J. H.; Rümmeli, M. H.; Ge, L.; Gemming, T.; Montanari, B.; Harrison, N. M.; Büchner, B.; Briggs, G. A. D. Structural Transformations in Graphene Studied with High Spatial and Temporal Resolution. *Nat. Nanotechnol.* **2009**, *4*, 500–504.

Chapter 7

Conclusion and Future Outlook

7.1 Conclusion

The purpose of this doctorate thesis is to make contributions to a more detailed and systematic understanding of the configurations and dynamics of defective structures in 2D materials. It covers four specific topics in this broad area: i) Bond length variations and strain distributions at divacancy structures in monolayer graphene; ii) The configurations of Si dopants at graphene edges; iii) The interactions between gold nanoclusters and monolayer graphene lattice; iv) The fabrication of atomically smooth line defects and zigzag edges in monolayer MoS_2.

It have been proved that without the introduction of foreign atoms, defects purely based on absent C atoms have great influence on the electronic and magnetic properties of graphene. Therefore a deep understanding of the intrinsic defects in atomic scale is necessary, which is also the starting point of this thesis. Divacancies are one of the most common defects in graphene and can take three structural different forms (5-8-5, 555-777 and 5555-6-7777) through various sequences of bond rotations to minimize the energy. Using AC-TEM with monochromation of the electron source, the position of C atoms in graphene are clearly resolved, enabling a map of bond strain to be generated. The results indicate that bond rotations within divacancies reduce the maximum single bond strain within a divacancy and help evenly distribute the strain

over a larger number of bonds, which is believed to be the motivation for structural change.

How the introduced foreign atoms interact with the host 2D materials has also attracted special attentions from researches. With the use of in-situ heating system, the decoration of Si dopants at monolayer graphene edge is investigated as the second topic. Si atoms are bonded to both armchair and zigzag edges with various configurations, and the most frequently observed ones are summarized to provide structural information for potential applications of the Si-doped monolayer graphene system. In comparison to the substitutional dopants in the bulk lattice, Si atoms bonded to the edge of graphene reveal reduced out-of-plane distortion and bond elongations based on the observation.

Foreign atoms also can be adatoms settling on the surfaces of 2D materials, and in some cases, they aggregate into nanoclusters which have interesting behaviours. The third part of results in this thesis focuses on the structures and dynamics of planar gold nanocrystals on the graphene surface and anchored to defect sites in graphene. Two unique crystalline phases, squared and hexagonal corresponding to {100} and {111} crystal planes, are observed above the melting temperature of gold nanoparticles due to the strong interaction between gold and graphene. The interaction is also confirmed by the epitaxial correlation between graphene and planar gold crystals.

The final part of the experiments is based on another 2D material, monolayer MoS_2. Linear defective structures in MoS_2 including line defects and zigzag edges have been possess novel electronic, magnetic and optical properties. Therefore methods to create atomically flat and long line defects and edges are essential for future exploitation on the applications. Heating monolayer MoS_2 to 800 °C in vacuum induces the

evaporation of surface contaminates, therefore the line defects created in this circumstance are atomically flat without any flaw. Line defects and edges as long as 65 nm have been created by this method. The atomic structures for the line defects created at elevated temperatures are more compacted along width direction with more out-of-plane displacement in comparison with the counterparts at room temperature. Line defects are able to serve as transport channels for Mo atoms. Pores are created within the areas where the MoS_2 surface is covered by carbon residues, and atomically flat zigzag edges will form when the hole propagating into clean MoS_2 lattice. The zigzag edges along both $(10\bar{1}0)$ and $(\bar{1}010)$ planes are terminated with Mo atoms. Layer-by-layer etching process is directly imaged with the support of theoretical calculations. The atomically sharp edges retain atomic smoothness, confirming the robustness of the edge states after cooling back to room temperature.

7.2 Future Outlook

The next step of experimental design is to continue the study of the structures and behaviours of other intrinsic defects in MoS_2 at elevated temperatures and understand why some unique structures can only be formed at high temperatures. Patterning defective structures in a more controllable approach may also be worth exploration. This approach can extend to other 2D materials. Furthermore, the study of gold-graphene interactions can be replicated to TMDs and other metals with the use of STEM, which can provide more straightforward results when multiple-elemental material systems are involved.

Appendix A

Supplementary Materials for Chapter 4

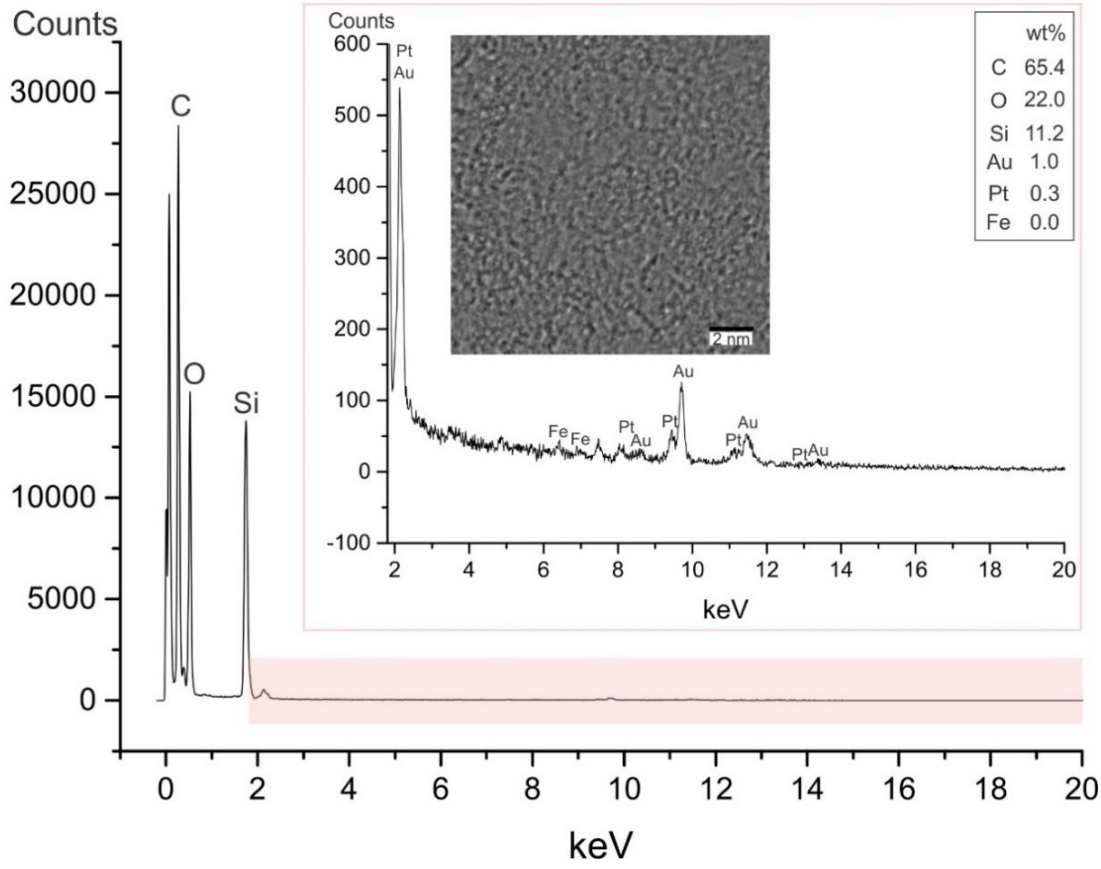

Figure A1 Low magnification image and EDX spectrum, and magnifying spectrum showing detailed peaks from 2 keV to 20 keV.

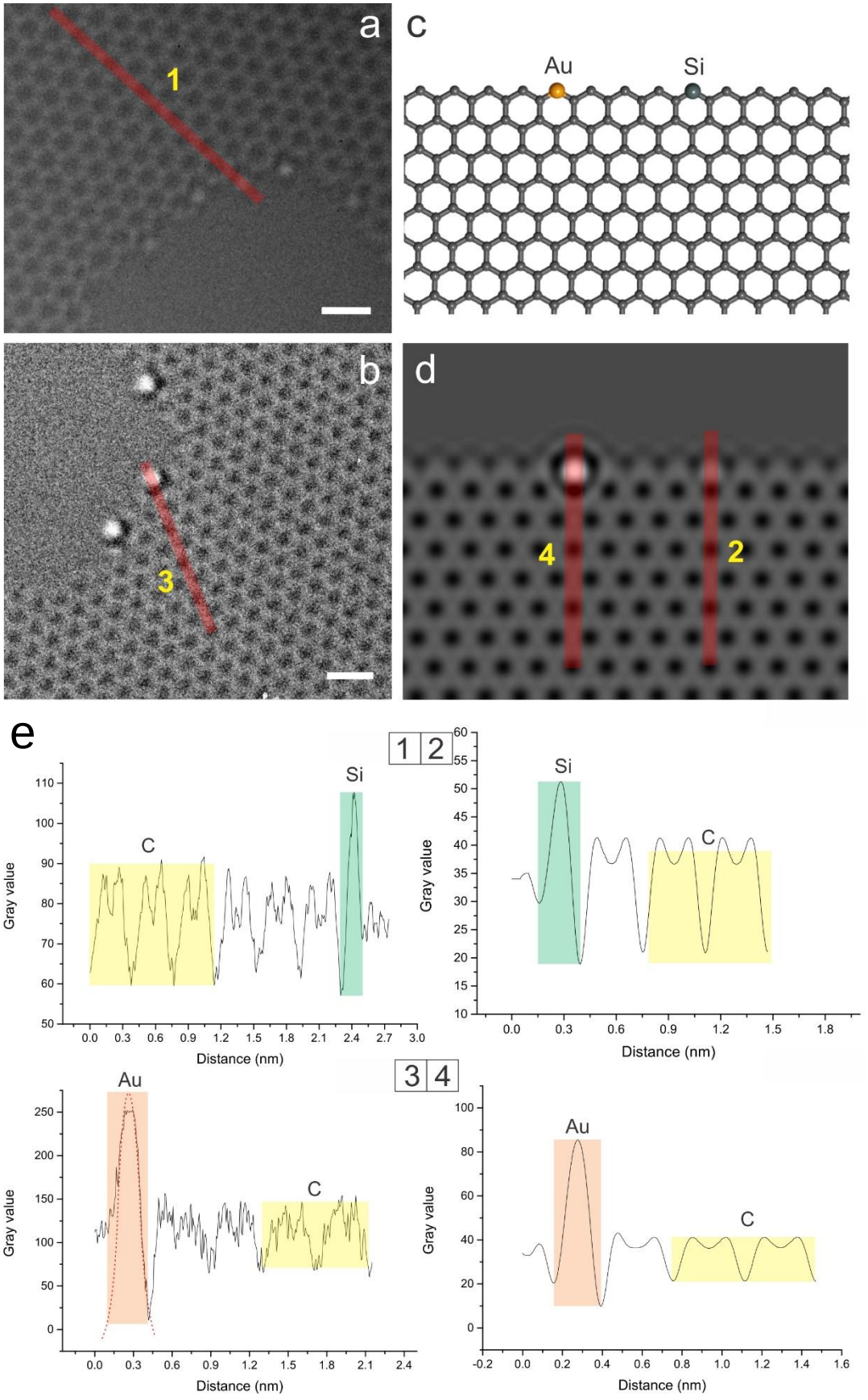

Figure A2 Comparison of contrast ratios for single Si/Au atoms to C atoms. (a) AC-TEM image with Si atoms sitting at the graphene edge. (b) AC-TEM image with Au atoms sitting

at graphene edge. (c,d) Atomic model and its image simulation of a Si atom and a gold atom at graphene edge. (e) Box-average Intensity profiles corresponding to the red rectangles 1-4 in (a,b and d). Coloured box in the intensity profiles demonstrate the contrast for different elements. Scale Bar: 0.5 nm.

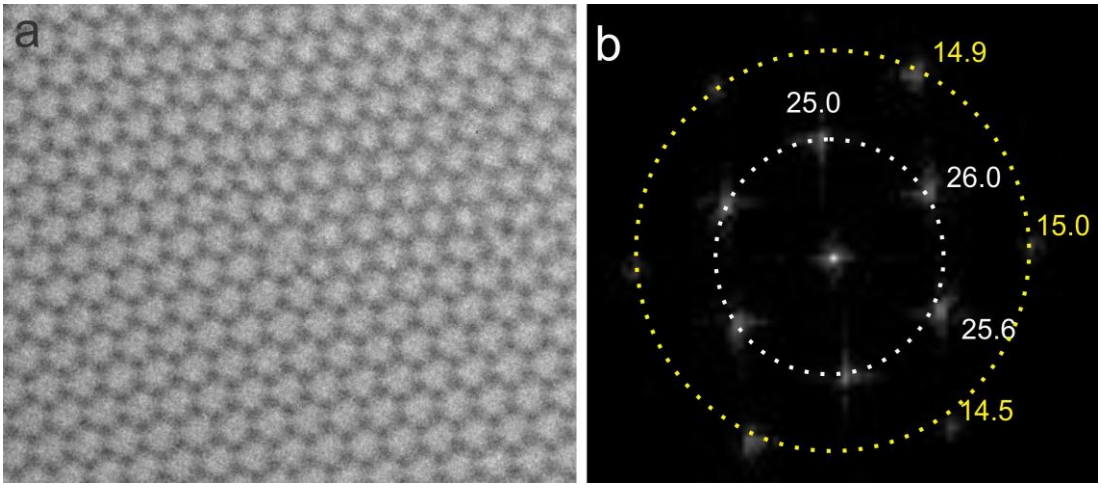

Figure A3 Setting scales for individual orientations based on the d-spacings of $\{10\bar{1}0\}$ and $\{11\bar{2}0\}$ planes of graphene. (a) AC-TEM image of a 5-8-5 defect with its surrounding hexagonal lattice. (b) Corresponding FFT of (a). While and yellow dashed ellipses represent $\{10\bar{1}0\}$ and $\{11\bar{2}0\}$ planes of graphene corresponding to 2.13 Å and 1.23 Å in real space respectively. The values are directly read from the image in pixel/cycle.

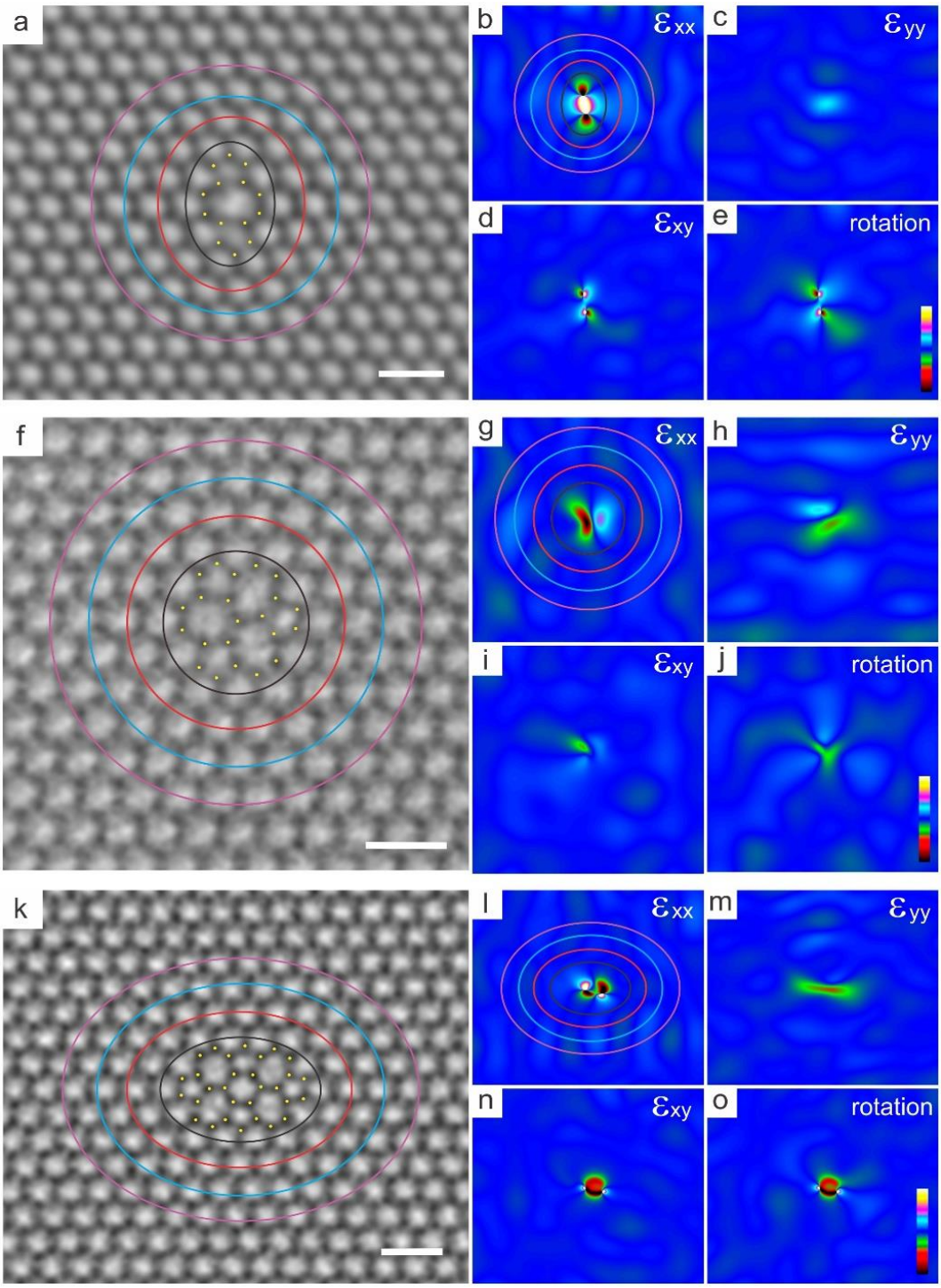

Figure A4 Strain mappings of the three DVs based on TEM images. Scale bar: 500 pm. (a,f,k) Gray scale TEM image of 5-8-5, 555-777 and 5555-6-7777 defect. (b-e,g-j,l-o) Strain mappings for the three DVs with the type of strain marked at upper-right corner in each mapping. The CLUT palette covers the range from -50% to 50% for the normal and shear strain field and ± 0.5 radians for the rotation. The four ellipses in both TEM images and ε_{xx} mappings correspond to the most (black), second (red), third (blue) and fourth (violet) nearest hexagonal rings from the defect boundaries.

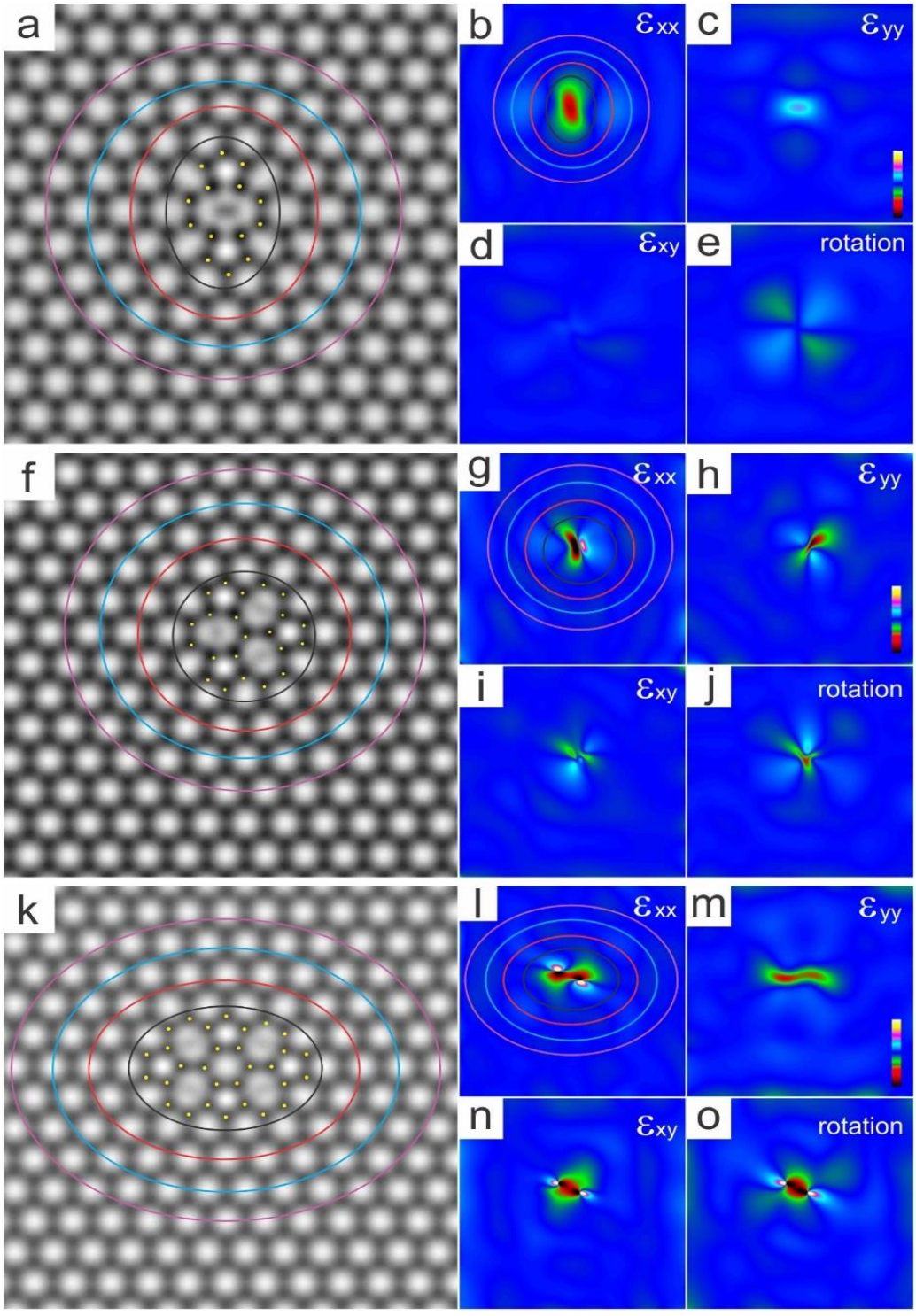

Figure A5 Strain mappings of the three divacancies based on image simulations of DFT calculated models. Scale bar: 500 pm. (a,f,k) Gray scale image simulations of 5-8-5, 555-777 and 5555-6-7777 defect (b-e,g-j,l-o) Strain mappings for the three divacancies with the type of strain marked at upper-right corner in each mapping. The CLUT palette covers the range from -50% to 50% for the normal and shear strain field and ± 0.5 radians for the rotation.

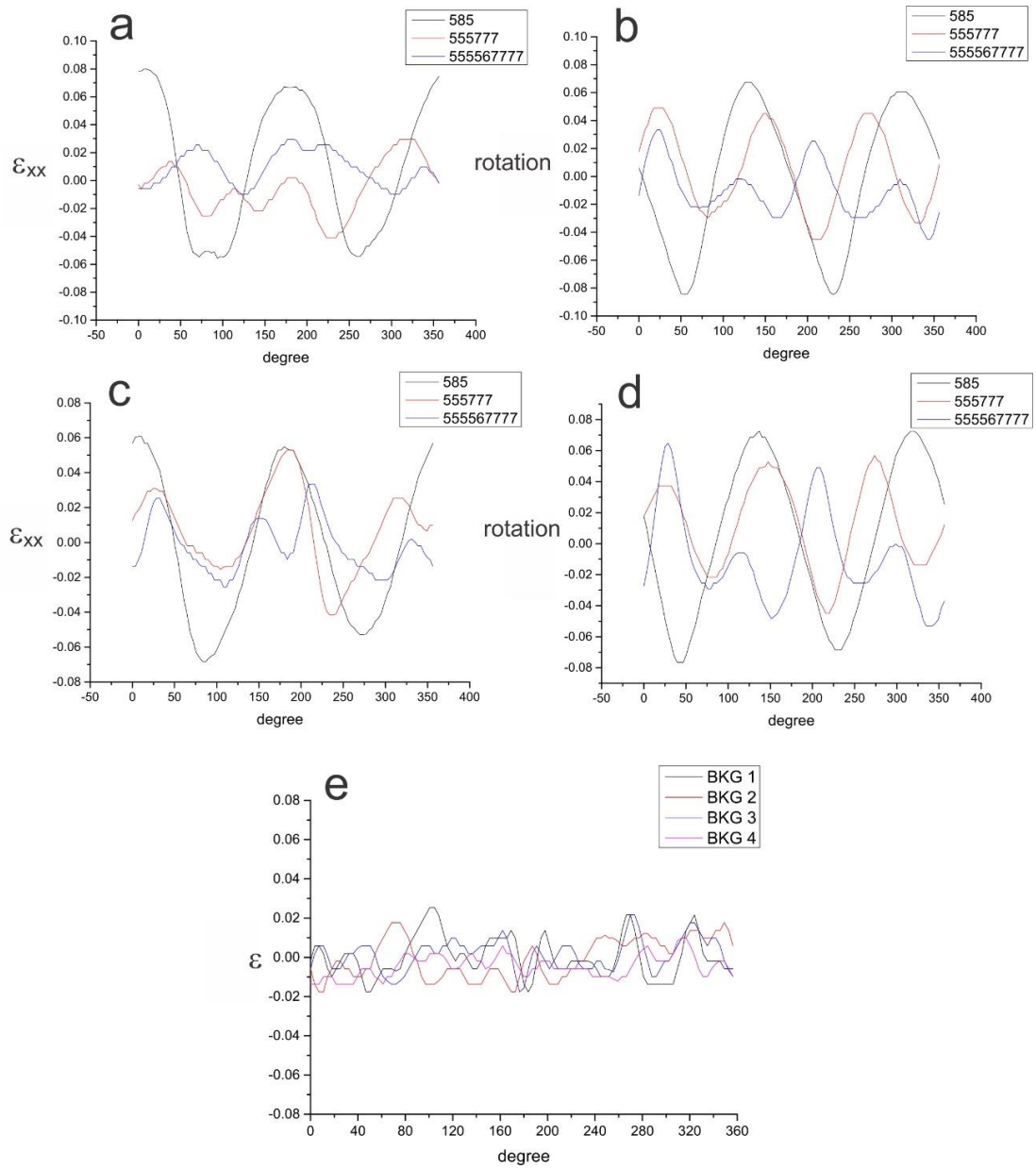

Figure A6 Oval strain profiles of (a) ε_{xx} (TEM), (b) rotation (TEM), (c) ε_{xx} (DFT), (d) rotation (DFT) along the nearest hexagonal neighbours. (e) Background profiles in unstrained graphene, with one for each strain type.

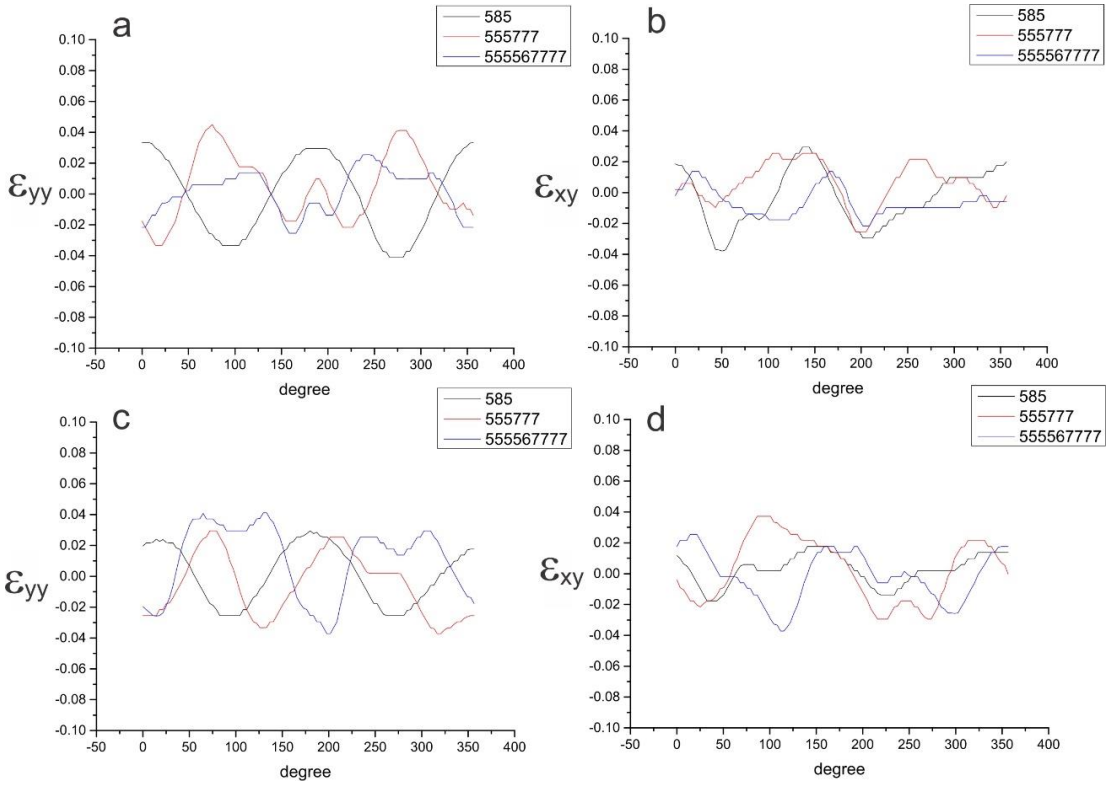

Figure A7 Oval strain profiles of (a) ε_{yy} (TEM), (b) ε_{xy} (TEM), (c) ε_{yy} (DFT), (d) ε_{xy} (DFT) along the nearest hexagonal neighbours.

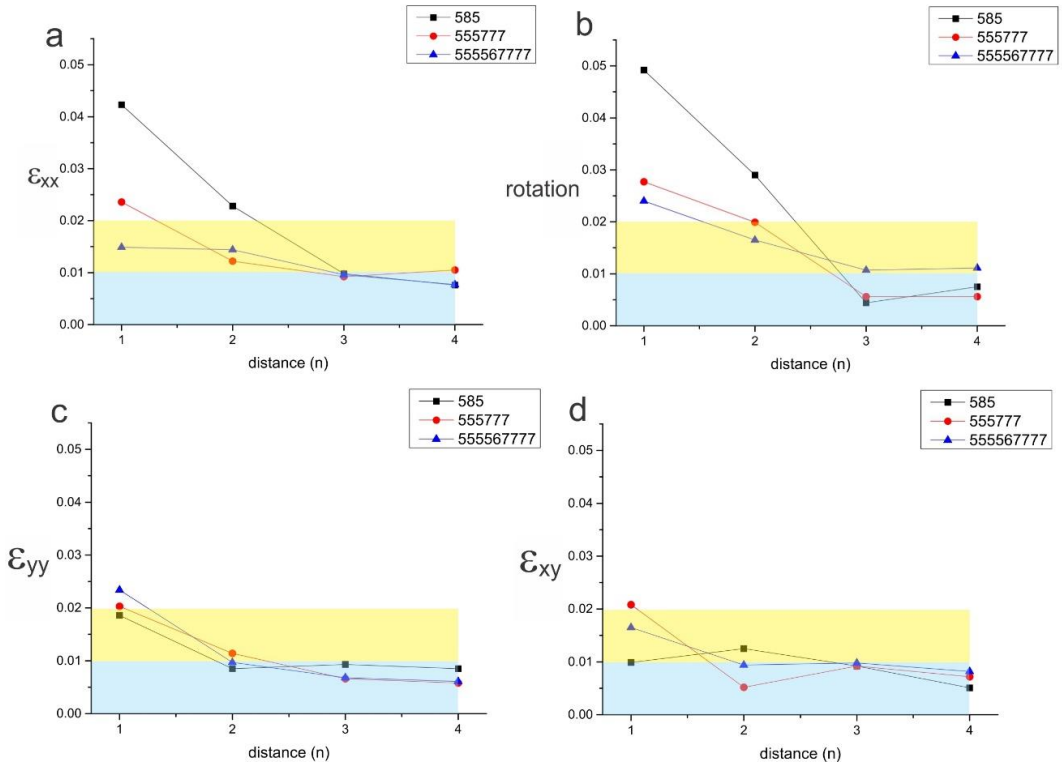

Figure A8 Standard deviations of strains from the first to fourth nearest neighbours measured on simulated images. (a) ε_{xx}, (b) rotation , (c) ε_{yy} and (d) ε_{xy}. The pale blue regions (0-0.01)

represent for the standard deviation of the background and the pale yellow boxes reach the value of double standard deviations (0.02).

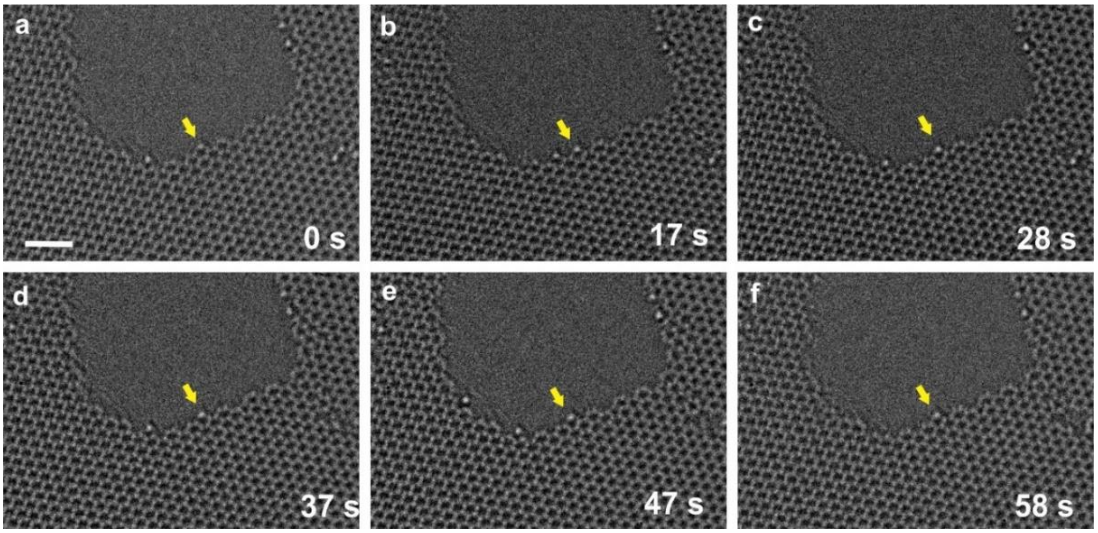

Figure A9 (a-f) A Si atom at pentagon configuration (pointed by yellow arrows) in 6 continuous frames. Scale bar: 1 nm.

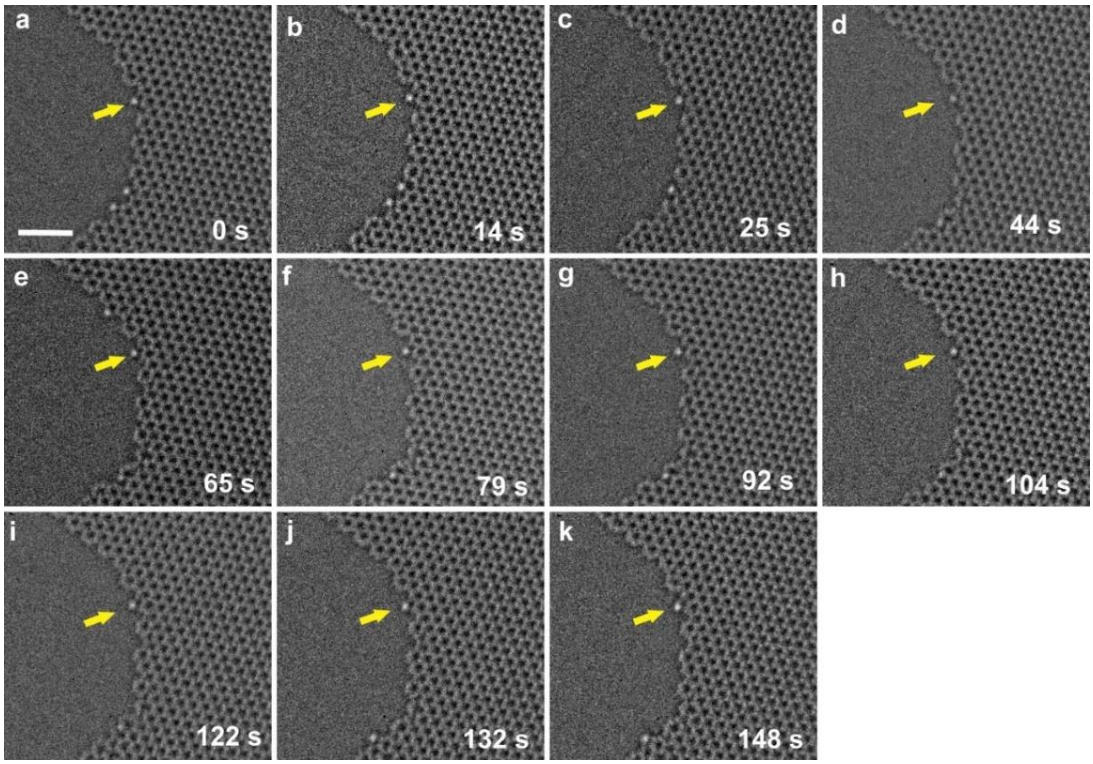

Figure A10 (a-k) A Si atom at tetragon configuration (pointed by yellow arrows) in 11 continuous frames. Scale bar: 1 nm.

Appendix B

Supplementary Materials for Chapter 5

The quantitative relationship between melting temperature and particle size can be expressed by Gibbs-Thomson equation:

$$\mathrm{T} = T_{\infty}(1 + \frac{3\Delta\sigma}{r\Delta H(T_{\infty})})$$

Where T_{∞} is the melting temperature of bulk gold crystal (1337.6 K), $\Delta\sigma$ is the solid-liquid interface energy per unit area ($\sigma_S = 1.325\, J/m^2$, $\sigma_L = 1.125\, J/m^2$), $\Delta H(T_{\infty})$ is the enthalpy of fusion per unit volume for gold ($1.243 \times 10^9 J/m^3$), and r is the radius of the gold particle.

The equation can be used to estimate the melting temperature of gold nanocrystals with 2nm diameter. The melting point of a 3D gold crystal with 2 nm-diameter is about 690 K, which is significantly lower than the experimental temperature (1073 K).

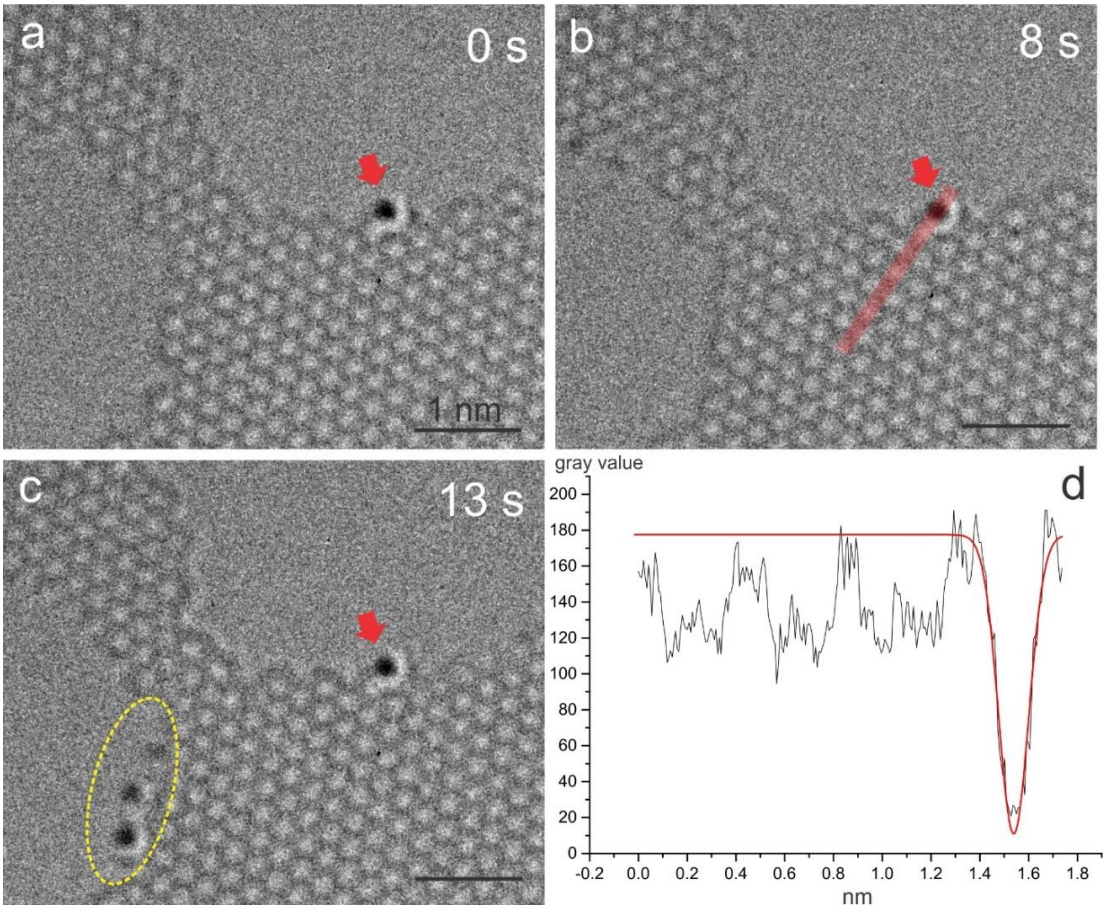

Figure B1 (a-c) AC-TEM images showing a gold atom at graphene edge (pointed by the red arrows) without migration within 13 s. (d) Box-average intensity profiles for the area within the red box in (b).

Figure 5-7(g) shows the statistic result for the intensity values of 20 gold atoms at graphene edges. The samples are carefully selected as most of the gold atoms at graphene edge are highly mobile. The intensity of a contrast spot of gold is greatly dependent on the stability within the 2 s acquisition time. In order to obtain the actual contrast of the isolated gold atoms without the distraction caused by the stability, gold atoms that occurring in three sequential frames without migration are chosen, as the gold atom pointed by the red arrows, and the intensity values are collected from the middle frame. The yellow dashed ellipse in Figure B1(c) highlights three contrast spots for gold atoms that shows high mobility. It can be seen that they are lighter than the most stable one.

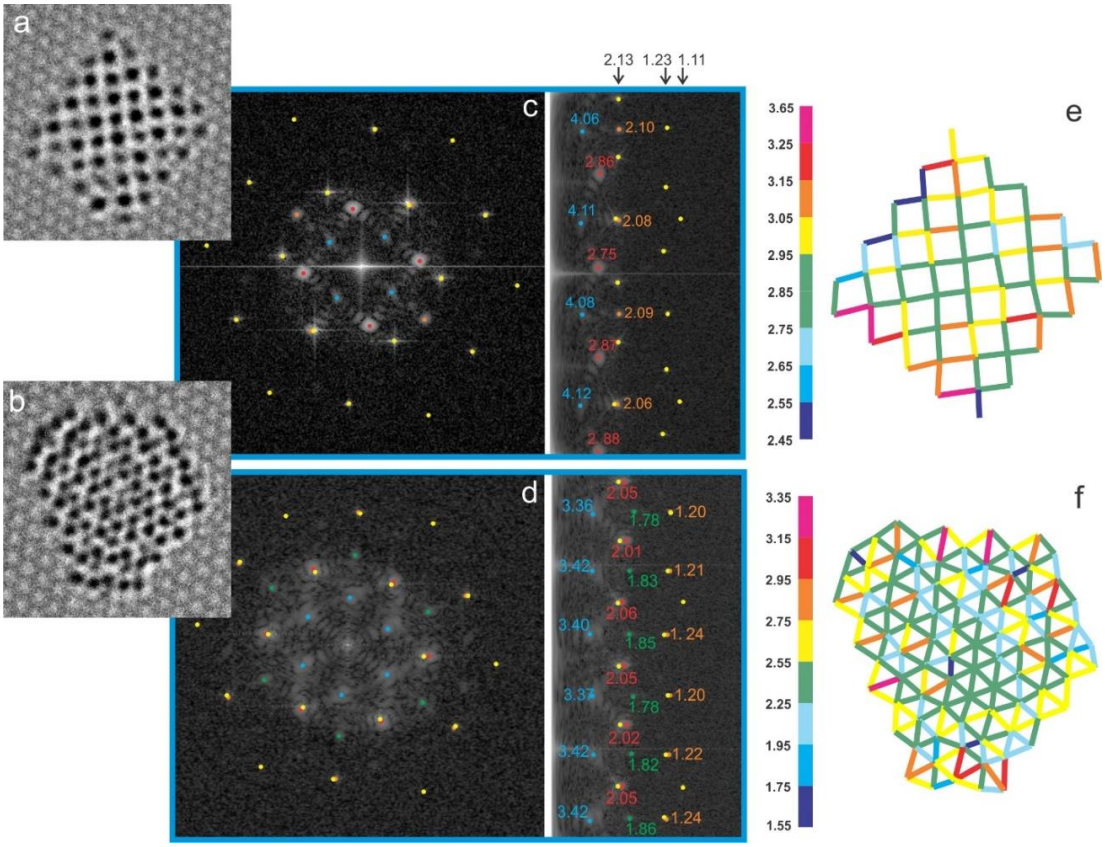

Figure B2 (a,b) TEM images of the two crystalline phases of gold. (c,d) Original and polar transformed FFT patterns, with d-spacings exhibiting in different colours in Angstrom for different crystal planes. Yellow spots are for graphene lattice, $\{10\bar{1}0\}$, $\{11\bar{2}0\}$ and $\{20\bar{2}0\}$, with their d-spacings of 2.13, 1.23, and 1.11 Å. (e,f) The distances between each two adjacent contrast spots in (a) and (c). Green lines are for the distances around the average, warm colours are for expansion, and cold colours are for contraction. Values in colour bars are in Angstrom.

The variations of the d-spacing values are from slight astigmatism and measurement error, but the lattice constant of the original FCC unit can still be calculated based on these values for the two crystalline phases. For the case of the squared crystalline phase, the lattice constant is 4.08 ± 0.07 Å, while for hexagonal phase, the lattice constant is 3.25 ± 0.10 Å. The distances between gold atoms shown in Figure B2(e,f) demonstrate that most deviations, including elongation and shrinkage, happen at the edge areas, where the gold atoms are with fewer neighbours and less restrictions.

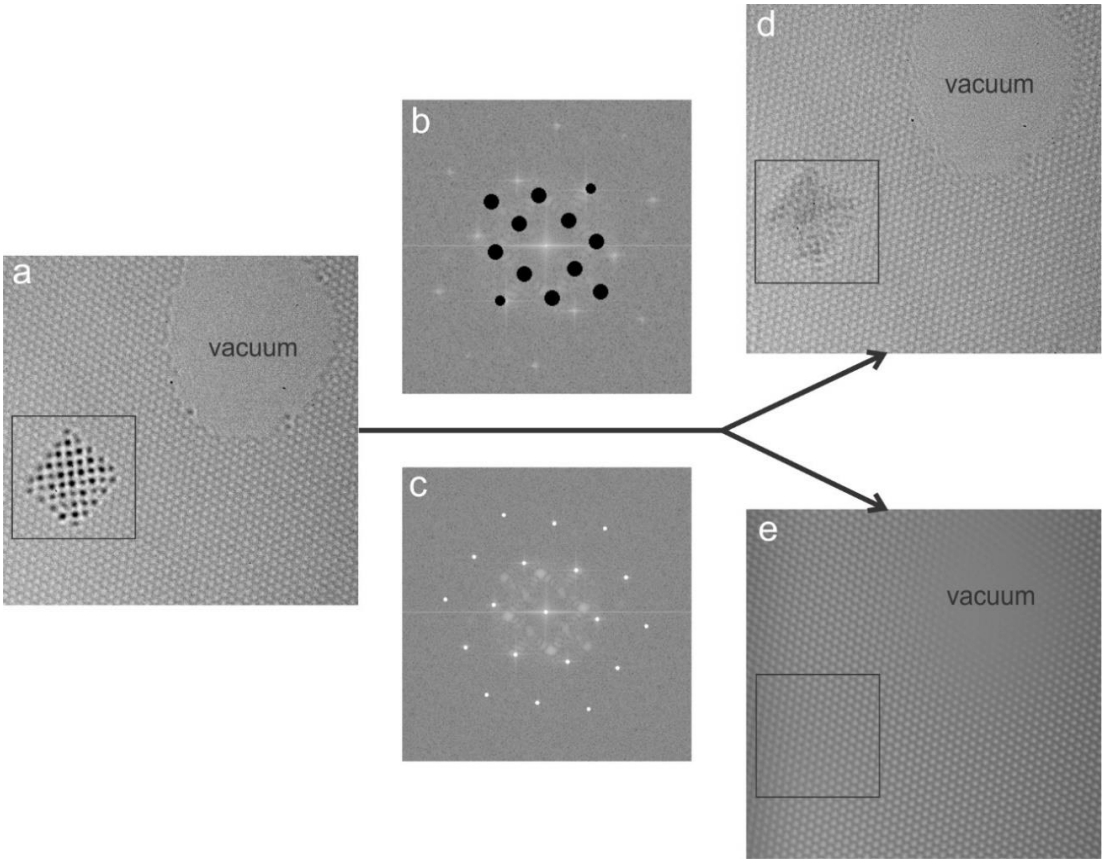

Figure B3 (a) AC-TEM image of the gold particle with square crystalline phase on monolayer graphene. (b) Corresponding FFT pattern with the elimination of the information of the gold crystal. (c) FFT pattern with the selection of the information of the monolayer graphene. (d) Reconstructed TEM image based on (b). (e) Reconstructed TEM image based on (c).

The crystal information of gold and graphene can be separated with the assistance of FFT pattern, where two sets of patterns are shown, and the information of one of the crystal can be selected or removed by colouring them in white (Figure B3(c))or black (Figure B3(b)). The inverse transform of the selected FFT patterns in Figure B3(d,e) show only the graphene signal. In both cases, the information underneath the gold crystal (highlighted in black box) is entirely different with the vacuum area. Combining with the periodic structure in surroundings, one can confirm the presence of a monolayer graphene beneath the gold crystal.

Appendix C

Supplementary Materials for Chapter 6

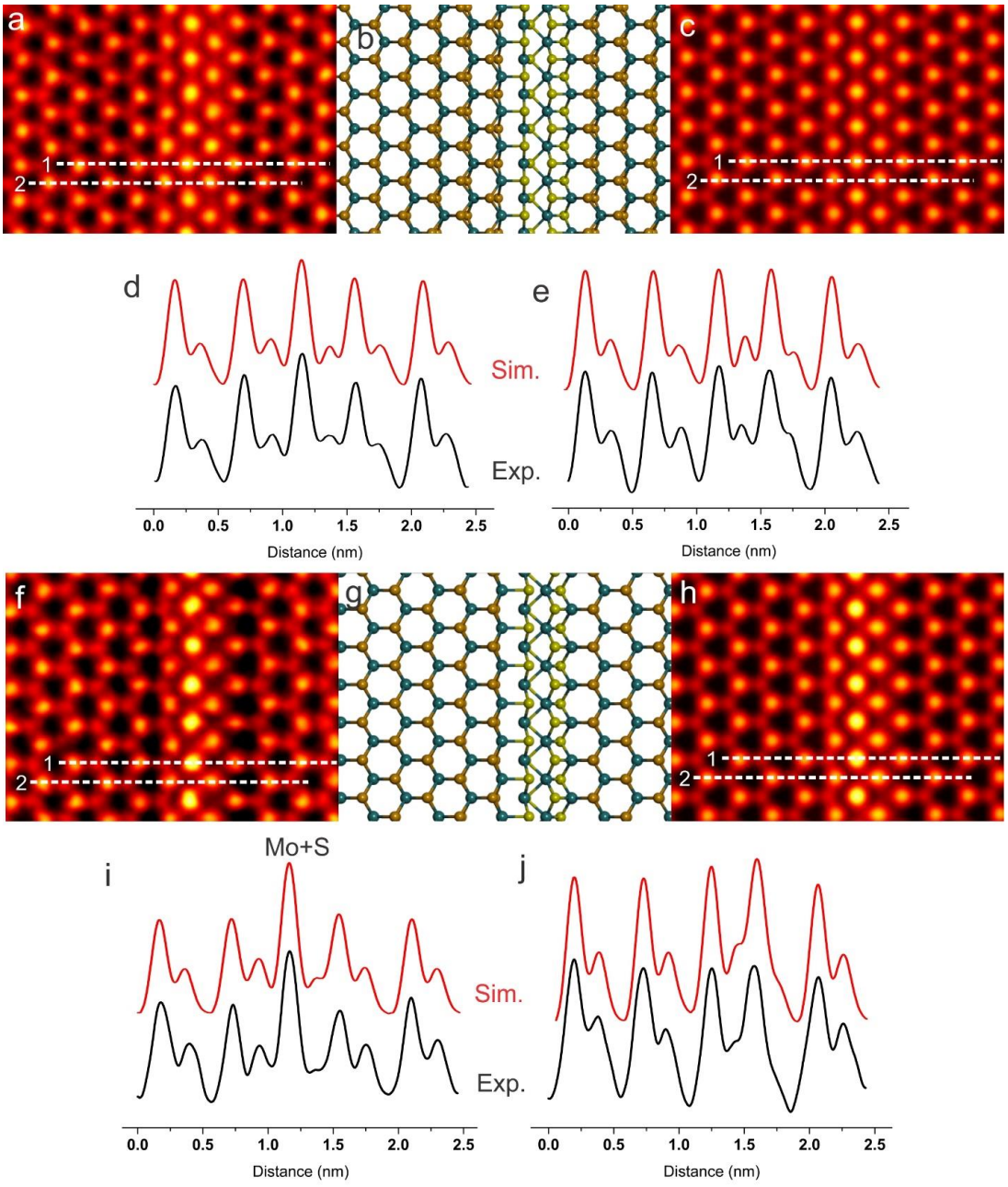

Figure C1 Experimental and simulated images of two types of line defects. (a) Smoothed HAADF image of a type 1 line defect. (b,c) DFT calculated model for type 1 line defect and its corresponding image simulation. (d,e) Box-average intensity profiles for the line 1 and 2 in (a) and (c) respectively. (f) Smoothed HAADF image of a type 2 line defect. (g,h) DFT calculated model for type 2 line defect and its corresponding image simulation. (i,j) Box-average intensity profiles for the line 1 and 2 in (f) and (h) respectively.

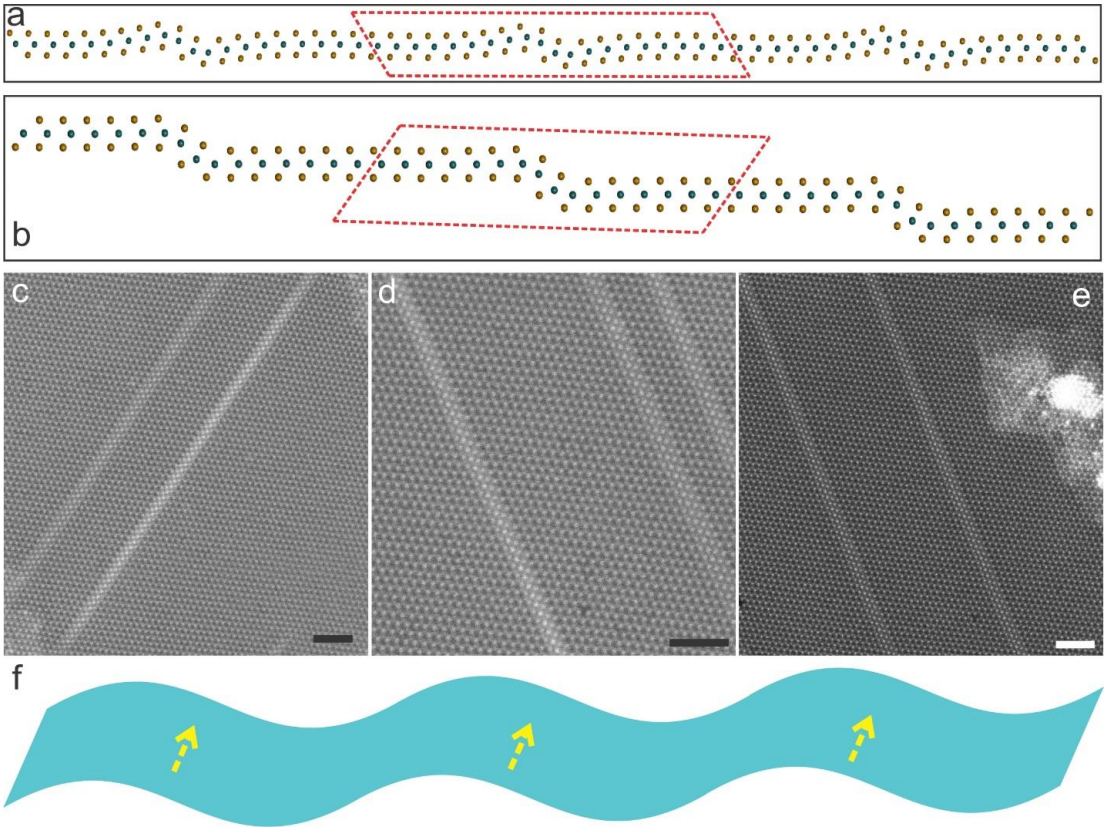

Figure C2 (a,b) Side views of DFT models of type 1 and 2 line defect with the unit cell highlighted in red boxes. (c-e) HAADF images showing examples of parallel line defects. (f) A schematic of rippling nature of monolayer MoS_2 with the yellow arrows indicating the line defect length directions.

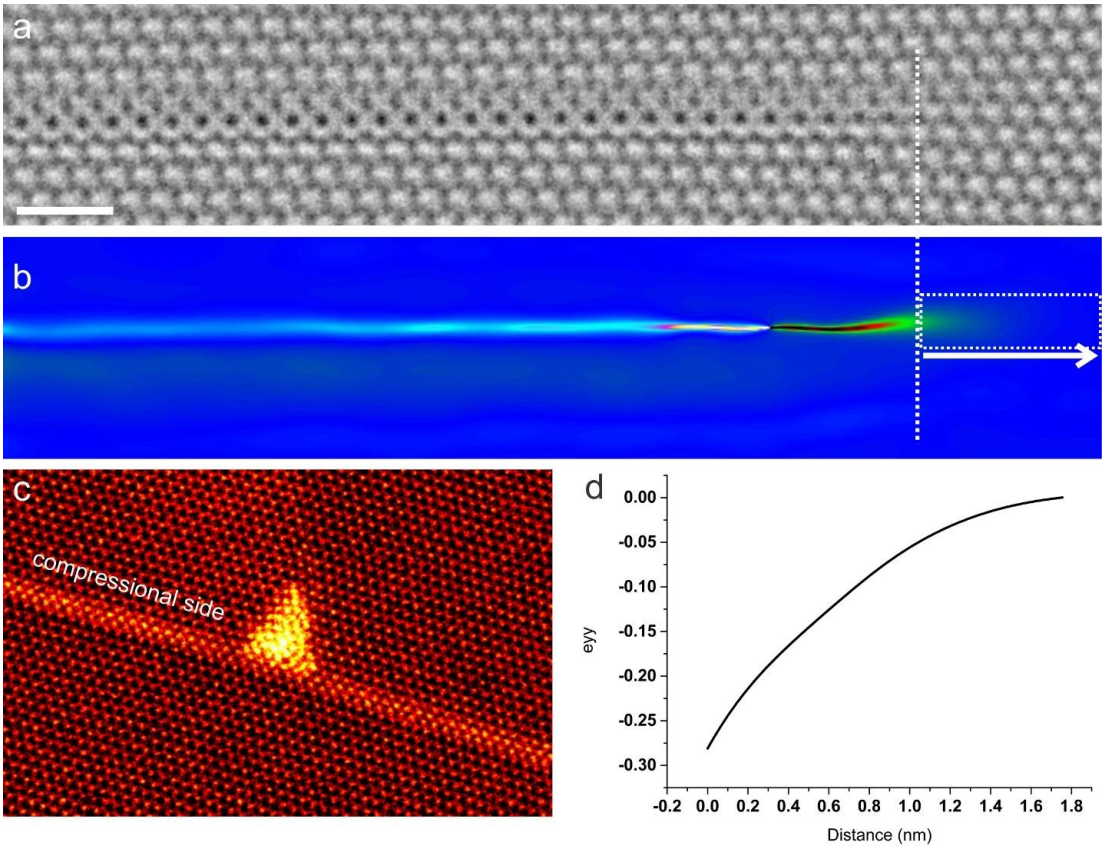

Figure C3 Surrounded strain field of a type 2 line defect. (a) AC-TEM image of a line defect (type 2). (b) Corresponding normal strain field along y direction. The white dash line indicates the end of the line defect and the while box includes the strain field at the line defect tip with the corresponding box-average profile along the arrow direction shown in (d).(c) A HAADF image showing a Mo cluster trapped at the compressional side of a line defect.

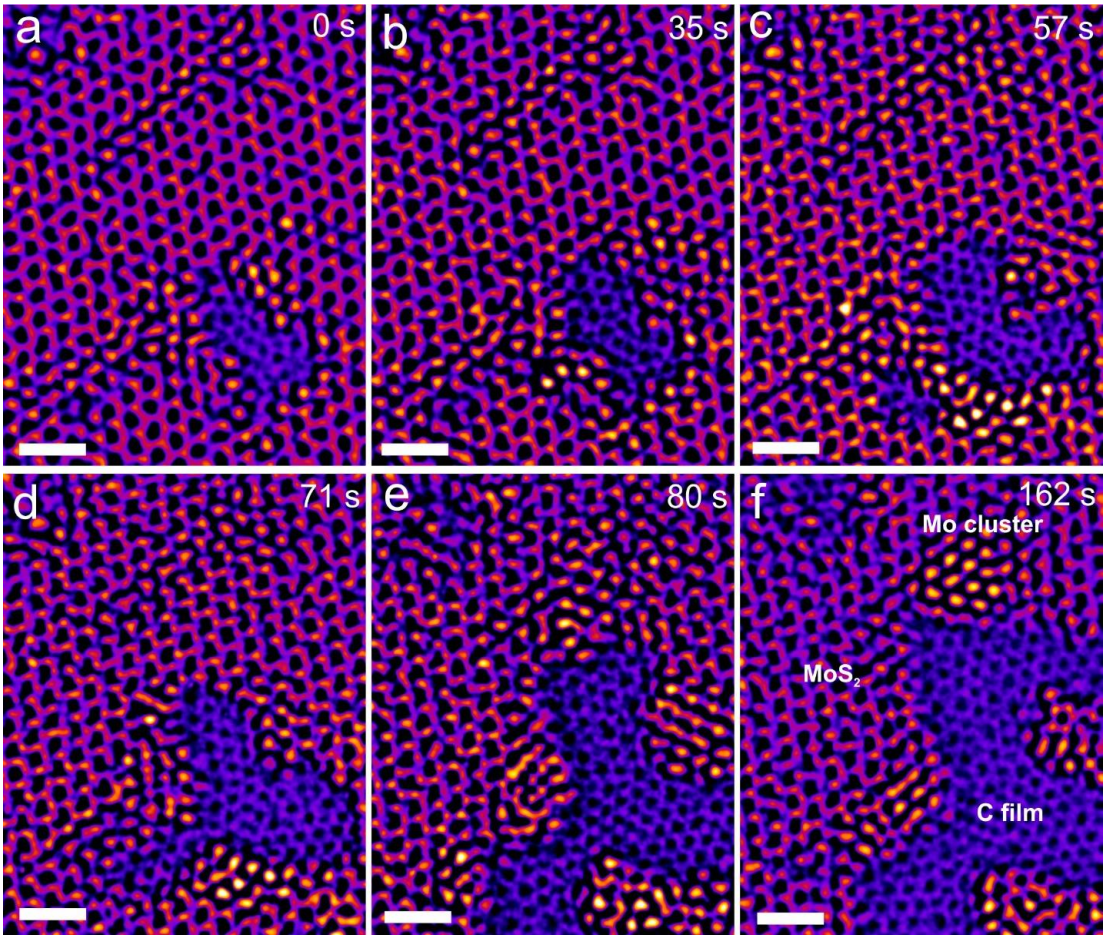

Figure C4 (a-f) Propagation of a hole in MoS_2 lattice at 800 °C with carbon film covered on the surface. Scale bar in (a-f), 1 nm.

The intermediate state before the formation of reconstructed S edge is a Mo terminated Klein edge. S vacancies are highly mobile on the clean MoS_2 lattice with a low energy barrier of 2.33 eV per S vacancy. They rapidly migrate to the edge site to replace the outermost line of S atoms, resulting in reconstruction of the edge. This transition is extremely fast and the intermediate Klein edge state is rarely observed (Figure C5(a) is the only example that have been captured in the experiment). Considering the maximum energy that can transfer from the 80 kV electron beam, the possibility of directly knocking out unsaturated S atoms from the edge cannot be ruled out. Figures C5(c-f) illustrate a plausible route for the reconstruction. The intermediate state in Figure C5(a) is the model shown in Figure C5(e) and Figure C5(g) corresponds to the

reconstructed S edge (Figures C5(a) and Figure C5(b)). The values shown in the figure indicates the energy required for ejection of the marked S atoms.

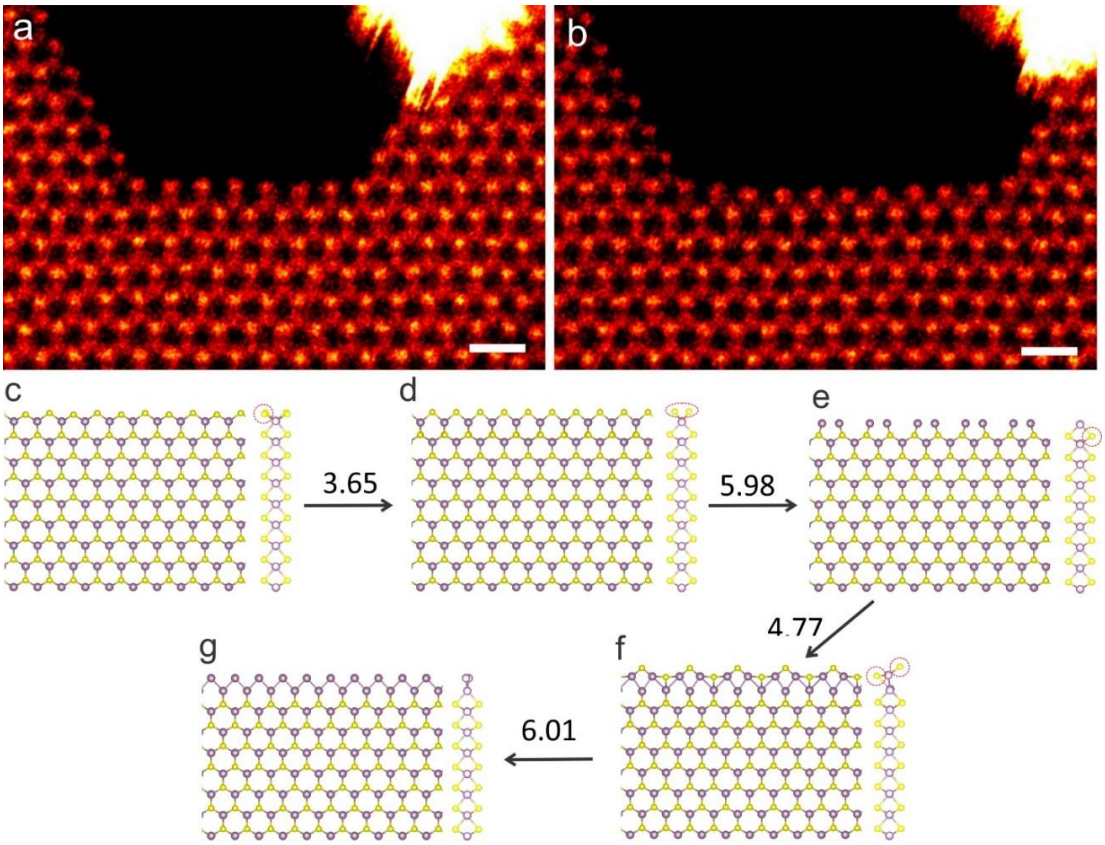

Figure C5 ADF images of an S edge (a) before and (b) after reconstruction. (c-f) illustration of a possible reconstruction route calculated from DFT. Red circles represent S atoms in the subsequent frame. Values are in eV/S atom. Scale bars in (a) and (b), 0.5 nm.

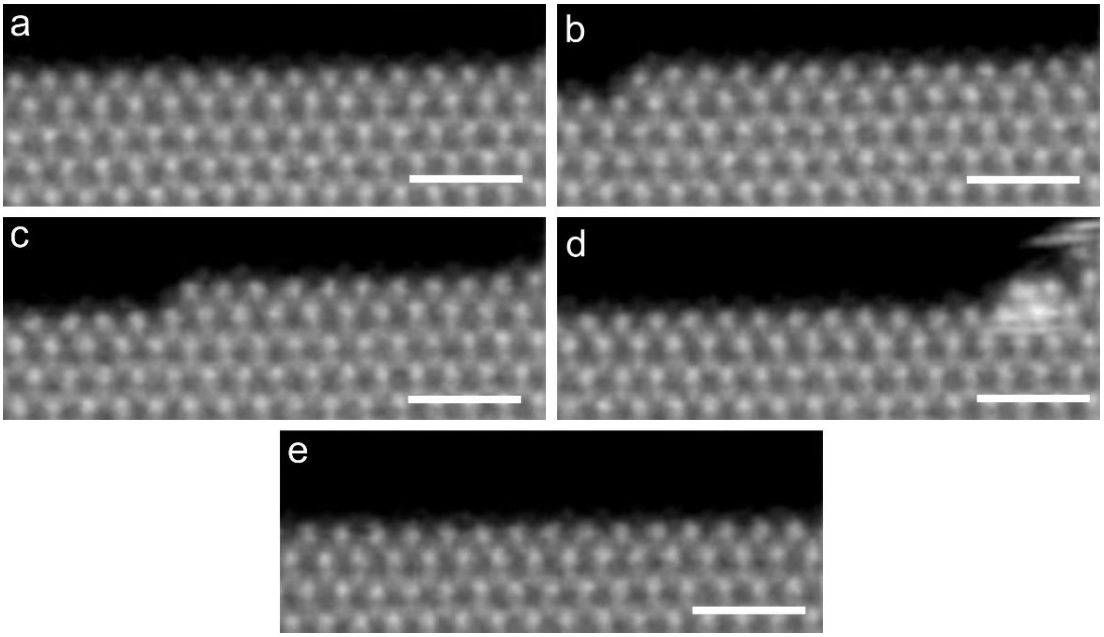

Figure C6 (a-e) Time series of HAADF-STEM images showing etching along a double Mo terminated edge. Time duration between each two frames ~4 s. Scale bars in (a-e), 1nm.

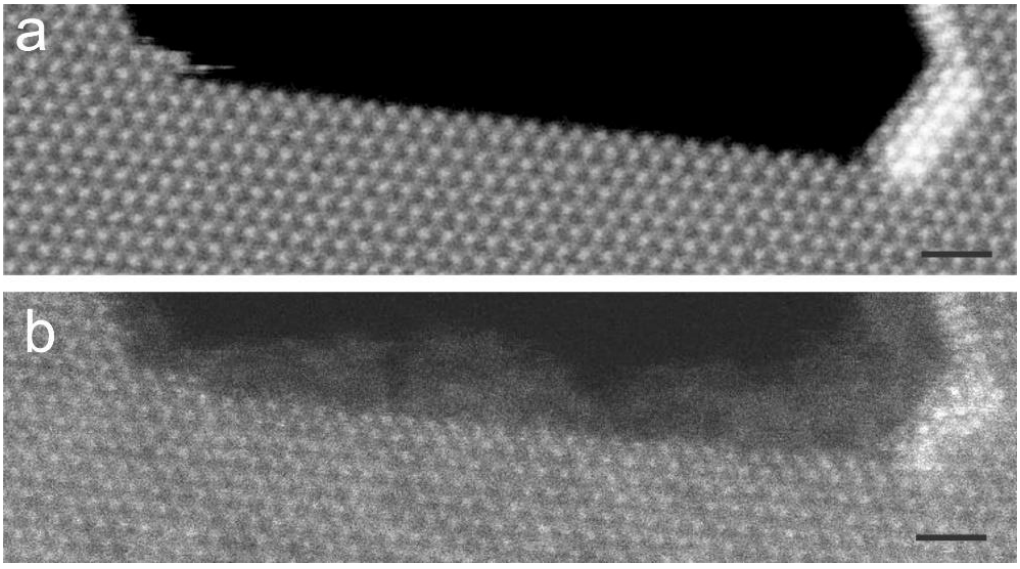

Figure C7 ADF images of the same edge at (a) 800 °C and (b) room temperature after cooling. The cloud-like shadow on MoS_2 surface in (b) is carbon contaminates absorbed after cooling down. Scale bar, 1 nm.